

# **Holistic fuel cycle modelling of a future fusion reactor**

## **Holistische Modellierung des Brennstoffkreislaufs eines zukünftigen Fusionsreaktors**

Zur Erlangung des akademischen Grades eines  
DOKTORS DER INGENIEURWISSENSCHAFTEN (Dr.-Ing.)

von der KIT-Fakultät für Maschinenbau des  
Karlsruher Instituts für Technologie (KIT)

genehmigte

DISSERTATION

von

Yannick Nicolas Hörstensmeyer M.Sc.

aus Córdoba, Argentinien

Tag der mündlichen Prüfung:	29.4.2022
Erster Gutachter:	Prof. Dr. Robert Stieglitz Karlsruher Institut für Technologie (KIT)
Zweiter Gutachter:	Prof. Dr. Rudolf Neu Max-Planck-Institut für Plasmaphysik (IPP) Garching







# Danksagung

Die vorliegende Arbeit entstand im Rahmen meiner Tätigkeit als Doktorand am Institut für technische Physik (ITEP) in Kooperation des Karlsruher Instituts für Technologie (KIT).

Dank gebührt dem Hauptreferenten Prof. Dr.-Ing. Robert Stieglitz für den Rahmen dieser Arbeit, dessen Betreuung, Diskussion und Durchsicht. Für die Anregungen insbesondere zur Plasmaphysik danke ich auch dem Korreferenten Dr. Rudolf Neu aus München.

Ermöglicht hat die Arbeit erst Herr Dr. Christian Day, in dessen Reich zwischen Stapeln aus Papier der Grundstein dieser Arbeit ersonnen und regelmäßig iteriert worden ist. Danke für die vielen wegweisenden Worte und Ihren Beitrag zu diesem nach Bachelor- und Masterarbeit nun dritten (und abschließenden) Dokument. Danke auch der Vakuumgruppe, Dr. Thomas Giegerich über den der Weg begann, Stefan Hanke und Katharina Battes, Santiago Ochoa und Volker Hauer für den herzlichen Empfang und stetige Unterstützung im Alltag der Wissenschaft.

Die einzelnen Komponenten des inneren Brennstoffkreislaufes zu verstehen und in ein Modell zu überführen entsprang den Diskussionen in internationaler Partnerschaft mit den jeweiligen Experten. Hierfür möchte ich mich bei Dr. Peter Lang, Bernhard Plöckl, Dr. Barry Butler, Dr. Fabio Cismondi, Prof. Dr. Silvano Tosti, und Dr. Alessia Santucci bedanken.

Auch den von mir betreuten Studierenden Stefanie Blust und Daniel Bitter danke ich für ihren Beitrag an dieser Arbeit.

Danke an meine Mitdoktoranden, insbesondere Benedikt Peters und Cyra Neugebauer für die intensive Zusammenarbeit und die gemeinsame Zeit.

Für Rückhalt, Optimismus und Kampfesgeist bis zuletzt, für Eloquenz und Geist, Herz und Verstand - den Mut es anders zu machen - danke ich meinen Eltern und meinem Bruder.

Liebe Tina, von ganzem Herzen danke ich dir für deine Hilfe, deine Bekräftigung, den Rückhalt, die Durchsicht der Arbeit und dessen grafische Überarbeitung.

---

---

# Kurzfassung

Die Gewinnung elektrischer Energie mittels magnetisch eingeschlossener Fusion stellt eine noch unerschlossene Quelle dar, dessen Verwirklichung derzeit weltweit vorangetrieben wird. Diese Arbeit beschreibt einen essenziellen Bestandteil der Infrastruktur eines solchen Kraftwerkes in einer umfassenden Simulation: den Brennstoffkreislauf.

Dabei handelt es sich um eine komplexe chemische Anlage, die im Wesentlichen die Wasserstoffisotope Deuterium und Tritium als Edukte zur Fusion bereitstellt. Um die Konzentration des Fusionsprodukts Helium im Reaktor zu begrenzen, ist der Durchsatz des Brennstoffgemischs wesentlich höher als die Reaktionsrate der Fusion selbst. Infolgedessen stellt unverbrannter Wasserstoff den überwiegenden Teil der Prozessgases am Reaktorausgang dar.

Der Brennstoffkreislauf muss sicherstellen, dass dieser Wasserstoff mit hoher Effizienz aus dem Abgasstrom zurückgewonnen und wiederverwertet werden kann. Dafür muss das Prozessgas erst mittels Vakuumpumpen aus dem Reaktor gesaugt werden. Anschließend wird der Wasserstoff über verschiedene Trennprozesse aus dem Abgasgemisch gefiltert. Schließlich wird das Wasserstoffgemisch dem Reaktor wieder zugeführt.

Im Detail werden in dieser Arbeit zuerst die Funktion und der Aufbau des Inneren Brennstoffkreislaufes für das Demonstrationskraftwerk DEMO aus dessen Randbedingungen hergeleitet. Danach werden die relevanten physikalischen Zusammenhänge der verwendeten Technologien beschrieben und als eigenständige Modelle in das Simulationsprogramm integriert. Besonderer Fokus liegt dabei auf den physikalischen Wechselwirkungen von Wasserstoff mit sich selbst, Flüssigkeiten wie Wasser sowie verschiedenen Metallen, die die Grundlage der verwendeten Trennprozesse bilden.

Zur Einbindung aller Subsysteme bildet das Simulationsprogramm den kompletten Kreislauf transient in der kommerziellen Software ASPEN<sup>®</sup> Custom Modeler ab. So können das Verhalten am Betriebspunkt, während des Anfahrprozesses und für veränderliche Randbedingungen abgebildet werden.

Insbesondere die Verwendung von Tritium beeinflusst das Design des Brennstoffkreislaufes. Das Inventar dieses seltenen und radioaktiven Isotopes ist auf ein Mindestmaß zu beschränken. Gleichzeitig darf nur ein Bruchteil des Tritiums in die Atmosphäre entweichen. Entsprechend hohe Anforderungen werden an die einzelnen Elemente des Kreislaufes gestellt.

Anhand eines repräsentativen Referenzpunktes wird eine Optimierung des Brennstoffkreislaufes nach seinen Hauptdesignkriterien durchgeführt. Aus der Betrachtung des Gesamtsystems ergibt sich dabei ein geschätzter Tritiumverlustterm in Höhe von 1.6 g pro Jahr, der im Verhältnis zu einem operativen Tritiuminventar von 6.3 kg steht. Die einzelnen Beiträge zu dem Gesamtinventar werden hergeleitet und sind zum großen Teil in flüssiger Form oder in Feststoffbetten vorzufinden.

Mithilfe von Massenbilanzen wird, unter Berücksichtigung der Verlustterme, der Einfluss jedes Teilsystems auf den Referenzpunkt diskutiert. In einer Parameterstudie werden dann die

---

wichtigsten Randbedingungen des Brennstoffkreislaufs variiert und entsprechende Anpassungsmöglichkeiten des Systems beschrieben.

Das Ergebnis dieser Arbeit ist ein umfassendes, modular aufgebautes und fundiertes Werkzeug zur Optimierung zukünftiger Brennstoffkreisläufe.



# Abstract

The production of electrical energy by means of magnetically confined fusion represents a yet unexploited source, the realisation of which is currently under development around the world. This work describes an essential component of the infrastructure of such a power plant in a comprehensive simulation: the fusion fuel cycle.

It represents a complex chemical plant tasked to provide the hydrogen isotopes deuterium and tritium as educts to the fusion reaction. To limit the concentration of the fusion product helium in the reactor, the throughput of the fuel mixture is maintained at a much higher rate than the rate of the fusion reaction itself. As a result, unburned hydrogen represents the predominant fraction of the reactor exhaust gas.

The fuel cycle must ensure that this hydrogen can be recovered and resupplied with high efficiency from the exhaust gas stream. To do this, the process gas must first be evacuated from the reactor environment with continuous vacuum pumps. Then the hydrogen is removed from the exhaust gas mixture using various separation processes. Finally, the hydrogen mixture is fed back into the reactor.

In detail, the function and structure of the Inner Fuel Cycle for the first-of-its-kind fusion reactor “DEMO“ are first derived from its boundary conditions. Then every technology is described by its relevant physics from the literature and integrated into the simulation programme as a stand-alone model. Particular focus is placed on the hydrogen chemistry underlying the different separation processes. Especially, the incorporation of tritium and tritiated species influences the design of the fuel cycle. This rare and radioactive isotope significantly limits the choice of technology and its emissions must be kept to an absolute minimum.

In order to integrate all subsystems, the fuel cycle simulator maps the complete cycle transiently within the commercial software ASPEN® Custom Modeler. In this way, the behaviour in steady state operation, during start-up and for mutable boundary conditions can be modelled.

On the basis of a representative reference point, an optimisation of the fuel cycle is carried out according to its main design criteria: (i) tritium self-sufficiency (ii) stable fuel composition and (iii) tritium retention and inventory. Consideration of the overall system results in an estimated tritium loss term of 1.6 g per year, which relates to an operational tritium inventory of 6.3 kg. Tritium losses in this context denote all loss terms to outside the confinement of the fuel cycle. The individual contributions to the total inventory are derived and are largely found in liquid form or bound in absorption beds.

Using mass balances, the influence of each subsystem on the performance at the reference point is discussed. In a parameter study, the most important boundary conditions of the fuel cycle are varied, and corresponding adaptation strategies are described.

In summary, the result of this work is a comprehensive, modular and well-founded tool to help optimize future fuel cycles.



# Table of Contents

<b>Kurzfassung.....</b>	<b>v</b>
<b>Abstract.....</b>	<b>ix</b>
<b>1 Introduction .....</b>	<b>1</b>
1.1 Approach and Objective of Work .....	2
1.2 Structure of Work.....	2
<b>2 Function of the Fusion Fuel Cycle .....</b>	<b>5</b>
2.1 Reactor Operation and Interfaces to the Fuel Cycle.....	5
2.2 DEMO as Design Driver of the Fuel Cycle.....	6
2.3 Breeding Blankets and other Fuel Cycle Boundaries .....	10
2.4 Fuel Cycle Architecture and Technologies .....	12
<b>3 Gas Transfer and Balance Processes in a Fusion Fuel Cycle.....</b>	<b>15</b>
3.1 Gas Species Characterisation .....	15
3.2 Simplified Hydrogen Treatment.....	17
3.3 Hydrogen Interaction Processes .....	18
3.4 Operational Aspects .....	24
3.5 Reference Design Point.....	26
<b>4 Fuel Cycle Simulator.....</b>	<b>29</b>
4.1 On the Choice of the Software Framework.....	30
4.2 Numerical Solution Approach.....	31
4.3 Decomposition of the Plant in Functional Blocks .....	33
<b>5 The Direct Internal Recycling Loop.....</b>	<b>35</b>
5.1 Matter Injection.....	37
5.2 Metal Foil Pumps .....	42
5.3 Vacuum Pumping.....	44
5.4 Gas Distribution Control and Metering.....	46
5.5 Direct Internal Recycling Loop Summary .....	47
<b>6 The Inner Tritium Loop .....</b>	<b>49</b>
6.1 Exhaust Processing.....	51
6.2 Isotope Rebalancing and Protium Removal .....	62
6.3 Inner Tritium Loop Summary .....	76
<b>7 The Outer Tritium Loop .....</b>	<b>77</b>
7.1 Exhaust Detritiation .....	79
7.2 Water Detritiation.....	83
7.3 Isotope Separation.....	90
7.4 Storage Solutions .....	100
7.5 Outer Tritium Loop Summary.....	102
<b>8 Fuel Cycle Holistic Simulation.....</b>	<b>103</b>
8.1 Tritium Inventory and Mass Balances.....	103
8.2 Parameter Study of Input Boundaries .....	110
8.3 Transient Behaviour .....	117
8.4 Performance Evaluation and Optimization Potential .....	121
<b>9 Summary and Outlook .....</b>	<b>123</b>
<b>References.....</b>	<b>127</b>

---

<b>Appendix.....</b>	<b>139</b>
A1 The Helium Cooled Pebble Bed Breeding Blanket .....	139
A2 The Water Cooled Lithium Lead Breeding Blanket.....	141
A3 Diffusion Process through a Metal Foil .....	143
A4 Hydrogen Absorption in Vanadium and Palladium .....	144

# List of Symbols and Abbreviations

## Latin symbols

Name	Description	Unit	$L_{\text{low}}^i$	$L_{\text{up}}^i$
$A$	Area	(m <sup>2</sup> )	0	10 <sup>26</sup>
$Av$	Availability	(s/s)	Parameter	
$c$	Concentration	(mol/m <sup>3</sup> )	0	10 <sup>6</sup>
$c_{Q/M}$	Hydrogen to metal ratio	(mol/mol)	0	10 <sup>6</sup>
$c_p$	Specific heat capacity	(J/(mol · K))	0	10 <sup>6</sup>
$C$	Constant	as indicated	Parameter	
$d$	Diameter	(m)	0	10 <sup>6</sup>
$D$	Diffusivity	(m <sup>2</sup> /s)	0	10 <sup>26</sup>
$dt$	Time derivative or step	(s)	10 <sup>-10</sup>	3600
$E$	Energy	(J)	0	10 <sup>26</sup>
$E_A$	Activation energy	(J/mol)	Parameter	
$f$	Frequency	(1/s)	0	10 <sup>26</sup>
$F$	Molar flow	(Pa · m <sup>3</sup> /s) <sup>ii</sup>	-10 <sup>10</sup>	10 <sup>26</sup>
$I$	Molar inventory	(mol)	0	10 <sup>26</sup>
$j$	Permeation Flux	(Pa · m <sup>3</sup> /(m <sup>2</sup> · s))	-10 <sup>10</sup>	10 <sup>26</sup>
$J$	Permeation flow	(mol/s)	0	10 <sup>26</sup>
$h$	Specific molar enthalpy	(J/mol)	0	10 <sup>26</sup>
$H$	Enthalpy	(J)	0	10 <sup>26</sup>
$K$	Equilibrium constant	(mol/mol)	0	10 <sup>26</sup>
$K_S$	Sieverts' constant	(mol/(m <sup>3</sup> · √Pa))	0	10 <sup>26</sup>
$Kn$	Knudsen number	(m/m)	0	10 <sup>26</sup>
$l$	Length	(m)	0	10 <sup>6</sup>
$L_c$	Characteristic length	(m)	Parameter	
$\bar{M}$	Molar mass	(kg/mol)	Parameter	
$N$	Amount or quantity	(-)	0	10 <sup>26</sup>
$p$	Pressure	(Pa)	0	10 <sup>26</sup>
$P$	Power	(W)	0	10 <sup>26</sup>
$Pe$	Permeability	(mol/(m · s · √Pa))	0	10 <sup>26</sup>
$Q$	Pumping throughput	(Pa · m <sup>3</sup> /s)	0	10 <sup>26</sup>
$s$	Thickness	(m)	Parameter	
$S$	Pumping Speed	(m <sup>3</sup> /s)	0	10 <sup>26</sup>
$t$	Time	(s)	0	10 <sup>26</sup>
$T$	Temperature	(K)	0	10 <sup>26</sup>
$v$	Velocity	(m/s)	0	10 <sup>26</sup>
$V$	Volume	(m <sup>3</sup> )	0	10 <sup>26</sup>
$x$	Solid phase molar fraction	(mol/mol)	0	1
$y$	Gaseous phase molar fraction	(mol/mol)	0	1
$z$	Liquid phase molar fraction	(mol/mol)	0	1

<sup>i</sup>  $L_{\text{low}}$  and  $L_{\text{up}}$  refer to the lower and upper variable boundary applied in the simulation (cf. Section 4.2).

<sup>ii</sup> The units Pa · m<sup>3</sup>/s and mol/s are used interchangeably in this work. The conversion factor is:  
 $1 \text{ mol/s} = \frac{2271.11}{\text{J}\cdot\text{mol}^{-1}} \text{ Pa} \cdot \text{m}^3/\text{s}$  and refers to the standard temperature ( $T_{\text{STP}} = 273.15 \text{ K}$ ).

## Greek symbols

Name	Description	Unit
$\alpha$	Bypass fraction	(mol/mol)
$\beta$	Tritium burnup fraction	(g/g)
$\Delta$	Difference	as indicated
$\varepsilon$	Termination criterion	(-)
$\theta$	Decay constant	(1/s)
$\eta$	Efficiency	(mol/mol)
$\vartheta$	Substitution parameter	(-)
$\Lambda$	Feed ratio	(mol/mol)
$\kappa$	Split fraction	(mol/mol)
$\lambda$	Mean free path	(m)
$\mu$	Dynamic viscosity	(Pa · s)
$\tau$	Residence or dwell time	(s)
$\chi$	Probability	(-)

## Frequently used indices

Name	Description
■ <sub>bot</sub>	at the bottom
■ <sub>D</sub>	of Deuterium ( ${}^2_1H$ )
■ <sub>gas</sub>	of the gas phase
■ <sub>H</sub>	of Protium ( ${}^1_1H$ )
■ <sub>Q</sub>	of any hydrogen <sup>iii</sup> isotope H, D or T
■ <sub>Q<sub>2</sub></sub>	of any hydrogen isotopologue H <sub>2</sub> , D <sub>2</sub> , T <sub>2</sub> , HD, HT, DT
■ <sub>liq</sub>	of the liquid phase
■ <sub>n</sub>	of the derivative in a one-dimensional spatial discretization
■ <sub>Pd</sub>	of the element palladium
■ <sub>RDP</sub>	of the value assumed in the Reference Design Point of DEMO
■ <sub>T</sub>	of Tritium ( ${}^3_1H$ )
■ <sub>top</sub>	at the top
■ <sub>V</sub>	of the element vanadium
■ <sub>vap</sub>	of the vapour phase

## Frequently used constants

Name	Description	Value	Unit
$k_b$	Boltzmann constant	$1.3807 \cdot 10^{-23}$	(J/K)
$N_A$	Avogadro constant	$6.0221 \cdot 10^{23}$	(1/mol)
$R$	Universal gas constant	8.3145	(J/(mol · K))
$\pi$	Pi	3.14159	(-)
exp(■)	Euler's number	2.7182818 <sup>■</sup>	(-)

<sup>iii</sup> In contrast to colloquial use, the word “hydrogen” is consistently used in this work as a collective term for all hydrogen isotopologues and not exclusively to refer to its most common isotope protium ( ${}^1_1H$ ).

## Abbreviations

<b>Abbreviation</b>	<b>Description</b>	<b>Short explanation</b>
ACM	Aspen Custom Modeler	software used in this work
ALARA	As Low As Reasonably Achievable	a nuclear safety principle
AUG	Asdex UpGrade	a tokamak experiment
BB	Breeding Blanket	produces tritium
CD	Cryogenic Distillation	a separation process
CECE	Combined Electrolysis and Catalytic Exchange	a separation process
CPS	Coolant Purification System	a boundary condition
DEMO	DEMOstration Power Plant	a future fusion power plant
DIRL	Direct Internal Recycling Loop	a fuel cycle loop
DSMC	Direct Simulation Monte Carlo	a calculation method
DTT	Divertor Test Tokamak	a tokamak experiment
EDS	Exhaust Detritiation System	a fuel cycle system block
ELM	Edge Localized Mode	a plasma instability
EQ	Equilibrator	a fuel cycle subsystem
EPS	Exhaust Processing System	a fuel cycle system block
GDCM	Gas Distribution Control and Metering	a fuel cycle system block
GPS	Gas Puffing System	a fuel injection technology
HCPB	Helium Cooled Pebble Bed	a Breeding Blanket concept
INTL	Inner Tritium Loop	a fuel cycle loop
IRPR	Isotope Rebalancing and Protium Removal	a fuel cycle system block
ITER	Intern. Thermonuclear Experimental Reactor	a future fusion experiment
ISS	Isotope Separation System	a fuel cycle system block
JET	Joint European Torus	a tokamak experiment
LDP	Linear Diffusion Pump	a high vacuum pump
LPCE	Liquid Phase Catalytic Exchange	a water detritiation process
LRP	Liquid Ring Pump	a vacuum backing pump
MAST	Mega Ampere Spherical Tokamak	a tokamak experiment
MFP	Metal Foil Pump	a separation process
MHFS	Magnetic High Field Side	a specific plasma region
MIS	Matter Injection System	a fuel cycle system block
MIV	Matter Injection Vacuum	a gas recuperation system
MSB	Molecular Sieve Beds	a separation technology
NBI	Neutral Beam Injector	a plasma heating system
PEG	Plasma Enhancement Gases	non-hydrogen gases used
PLS	Pellet Launching System	a fuel injection subsystem
OUTL	Outer Tritium Loop	a fuel cycle loop
RDP	Reference Design Point	fuel cycle reference case
TBR	Tritium Breeding Ratio	a fusion plant parameter
TCAP	Thermal Cycling Absorption Process	isotope separation process
TCV	Tokamak à Configuration Variable	a tokamak experiment
TERS	Tritium Extraction and Removal System	a boundary condition
TSA	Temperature Swing Absorption	isotope separation process
WCLL	Water Cooled Lithium Lead	a Breeding Blanket concept
WDS	Water Detritiation System	a fuel cycle system block
WS	Wet Scrubber	a water detritiation process





# 1 Introduction

The increasing demand for energy around the globe calls for the search for new, exploitable sources of electric energy. Fusion represents a potential solution and simultaneously a particularly challenging endeavour to realize. Inspired by the sun, humankind progressively strives to tame the reaction that continues to burn in the star's core for billions of years. However, to encapsulate a star with the purpose to harness its energy, an elaborated machine is required with a multitude of auxiliary systems supporting it. One essential component of such a power plant is given by the fuel cycle, which manages the supply and handling of gaseous reactants.

Fundamentally, the fuel cycle is a complex chemical plant, which processes the fusion fuel: a mixture of deuterium and tritium. These hydrogen isotopes fuse in the reactor under formation of helium and release of thermal energy. To limit the concentration of helium in the reactor, the hydrogen fuel rate exceeds the rate of the fusion reaction. Consequently, only a fraction of the fuel conducts the fusion reaction before being pumped away and the requirement of a closed recycling concept arises.

To efficiently reuse the unburned fuel, several successive tasks have to be covered by the fuel cycle. First, the exhausted gas is to be continuously removed from the fusion reactor. Thereafter, the exhaust must be separated into a reusable fuel component on the one hand and a waste component to be removed from the cycle on the other hand. Finally, the former is reinjected into the fusion device. Figure 1.1 sketches the general layout of such a closed fuel cycle.

Specifically, the present dissertation describes the fuel cycle within the framework of the demonstration fusion power plant DEMO. The plant is currently under design and supposed to bridge the gap between the present experimental state of fusion and the application in commercial use in the future. The procedure delineated in this work is applicable as a blueprint for upcoming fuel cycles. Many technological challenges remain to be overcome to realise this ambitious project and efficient fuel management is one of them.

In this context, tritium shapes the design of fuel cycle elements to suit its needs. This rare and radioactive species puts a strong emphasis on safe containment and high process efficiency. Only a minuscule portion of the tritium in circulation may escape the confinement of the fuel cycle.

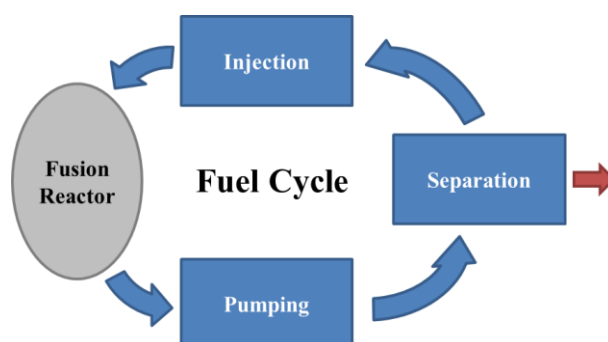


Figure 1.1: Sketch of a closed fuel cycle concept for the continuous recycling of hydrogen fuel of a fusion reactor. Only a minuscule fraction of the overall throughput is emitted from the fuel cycle. This exhaust is denoted by a red arrow.

---

## 1.1 Approach and Objective of Work

To assess the efficiency of the recycling process as a whole, the interplay of all involved components must be considered. Hence, the task of this work consists of the representation of all main functions of a fusion fuel cycle in a self-consistent model, the evaluation of their interaction as well as quantification of key performance criteria.

Given this system, the requirements of the individual fuel cycle components can be derived from its interplay in an overarching structure. All relevant boundary conditions including the pulsed operation of a fusion reactor must be incorporated into the assessment. The fuel cycle architecture and the choice of technologies must reflect these boundary conditions. All of these constitute the objective of this work.

Specifically, this work focuses on the aspect of tritium handling. On the one hand, the release of tritium is to be minimized to satisfy the safety requirements. On the other hand, the overall tritium inventory is also to be kept minimal to account for its scarcity and decay. The physical correlations must be modelled to a degree to evaluate achievable performance and the associated tritium inventory of a given functionality.

In order to carry out the optimisation, the DEMO fuel cycle is reproduced in its entirety in a simulation program on the ASPEN<sup>®</sup> Custom Modeler platform. This commercial software incorporates the capability of processing self-written models in a transient environment. In total over thirty individual model blocks are brought together into a complex fuel cycle architecture handling over fifteen different species, each expected to occur in relevant quantities.

The functionality of every subsystem is described as a self-contained model and connected to other parts of the fuel cycle via streams. The physical processes in each entity are self-coded and shaped in a way to draw meaningful conclusions about the performance, scale and parameter dependencies of the system in isolation or embedded into the fuel cycle. Quantification of the fuel cycle is achieved by establishing a representative Reference Design Point applicable for the current design of DEMO. Any deviations from this reference case are covered by a subsequent exploration of the parameter space.

This work pioneers towards building a holistic physics-based simulator, a pivotal tool used to shape the layout and optimize future iterations of fusion fuel cycles.

## 1.2 Structure of Work

This work is divided into nine chapters, intended to partition the content into a conclusive chain of thought:

- (1) This **first chapter** establishes the motivation, objective and structure of the work.
- (2) In the **second chapter**, the task and layout of the fuel cycle is derived from the requirements of fusion reactors in general as well as in the specific case of DEMO.
- (3) The **third chapter** elaborates on the main hydrogen chemistry as well as plant operational aspects that further shape the design of the fuel cycle.
- (4) The **fourth** chapter covers the setup of the fuel cycle modelling framework.

The next three chapters deal with the fuel cycle plant, which is subdivided into three consecutive loops, each tasked with a specific aspect of fuel cycle treatment and mirrored with a dedicated chapter (5), (6) and (7). A loop contains a variety of process engineering steps depicted as system blocks, which represent a particular functionality. In turn, each system block is composed of several subsystems as depicted in Figure 1.2. In this work, each system block is described using the same procedure.

- (a) First, the requirements for the system block and its boundary conditions are described. In addition, the layout of the system block as well as the technology choices implemented are outlined.
- (b) Then, the functionality of all subsystem technologies is elaborated in detail in conjunction with their mathematical implementation into the fuel cycle model.
- (c) Lastly, the expected performance of a system block is presented and conclusions are drawn concerning scale and efficiency of the subsystem.

At the end of each of these chapters the main results are summarised for that particular loop.

- (5) The **fifth chapter** covers the fuel cycle elements in the Direct Internal Recycling Loop (DIRL), which represents the boundary condition to the fusion device and the innermost and fastest fuel recycling path. Here the fuel is injected and removed from the reactor.
- (6) The **sixth chapter** comprises the system blocks of the Inner Tritium Loop (INTL). Here the bulk of fuel species is separated from the exhaust gas and conditioned for reinjection.
- (7) The **seventh chapter** encompasses the Outer Tritium Loop (OUTL), where the exhaust gas is rectified to minimize the discharge of tritium to the environment.
- (8) In the **eighth chapter** the performance of the fuel cycle as a whole is analysed.
- (9) Finally, the **ninth chapter** summarises the work and provides an outlook.

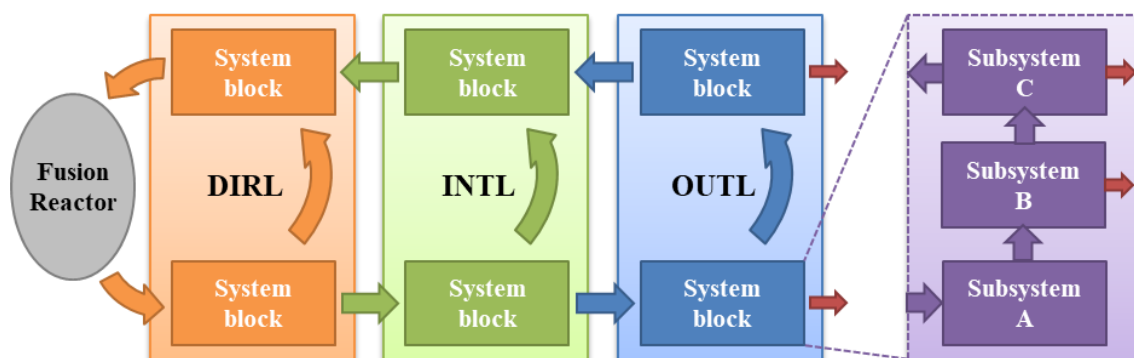


Figure 1.2: Breakdown of the fuel cycle into three loops: Direct Internal Recycling Loop (DIRL), Inner Tritium Loop (INTL) and Outer Tritium Loop (OUTL). The loops are then subdivided into system blocks and finally subsystems. Similar to Figure 1.1, exhaust streams of the fuel cycle are coloured in red.

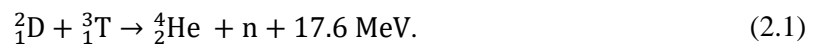


## 2 Function of the Fusion Fuel Cycle

To determine the duty of the fuel cycle it is paramount to observe at first the intricacies of the fusion device it is attached to. Large portion of the design needs can typically be deduced from this boundary condition alone. Thus, the fundamental structure of a fusion device is delineated with a focus on key features that define the requirements of the fuel cycle. This generic approach is then narrowed down to the specific design implications of the future fusion reactor DEMO in its current design iteration as well as its auxiliary systems. Given these interfaces, the multi-loop architecture of the fuel cycle is derived as well as the technologies are implemented.

### 2.1 Reactor Operation and Interfaces to the Fuel Cycle

Fundamental principle of fusion is the unification of two atomic nuclei to form a different element. For certain combinations of educts, the reaction is exothermic with a release of energy corresponding to the total difference of the mass defects of the reactants and the products. To harness energy with this phenomenon in a power plant, the fusion of the two hydrogen isotopes deuterium (D) and tritium (T) - forming helium (He) and a neutron (n) as per Equation (2.1) - is considered particularly promising [1].



However, this reaction has a cross section that peaks at temperatures of about 70 keV and must be maintained over an extended period of time to reliably yield net energy production. As no solid material is able to withstand these conditions without melting, the reaction is enclosed in a plasma core confined magnetically in an evacuated vessel. The reactor - commonly referred to as torus given the ring-shape of the plasma - is surrounded with a variety of auxiliary systems to sustain the fusion reaction at its centre.

Two reactor concepts are currently most advanced on how to realize the magnetic confinement with a technical design, the stellarator and the tokamak, each with its advantages and challenges [2]. In general, the fuel cycle of a magnetic fusion device is independent of its confinement technology. A crucial difference, however, is implied by the simpler design of the tokamak. The tokamak based on the transformer principle does not allow for a steady magnetic confinement and, thus, entails a pulsed operation, where the reactor alternates between a burn and a dwell phase. In contrast, the stellarator can theoretically be operated for an unlimited time. The fuel cycle described in this work is optimized for a tokamak reactor. Therefore, it is adapted to cope with boundary conditions that change in quality and quantity in intervals. In principle, the same fuel cycle concept is also applicable to a stellarator device given some adjustments.

Independent of the confinement concept, the effectiveness of the fusion reaction is constrained. The confinement time of particles in the plasma core is limited by the device design, therefore only a fraction of the hydrogen particles undergoes a fusion reaction. Instead the majority of fuel remains unburned, leaves the plasma core and is neutralized in the divertor. Once outside the plasma core, the bulk of particles lack the required energy to re-enter and must be

---

removed to avoid accumulation of matter in the torus. Low pressure in the reactor is upheld by a set of vacuum pumps to minimize the convective heat transport from the hot plasma to the reactor wall. These pumps mark the first interface to the fuel cycle.

To keep the reaction running, plasma density must be upheld, and the gas emitted from the fusion device must simultaneously be replaced. This defines the second interface to the fuel cycle. A Matter Injection System (MIS) is installed to continuously top up the plasma core with the required amount and composition of fuel. Additionally, other species are injected throughout the torus for the use of radiative cooling, which facilitates handling of the plasma. These are referred to as Plasma Enhancement Gases (PEG) and require an additional injection infrastructure.

As the gas composition of the torus feed and exhaust differ, the fuel cycle is either conceptualized in an open or a closed loop. In the former, much simpler approach, the exhaust gas is discarded and new matter from an external source is supplied in its place. The latter comprises a multitude of systems designed to separate, purify, rebalance and re-inject the unused matter repeatedly. As the exhaust gas of the torus predominantly consists of unburned hydrogen including tritiated and activated species, the closed loop fuel cycle concept is the standard approach to a large fusion device such as DEMO.

## 2.2 DEMO as Design Driver of the Fuel Cycle

On the development path towards a fusion power plant, a series of successive steps in the form of increasingly powerful and larger test facilities are foreseen. As of the year 2020, multiple devices are under operation in the framework of the European fusion programme for the development of a suitable plasma scenario for commercial fusion. The Mega Ampere Spherical Tokamak (MAST) in Culham explores the intricacies of spherical tokamak plasmas. The ASDEX Upgrade (AUG) in Garching, Germany as well as the Tokamak à configuration variable (TCV) in Lausanne, Switzerland test plasma scenarios. All these devices use protium or deuterium plasmas. The Joint European Torus (JET) also in Culham, England is currently the only European device to incorporate a tritium infrastructure and test deuterium-tritium plasmas.

In the future, other fusion related facilities will continue the development. The Divertor Test Tokamak (DTT) to be constructed in Frascati, Italy will focus on different divertor configurations. A fusion test device, ITER (Cadarache, France), is currently under construction to prove the feasibility of a fusion power plant by demonstrating net output of thermal energy. Thereafter, a full scale first-of-a-kind Demonstration Power Plant (DEMO) is to bridge the gap towards commercialisation. DEMO is currently at the end of its pre-conceptual design phase, which defines the main features and scope of the plant and all subsystems.

Table 2.1 lists these European tokamak devices, their main purpose and key parameters that exemplify the progress of reactor parameters. The size of the total plasma volume, composed of the plasma core and the plasma edge surrounding it, is given by  $V_{\text{plasma}}$ . The pulse length  $t_{\text{pulse}}$  indicates the maximum time span of maintaining a plasma pulse. The nominal thermal power released by the fusion reaction is denoted as  $P_{\text{thermal}}$ , whereas  $P_{\text{aux}}$  refers to the integral amount of heating power installed in the device.

Table 2.1: Selected fusion devices and their characteristics for scale comparison purposes. The values are extracted from literature and for planned facilities DTT, ITER & DEMO, they represent reported design targets.

Device	Date of completion	Main research purpose	$V_{\text{plasma}}$ (m <sup>3</sup> )	$t_{\text{pulse}}$ (s)	$P_{\text{thermal}}$ (MW)	$P_{\text{aux}}$ (MW)	Source
JET	1983	DT plasma	80	$\leq 60$ [3]	16	30	[4]
MAST	1991	Spherical tokamak plasma	8	$\leq 1$	-	5	[5]
AUG	1991	Plasma scenario	14	$\leq 10$	-	30	[6]
TCV	1992	Plasma configuration	varying	$\leq 2$	-	2.25	[7]
DTT	2025	Divertor testing	33	$\leq 95$	-	45	[8]
ITER	2025	Fusion test device	837	$\leq 500$	500	50-110	[9]
DEMO	>2050	Power plant	2500	$\leq 7200$	2000	50	[10]

Naturally, an increase of fusion reactor parameters necessitates a scale-up and redesign of the auxiliary systems. As such, the fusion fuel cycle has adapted to its requirements and evolved with each iteration step. ITER - for example - demands wide-ranging capabilities of all its auxiliary systems as it is inherently designed as a test facility to explore various plasma operation points or load profiles. Contrary, DEMO is envisaged to target a predictive power production. In consequence, the process parameters of its fuel cycle are defined much narrower and the design intentions diverge significantly in certain aspects from ITER.

A shared issue of large-scale fusion devices - irrespective of their intricacies in fuel cycle design - resides in the consumption of DT-fuel. An equimolar mixture of deuterium and tritium is required to maintain a peak performance of the fusion reaction rate [11]. In this context, tritium represents a particularly scarce and expensive resource [1].

To remain sustainable, a requirement of tritium self-sufficiency is imposed on DEMO and follow-up fusion power plants [12]. Over their lifetime, they must therefore produce tritium equal to or at a higher rate than consuming it. To quantify this requirement, the consumption of tritium in a fusion power plant can be partitioned into four distinguishable sink rates:

- (i)  $F_{\text{burn}} = f(P_{\text{thermal}}, Av)$  Consumption of tritium by the fusion reaction itself. This term is a function of the fusion power ( $P_{\text{thermal}}$ ) as stated in Equation (2.2) and the overall reactor availability  $Av$ .
- (ii)  $F_{\text{passive}} = f(\text{Material})$  Loss of tritium by permeation into the structure materials, where it permanently resides. This term is a time-based saturation function strongly dependent on material properties treatment and neutron damage.
- (iii)  $F_{\text{decay}} = f(I_{T_2})$  Tritium decay as a function of the plant tritium inventory.
- (iv)  $F_{\text{loss}} = f(\eta_{\text{Fuel Cycle}}, \eta_{\text{leak}})$  Tritium emitted from the fuel cycle in exhausts as a function of separation efficiency of the back-end processes ( $\eta_{\text{Fuel Cycle}}$ ) of the fuel cycle and the leak rate of the secondary confinement ( $\eta_{\text{leak}}$ ).

---

From Equation (2.1), a direct dependency can be drawn from the amount of thermal energy released ( $P_{\text{thermal}}$ ) to the consumption of fuel. This relation is quantified in Equation (2.2).

$$F_{\text{burn}} = P_{\text{thermal}} \cdot 2.943 \cdot 10^{-7} \text{ mol/MJ}, \quad (2.2)$$

with  $F_{\text{burn}}$  in mol/s of tritium,  $P_{\text{thermal}}$  in MW and the conversion factor<sup>1</sup> in mol/MJ as indicated.

Equation (2.2) provides a quick way to assess the minimum tritium consumption of DEMO. For a full operation cycle of two hours the demand of fuel exceeds 4.2 mol (25.5 g) of tritium. To quantify the consumption over a larger timespan  $F_{\text{burn}}$  is multiplied by the reactor availability  $Av$ . Integrated over the plant lifetime, the first sink term alone considerably surpasses the worldwide production rate of tritium. Thus, to realise fusion of the deuterium-tritium mixtures, an efficient use of tritium is paramount.

Incorporating infrastructure materials and plasma facing components with low tritium diffusion properties represents a key design aspect to reduce passivated tritium inventory  $F_{\text{passive}}$  (ii). This facet is still under research [13][14][15]. Particularly in the vicinity of the fusion reactor careful design is required as the uphold of tritium in infrastructure can be increased by neutron damage by three orders of magnitude [16]. It is assumed that proper coating can leverage the impact of this sink term, which is also not considered here.

The demand to minimize the sink terms of decay (iii) and loss (iv) sets the key design criterion of the fuel cycle to implement technologies of low tritium inventory and high separation efficiencies. The decay rate  $F_{\text{decay}}$  in mol/s is related to the plant inventory of tritium  $I_{\text{T}_2}$  in mol by the decay constant  $\Theta^2$  as shown in Equation (2.3). Both terms are discussed in Chapter 8.

$$F_{\text{decay}} = \Theta \cdot I_{\text{T}_2} = I_{\text{T}_2} \cdot 1.7828 \cdot 10^{-9} \text{ s}^{-1}. \quad (2.3)$$

To assess the tritium inventory, the overall throughput of the reactor, must be taken into account since this is processed in the fuel cycle. In theory,  $F_{\text{burn}}$  constitutes the minimum amount of matter cycled. However, in reality, the duty of the closed loop fuel cycle is amplified by the low burning efficiency of the fusion reaction. To illustrate the low conversion rate, the amount of tritium burned  $F_{\text{burn}}$  is put into relation with the total amount of tritium injected into the reactor  $F_{\text{MIS}}(\text{T})$ . It is defined in Equation (2.4) as tritium burnup fraction  $\beta$ .

$$\beta = \frac{F_{\text{burn}}}{F_{\text{MIS}}(\text{T})}. \quad (2.4)$$

For DEMO a burning efficiency of  $\beta = 0.64 \%$  is considered in this work. The number is deduced later in Section 3.5. This in turn, exemplifies the need of a closed recycle loop as less than one percent of the hydrogen fuel actually reacts in the torus. Apart from this small fraction, all species are expected to exit the reactor without further reaction. Hence, input and output of the fusion reactor are almost identical.

---

<sup>1</sup> This is derived from the reaction described in Equation (2.1). After conversion of units, the released energy translates to  $\sim 3400$  GJ/mol of tritium molecules burned.

<sup>2</sup> The decay constant  $\Theta$  in the unit of 1/s is given by the half-life of tritium  $t_{1/2} = 12.323 \text{ a} = \frac{\ln(2)}{\Theta}$ .



Given the definition of the loss terms, the tritium self-sufficiency requirement can be formulated as in Equation (2.5) using the plant mass balance of tritium:

$$\frac{d(I_{T_2})}{dt} = F_{\text{breed}} - F_{\text{burn}} - F_{\text{passive}} - F_{\text{decay}} - F_{\text{loss}}. \quad (2.5)$$

Tritium self-sufficiency is achieved once  $d(I_{T_2})/dt \geq 0$  over an extended period of time. To provide this, two additional parameters must be considered. First, a certain tritium start-up inventory  $I_{\text{start},T_2}$  is needed to saturate the reactor and all auxiliary systems, which defines this task as an initial value problem best approached by numerical simulation. Secondly, a source term of tritium is required ( $F_{\text{breed}}$ ). For this purpose, Breeding Blankets are installed in the vicinity of the fusion reactor and presented in the next section.

Figure 2.1 shows a cross section of the DEMO tokamak from the side and the top including the main auxiliary systems.

- (a) the ring-shaped plasma surrounded by (b) the Breeding Blankets, (c) the vacuum vessel and (d) the divertor.
- The magnet infrastructure consisting of (e) poloidal and (f) toroidal field coils.
- The top view shows how the DEMO tokamak is segmented into sixteen sections (of which eight are displayed), each covering  $22.5^\circ$  and housing three access ports. (g) the upper port, in the most part for Breeding Blanket maintenance, (h) the equatorial, primarily for diagnostics and heating and (i) the lower port intended for divertor maintenance and location of the vacuum system.
- The structure displayed - including ports - is approximately 22.5 m high, with a diameter of about 31.5 m.

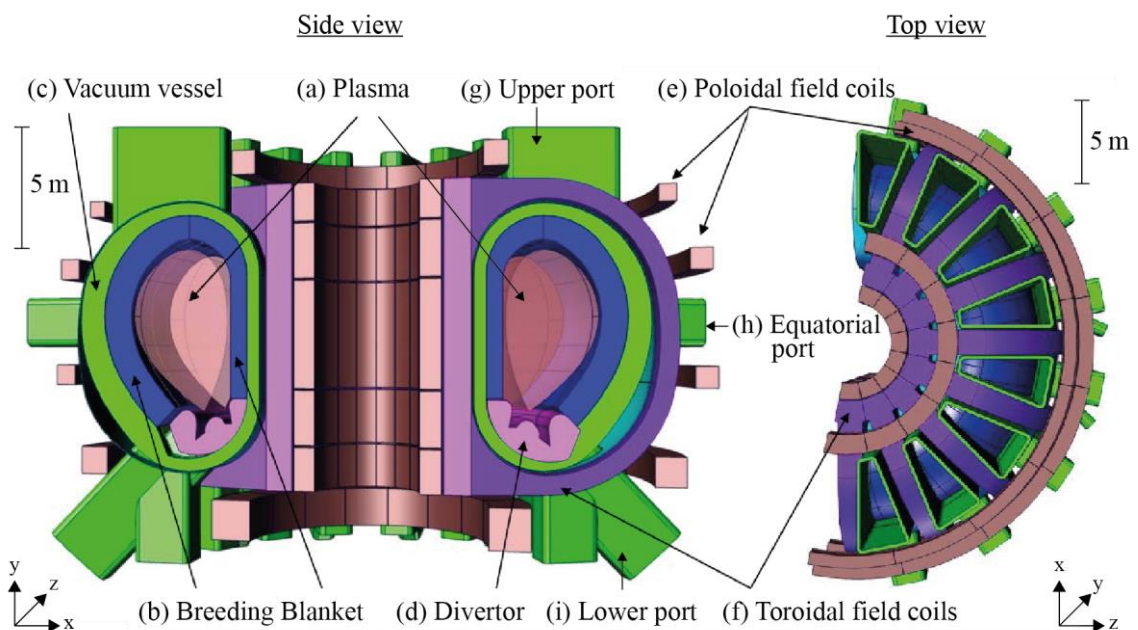


Figure 2.1: Schematic cross sections of the DEMO tokamak. **Left:** Side view displaying the main components, (a) the plasma surrounded by (b) the Breeding Blanket and (d) divertor encased in (c) the vacuum vessel with its three access ports (g, h, i) as well as the magnet structure (e, f). **Right:** Top view showing eight of the sixteen sections, which brought together form the distinctive ring shape of a tokamak torus. Picture adapted from [18].

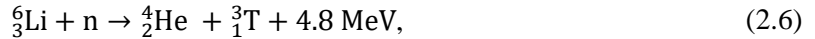
---

## 2.3 Breeding Blankets and other Fuel Cycle Boundaries

Apart from the fusion reactor, the fuel cycle is also connected to a number of power plant auxiliary systems. Each of these systems impose a requirement and thereby shapes the design of the fuel cycle. The Breeding Blankets (BB) represent an essential boundary condition. Here the tritium is bred, which is required for the long-term preservation of fuel supply. The output of the BB requires processing by the fuel cycle. The other boundary conditions mentioned below demand more general design implications to the fuel cycle. They are mentioned here for the sake of completeness but will not be further elaborated in this work.

### Breeding Blankets

Tritium is produced in a nuclear reaction from both natural isotopes of lithium as per Equation (2.6) and (2.7) [14]. The reaction is induced by neutrons  $n$  produced in the fusion reaction of Equation (2.1). Their interaction with  ${}^7\text{Li}$  releases another neutron  $n'$  in the process.



This forms a cycle of a fused triton creating a neutron, which in turn creates again a new triton, and requires a high capture rate of the released neutrons. To enable a high breeding ratio a high plasma surface coverage factor of blankets holding the lithium is required. In sum, the ratio between tritium generated in the Breeding Blankets  $F_{\text{breed}}$  to  $F_{\text{burn}}$  as shown in Equation (2.8) is called the Tritium Breeding Ratio ( $TBR$ ).

$$TBR = \frac{F_{\text{breed}}}{F_{\text{burn}}}. \quad (2.8)$$

Given the tritium losses discussed in the previous section,  $TBR$  must exceed unity to achieve self-sufficiency. In addition, a fraction of the neutrons generated are lost as they stream through the surrounding structure without interacting with the breeder. To counteract these losses, neutron multipliers - in the form of beryllium or lead - are implemented into the blankets in conjunction with lithium. Proof of concept linked to DT fusion is expected to be carried out in ITER [19]. However, only a fraction of the first wall in ITER is covered by test blankets. Thus, the tritium consumption of ITER will heavily outweigh its production. To complete the cycle, the bred tritium must subsequently be removed from the BB and directed to the fuel cycle. For this purpose, a Tritium Extraction and Removal System (TERS) is implemented. The output of the TERS then represents the third crucial interface to the fuel cycle.

### Cooling

The first wall components of the fusion reactor as well as the Breeding Blankets require extensive cooling. Thus, a comprehensive cooling system branches through the whole reactor building as the primary coolant loop. The heated coolant is transferred to a secondary loop feeding a steam generator, which powers the turbines. Given the sheer size and estimated temperature range spanned by this infrastructure element, permeation of tritium into the coolant must be considered. Accordingly, an additional clean-up system is implemented to prevent tritium

accumulation or contamination of the secondary loop. This is achieved by removing the tritium in a Coolant Purification System (CPS), which again feeds into the fuel cycle.

The Breeding Blanket and in extension the TERS and CPS system blocks form the Outer Fuel Cycle as they introduce tritium from outside to the closed fuel recirculation loop of the fusion reactor. Since there are currently several concepts for the design of the Breeding Blankets - each associated with a different coolant - the interface to the fuel cycle varies in throughput and degree of tritium purity received. Two Breeding Blanket concepts - Helium Cooled Pebble Bed (HCPB) and Water Cooled Lithium Lead (WCLL) - are considered in this work as they cover all design approaches currently under discussion. From the perspective of the fuel cycle, a permutation of breeder and coolant is possible. A detailed discussion of both concepts and a quantification of their input to the Inner Fuel Cycle is presented in Appendixes A1 and A2.

### **Plant Safety**

Safe operation of the fuel cycle is a crucial requirement to the success of the power plant. All elements involved must remain controllable during operation or any form of incident. This applies in particular to the handling of tritium, which may under no circumstances leak from the fuel cycle in large quantities. Furthermore, the total amount of tritium emitted to environment must be kept below an administrative threshold set by a nuclear regulator and beyond that remain as low as reasonably achievable (ALARA principle).

To account for the safety requirements, all systems presented in the following chapters are envisaged to be surrounded by a secondary confinement system to recover leaked species. Even beyond this confinement, small scale tritium contamination of ambient air is unavoidable. Accordingly, the ventilation system of the plant must be equipped with a filter and recirculation system that constitutes a third tritium confinement loop.

On top of that, every part of the fuel cycle must be implemented redundantly in accordance with nuclear safety regulations. This considerably increases the tritium inventory to be expected within each system block. All of the above is to be considered in a comprehensive safety concept in the conceptual design phase, which will affect the fuel cycle design and scale. This does not form part of this work.

### **Balance of Plant**

Since the fuel cycle is part of a power plant, its total energy consumption must be minimized. Other boundary conditions must be regarded as well. For example, the tritium retention of the Outer Fuel Cycle impacts the tritium concentration and thus safety requirements of the water steam cycle. Also, the achievable pump down time in the fusion dwell phase defines the size of the energy storage system of the Balance of Plant. This is to be reflected by the selection of technologies and layout of the fuel cycle.

### **Cryogenics, water supply and other inputs from outside**

Several processes in the fuel cycle require external supply of energy or matter. A cryogenic infrastructure is assumed as provided given the inclusion of cooled super-conducting magnets in DEMO. The availability and boundary conditions of other external sources to the fuel cycle are regarded as given and not considered here.

---

## 2.4 Fuel Cycle Architecture and Technologies

Given all boundary conditions, the architecture of the DEMO Inner Fuel Cycle can be derived. Essentially six main tasks can be identified:

- 1 Evacuation of the torus must be upheld by continuous pumping.
- 2 The reusable species must be isolated from the exhaust gas in a separation process.
- 3 In a subsequent process step, the exhaust gas must undergo a final detritiation step before being released to the environment to minimize losses and comply with regulatory requirements.
- 4 The recycled gas must be refined and topped up before reinjection. This includes re-establishing the correct composition of hydrogen isotopes in the fuel.
- 5 To close the cycle the fuel must be reintroduced to the fusion reactor with a multi-part injection system tailored to the reactors requirements.
- 6 The architecture is completed by long-term storage tanks and a gas distribution system in which gases are retained and distributed in the fuel cycle.

In order to reduce the overall scale, it is avoided to process the entire throughput in every system. Instead, the fuel cycle is divided into three loops [20]. Progressively, the processed throughput decreases, while residence time and tritium separation capabilities increase with every loop. The three loops are the Direct Internal Recycling Loop, the Inner Tritium Loop and the Outer Tritium Loop, as indicated in Figure 2.2.

The **Direct Internal Recycling Loop** is a direct connection between the vacuum and Matter Injection Systems. The DIR concept was developed by Day et al. [21] and is used as baseline in this thesis. The bulk of hydrogen is circulated in this loop at minimal process times.

In the **Inner Tritium Loop**, the remaining gas is separated into a reusable fraction and an exhaust gas containing trace-tritium. Then, the isotopic composition of the recycled hydrogen is readjusted. All reusable species (hydrogen and certain PEG's) are gathered and topped up prior to being reinjected to the torus.

Finally, the **Outer Tritium Loop** holds the separation processes that guarantee high degrees of detritiation. Additionally, input from the Outer Fuel Cycle is processed in this loop.

The storage system is used to cushion dynamic processes and to guarantee a constant availability of all required species. Storage of large quantities of fuel is not foreseen. The systems blocks are connected by pipelines and dwell tanks. As the fuel cycle is a process engineering plant, which operates best at steady state, dynamic processes are to be dampened as far as possible. Semi-continuous process steps in the fuel cycle and the discontinuous behaviour of the fusion reactor itself are circumvented with bypass streams and series of dwell tanks. This way - with the exception from within the DIR Loop - all system blocks are isolated from this dynamic.

Figure 2.2 shows the Inner Fuel Cycle to the extent covered in this work with all system blocks and their connections in its three-loop architecture. Breakdown of each system block into its subsystems is conducted in the individual section.

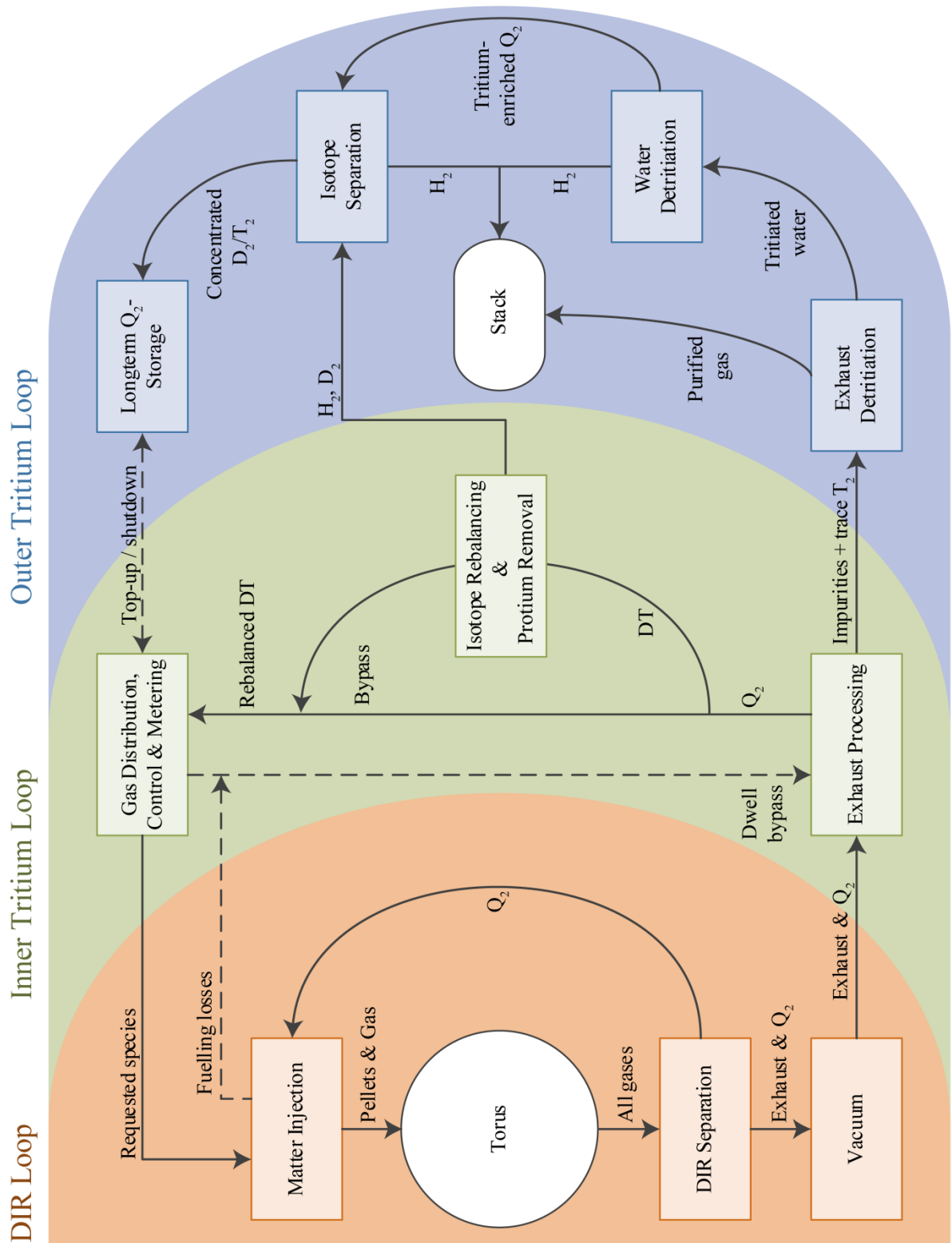


Figure 2.2: DEMO Inner Fuel Cycle architecture with its three loops and all system blocks. The input streams of the Outer Fuel Cycle are omitted here for the sake of readability. They feed into the Inner Fuel Cycle at different points depending on the breeding concept as explained in detail in Appendixes A1 and A2.

The depicted part of the fuel cycle is dedicated to recycling the exhaust gas of the torus and is referred to as the Inner Fuel Cycle, which comprises the Direct Internal Recycling Loop, Inner Tritium Loop and Outer Tritium Loop<sup>3</sup>. It is complimented by the Outer Fuel Cycle, which processes the bred tritium in the TERS and CPS system blocks. These feed into the Inner Fuel Cycle at different points depending on the composition of species (cf. Appendixes A1/A2).

Each system block is realized using a dedicated technology. The technology choice is the result of a selection process [22][23][24], most of which has been evaluated by the author [25] in the process of this work. Table 2.2 lists the different technologies for each system block.

Table 2.2: Technology selection for all Inner Fuel Cycle subsystems [22][23][24]. The Gas Distribution Control and Metering System is effectively part of all loops. It is listed and covered as part of the DIRL loop in the context of this work.

Loop	System Block	Subsystem	Technology	Section
		Pellet injection	Centrifuge Pellet Injector	5.1
	Matter Injection	Gas injection	Gas Puffing System	5.1
		Neutral beam heating	Neutral Beam Injector	5.1
DIRL	Direct Internal Recycling Separation		Metal Foil Pump	5.2
	Vacuum	High vacuum	Linear Diffusion Pump	5.3
		Fore-vacuum	Liquid Ring Pump	5.3
		Gas Distribution Control and Metering	Gas valve box	5.4
		Hydrogen isolation	Palladium Permeators	6.1
INTL	Exhaust Processing	Catalytic cracking	Nickel Catalyst Beds	6.1
		Isotope Rebalancing & Protium Removal	Temp. Swing Absorption	6.2
	Exhaust Detritiation	Gas detritiation	Combiner & Condenser	7.1
		Residual detritiation	Wet Scrubber column	7.1
	Water Detritiation	Water detritiation	LPCE column	7.2
OUTL		Tritium enrichment	Electrolyser	7.2
	Isotope Separation	Trace-tritium removal	Cryogenic Distillation	7.3
		Isotopologue cracking	Equilibrator	7.3
	Storage	Long term storage	Uranium Getter Beds	7.4

<sup>3</sup> The terminology is repeated here explicitly to clarify a source of constant confusion: The Inner Fuel Cycle and the Inner Tritium Loop are not interchangeable terms. The same applies to the Outer Fuel Cycle and the Outer Tritium Loop. Moreover, the Outer Tritium Loop is part of the Inner Fuel Cycle as shown in Figure 2.2 above.

## 3 Gas Transfer and Balance Processes in a Fusion Fuel Cycle

In a fusion fuel cycle a multitude of different physical and chemical processes take place. To integrate these into the model, first, the gaseous species present in the fuel cycle are characterized. Thereafter, the chemical interactions of the predominant species, hydrogen, with itself and other species is elucidated. The essential interactions are categorized into four different types to streamline the computational effort. For each of these exchange reactions, a correlation is provided to simulate the equilibrium state. Finally, key operational aspects of the fuel cycle process plant are defined and quantified for a benchmark case.

### 3.1 Gas Species Characterisation

A total of seventeen different species are introduced in this work as they are expected to occur in considerable amount in the fuel cycle of DEMO. In this context, gaseous hydrogen in varied compositions constitutes the main ingredient circulated. In addition, hydrogen bound in water as well as a selection of non-hydrogen species are characterized.

#### 3.1.1 Hydrogen Species

Hydrogen represents the lightest element in existence with a single proton in its core and occurs as one of three isotopes. In principle, all three isotopes show a similar chemical behaviour with minor differences in their physical properties. They all readily bond with carbon forming hydrocarbons spanning the vast field of organic chemistry. At ambient conditions, hydrogen is an odourless transparent gas. In combination with oxygen it forms an explosive gas over a very wide concentration range. On top of that it represents a volatile element, which easily permeates through solid matter given its small atomic diameter.

Among the three isotopes, protium ( ${}^1_1\text{H}$ ) is naturally the most common isotope. Although not part of the fusion reaction per se, the presence of protium in the fuel cycle is unavoidable as it enters the fuel cycle in the form of purge gas, water or simply permeates through walls from the exterior. This is especially the case in the evacuated fusion reactor, where it represents the most relevant outgassing species from the first wall.

Deuterium ( ${}^2_1\text{H}$ ) is the second stable isotope commonly referred to as heavy hydrogen. Given that deuterium has twice the molar mass in relation to protium, it can be isolated relatively easy by distillation or electrolysis. With a natural occurrence of 1:5000 hydrogen atoms in water, it is considered abundantly available in the context of fusion.

The third isotope Tritium ( ${}^3_1\text{H}$ ) is known as super-heavy hydrogen. This isotope decays with a half-life of 12.323 years under release of  ${}^3\text{He}$  and kinetic energy. For any amount of tritium in a

given system, the average heat of decay can be quantified by the correlation in Equation (3.1)<sup>4</sup>. This phenomenon is relevant in low-temperature applications in the fuel cycle.

$$Q_{\text{decay}} = I_{T_2} \cdot 0.599 \text{ W/mol}, \quad (3.1)$$

where  $I_{T_2}$  denotes the amount of tritium molecules in mol and  $Q_{\text{decay}}$  is the heat flow due to decay in W released in the observed system. Constrained by decay, the concentration of tritium in the hydrosphere is minuscule with an estimated relative occurrence of 1 in  $10^{18}$  hydrogen atoms [26]. This amounts to a few kilograms of natural supply of tritium on earth [27].

The intake of tritium or tritiated species poses a health hazard to the human body. Therefore, proper containment of tritium and minimization of its release is a stiff requirement to the fuel cycle.

All isotopes of hydrogen naturally occur as gas in their bi-molecular form. This entails the formation of the three mixture isotopologues, which are of relevance specifically in certain separation processes. Throughout this document the symbols Q and Q<sub>2</sub> are used to refer to any of the three isotopes (H, D, T) and isotopologues (H<sub>2</sub>, D<sub>2</sub>, T<sub>2</sub>, HD, HT, DT), respectively. The word “hydrogen” also implies any of the isotopes, whereas “protium” is used to indicate specifically “<sup>1</sup>H”.

Additionally, to avoid confusion, all variables that refer to a quantity of hydrogen in this document do so as an amount of diatomic hydrogen molecules in the unit of mol independent of their state. An excerpt of the material properties of the six hydrogen isotopologues - as implemented into the fuel cycle simulator - is listed in Table 3.1. Wherever the isotopologues are compared in a plot the indicated colour is used throughout this document.

Furthermore, the material properties of oxidized hydrogen (Q<sub>2</sub>O) in all six isotopological variations are included to model the water chemistry in the fuel cycle. They are elaborated in Section 3.3. Carbonized and nitrogenized species (C<sub>x</sub>Q<sub>y</sub>, N<sub>x</sub>Q<sub>y</sub>) on the other hand are disregarded in the context of this work as they incur a high complexity, which would entail a large computational effort. If carbon is present in any way, cracking of hydrocarbons is required as a process step in the fuel cycle. In this work, both elements are covered by the Exhaust Processing System and the procedure is explained in Section 6.1.2.

Table 3.1: Basic material properties of the hydrogen isotopologues with the data extracted from [17].  $T_{\text{crit}}$  and  $p_{\text{crit}}$  are the temperature and pressure at the critical point and  $T_{\text{trip}}$  is the triple point temperature. The boiling temperature  $T_{\text{boil}}$  refers to a standard pressure of 1.013 bar.

Variable	H <sub>2</sub>	HD	HT	D <sub>2</sub>	DT	T <sub>2</sub>	Unit
Colour							
$\tilde{M}$	2.01565	3.02193	4.02388	4.02820	5.03015	6.03210	(g/mol)
$T_{\text{crit}}$	33.145	35.91	37.13	38.34	39.42	40.44	(K)
$T_{\text{trip}}$	13.81	16.60	17.70	18.69	19.79	20.62	(K)
$p_{\text{crit}}$	12.964	14.840	15.710	16.796	17.730	18.500	(bar)
$T_{\text{boil}}$	20.369	22.142	22.969	23.661	24.288	25.040	(K)

<sup>4</sup> The correlation is based on [27]. A single event of tritium decay releases on average 5.7 keV. After consideration of the tritium half-life and conversion of units one obtains the factor of 0.599 W/mol.



### 3.1.2 Non-Hydrogen Species

In addition, five non-hydrogen species are considered. They represent reaction products (both isotopes of helium) and the Plasma Enhancement Gases (nitrogen, argon and xenon) injected into the fusion reactor. The noble gases exhibit their intrinsic inertness and trespass the fuel cycle system without reacting in a significant way apart from activation reactions [28]. The chemistry of nitrogen as well as other hydrogen compound molecules represents a considerable interaction, which will be discussed in Section 6.1.2. An excerpt of the gas properties is summarized in Table 3.2.

The concentration of the tritium decay product  ${}^3\text{He}$  is measured in every system to obtain a system-wide tally of  $F_{\text{decay}}$ . As it is not circulated in the fuel cycle, its concentration remains at a low level  $y({}^3\text{He}) < 1 \cdot 10^{-7}$  mol%. Consequently,  ${}^3\text{He}$  is omitted in the following chapters although in later design phases an export function may be developed for this species.

Table 3.2: Selected material properties of non-hydrogen isotopes.  $T_{\text{crit}}$  and  $p_{\text{crit}}$  are the temperature and pressure at the critical point taken from [29]. The boiling temperature  $T_{\text{boil}}$  refers to a standard pressure of 1.013 bar.




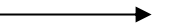
Variable	${}^3\text{He}$	${}^4\text{He}$	$\text{N}_2$	Ar	Xe	Unit
$\tilde{M}$	3.01603	4.00260	14.0067	39.9481	131.293	(g/mol)
$T_{\text{crit}}$	3.32	5.20	126.19	150.86	289.74	(K)
$p_{\text{crit}}$	1.146	2.275	33.96	4.8979	58.42	(bar)
$T_{\text{boil}}$	3.197	4.15	77.15	87.15	165.02	(K)
Source	[30]	[31]	[31]	[32]	[33]	

## 3.2 Simplified Hydrogen Treatment

Given the strong congruence of the hydrogen isotopes behaviour, in a majority of cases, a differentiation of isotopes can be omitted in the model procedure to minimize computation time. Therefore, this thesis provides a treatment of the thermodynamic description of the hydrogen systems involved, that reduces the complexity where possible, and thus allows for fastest convergence of the calculated points.

Wherever necessary, the hydrogen chemistry is expanded to include the three isotopes (e.g. mono-atomic absorption) or the six isotopologues (most other cases). Conversely, in parts of the fuel cycle, only hydrogen isotopologues are processed and other species can be neglected. To illustrate the list of species implemented in all parts of the fuel cycle, the streams connecting subsystems in this document are colour-coded from this point onwards as indicated in Table 3.3.

Table 3.3: Streams transporting species at different resolutions across the model boundaries to limit complexity.  ${}^3\text{He}$  is present everywhere throughout the fuel cycle as the decay product of tritium.

Stream	Isotopologues	Water	Simplified	Everything
colour-code				
Species included in the stream	$\text{H}_2, \text{D}_2, \text{T}_2$ $\text{HD}, \text{HT}, \text{DT}$ ${}^3\text{He}$	$\text{H}_2\text{O}, \text{D}_2\text{O}, \text{T}_2\text{O}$ $\text{HDO}, \text{HTO}, \text{DTO}$ ${}^3\text{He}$	$\text{H}_2, \text{D}_2, \text{T}_2$ ${}^3\text{He}, {}^4\text{He}$ $\text{N}_2, \text{Ar}, \text{Xe}$	All $\text{Q}_2$ , All $\text{Q}_2\text{O}$ ${}^3\text{He}, {}^4\text{He}$ $\text{N}_2, \text{Ar}, \text{Xe}$

---

In terms of required effort and system size, the most demanding aspect is represented by the chemical reactions of hydrogen for the purpose of their separation from impurities or isolation of individual isotopes. Likewise, the highest amount of computing power is required to represent these processes in the simulation program. To streamline this aspect, the separation mechanisms are categorized into four hydrogen interactions:

- |  |   |
|--|---|
| 1. hydrogen $\Leftrightarrow$ gaseous hydrogen | 2. hydrogen $\Leftrightarrow$ liquid hydrogen |
| 3. hydrogen $\Leftrightarrow$ water            | 4. hydrogen $\Leftrightarrow$ metal           |

For each of these chemical interactions, a determined system of equations for the equilibrium state is presented in the following chapter. This approach is used throughout all components of the fuel cycle and neglects the reaction kinetics. This simplification is chosen to limit computational complexity. In consequence, the results presented in this work assume an idealized case. They are indicative of the separation capabilities of the various fuel cycle components and underestimate the setup sizes required.

### 3.3 Hydrogen Interaction Processes

#### 3.3.1 The Hydrogen - Gaseous Hydrogen Interaction

In the gas phase, hydrogen molecules perform exchange reactions approaching an equilibrium state of isotopologues that is determined by the prevailing temperature. The interaction is exemplified for hydrogen and deuterium in Equation (3.2).



If no catalyst is present, the time scale of these exchange reactions is given by the dissociation of hydrogen molecules, which marks the time-relevant step. However, in many instances throughout the fuel cycle, the decomposition of molecules is induced via a source of energy or the presence of a catalytic metal surface. Any subsequent recombination into hydrogen molecules occurs as a mixture of isotopologues in thermal equilibrium, which can be quantified by using Equations (3.3), (3.4) and (3.5). This approach assumes ideal gas behaviour and ab initio instantaneous thermodynamic equilibrium between all hydrogen isotopologues.

$$K_{\text{HD}} = \frac{y_{\text{HD}}^2}{(y_{\text{H}_2} \cdot y_{\text{D}_2})} \quad (3.3), \quad K_{\text{HT}} = \frac{y_{\text{HT}}^2}{(y_{\text{H}_2} \cdot y_{\text{T}_2})} \quad (3.4), \quad K_{\text{DT}} = \frac{y_{\text{DT}}^2}{(y_{\text{D}_2} \cdot y_{\text{T}_2})} \quad (3.5),$$

where  $y_{\text{Q}_2}$  is the molar fraction of a hydrogen isotopologue in the gaseous phase and  $K_{\text{Q}_2}$  is the equilibrium constant. The latter can be calculated as a function of the temperature via the correlations listed in Table 3.4. They are derived by Peters [34] and originate from the literature [17][35][36][37]. Above a temperature of 1250 K, the equilibrium constant of all reactions converges asymptotically to  $K_{\text{Q}_2} = 4$ , which represents the stochastic distribution. Combined with the mass balance of a given system, the equilibrium state of isotopologues can be numerically calculated by the simulator.

Table 3.4: Equilibrium constants of the hydrogen-hydrogen exchange reaction in the gas phase, based on a literature study performed by Peters [34].

Range	$4.2 \text{ K} \leq T < 50 \text{ K}$	$50 \text{ K} \leq T \leq 250 \text{ K}$	$250 \text{ K} < T \leq 1250 \text{ K}$
$K_{\text{HD}} =$	$6.785 \cdot \exp\left(\frac{-78.70 \text{ K}}{T}\right)$	$3.804 \cdot \exp\left(\frac{-51.178 \text{ K}}{T}\right)$	$4.207 \cdot \exp\left(\frac{-75.316 \text{ K}}{T}\right)$
$K_{\text{HT}} =$	$10.22 \cdot \exp\left(\frac{-171.10 \text{ K}}{T}\right)$	$4.082 \cdot \exp\left(\frac{-143.064 \text{ K}}{T}\right)$	$4.518 \cdot \exp\left(\frac{-166.588 \text{ K}}{T}\right)$
$K_{\text{DT}} =$	$5.924 \cdot \exp\left(\frac{-20.24 \text{ K}}{T}\right)$	$4.149 \cdot \exp\left(\frac{-23.708 \text{ K}}{T}\right)$	$4.075 \cdot \exp\left(\frac{-19.456 \text{ K}}{T}\right)$

In most instances this phenomenon occurs as an undesired side-effect. For the fuel cycle this represents a problem to be overcome as especially the similarity of physical properties of the HT and the D<sub>2</sub> molecules is a limiting factor to the separation efficiency of most isotope-related processes. As the composition is temperature-dependent and favours the formation of pure species at low temperatures, this phenomenon can deliberately be applied in an equilibrator to manipulate the hydrogen composition prior to a separation step. However, operation of an equilibrator at low temperatures incurs a reduction of reaction kinetics.

### 3.3.2 The Hydrogen - Liquid Hydrogen Interaction

Hydrogen can be liquefied at cryogenic temperatures. Due to the different boiling points of the individual isotopologues (cf. Table 3.1) a separation effect can be achieved in a distillation process. In this context, hydrogen molecules with a larger mass exhibit a higher boiling temperature. The molar fraction of an isotopologue  $y(Q_2)$  in the gas phase is defined in Equation (3.6). Additionally, in equilibrium this equates the ratio of the temperature-dependent saturation vapour pressure of that isotopologue.

$$y(Q_2) = \frac{p(Q_2)}{p} = \frac{p_{\text{sat}}(Q_2)}{\sum_{Q_2} p_{\text{sat}}(Q_2)}, \quad (3.6)$$

where  $p(Q_2)$  and  $p_{\text{sat}}(Q_2)$  indicate the partial pressure and saturation vapour pressure of a hydrogen isotopologue, respectively.  $p$  denotes the total pressure of a given system provided that no non-hydrogen species are present, and assuming the validity of Dalton's law. The saturation vapour pressure of any isotopologue is calculated with a fit function of the saturation pressure curve given in Equation (3.7) for any temperature  $T_{\text{trip}} < T < T_{\text{crit}}$ .

$$\ln\left(\frac{p_{\text{sat}}}{\text{Pa}}\right) = C_1 + \frac{C_2}{T} + C_3 \cdot T + C_4 \cdot \ln\left(\frac{T}{\text{K}}\right) + C_5 \cdot T^2, \quad (3.7)$$

with  $T$  in the unit of K and the constants  $C_{1-5}$  taken from the literature as indicated in Table 3.5.

 Table 3.5: Correlation constants used to calculate the saturation pressure of all hydrogen isotopologues Q<sub>2</sub>.

Constant	H <sub>2</sub>	HD	HT	D <sub>2</sub>	DT	T <sub>2</sub>	Unit
C <sub>1</sub>	14.3314	16.8374	21.5217	20.741	18.288	19.073	(-)
C <sub>2</sub>	-98.9298	-129.372	-181.006	-161.604	-167.989	-181.732	(K)
C <sub>3</sub>	0.0346	0.019	-0.1296	0.0466	0.0045	-0.023	(1/K)
C <sub>4</sub>	0.4468	0	0	-1.1027	0	0	(-)
C <sub>5</sub>	0	0.0002	0.0016	0	0.0001	0.0005	(1/K <sup>2</sup> )
Source	[38]	[39]	[39]	[38]	[39]	[40]	

Combined with the transient energy balance for all liquid and gaseous hydrogen isotopologues - as written in Equation (3.8) - the equilibrium of the exchange reaction can be calculated as:

$$\frac{dH}{dt} = \sum_n F_{\text{input}}(n) \cdot h(n) - \sum_n F_{\text{output}}(n) \cdot h(n) + H_{\text{ext}} + Q_{\text{decay}}, \quad (3.8)$$

where  $H$  denotes the enthalpy of a given species and  $h$  the specific enthalpy of a given stream  $n$  into or out of the observed system in J and J/mol, respectively. The term  $H_{\text{ext}}$  denotes an external source or sink term of heat in W and  $Q_{\text{decay}}$  is the heat flow of decay from tritiated species specified in Equation (3.1). The equation assumes that no work is executed by the system and that pressure remains a constant scalar.

The specific enthalpy  $h$  of any liquid and vapour component  $Q_2$  is given by the literature using a linear function of temperature as described in Equation (3.9).

$$h(Q_2) = C_6(Q_2) + T \cdot C_7(Q_2). \quad (3.9)$$

The parameters  $C_6$  and  $C_7$  are listed in Table 3.6 using a linearization performed by Souers [17]. To calculate the total specific enthalpy of a mixture of isotopologues, the values of  $h(Q_2)$  are weighted by their molar fraction in the fluid. This approach assumes no two-phase flow occurs in a domain as well as perfect mixing of the hydrogen isotopologues in equilibrium.

Table 3.6: Parameters used to calculate the specific enthalpy of all six hydrogen isotopologues [17], with the reference total enthalpy being the dilute ideal gas at 0 K.

Constant	H <sub>2</sub>	HD	HT	D <sub>2</sub>	DT	T <sub>2</sub>	Unit
C <sub>6</sub> (vap)	218.3	149.3	94.8	129.6	50.6	95.6	(J/mol)
C <sub>7</sub> (vap)	7.95	12.55	15.8	13.6	18.9	15.6	(J/mol · K)
C <sub>6</sub> (liq)	-176.5	-259.0	-259.2	-325.0	-285.0	-300.0	(J/mol)
C <sub>7</sub> (liq)	21.25	26.5	26.8	30.0	30.0	30.0	(J/mol · K)

### 3.3.3 The Hydrogen - Water Interaction

Hydrogen also carries out exchange reactions with water in liquid and vapour form according to Equation (3.10). Here heavier hydrogen isotopes preferentially accumulate in the water molecule.



In order to represent the complex reaction scheme in its entirety, all 18 reactants involved have to be correlated - six isotopologues in three phases. Following an approach of Busigin [41], a simplification is made here. The reaction kinetics of hydrogen with vapour can be assumed to be significantly higher than with liquid water.

The equilibrium reaction of hydrogen with water vapour can be represented with a dimensionless equilibrium constant  $K_{Q_2-Q_2}$  defined in Equation (3.11) as the ratio of the liquid and gaseous hydrogen inventories. The equilibrium constants are dependent on temperature as given in Table 3.7.

Table 3.7: Equilibrium constants of the Q<sub>2</sub>-Q<sub>2</sub>O reaction at selected temperatures based on Urey [42].

$T$ (K)	$K_{\text{HD-H}_2}$ (-)	$K_{\text{D}_2\text{-HD}}$ (-)	$K_{\text{HT-H}_2}$ (-)	$K_{\text{T}_2\text{-HT}}$ (-)	$K_{\text{DT-D}_2}$ (-)	$K_{\text{T}_2\text{-DT}}$ (-)
273	4.29	3.46	7.64	5.54	1.63	1.75
298	3.70	3.05	6.19	4.63	1.55	1.65
338	2.8	2.5	4.4	3.3	1.5	1.45
400	2.46	2.14	3.46	2.84	1.34	1.40
500	1.94	1.75	2.47	2.15	1.23	1.28
600	1.66	1.53	1.99	1.80	1.16	1.21

$$K_{\text{HD-H}_2} = \frac{I_{\text{gas}}(\text{H}_2)}{I_{\text{gas}}(\text{HD})} \cdot \frac{I_{\text{liquid}}(\text{HDO})}{I_{\text{liquid}}(\text{H}_2\text{O})} \quad (3.11)$$

The water vapour and the liquid are assumed to be perfectly mixed, which entails identical isotopologic composition. Gas in contact with a body of water is assumed saturated with water vapour at saturation pressure. The fit function given in Equation (3.12) links the saturation pressure to the temperature.

$$\ln\left(\frac{p_{\text{sat}}}{p_{\text{crit}}}\right) = C_8 \cdot \vartheta \cdot \frac{T_{\text{crit}}}{T} + C_9 \cdot \vartheta^{1.5} + C_{10} \cdot \vartheta^3 + C_{11} \cdot \vartheta^{3.5} + C_{12} \cdot \vartheta^4 + C_{13} \cdot \vartheta^{7.5}, \quad (3.12)$$

where  $p_{\text{sat}}$  and  $p_{\text{crit}}$  denote the saturation and critical pressure of a water isotopologue Q<sub>2</sub>O, respectively.  $T$  and  $T_{\text{crit}}$  are the temperature and critical temperature of that water isotopologue.  $\vartheta$  represents a substitution parameter as given in Equation (3.13).

$$\vartheta = 1 - \frac{T}{T_{\text{crit}}}. \quad (3.13)$$

The fit function and the equilibrium constants C<sub>8</sub>-C<sub>13</sub> in Table 3.8 are given by Matsunaga and Nagashima [43] for the pure isotopologues H<sub>2</sub>O, D<sub>2</sub>O and T<sub>2</sub>O. The mixture isotopologues are estimated by linear interpolation of the corresponding pure isotopologues.

 Table 3.8: Correlation constants used to calculate the saturation pressure of all water isotopologues Q<sub>2</sub>O. Properties of the pure water species are taken from [43]. Columns denoted with an \* are interpolated from their pure species counterparts.

Constant	H <sub>2</sub> O	HDO*	HTO*	D <sub>2</sub> O	DTO*	T <sub>2</sub> O	Unit
$T_{\text{crit}}$	647.14	645.52	644.42	643.89	642.80	641.7	(K)
$p_{\text{crit}}$	220.64	218.68	217.37	216.71	215.41	214.1	(bar)
$C_8$	-7.8582	-7.8983	-7.8975	-7.9384	-7.9376	-7.9368	(-)
$C_9$	1.8399	1.8384	1.7900	1.8369	1.7885	1.7402	(-)
$C_{10}$	-11.781	-11.8871	-11.6469	-11.993	-11.7530	-11.513	(-)
$C_{11}$	22.6705	22.6288	22.4010	22.5871	22.3593	22.1314	(-)
$C_{12}$	-15.939	-15.9878	-16.1601	-16.0363	-16.2086	-16.381	(-)
$C_{13}$	-1.7752	-1.4299	-1.6595	-1.0848	-1.3143	-1.5438	(-)

---

### 3.3.4 The Hydrogen - Metal Interaction

Gaseous diatomic hydrogen molecules exhibit the affinity to adsorb on the surface of a metal. In a process of chemisorption, the molecule activated by thermal energy is able to dissociate into single atoms. This phenomenon represents the first step of a multitude of different subsequent chemical reactions, all of which are used in fuel cycle processes. Firstly, if followed by desorption, the metal functions as a catalyst accelerating the aforementioned isotopic exchange in the gaseous phase. Secondly, the atoms may **absorb** and reside in the interstitial sites of the metal lattice. In this way, hydrogen is chemically bound and can be stored safely and in a space-saving manner over longer periods of time. Furthermore, the absorption equilibrium of the individual isotopes varies with the type of metal. A **separation** phenomenon can be exploited using an absorption bed of specific material properties. Once absorbed, hydrogen atoms diffuse through the metal lattice and may recombine at and desorb from a different point on the surface of the metal, effectively creating a **permeation** flux through the bulk. Given its small atomic diameter, hydrogen exhibits a comparably large diffusivity in metals. For specific metals, hydrogen can be isolated from larger species as these are not able to permeate through the lattice.

#### Absorption

For each hydrogen isotope  $Q$  in contact with a metal, absorption and desorption reactions occur in tandem until an equilibrium state is reached. In this equilibrium state the amount of a specific hydrogen isotope in the solid phase  $I_{\text{solid}}(Q)$  can be correlated to the amount in the gas phase  $I_{\text{gas}}(Q)$ . The equilibrium state depends on the temperature  $T_{\text{metal}}$  and the hydrogen isotope saturation in the metal lattice  $c_{Q/M}$  in the metal. It varies substantially for different metals and can be described in the form of Equation (3.14). In the according sections, the specific function of each metal implemented into the fuel cycle simulator is derived from the literature.

$$p_{\text{eq}}(Q) = f(c_{Q/M}, T_{\text{metal}}), \quad (3.14)$$

where the equilibrium pressure of an isotope  $p_{\text{eq}}(Q)$  is linked to the corresponding gaseous inventory  $I_{\text{gas}}(Q)$  by the ideal gas law as shown in Equation (3.15);

$$\frac{I_{\text{gas}}(Q)}{V_{\text{gas}}} = \frac{p_{\text{eq}}(Q)}{R \cdot T_{\text{gas}}}, \quad (3.15)$$

with  $V_{\text{gas}}$  and  $T_{\text{gas}}$  as the volume and temperature of the gas phase. Similarly,  $c_{Q/M}$  is defined in Equation (3.16) as the molar ratio of absorbed hydrogen over the total amount of metal absorbent  $I_{\text{Metal}}$ .

$$c_{Q/M} = 2 \cdot \frac{I_{\text{solid}}(Q_2)}{I_{\text{metal}}}. \quad (3.16)$$

Although absorption of hydrogen into metal occurs via dissociated atoms, the quantities of hydrogen bound in a metal lattice  $I_{\text{solid}}(Q_2)$  - are indicated in reference to diatomic molecules in the unit of mol. This definition avoids conversion errors. To address this definition, Equation (3.16) includes the factor of 2.

Controlled storage of hydrogen in absorption beds is made possible by utilising this dependency. The equilibrium state of a system is changed by manipulation of  $T_{\text{bed}}$ , which results in binding or releasing hydrogen. In this context, an increase in temperature correlates with higher equilibrium pressure and a release of absorbed hydrogen.

### Separation

For certain metals, Equation (3.14) strongly deviates for the different hydrogen isotopes. Equation (3.17) defines the separation factor  $K_{AB}$ , which quantifies the effect for two given hydrogen isotopes A and B.

$$K_{AB} = \frac{I_{\text{gas}}(B)}{I_{\text{gas}}(A)} \cdot \frac{I_{\text{solid}}(A)}{I_{\text{solid}}(B)}. \quad (3.17)$$

It indicates the equilibrium state of both isotopes in the gas and solid state. For most metals  $K_{\text{HD}} > 1$ , whereas some metals show an inverse isotope effect  $K_{\text{HD}} < 1$ . The separation factor is dimensionless and determined experimentally as a function of material properties and the temperature  $T_{\text{bed}}$  of the metal.

### Permeation

The phenomenon of permeation is the combined effect of solution and diffusion of an atom in a metal lattice. The solubility of hydrogen in the metal is given by Sieverts' law in Equation (3.18).

$$c_{\text{solid}} = K_S \sqrt{p}, \quad (3.18)$$

where  $K_S$  is the Sieverts' constant in  $\text{mol}/(\text{m}^3 \sqrt{\text{Pa}})$  and  $p$  is the partial pressure of hydrogen in the gas phase in Pa.  $c_{\text{solid}}$  denotes the concentration of hydrogen in the solid phase in  $\text{mol}/\text{m}^3$ . Diffusion of hydrogen is modelled using Fick's law (cf. Equation (3.19)).

$$j = D \frac{dc_{\text{solid}}}{dx}, \quad (3.19)$$

where  $j$  denotes the hydrogen flux through the metal lattice in  $\text{mol}/(\text{m}^2 \cdot \text{s})$  and  $D$  is the diffusivity in  $\text{m}^2/\text{s}$ . The permeability  $Pe$  is defined as the product of solubility  $K_S$  and diffusivity  $D$ , both of which are material properties and temperature dependent. In practise, the permeability of a metal for a given permeate is derived from experiments and described as an Arrhenius expression as written in Equation (3.20):

$$Pe = K_S \cdot D = Pe_0 \cdot \exp\left(-\frac{E_A}{RT}\right), \quad (3.20)$$

where  $E_A$  and  $Pe_0$  are the activation energy and pre-exponential factor in  $\text{J}/\text{mol}$  and  $\text{mol}/(\text{m} \cdot \text{s} \cdot \sqrt{\text{Pa}})$ , respectively. In practise, separation processes by means of permeation are realized by dividing an upstream and a downstream chamber with a metallic membrane of elevated temperature. To generate a permeation flux of quantitative relevance, a hydrogen concentration

---

gradient  $\Delta c$  must be established over the foil. Typically, the gradient is imposed by a pressure difference  $\Delta p$  in both chambers, referred to as gas-driven permeation. In this case, Equations (3.18) and (3.19) can be combined to Equation (3.21).

$$j = \frac{Pe}{s} \cdot \Delta\sqrt{p}, \quad (3.21)$$

where  $s$  represents the thickness of the metal foil in m and  $\Delta\sqrt{p}$  is the difference of the square root pressure of upstream and downstream chamber in Pa.

## 3.4 Operational Aspects

Key operational aspects govern the requirements imposed onto the fuel cycle and its performance. Most importantly, the throughput of the fusion reactor settles the overall scale of the fuel cycle. Then, the contributions of each fuel cycle loop to the retrieval of hydrogen must be allocated, which determines the scope of the individual subsystems. Finally, the fuel gas composition leads to certain considerations with regards to the mass balance of the three hydrogen isotopes. This section defines all these requirements in general terms, whereas the section thereafter provides a quantification for a specific case.

### 3.4.1 Fusion Reactor Throughput

The required throughput of fuel of a fusion reactor is governed by the control and stability of the particle and energy confinement of the fusion plasma in the fusion reactor. The injection requirements to sustain steady state fusion reaction are derived from upscaling engineering solutions implemented in running experiment facilities. Day et al. conducted an estimation of the different fuelling contributions to the DEMO tokamak [20]:

- A. Fuel is injected into the plasma core to (i) control the helium concentration, (ii) replenish burned fuel and (iii) maintain plasma density.
- B. Additional fuel is injected as pellet into the core to mitigate strong plasma-wall interactions, called Edge Localized Mode (ELM) [44].
- C. During the pellet fuelling process, losses occur at the plasma edge and must be compensated.
- D. In addition, losses within the supply lines upstream the torus must be considered.
- E. Injecting fuel gas into the reactor perimeter and the divertor has proven to facilitate plasma handling.
- F. Argon is used in conjunction with item E as a radiative divertor seeding gas.
- G. The first wall is protected by the use of PEGs, which dissociate the heat by radiation and are injected as a gas. Nitrogen is assumed to be used for this purpose.
- H. Xenon is used in small quantities to promote core radiation. It is injected by doping the fuel gas (items A-D).
- I. Neutral Beam Injectors, a potential source of heating the DEMO plasma, inject hydrogen gas into the core.



During dwell, the input of matter to the fusion reactor is halted. The vessel is pumped down in preparation of a new pulse and to counteract outgassing of the first wall. Immediately prior to a new pulse, fuel gas is puffed into the tokamak vessel to provide the start-up conditions for the plasma.

### 3.4.2 Hydrogen Recuperation

The retrieval of hydrogen fuel gas from the exhaust stream is a shared task of the three consecutive loops. Preferably, a large fraction of the fuel in the exhaust gas is processed immediately downstream the reactor to minimize process times and tritium inventory. In each loop, the amount of hydrogen retrieved is quantified by a hydrogen removal efficiency defined as the molar ratio of recuperated fuel gas over fuel gas input.

For the OUTL, a distinction is to be made between the hydrogen isotopes. Protium poisons the fusion reaction efficiency and its recuperation proves detrimental. Retrieval of deuterium is desirable from an economic perspective but can equally be discharged safely to the environment. The emission of the hazardous tritium isotope however - as mentioned in Chapter 2.3 - must be minimized as per the ALARA principle. ITER administers the same approach and quantifies the estimated annual release of tritium to about 0.6 g/a for years of regular operation. In years of heavy maintenance, more tritium is expected to be released, which yields 2.5 g/a [45]. These figures can be used as measurement criteria for the tritium release of DEMO. The equivalent steady state throughput of tritium is derived for the ITER annual release in Equation (3.22) from the heavy maintenance threshold.

$$F_{\text{loss,ITER}}(T_2) < 2.5 \text{ g/a} = 1.313 \cdot 10^{-8} \text{ mol/s.} \quad (3.22)$$

The release of tritium is assumed in the form of tritiated water (QTO), which represents the worst-case assumption as tritium bound in water exhibits higher levels of toxicity than molecular tritium [46]. When comparing this figure to the amount of tritium processed in the same period of time for DEMO, the extent of required detritiation is made apparent. As shown in Equation (3.23), less than one per 8.4 million circulated tritium molecules may leave the fuel cycle via the stack to satisfy ITER-like regulations.

$$\frac{F_{\text{MIS}}}{F_{\text{Loss}}} = \frac{F_{\text{Burn}} \cdot Av}{F_{\text{loss,ITER}}(T_2) \cdot \beta} \approx 8.4 \cdot 10^6 \frac{T_2 \text{ molecules circulated}}{T_2 \text{ molecules lost to atmosphere}}, \quad (3.23)$$

in which  $F_{\text{MIS}}$  - in the unit of mol/s - is calculated using Equation (2.4) with the assumed values of a burn-up fraction of  $\beta = 0.64 \%$  and an annual plant availability of  $Av = 0.3$ .

As all potentially tritium-contaminated streams pass through the detritiation systems of the Outer Tritium Loop, they must focus on efficient retention of this isotope. Within the model, the tritium output to environment is constantly monitored as a combined value of all output streams of the fuel cycle. The efficiency of each system block is measured by a detritiation factor ( $DF$ ), which is defined as the molar ratio of tritium in the input stream over tritium in the discharge stream. To comply with the safety regulations, high detritiation factors  $DF > 1000$  are required in the OUTL depending on input tritium concentrations. These are typically achieved by forcing exchange reactions with protium in the detritiation system blocks.

---

### 3.4.3 Fuel Gas Composition

Fusion reaction performance is tied to the ratio of deuterium and tritium in the fuel gas. From a reaction efficiency point of view, an equimolar ratio  $D : T = 50 : 50$  is desirable within the plasma core. A deliberate deviation from this optimum for a fusion power plant with the aim to minimize tritium inventory is under discussion [11]. However, as the reaction efficiency is diminished, this approach entails a higher rate of plasma heating to thermal reaction output. Ultimately, the design of a future commercial fusion power plant will have to weigh these factors to achieve an optimized setup.

An additional consideration is that several phenomena within the torus and the three fuel cycle loops constitute a potential cause of fuel gas composition offset. On the one hand, local imbalances may occur in the fuel cycle stemming from undesired isotope separation such as isotope-sensitive permeabilities. On the other hand, evidently, source terms of a single isotope, for example the tritium generated in the Breeding Blankets, entail an additional asymmetry. Finally, the decay of tritium and the different leak rates through infrastructure must be considered. Each fuel cycle loop reacts differently to imposed imbalance; hence each loop must be examined individually.

Apart from its deliberate use as flushing agent in the Outer Tritium Loop, the ingress of protium into the other tritium loops proves as undesirable as unavoidable, given that permeation from protium sources outside the fuel cycle such as cooling water cannot be prevented. An increasing protium concentration in the circulated fuel gas implies a decreasing efficiency of the fusion reaction and the necessity of time- and energy-intensive isotope separation processes. As a result, the input of protium into the confinement of the INTL must be minimized. This includes permeation of hydrogen into the torus, the fuel cycle itself and recirculation of protium from the OUTL.

## 3.5 Reference Design Point

A number of quantitative assumptions pose prerequisites to initiate the holistic modelling of the DEMO fuel cycle. In this section, the framework conditions and process parameters of a reference case are setup for the model, which aims to place representative requirements on the fuel cycle as a whole and each process step in isolation. This benchmark case is referred to as Reference Design Point (RDP) of the fuel cycle, which assumes steady state fusion in the reactor and will be used consistently as the baseline design in Chapters 5, 6 and 7. The dwell phase as well as variations of the RDP are discussed in Chapter 8.

### 3.5.1 Benchmark Reactor Throughput

Table 3.9 lists the assumed species, their function, destination and input quantities injected into the reactor of DEMO [20]. In it the items A-I refer to the throughput contributions introduced in the previous section. The baseline values are marked as RDP and the quantity range marks one of the parameter studies explored in Section 8.2.

Table 3.9: Matter injected into DEMO to sustain steady state operation [20]. "RDP" indicates the chosen mean value for the Reference Design Point. The losses upstream the torus (D) marked with an asterisk (\*) are derived in Chapter 5.1.

#	Species	Purpose	Target location	Quantity range (Pa · m <sup>3</sup> /s)	RDP (Pa · m <sup>3</sup> /s)
A	DT	Core density control	Plasma core	50-260	200
B	DT	ELM-pacing	Plasma core	0-20	20
C	DT	Pellet losses in the plasma edge	Plasma core	22-110	100
D	DT	PLS unrecoverable losses	Plasma edge	6-110% of A-C*	54*
E	DT	Detachment sustain	Wall surface	50	50
F	Ar	Radiative seeding	Divertor	0.10% of A-E	0.39
G	N <sub>2</sub>	Wall protection	Wall surface	0-20	20
H	Xe	Radiative seeding	Plasma core	0.04% of A-E	0.16
I	D <sub>2</sub> /DT	Neutral Beam Injector heating	Plasma core	0.6	0.6 (D <sub>2</sub> )
$\Sigma$				132.3 - 890.1	445.44

During operation, the fusion reaction is assumed as constantly ongoing stable reaction, which converts 2.67 Pa · m<sup>3</sup>/s of DT into <sup>4</sup>He - following Equations (2.1) and (2.2) for a thermal output of  $P_{\text{thermal}} = 2$  GW. No further reaction is assumed to occur within the fusion reactor in this context. This way, apart from the fusion reaction during operation and the wall outgassing, the torus output set equal to its input.

### 3.5.2 Hydrogen Recuperation Efficiencies

Quantification of the hydrogen recuperation efficiencies in each loop considerably determines the performance requirements of each associated system block, hence the assumptions made must be carefully chosen. To minimize the duty of detritiation systems in the Outer Tritium Loop, it is a sensible approach to front-load the retrieval of hydrogen as far as technically feasible. For the Metal Foil Pumps in the Direct Internal Recycling Loop, Day et al. consider a hydrogen recuperation efficiency of  $\eta_{\text{DIR}} = 80\%$  as feasible [20]. Consequently, this value is chosen as the benchmark for the Reference Design Point.

The remaining exhaust gas including the 20% unrecovered and chemically bound hydrogen is transferred to the Exhaust Processing System in the Inner Tritium Loop. Here, a large fraction of the remaining hydrogen is isolated from the exhaust gas using palladium permeators. To process hydrogen bound in compound molecules, a cracking step is implemented as well as an intermediate step of a two-staged permeator setup. Overall a hydrogen recuperation efficiency of  $\eta_{\text{EPS}} > 99\%$  in the INTL is assumed. The technical setups to achieve the target efficiencies are elucidated for the Metal Foil Pumps in Section 5.2 and for the permeators in Section 6.1.

For the Outer Tritium Loop, the treatment of the three hydrogen isotope is prioritized differently. First, the system blocks of the Outer Tritium Loops are optimized to minimize the release of tritium to the environment. Considering the size of DEMO in comparison to ITER, the upper release limit benchmark is set to the ITER heavy maintenance release limit of 2.5 g/a. Second, all protium entering the fuel cycle must be removed via the OUTL and the propagation of protium into the Inner Tritium Loop must be constrained. Finally, as intermediary isotope, deuterium is bound to escape the fuel cycle in larger quantities than tritium. Large quantities of lost deuterium are to be avoided.

### 3.5.3 Fuel Gas Composition

A robust quantification of the DT imbalance is not obtainable at this stage of design. For the RDP a surplus of deuterium in the fuel cycle is assumed, although the inversed case is equally conceivable. As representative source of a fuel gas composition disparity, a considerable asymmetry is generated in the RDP by a deuterium-only Neutral Beam Injector (NBI), which feeds matter directly into the tokamak reactor ( $0.6 \text{ Pa} \cdot \text{m}^3/\text{s}$  as specified in Table 3.9). In addition, its vacuum systems accumulate deuterium, which is partially forwarded to the Exhaust Processing System ( $F_{\text{NBI\_Vac}} = 10 \text{ Pa} \cdot \text{m}^3/\text{s}$ ).

Similarly, a robust quantification of the integral protium source term is currently not feasible as it depends on multiple, still undefined design parameters. Main factors are (i) the choice of the Breeding Blanket technology, (ii) the extent to which conventional water is utilized as a vacuum vessel or breeder coolant, (iii) the protium content and permeation properties of the fuel cycle support structure and (iv) the usage and efficiency of anti-permeation coatings on water or hydrogen confining surface structures.

To provide a starting point for the RDP the simulation assumes the source terms listed in Table 3.10. The way these values determine the design of the fuel cycle is discussed in Chapter 8.

The protium ingress in the DIRL loop is assumed as outgassing of the vacuum vessel and represents a constant source of  $0.1 \text{ Pa} \cdot \text{m}^3/\text{s}$  over both the dwell and burn phase [47]. For the INTL, the value chosen for the protium ingress represents the maximum capacity of the Isotope Rebalancing and Protium Removal system (cf. Section 6.2). In the OUTL, protium is used in large quantities as flushing agent. Any additional ingress of protium is negligible there in comparison.

To guarantee a supply of DT fuel to the torus in the optimal ratio, the underrepresented species must be enriched. Three actuators are foreseen in the fuel cycle to manipulate the isotope concentration in the fuel cycle. Each is assumed with the following requirements in the RDP:

- (i) The Isotope Rebalancing and Protium Removal system block in the INTL must be designed with the capability to equilibrate the steady state torus throughput on its own.
- (ii) Trace-tritium recovery from the exhaust gas and the Outer Fuel Cycle is conducted by the OUTL. The excess isotope must be isolated in the Isotope Separation System at high purity to remove it from the fuel cycle.
- (iii) Top-up of deuterium is provided by external supply.

Table 3.10: Reference Design Point assumptions for the source terms of the individual hydrogen isotopes in the different loops. The tritium input quantity is equivalent to a Tritium Breeding Ratio of  $\text{TBR} = 1.05$ .

Isotope	DIRL ( $\text{Pa} \cdot \text{m}^3/\text{s}$ )	INTL ( $\text{Pa} \cdot \text{m}^3/\text{s}$ )	OUTL ( $\text{Pa} \cdot \text{m}^3/\text{s}$ )	Source
H	0.1	0.22	-	Permeation
D	0.6	10.0	-	Deuterium NBI
T	-	-	1.405	Breeding Blanket

## 4 Fuel Cycle Simulator

In order to reproduce the fuel cycle in its entirety in a simulation program, essentially, its complexity must be managed. This can be achieved by (i) selecting a suitable software framework, (ii) partitioning the fuel plant into stand-alone functional blocks and (iii) choosing the appropriate numerical approach. To provide some background on the scope of fuel cycle modelling, a short summary of the development over time is provided first.

### Past and Present of Fusion Fuel Cycle Simulation

Over the course of several decades different approaches have been chosen to assist fuel cycle design by predicting its behaviour in a computerized model. An analytic approach marks one of the first prominent fusion fuel cycle models in the year of 1986 [48]. The model was expanded later to derive the requirements of a Breeding Blanket [49]. The model approach is based on a web of interlinked black boxes, each characterised with a residence time  $\tau$  and a hydrogen inventory  $I_Q$ . The evolution of  $I_Q$  in dependence on time  $t$  is then determined using a simple mass balance given in Equation (4.1). Typically, the whole model focusses on tritium inventories in the unit of mol to address tritium distribution among the system and pin-point the technical requirements of tritium self-sufficiency.

$$\frac{dI_Q}{dt} = F_{in,Q} - F_{out,Q} = F_{in,Q} - \frac{I_Q}{\tau}, \quad (4.1)$$

where  $F_{in,Q}$  denotes the input stream from upstream system blocks. The output stream  $F_{out,Q}$  is given as the product of the residence time multiplied by inventory of hydrogen isotope  $Q$  in that system block. The values of  $\tau$  as well as split factors - provided a system block features multiple outputs - are taken as empirical values from the literature or postulated as design requirements and implemented as rigid parameters into the code. The resulting set of ordinary differential equations can in theory be solved analytically for a simple fuel cycle. However, the complexity escalates rapidly as the number of incorporated system blocks increases [48]. Hence the numerical approach is favoured in more recent fuel cycle simulator adaptations for different fusion-related facilities all around the world [50][51][52].

The inclusion of physics-based models - to expand on the black box approach - was pushed during the Engineering Design Activities of ITER [53] such as the tailor-made TRUFFELS and CFTSIM codes [54][55], which evolved into the TRIMO code [56] to model in detail the behaviour of the water detritiation facility of ITER. In the meantime, commercial software developed into a valuable tool for the design of chemical plants, featuring intricate material property databases, dynamic process optimization tools and user-friendly interfaces. The software platforms gPROMS, EcoSimPro and the ASPEN® Custom Modeler (ACM) are well-established framework tools and already used in the context of fusion [57][58]. They all comprise a proprietary program language and an equation-based code.

## 4.1 On the Choice of the Software Framework

From these candidates, the most suitable is selected for the DEMO fuel cycle simulator to initiate this work. The choice of the most suitable software platform is based on their performance for a set of imposed requirements for the task at hand:

- A Tritium data** Are properties of tritiated species integrated or implementable?
- B Customisation** Can model blocks be programmed and integrated into the setup?
- C Transient** Does the software feature dynamic simulation?
- D Licensing** Is the software available as open-source? What is the cost of licensing?
- E Solver** Is the numerical solver robust? Are there multiple options included?
- F Support** Is the software updated regularly and is customer support available?
- G Add-ons** Does the software feature an additional asset for the work?
- H User interface** Is the software and coding aspect easy to learn and operate?
- I Interfaces** Can the software handle interfaces to external input/outputs?

The requirements are compared to one another in a Pugh decision matrix as listed in Table 4.1.

Table 4.1: Pugh decision matrix of the requirements imposed on the software platform of the fusion fuel cycle.

Criterion	A	B	C	D	E	F	G	H	I
<b>A</b>	-	2	1	0	0	0	0	0	0
<b>B</b>	0	-	1	0	0	0	0	0	0
<b>C</b>	1	1	-	0	0	0	0	0	0
<b>D</b>	2	2	2	-	2	0	1	1	1
<b>E</b>	2	2	2	0	-	1	0	0	1
<b>F</b>	2	2	2	2	1	-	1	2	2
<b>G</b>	2	2	2	1	2	1	-	0	1
<b>H</b>	2	2	2	1	2	0	2	-	2
<b>I</b>	2	2	2	1	1	0	1	0	-
<b>Σ</b>	<b>13</b>	<b>15</b>	<b>14</b>	<b>5</b>	<b>8</b>	<b>2</b>	<b>5</b>	<b>3</b>	<b>7</b>

In a subsequent step the software features of Chemcad Dynamics, Aspen Custom Modeler, gPROMS, Dymola, EcosimPro and ProSimDAC are analysed and rated on their applicability to items A-I on a grade between 0 (not applicable) and 5 (fully applicable) as shown in Table 4.2.

Table 4.2: Rating of the different software frameworks based on the decision matrix shown in Table 4.1.

Criterion	Chemcad Dynamics	ACM & gPROMS	EcoSimPro & Dymola	ProSimDAC
<b>A</b>	0	5	5	5
<b>B</b>	4	5	5	5
<b>C</b>	5	5	5	5
<b>D</b>	4	3	4	2
<b>E</b>	5	5	3	5
<b>F</b>	2	5	4	4
<b>G</b>	4	5	5	5
<b>H</b>	5	3	4	5
<b>I</b>	4	5	5	5
<b>Compatibility</b>	257/360	344/360	334/360	343/360

As can be seen in Table 4.2, for a target compatibility of 90 % (>324) most candidate software is applicable to model the fusion fuel cycle. From them, the commercially available, Aspen Custom Modeler (ACM) is chosen, as a campus license is readily available. Specifically, the program comprises a set of additional features. First, it holds the possibility to incorporate multiple models in a single solver entity in an intuitive drag-and-drop flowchart environment. Second, it is capable of modelling processes transiently and allows for manipulation of variables while running the simulation. Third, it uses a cross-reference to an internal material property database, which includes most relevant components. However, the database is found to lack most material properties at cryogenic temperatures and of tritiated species in general. Finally, it features the capability to implement self-coded models and compare them to a library of pre-coded models developed for typical chemical engineering functions.

## 4.2 Numerical Solution Approach

### Numerical Solver

The Aspen Custom Modeler is equipped with an integrated solver, which provides a solution of determined system of equations numerically. The software comes with a selection of four different integration solvers. A thorough introduction to numerical analysis in engineering can be found in [59]. The simplest, most time-efficient approach among them is the **explicit Euler** method:

$$y(t + dt) = y(t) + h \cdot \dot{y}(t), \quad (4.2)$$

where  $t$  is the current time step and  $dt$  is the time step interval.  $y(t)$  and  $y(t + dt)$  represent the solution of a function at their respective time step;  $y(t = 0)$  is given as initial value and  $\dot{y}(t)$  denotes the time derivative of said function. In the program, the explicit Euler method can be refined by applying a variable step, fourth order, explicit **Runge-Kutta** integrator. Here for each time interval  $dt$ , the latter term of Equation (4.2) is substituted with the weighted average of four increments. Every increment is then derived by the solution of the previous increment whereby the initial increment is given by the explicit Euler method.

However, all explicit integrators are prone to instabilities as they tend to oscillate around the actual solution if the initial values are ill-posed. This issue is aggravated by the fact, that the boundary conditions of all models change abruptly over the course of the simulation to mirror the dynamic behaviour of the fusion reactor. Both explicit solvers have been tested extensively for various models in an environment of rapidly changing boundary conditions. They often failed to procure a stable solution and are hence disregarded in this work.

Instead an implicit integrator is used in all calculations, which is capable of a more robust simulation procedure. The method entails higher computational effort and requires a stiff system of equations as well as being prone to problems involving steep gradients or singularities. The basis is given by the **implicit Euler** method in Equation (4.3) with the same denotation as in the explicit Euler method but with the key distinction that the time derivative is dependent on the desired solution  $y(t + dt)$  instead of the initial solution  $y(t)$ . This approach requires an

---

additional layer of numerical approximation, which increases the computation time. A sequence of iterations occurs within each time step and persists until a termination criterion  $\varepsilon$  is reached.

$$y(t + dt) = y(t) + h \cdot \dot{y}(t + dt), \quad (4.3)$$

To further improve the stability of the numerical solver, **Gear's algorithm** is provided as an option, which expands on the implicit Euler method by applying Lagrange interpolation. This integrator is implemented in ASPEN with an automatically varying time step size and is tailored to solve stiff differential equations. Both implicit procedures are able to provide a stable solution, but the computation time of Gear's algorithm exceeded that of the implicit Euler by a factor of two with no visible benefit to simulation stability or output accuracy. As the code structure of ASPEN does not support parallelization, the computation time is limited by the capacity of a single processor core. In the context of adopting the fuel cycle in its entirety into the model, computation time quickly arises as a bottleneck. Consequently, the implicit Euler solver is chosen as integrator.

### **Convergence**

For the convergence of the numerical solver both the relative and absolute error are considered as termination criterion. A value of  $\varepsilon = 10^{-5}$  is used in all instances.

### **Time Scale and resolution**

Modelling of the fuel cycle is performed over the course of several burn and dwell phases (~10 hours) at a resolution of 1 s. Depending on the level of perturbation introduced in comparison the former equilibrium state, the computation time of the fuel cycle model varied between factors of 0.1-1 in relation to real time.

### **Variables and Parameters**

In every model a series of variables and parameters are defined as well as a set of equations that connect them. Variables in this context represent values that may change over time (e.g. the gas pressure), while parameters remain constant (e.g. the vessel volume under the assumption that no thermal expansion occurs). For every variable at any time, the program performs a consistency check against a numerical boundary. For example, if the absolute pressure in a system ever reaches a negative value, the whole simulation is aborted. The lower and upper numerical boundaries implemented in all simulations are denoted in the list of symbols as  $L_{low}$  and  $L_{up}$ .

### **Discretization**

Many processes, such as the separation of hydrogen species in a column, are modelled by segmenting the process into a number of nodes along the concentration gradient in a single dimension. Then each node is solved for the equilibrium state in dependence of a physics-based interrelation between the affected species. This simplifies the simulation in two aspects. First, all absolute quantities are reduced to a scalar and second all gradients become unidirectional. Thereby the problem becomes hyperbolic in nature and reversed flow is generally not possible. For each subsystem the relevant relations are elucidated in the corresponding chapters.



## Mass Balance

Each model is completed by correlations specific to the related process as well as a generic mass balance for each species  $i$  given in Equation (4.4).

$$\frac{dl_i}{dt} = \sum_i F_{\text{input}}(i) - \sum_i F_{\text{output}}(i) - F_{\text{decay}} - F_{\text{loss}}, \quad (4.4)$$

where the input and output streams are specified for the subsystems in each chapter. The decay of tritium is calculated for every tritium inventory but omitted in mass balances beyond this point of the work for the sake of improved readability.

## 4.3 Decomposition of the Plant in Functional Blocks

In the context of the equation-based solver of the Aspen Custom Modeler, the programming task revolves around building a determined system of equations as well as a sensible initial state for the entire system. To partition the problem, the whole fuel cycle is divided into system blocks, representing a functional block - e.g. the Matter Injection System introducing matter to the fusion reactor. Each system block is composed of stand-alone models, each constituting a determined system in itself.

Every model represents a single piece of technology on the subsystem level. This way any model can be analysed in isolation - provided that the input boundary conditions are fixed, in context of the system block it is part of as well as in conjunction with any or all other models. Then, each subsystem is connected to other subsystems via input and output streams. Different types of streams are implemented depending on the composition of the content conveyed, applying the nomenclature defined in Table 3.3. Key input and output streams of system blocks are assigned an encircled number between ①-⑳ and quantified for the Reference Design Point.

Different physical processes involving hydrogen can be found throughout the functional blocks of the fuel cycle. The interaction processes partially overlap and correspond to those defined in Section 3.2. The computational effort can be streamlined by applying the same correlations throughout multiple models. Therefore, as a basis of defining a determined system in each of them, a combination of the four hydrogen interactions represents the foundation of every code, linking the different components together in their equilibrium state. This foundation is then expanded upon with additional correlations specific to the technology.

The different subsystems of the fuel cycle each comprise a combination of these four interactions as illustrated in Figure 4.1 expands upon Figure 2.2 and illustrates, which hydrogen interaction processes must be considered in the different fuel cycle system blocks. The following Chapters 5, 6 and 7 correspond to the three different loops of the DEMO fuel cycle and define in detail the specific function of each system block, the subsystems comprised therein as well as how these are translated into a set of correlations forming consistent models.

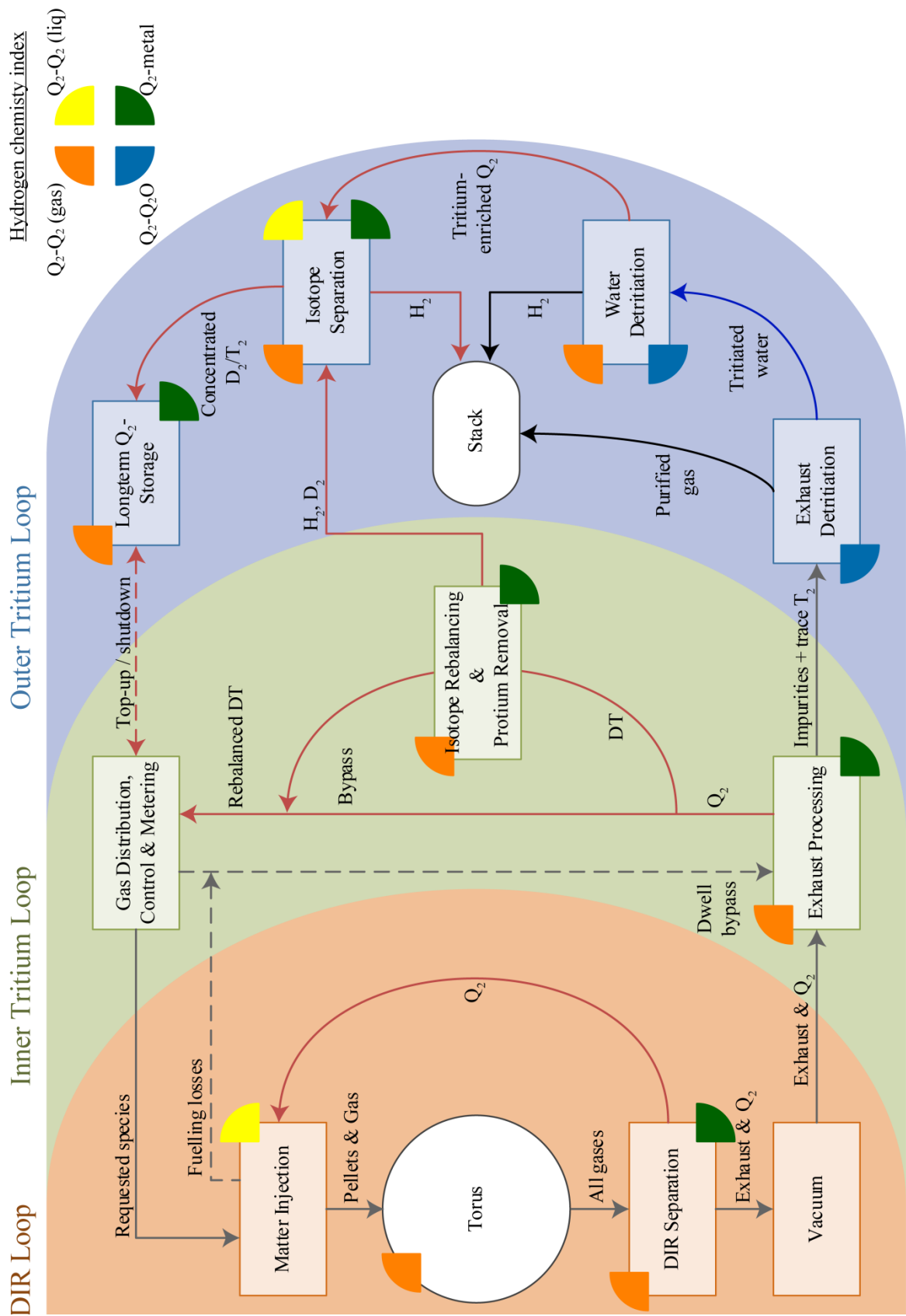


Figure 4.1: The Inner Fuel Cycle architecture expanded by the hydrogen interaction processes modelled in every system block.

## 5 The Direct Internal Recycling Loop

The DIR loop links the fusion reactor to the fuel cycle. It essentially consists of the Matter Injection System (MIS) block upstream and the Vacuum system block downstream of the torus vessel. The former must fulfil a set of tasks each realized with a different technology and connections allocated all around the torus. The latter will be installed as a series of pump casks in the lower port ducts of DEMO, close to where expelled particles hit the divertor.

Integrated into the vacuum pump cask is a separation stage, which is intended to optimise the fuel cycle. Here, unburnt  $Q_2$  ( $D_2$ ,  $T_2$  and  $DT$ ) is separated from the exhaust gas in a process step near the torus and directly recycled internally - hence the name of the loop. The candidate technology is called Metal Foil Pumps (MFP), which isolates supra-thermal hydrogen by superpermeation through a thin membrane from the rest of the exhaust gas.

Both outputs of the MFP are processed by similar vacuum pump trains, which on the one hand return the isolated hydrogen to the matter injection and on the other hand transfer the remaining exhaust gas to the INTL. In both cases, the incoming gas is compressed to almost atmospheric pressure by a high vacuum pump and a fore vacuum pump.

The MIS supplies the fusion reactor with all the necessary species, using different supply technologies to meet the requirements of the reactor. The injection methods reach from accelerating hydrogen pellets over gas injection to neutral beam injection.

Central hub of the fuel cycle is the Gas Distribution, Control and Metering system (GDCM). Tasked with the collection and distribution of matter, it consists of several buffer vessels and gas valve boxes.

Table 5.1 lists the throughputs of the streams ①-⑧, indicated in Figure 5.1, which connect the system blocks as well as their compositions.

Table 5.1: Throughput and composition of all streams between system blocks in the DIR loop for the Reference Design Point of DEMO. The stream marked with an asterisk (\*) consists of multiple streams each with pure species.

Stream	$F_{GPS}^*$ ①	$F_{NBI}$ ②	$F_{PLS}$ ③	$F_{loss}$ ④	$F_{MIS}$ ⑤	$F_{torus}$ ⑥	$F_{DIR}$ ⑦	$F_{ret}$ ⑧	Unit
F	70.39	10.6	464.37	89.92	445.44	445.54	346.28	99.26	(Pa·m <sup>3</sup> /s)
$y(H_2)$	0.76	0	1.07	1.07	1.02	1.04	1.10	0.84	(mol%)
$Q_2$ $y(D_2)$	35.14	100	49.44	49.44	47.25	46.94	49.52	37.92	(mol%)
$y(T_2)$	35.14	0	49.44	49.44	47.25	46.80	49.38	37.81	(mol%)
$y(N_2)$	28.41	-	0	0	4.49	4.49	-	20.15	(mol%)
$y(Ar)$	0.55	-	0	0	0.09	0.09	-	0.39	(mol%)
$y(Xe)$	0	-	0.05	0.05	0.04	0.04	-	0.18	(mol%)
$y(He)$	0	-	0	0	0	0.60	-	2.70	(mol%)

The layout of the DIR loop with all its subsystems and connecting streams is shown in Figure 5.1 below. Streams ⑨ and ⑩ are discontinuous and covered by Sections 5.4 and 8.1, respectively. Streams ⑪ and ⑱ are discussed in the Inner Tritium Loop chapter. Streams ⑳ and ㉔ are given in the Outer Tritium Loop chapter.

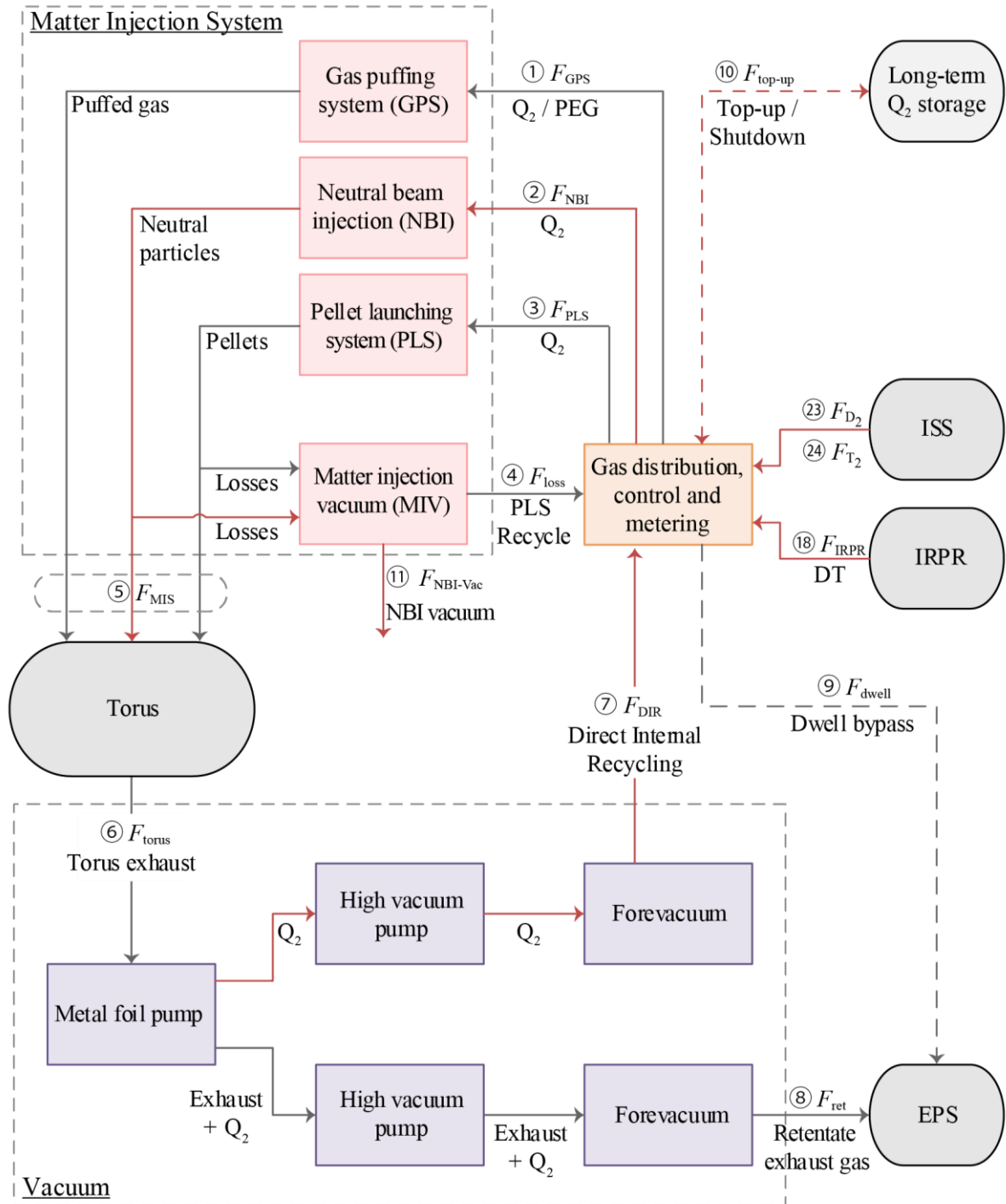


Figure 5.1: Flow chart of the DEMO Direct Internal Recycling Loop with its three system blocks “Vacuum”, “Matter Injection” and “Gas Distribution Control and Metering” including all subsystems and boundary conditions. Discontinuous streams ⑨ and ⑩ are represented by dashed lines.

## 5.1 Matter Injection

The technical implementation of the Matter Injection System is always customized to the design of the fusion device and varies significantly for existing and planned facilities [60][61][62]. With growing size of the fusion device, the requirements tighten, demanding technical solutions that are increasingly large and sophisticated. In particular, the feed upstream of the torus must be optimized with regards to supply efficiency as the amount of non-recoverable losses therein are propagated downstream the reactor and thereby entail a considerable scale-up of the whole fuel cycle. Multiple requirements are posed by the fusion reactor, each fulfilled by a dedicated subsystem of the MIS.

The prime function of the MIS consists of maintaining the plasma density by replenishing lost fuel. Therefore, fuel is injected as solid material in the form of accelerated pellets to obtain sufficiently high fuel efficiencies and establish an equimolar DT ratio in the plasma core. The fuelling efficiency scales with the increasing velocity of the matter injected. The ramifications of this phenomenon for the DEMO MIS system are discussed in the literature [63].

To minimize losses a Pellet Launching System (PLS) is used, which supplies frozen pellets directly to the plasma core. The PLS predominantly conveys hydrogen fuel. Plasma Enhancement Gases for radiative core seeding (xenon in the RDP) are delivered to the core by doping them into hydrogen pellets. Additionally, certain boundary conditions between the torus first wall and the plasma must be upheld during reactor operation and start-up to enable control over the reactor dynamics. This comprises the need for a multitude of Gas Puffing Systems (GPS) realized with fast reacting gas valves, which deliver matter to various locations in the torus. Finally, Neutral Beam Injectors (NBI) are a candidate technology to realize heating of plasma. Although technically part of the heating infrastructure, they operate by injecting matter into the fusion plasma and thereby represent an interface to the fuel cycle.

As all these subsystems inject matter directly to the torus, which operates under constant vacuum, any connection lines must be evacuated and attached to internal recycling loops to minimize losses. In this work, these recycling loops are referred to as Matter Injection Vacuum (MIV) and assumed to operate in general detached from the fuel cycle.

The structure and implementation of each of these subsystems is briefly described in this chapter with regards to the expected scale. All matter injected via the MIS is supplied by the GDCM system in the tritium plant. Depending on the distance to the tritium plant a set of intermediate buffer vessels may be placed in the vicinity of the fusion reactor to ensure a quick response time and a continuous supply of gases. At this point in the fuel cycle, the purity of all species supplied to the MIS is assumed to be sufficiently high to not hamper the fusion reaction. If supply buffer tanks are used, they must be monitored and connected to an appropriate purification system to counteract a possible accumulation of impurities.

Each subsystem is designed to fit the required throughput as listed in Table 3.9 of the RDP. Scaling of the MIS is discussed in Section 8.2.

### 5.1.1 Pellet Launching

The necessity to freeze hydrogenic fuel prior to torus injection arises from the hot edge plasma, which prevents the atoms from entering the confined plasma and renders the penetration of hydrogen in a gaseous state almost impossible. Only a frozen pellet deposited at the torus high field side<sup>5</sup> and very high velocity is able to achieve viable fuelling efficiencies. This curious approach proves successful in current plasma devices and is considered for DEMO [63].

Typically, a Pellet Launching System consists of three consecutive steps: (i) pellet freezing, (ii) pellet acceleration and (iii) pellet guiding with different possible technical solutions. Within the framework of the fuel cycle simulator a conventional approach is adopted, using a liquefier and a twin-screw extruder for the first step, to cool down and freeze hydrogen into a continuous rod of ice at a temperature of below 15 K. A subsequent cutting device then generates pellets of the desired size from the rod. In the second step, pellets are propelled using a centrifuge at a given frequency and velocity. Finally, the pellets are guided to the injection location on the torus inboard via an evacuated, curved guiding tube. No PLS currently under operation is capable of fulfilling the DEMO requirements of quantity, pellet velocity and efficiency. To provide a sense of scale; the fuel cycle model includes a PLS with performance parameters deduced from state-of-the-art technologies. The scale-up to DEMO requirements is then performed under consideration of a set of PLS constraints [63]:

#### Pellet Efficiency

The process of forming, accelerating and guiding frozen hydrogen pellets towards the fusion reactor is accompanied by losses [64], which must be removed and are quantified by the delivery efficiency  $\eta_{\text{PLS}}$  as the molar ratio of matter delivered to the plasma core over the matter supplied to the PLS ( $F_{\text{PLS}}$  ③). The estimated delivery efficiencies are given in a range ( $\eta_{\text{min}}$ - $\eta_{\text{max}}$ ) for each section with a selected value for the RDP ( $\eta_{\text{RDP}}$ ) as listed in Table 5.2. Collectively, they form the overall efficiency  $\eta_{\text{PLS}}$  of the Pellet Launching System.

Table 5.2: Quantification of the DEMO Pellet Launching System delivery efficiency. The efficiencies  $\eta$  are taken from [64].

Section	Component	$\eta_{\text{min}}$ (%)	$\eta_{\text{max}}$ (%)	$\eta_{\text{RDP}}$ (%)	$F_{\text{RDP}}$ (Pa·m <sup>3</sup> /s)	Evacuated by
Pellet freezing	Screw extruder	95	99	99	464.37	MIV
P. acceleration	Centrifuge	95	95	95	459.73	MIV
Pellet guiding (partitioned by section crossed)	Confinement barrier	75	97	95	436.74	MIV
	Cryostat	75	97	95	414.91	MIV
	Vacuum vessel	95	97	95	394.16	torus vacuum
	Breeding Blanket	95	97	95	374.45	torus vacuum
Tokamak	Scrape-off layer	50	97	90	355.73	torus vacuum
	Plasma core	(cf. Table 3.9)			320.16	torus vacuum
$\Pi$	$\eta_{\text{PLS}} =$	22.9	79.1	68.9		

<sup>5</sup> In context of a tokamak reactor the Magnetic High Field Side (MHFS) refers to the inboard side of the plasma ring shape. Here, the magnetic configuration of the tokamak yields a radial drift propelling the injected matter towards the plasma core, which is an essential contributing factor to the overall injection efficiency [63]. Given the magnet infrastructure present at this particular location, the technical implementation of a guiding tube from this angle proves difficult for the tokamak design.

## Pellet Throughput

The total throughput processed by the PLS is given as  $F_{\text{PLS}} = 464.37 \text{ Pa} \cdot \text{m}^3/\text{s}$  ③ in Table 5.1. This represents about three times the target throughput of ITER, which will be produced by multiple twin screw-extruders operating in parallel. A test mock-up of a single deuterium extruder can generate a steady state throughput of up to  $F_{\text{Extr}} = 39 \text{ Pa} \cdot \text{m}^3/\text{s}$  of pure  $\text{D}_2$  ice [65]. Scale-up of these extruders is constrained by many parameters including heat transfer, slip and torque as thoroughly described by Fisher [66]. Therefore, a total of 10 to 12 extruders of similar design in parallel operation are a reasonable assumption for DEMO.

The throughput of the PLS is given as the product of a pellet content  $I_{\text{Pellet}}$  times the number of pellets injected per second  $f_{\text{Pellet}}$ . The size of pellets is limited by their impact on plasma stability. The current maximum is based on ITER assumptions of  $I_{\text{Pellet}} = 11.3 \text{ Pa} \cdot \text{m}^3 \cong 6 \cdot 10^{21}$  atoms [63], which yields an integral pellet injection frequency of  $f_{\text{Pellet}} \cong 41$  Hz. Recent considerations suggest injection of smaller pellets. For  $I_{\text{Pellet}} = 3.77 \text{ Pa} \cdot \text{m}^3 \cong 2 \cdot 10^{21}$  atoms [67], the frequency would have to be increased to  $f_{\text{Pellet}} \cong 123$  Hz. The integral injection rate is then distributed among multiple centrifuge injectors. Clocking of the cutting device as well as the centrifuge can be assumed a non-issue in this context as current setups already show pellet frequencies of up to  $f = 80$  Hz for a single device [68].

## Pellet Velocity

Efficient fuelling requires maximizing the pellet velocity perpendicular to the flux surface at the point of injection. However, the pellets progressively ablate on the trajectory to the torus with increasing speed. The maximum velocity of pellets is restricted by the geometry of the guiding tube favouring a single bend with a large curvature radius. A large radius however, results in a worse injection angle, given the limited space at the torus inboard. An optimization study on the current design of DEMO yields a pellet velocity of  $v_{\text{Pellet}} = 1194 \text{ m/s}$  for the highest possible perpendicular speed [67]. The velocity of a pellet  $v_{\text{Pellet}}$  is tied to the design and dimensions of the centrifuge as well as its rotational speed, which in turn is tied to the pellet frequency. For a single centrifuge with a straight arm, they correlate by the definition of the angular velocity in Equation (5.1).

$$v_{\text{Pellet}} = \sqrt{8\pi} \cdot f_{\text{Pellet}} \cdot rn, \quad (5.1)$$

where  $r$  denotes the centrifuge arm radius in m and  $n$  denotes the amount of centrifuge revolutions per pellet acceleration event.  $v_{\text{Pellet}}$  and  $f_{\text{Pellet}}$  are given in m/s and Hz, respectively.

Deduced from these considerations a PLS setup is chosen for the RDP including:

- (a) 10 extruders, each with a cutter and a steady state throughput of  $F_{\text{Extr}} = 47 \text{ Pa} \cdot \text{m}^3/\text{s}$ .
- (b) 5 centrifuges, each with a pellet frequency of  $f_{\text{Pellet}} = 8.2$  Hz and a design specification of  $rn = 3.28$  m. Given  $n = 3$ , the smaller-sized pellets can be injected as well.
- (c) 5 guiding tubes, each with a large bending radius leading to a point on the MHFS.
- (d) 5 recuperation systems (MIV) recovering 62.35 % of the losses.

### 5.1.2 Gas Puffing

Gas injection valves are installed all around the torus and serve multiple purposes during the dwell and the burn phase. These gaseous species are injected into the divertor area or the plasma boundary to establish and maintain controlled operation conditions for the plasma in the tokamak. Although the choice of gas species and their quantity remains to be finalised, three species are identified as suitable candidates in addition to the fuel gas, each to be injected with a specific assignment. The gases are quantified for the RDP in Table 3.9 under the items E through H.

Realisation of gas injection valves does not represent a significant technical challenge. Nonetheless, a quick response time and sufficient supply of matter are paramount and non-trivial factors to guarantee plasma control via gas injection. Hence, a RUN-VENT-cycle is foreseen for this purpose in close proximity to the torus [64]. In such a loop, gas is constantly circulated between a buffer vessel and a three-way valve by a dedicated pump. Upon request the valve permits a fraction of the circulating pressurized gas to surge into the torus. The pressure and gas content in each cycle is monitored via a manometer and topped-up via a second three-way valve to maintain steady state. The flow rate is controlled using a regulation valve as a throttle.

The ratio of recirculated to ventilated gas during operation is kept in a 5:1 ratio by the three-way valve. This way, for every mol fed to the torus, five mol are circulated through the loop to maintain a high level of pressure in the cycle. During dwell, no gas is fed to the torus and the total amount is fully recirculated instead. The setup of the RUN-VENT-cycle - as implemented into the model - is shown in Figure 5.2. Every item E-H stated above uses a similar setup, each contributing to the steady state throughput during reactor operation ( $F_{GPS}$  ① cf. Table 3.9). The capacity of each of these GPS loops is set with a gaseous inventory to cover supply for the fusion reactor for five minutes.

### 5.1.3 Neutral Beam Injection

The plasma heating concept of DEMO may comprise a set of Neutral Beam Injectors (NBI). In a three-step process, hydrogen particles are first ionized in a beam source, then accelerated and finally neutralized. The neutral hydrogen particles retain their initial energy and are injected into the plasma core through a duct in the vessel.

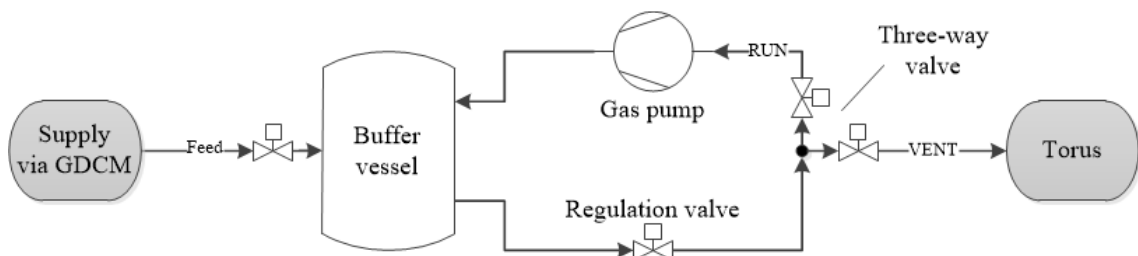


Figure 5.2: Operating principle of a RUN-VENT cycle as implemented for the Gas Puffing System into the fuel cycle model.



Operation of NBI devices inherently requires low pressure conditions and vacuum pumps of substantial size and throughput. A description of the DEMO NBI concept is given in [69]. The NBI contribution to the overall torus throughput is comparably small ( $0.6 \text{ Pa} \cdot \text{m}^3/\text{s}$  cf. Table 3.9). However, significantly larger quantities of gas are circulated internally by the attached vacuum pumping system.

Concerning the hydrogen species used in the NBI, it remains undecided whether the NBI uses the reactor fuel DT or  $\text{D}_2$  as operating species. Protium is not considered to minimize its concentration in the plasma core. The use of DT demands a tritium-compatible system and requires coupling the NBI to the fuel cycle for purification and accountancy purposes. Pure  $\text{D}_2$  results in lower tritium inventories and simpler design requirements but creates an imbalance in the fuel mixture. The RDP assumes a  $\text{D}_2$ -NBI in accordance with the preliminary NBI concept for DEMO based on the gas driven neutralizer [70].

#### 5.1.4 Matter Injection Vacuum

The matter injection technologies connected to the torus are equipped with their proper evacuation system to recuperate losses and uphold the vacuum conditions within the supply lines. In immediate proximity to the torus, vacuum pumps cannot be installed however, as a combined result of the lack of space, the level of irradiation and the strong electromagnetic field. Losses of process gas generated in this vacuum dead zone - beyond the reach of the Matter Injection Vacuum (MIV) - must be processed by torus vacuum systems and increase the total fuel cycle throughput. These constraining conditions, in addition to the required tritium compatibility, also severely limit the choice of applicable vacuum technology and the achievable level of evacuation. The vacuum pumps implemented in the MIV are assumed of similar design to those implemented for the torus vacuum. In the PLS, these vacuum pumps are installed in the guiding tube and in the centrifuge vessel for this purpose. The gas from the ablated pellets is captured and recovered to compensate losses ( $F_{\text{Loss}}$  (4)). The GPS access lines downstream the three-way valves are assumed short and will not be evacuated. The NBI vacuum is described as part of the NBI setup in [69].

Naturally, the presence of vacuum pumps upstream the ducts, creates backflow of gas particles from the fusion reactor into the MIS and its vacuum systems. As a result, tritium compatibility of the affected subsystems must be built into the final design. Moreover, a connection must be foreseen to the Exhaust Processing System to purify the contents of each MIS of accumulated impurities. Conversely to the occurrence of backflow, process gas may slip from the guiding tubes into the torus. From the fuel cycle point of view, the effect of backflow and forward flow cancel out.

Especially, for the large NBI vacuum system, however, the backflow of impurities must be considered which requires a steady state treatment of a fraction of recirculating gas within the fuel cycle. Consequently, it is assumed that the NBI vacuum pumps close to the torus duct are connected to the fuel cycle propagating the circulating NBI gas into the Exhaust Processing System. For the RDP a throughput of  $F_{\text{NBI-Vac}} = 10 \text{ Pa} \cdot \text{m}^3/\text{s}$  (11) is chosen as reference case.

---

## 5.2 Metal Foil Pumps

Metal Foil Pumps (MFP) represent the first hydrogen separation process of the fuel cycle downstream the plasma. In the current state of design, the implementation of multiple Metal Foil Pump modules is foreseen in the lower pump ducts of DEMO [71]. In the reference design, a high proportion of the total gas throughput is processed there with short residence times in order to significantly reduce the scale of the downstream fuel cycle loops. For this reason, process steps of long residence times, e.g. the separation of isotopes, are avoided in the DIR loop.

Like other permeation setups, they essentially consist of an upstream and downstream chamber separated by a thin metal membrane. In contrast to conventional pressure driven permeation however, the driving mechanism implemented in the MFP is determined by the concentration gradient of energised hydrogen particles over the foil. To generate this gradient, the hydrogen molecules upstream are excited to a suprathreshold state by exposing them to a plasma source, whereas no energised particles are generated in the downstream chamber. As the hydrogen is atomized by the plasma, its kinetic energy is increased by more than 1 eV in comparison to the molecular ground state [72]. As a result, the absorption into the metal lattice of the foil is greatly facilitated, given that the dissociation energy for the adsorption process is already provided. For the right design parameters, high transmission probabilities of  $\chi_{\text{trans}} = 0.1 - 1$  can be observed through a foil, where  $\chi_{\text{trans}}$  is defined as the ratio of energized hydrogen throughput upstream and downstream the foil. This phenomenon is referred to as superpermeation [73] and is observed to achieve permeation fluxes against a pressure gradient [74], effectively constituting an exploitable pumping mechanism. Additionally, as the energy provided allows only hydrogen atoms to exceed the required activation energy to enter the metal lattice, the process shows a high selectivity and can therefore be implemented as a separation mechanism [34].

In the fuel cycle of DEMO, the achievable hydrogen recuperation efficiency of the DIRL  $\eta_{\text{DIR}}$  is tied to the integral pumping probability  $\chi_{\text{Pump}}$  of the Metal Foil Pumps, which forms as the superposition of three steps of matter transport:

- 1) The probability that a hydrogen molecule finds its way from the torus into the Metal Foil Pump and the plasma source within it ( $\chi_{\text{enter}}$ ).
- 2) The probability that the hydrogen molecule dissociates into energized atoms, which reach the metal foil without recombining beforehand ( $\chi_{\text{dis}}$ ).
- 3) The probability that an energized hydrogen atom is absorbed, then diffuses through the metal lattice and finally recombines on the surface in the downstream chamber and does not reabsorb ( $\chi_{\text{trans}}$ ).

$\chi_{\text{enter}}$  is governed by the pressure regime and the geometry downstream the divertor and the entrance of the MFP.  $\chi_{\text{excited}}$  depends on the design of the pump, especially the distance between the plasma source and the metal foil and the ratio of the scatter radius of the former to the degree of coverage of the latter.  $\chi_{\text{trans}}$  is correlated to the permeation flux through the membrane  $j_{\text{MFP}}$  and the foil area  $A_{\text{foil}}$ . A detailed calculation of  $j_{\text{MFP}}$  achievable by Metal Foil Pumps made of niobium is derived in Appendix A3.

Since the three transport probabilities show interrelations and the particle transport cannot be assumed as a continuum due to the low pressure regime downstream the DEMO divertor - the particle behaviour in the MFP can only be predicted by probabilistic methods. For this reason, Direct-Simulation-Monte-Carlo studies were conducted on the DEMO divertor [75] and the Metal Foil Pump [71] to investigate the overall pumping probability of a preliminary MFP design for DEMO. The latter foresees a cylindrical setup with a length  $l = 2$  m and a diameter  $d = 0.5$  m encircling a coaxially arranged linearly extended plasma source of  $d_{\text{plasma}} = 0.1$  m. For this setup, the results indicate a pumping probability for hydrogen in the range  $\chi_{\text{Pump}} = 82 \dots 96$  % and a pumping speed of  $S_{\text{MFP}} = 13.4 \dots 23.9$  m<sup>3</sup>/s for a given foil parameter of  $\chi_{\text{trans}} = 5 \dots 20$  %.

The pump design and performance estimations obtained are implemented as benchmark in this work. They are used to estimate the number of pumps required  $N_{\text{MFP}}$  as per Equation (5.2).

$$F_{\text{DIR}} = F_{\text{torus}}(Q_2) \cdot \eta_{\text{DIR}} \leq S_{\text{MFP}} \cdot p_{\text{in}} \cdot N_{\text{MFP}}, \quad (5.2)$$

where  $F_{\text{torus}}(Q_2)$  is the total hydrogen throughput downstream the torus - given as 424.19 Pa · m<sup>3</sup>/s for the Reference Design Point. For a conservative assumption, the recuperation efficiency is coupled to the lower boundary of the pumping probability  $\eta_{\text{DIR}} = \chi_{\text{Pump}} = 0.82$ , which fixes the expected pumping speed per pump to  $S_{\text{MFP}} = 13.4$  m<sup>3</sup>/s. Assuming a low upstream pressure of  $p_{\text{in}} = 1$  Pa, a number of  $N_{\text{MFP}} = 26$  Metal Foil Pumps are to be implemented in DEMO for the RDP to satisfy Equation (5.2).

To evaluate this theoretical Metal Foil Pump performance, the permeation flux  $j_{\text{MFP}}$  - derived in Equation (5.3) - can be calculated.

$$j_{\text{MFP}} = \frac{S_{\text{MFP}} \cdot p_{\text{in}}}{A_{\text{foil}}} = 4.265 \frac{\text{Pa} \cdot \text{m}^3}{\text{s m}^2}, \quad (5.3)$$

where  $A_{\text{foil}}$  denotes the area of a single Metal Foil Pump in m<sup>2</sup>. Notably, this is an averaged value, as the pumping performance varies over the length of the pump [71].

In comparison, current fusion related MFP experiments report a constant progress in achieving higher values of the permeation flux, from  $j_{\text{MFP}} = 0.449$  Pa · m<sup>3</sup>/(s m<sup>2</sup>) [34], over  $j_{\text{MFP}} = 1$  Pa · m<sup>3</sup>/(s m<sup>2</sup>) [71] up to most recently  $j_{\text{MFP}} > 4.4$  Pa · m<sup>3</sup>/(s m<sup>2</sup>) [76]. This shows that the requirement as per Equation (5.2) above is feasible.

The collected hydrogen permeate  $F_{\text{DIR}} = 346.28$  Pa · m<sup>3</sup>/s (7) is compressed by the subsequent vacuum pumps and recycled to the MIS via the GDCM. The remaining hydrogen - in conjunction with all non-hydrogen species - leaves the Metal Foil Pump as retentate. It is compressed in the same way and directed to the EPS ( $F_{\text{ret}} = 99.26$  Pa · m<sup>3</sup>/s (8)).

## 5.3 Vacuum Pumping

To operate properly, the DEMO reactor has the following requirements on its vacuum system, depending on the phase of operation:

- i. As the fusion reaction takes place, the pressure in the vacuum chamber must be kept low to limit convective heat transfer to the wall [10].
- ii. In the dwell phase, the pressure in the reactor must be reduced as much as possible to enable subsequent plasma ramp-up [77].

Both duties are to be handled by the same vacuum pumps located downstream of the divertor in a series of pumping casks working in parallel. In the former phase, the vacuum systems operate in steady state with a throughput defined by the torus output. In the latter phase, they keep pumping, which results in a gradual reduction of pressure in the vacuum vessel until plasma ignition can be reinitiated. The achievable degree of evacuation is constrained by the duration of the dwell phase as well as the outgassing of the wall.

For DEMO, a high-vacuum pump - located in the vicinity of the torus - and a vacuum backing pump are arranged in sequence to compress the incoming matter to almost ambient pressure. The envisaged technological implementation for DEMO is described in the KALPUREX process [24] and incorporates Linear mercury Diffusion Pumps (LDP) and a Liquid mercury Ring Pumps (LRP). A preliminary setup with the intent of facilitated maintainability and accessibility is described in [47] and embeds the Metal Foil Pump with two LDPs in a pumping cask. The setup of such a cask is portrayed in Figure 5.3. Multiple of these casks are positioned in the lower port of DEMO. Downstream the casks the exhaust gas is joined with a ring-shaped collector line situated below the reactor. The pipework ends in the tritium plant, where the backing pumps are located.

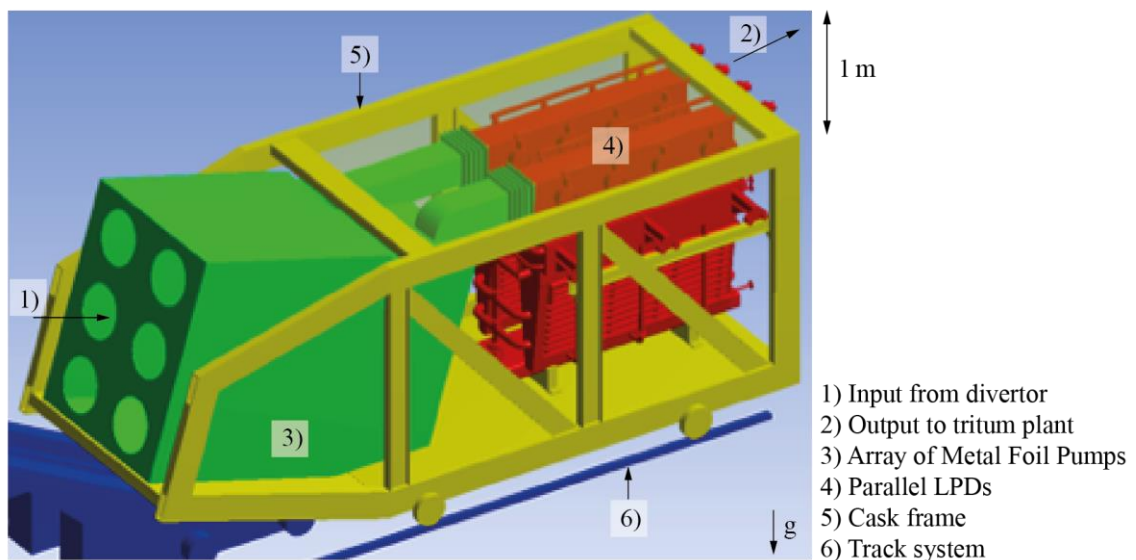


Figure 5.3: Conceptual design of a vacuum pump cask to be installed downstream the torus. The frame (in yellow) is mounted on a track system (in blue) and houses a box of 6 Metal Foil Pumps (in green) and two Linear Diffusion Pumps (LDP, in red). Picture adapted from [47].

To quantify the number of pumps and their total throughput following parameters are considered:

a) The torus **throughput** defines the target capabilities of the vacuum system. Given the requirements in Table 5.1 a total flow of  $F_{\text{torus}} = 445.54 \text{ Pa} \cdot \text{m}^3/\text{s}$  ⑥ must be processed. The DEMO tokamak layout includes 16 sub-divertor ports available for this purpose (cf. Figure 2.1) [78]. Hence, for this throughput each pumping cask allocated in one of the ports must at least process  $\approx 28 \text{ Pa} \cdot \text{m}^3/\text{s}$ , ideally more to increase contingency or free port space for other purposes.

b) The pressure regime downstream the divertor must be taken into account. To evaluate which **pressure regime** is present, the Knudsen number  $Kn$  is formed as the ratio of mean free path of a gas molecule  $\lambda$  over the characteristic diameter  $L_c$  of the flow domain along the path as given in Equation (5.4).

$$Kn = \frac{\lambda}{L_c}, \quad (5.4)$$

with  $\lambda$  defined in Equation (5.5) in dependence of the temperature  $T$  in K and pressure  $p$  in Pa as well as the particle diameter  $d_m$  in m.

$$\lambda = \frac{kT}{p\sqrt{2}\pi d_m^2}. \quad (5.5)$$

In the case of DEMO for divertor pressures of 1 – 10 Pa and  $Kn = 0.01$  [79], the vacuum regime resides in the slip-flow regime between transitional ( $Kn \approx 1$ ) and laminar flow ( $Kn \ll 1$ ) [80]. The quantification of the particle behaviour relies on three-dimensional statistical calculation methods such as a Direct Simulation Monte Carlo (DSMC) [81].

c) The throughput of a pump is given as the product of the inlet pressure  $p_{\text{in}}$  and the **pumping speed**, which is a characteristic of a pump and indicates the capacity of displaceable volume per time.

$$Q = S \cdot p_{\text{in}}, \quad (5.6)$$

where  $Q$  and  $S$  denote the pump throughput and pumping speed in  $\text{Pa} \cdot \text{m}^3/\text{s}$  and  $\text{m}^3/\text{s}$ , respectively. For the DEMO burn and dwell phases the estimated values in Table 5.3 are assumed based on the considerations made in [47].

Table 5.3: Estimated pump performance of the entirety of the DEMO torus high and fore vacuum systems [47].

Pump		Burn phase	Dwell phase	Unit
High-vacuum: LDP	$Q$	445.44	0.1	$(\text{Pa} \cdot \text{m}^3/\text{s})$
	$p_{\text{in}}$	3	>0.001	(Pa)
	$S$	148.48	100	$(\text{m}^3/\text{s})$
Fore vacuum: MRP	$Q$	445.44	0.1	$(\text{Pa} \cdot \text{m}^3/\text{s})$
	$p_{\text{in}}$	100	100	(Pa)
	$S$	4.45	0.001	$(\text{m}^3/\text{s})$

---

Assuming a mercury-based design of a Linear Diffusion Pump with the pumping speed capability of  $S = 10 \text{ m}^3/\text{s}$  [82][83] as well as a Liquid Ring Pump setup reaching  $S = 90 \text{ m}^3/\text{h}$  in an experiment [84], the number of pumps required in parallel for the high vacuum and fore vacuum stage can be calculated. For the Reference Design Point, a total of 15 high vacuum pumps and 178 backing pumps are required to process the combined steady state throughput of both  $F_{\text{DIR}}$  (7) and  $F_{\text{ret}}$  (8). In particular, the Mercury Ring Pump experiments represent again a proof-of-principal setup not tweaked to maximize throughput.

## 5.4 Gas Distribution Control and Metering

Gathering of the refined process outputs of the whole fuel cycle and distribution of matter is centralised in the Gas Distribution, Control and Metering system (GDCM). In a series of valve boxes and intermediate buffer tanks the concentration of impurities and hydrogen isotopes is constantly monitored and adjusted.

In particular, upholding the supply of the MIS systems during fusion operation must be guaranteed by the GDCM. In addition, the proportions of the three loops and of the bypass flows are controlled by the GDCM by manipulating the distribution of the input and output flows. The throughput and composition of all inputs is metered, and excess amounts of incoming matter is removed from the fuel cycle and sent to the long-term storage system. In the contrary case of a shortage of certain species, the same connection is used to top the fuel cycle up ( $F_{\text{top-up}}$  (10)).

To buffer inconsistencies and bridge the distance of fusion reactor and tritium plant of  $>50 \text{ m}$  [85], a reserve of all circulated species is sustained in proximity to the torus. In the fuel cycle model, each intermediary tank is designed with an inventory to sustain the fusion reaction for one minute. This alone constitutes a tritium inventory of or 33.5 g (5.55 mol). Attached to these buffer vessels is an emergency storage system with the capacity to hold the entire inventory of the fuel cycle.

As a ramp-down and subsequent start-up of involved processes is not sensible for the expected interruption of  $\sim 20$  minutes downtime, the Inner and Outer Tritium Loop will maintain in steady state operation. This is achieved by implementing a bypass stream ( $F_{\text{dwell}}$  (9)) essentially creating a short circuit within the fuel cycle by detaching the fusion reactor from the process as well as the auxiliary systems described in the previous chapters. For the sake of continuity and simplicity, the fuel cycle model assumes that this bypass mirrors the quantity and composition of the EPS input. To uphold steady state, this represents the equivalent of the two streams  $F_{\text{ret}}$  (8) and  $F_{\text{NBI}}$  (11). In practice, however, the bypass is expected to vary from the fusion reactor throughput.

As central element of the fuel cycle, the GDCM can be examined to display the contribution of each loop and to analyse the mass balance of each species.

## 5.5 Direct Internal Recycling Loop Summary

The Direct Internal Recycling Loop is modelled by managing the torus throughput with components scaled up to the Reference Design Point quantified in Table 5.1 from currently available pieces of technology. Four system blocks are comprised in the DIRL:

### Matter Injection Systems

For the Pellet Launching System a total of five setups are required each consisting of two extruders, one centrifuge and a guiding tube. They inject 84.06 mol% of the total torus input directly into the plasma core. The Neutral Beam Injectors (0.13 mol%) and Gas Puffing Systems (15.81 mol%) each contribute a smaller fraction to the overall input.

A Matter Injection Vacuum system recovers 62.35 mol% of the PLS losses.

### Metal Foil Pumps

A total of 26 Metal Foil Pumps are implemented to recover 82 mol% of the hydrogen throughput within the DIRL.

### Vacuum Pumping

The Metal Foil Pumps are distributed among 10-12 vacuum pump casks along with two Linear Diffusion Pumps each in the torus sub-divertor ports. The Linear Diffusion Pumps compress the gas from 3 Pa to a pressure of 100 Pa. The high vacuum pumps are backed by a set of about 180 liquid Mercury Ring pumps, which compress to ambient pressure.

### Gas Distribution Control and Metering

The GDCM is used to pilot the fuel cycle behaviour. A surrogate bypass stream is used to bridge the dwell period of the fusion reactor and uphold steady-state conditions in the INTL and OUTL. Additionally, top-up of various species to the fuel cycle is conducted via this system.

In total a steady state throughput of  $F_{\text{torus}} = 445.54 \text{ Pa} \cdot \text{m}^3/\text{s}$  (6) is processed in the Direct Internal Recycling Loop.





## 6 The Inner Tritium Loop

The central loop of the fuel cycle covers the two prime requirements of hydrogen isolation and rebalancing to a large extent. It enables maintaining the fusion reaction in stable conditions by providing fuel of sufficient quantity and satisfactory composition for a mid-term period of time. Two system blocks are attributed to the INTL, the Exhaust Processing System (EPS) and the Isotope Rebalancing and Protium Removal System (IRPR).

The EPS is required to isolate reusable species in the exhaust gas in a quick and efficient manner. The remaining hydrogen is separated via multiple stages of palladium permeators. Setup and functionality of each stage is described in Chapter 6.1. Efficient hydrogen removal in particular presupposes the decomposition of compound molecules containing hydrogen such as hydrocarbons. Therefore, the hydrogen removal is entwined with an intermediate step, where chemical compounds are cracked to increase the yield. Thereafter, the reusable species are captured in a series of separation processes. The remaining exhaust gas leaves the EPS and is sent to the Exhaust Detritiation System.

The captured hydrogen, on the other hand is directed to the IRPR system. Here, the composition of isotopologues is adjusted for reinjection by concentrating individual isotopes in a Temperature Swing Absorption (TSA) cycle. This is utilized to keep the amount of protium content in check as well as counterbalance any disequilibrium of the DT fuel mixture within the Inner Tritium Loop. The rebalanced hydrogen is forwarded to the GDCM and the remaining hydrogen excess is processed in the Outer Tritium Loop.

The Inner Tritium Loop as implemented with all its subsystems into the fuel cycle simulator is shown in Figure 6.1. The process streams ⑪-⑱, that constitute the inputs and outputs of system blocks are quantified for the Reference Design Point in Table 6.1.

Table 6.1: Throughput and composition of all streams connecting system blocks in the Inner Tritium Loop for the Reference Design Point of DEMO.

Stream	$F_{\text{NBI-Vac}}$ ⑪	$F_{\text{INTL}}$ ⑫	$F_{\text{exh}}$ ⑬	$F_{\text{PEG}}$ ⑭	$F_{\text{bypass}}$ ⑮	$F_{\text{low-trit}}$ ⑯	$F_{\text{high-trit}}$ ⑰	$F_{\text{IRPR}}$ ⑱	Unit
$F$	10.0	85.94	22.98	0.57	59.92	16.13	9.89	68.99	(Pa · m <sup>3</sup> /s)
$y(\text{H}_2)$	0	$1.99 \cdot 10^{-2}$	$1.57 \cdot 10^{-2}$	-	$1.99 \cdot 10^{-2}$	0.05	$1.49 \cdot 10^{-10}$	$1.49 \cdot 10^{-2}$	(mol%)
$y(\text{HD})$	-	1.42	-	-	1.42	2.83	$2.70 \cdot 10^{-5}$	1.09	(mol%)
$y(\text{D}_2)$	100.0	30.76	0.71	-	30.76	47.75	1.49	24.38	(mol%)
$y(\text{HT})$	-	0.99	-	-	0.99	1.07	$1.73 \cdot 10^{-4}$	0.99	(mol%)
$y(\text{DT})$	-	47.56	-	-	47.56	39.67	21.02	48.39	(mol%)
$y(\text{T}_2)$	0	19.25	0.56	-	19.25	8.63	77.49	25.14	(mol%)
$y(\text{N}_2)$	-	-	87.04	-	-	-	-	-	(mol%)
$y(\text{Ar})$	-	-	$1.70 \cdot 10^{-2}$	68.13	-	-	-	-	(mol%)
$y(\text{Xe})$	-	-	$7.94 \cdot 10^{-3}$	31.87	-	-	-	-	(mol%)
$y(^4\text{He})$	-	-	11.65	-	-	-	-	-	(mol%)

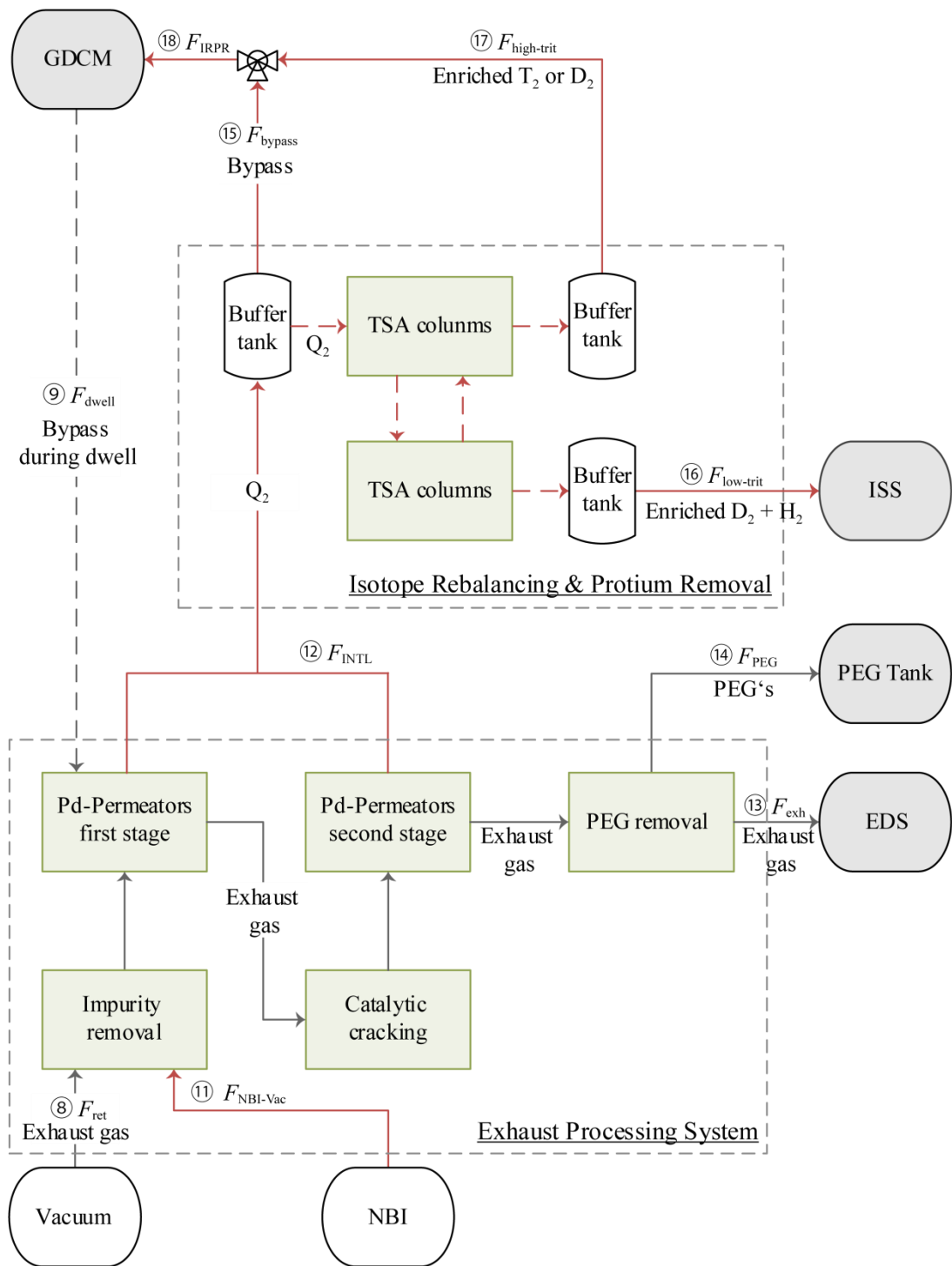


Figure 6.1: The Inner Tritium Loop with the subsystems of the “Exhaust Processing” and “Isotope Rebalancing and Protium Removal” system blocks.

## 6.1 Exhaust Processing

The bulk separation of hydrogen from the exhaust gas in DEMO is achieved using a well-established technology in tritium handling facilities - the palladium permeator [86][87][88]. A validated model of palladium alloy permeators for the application in the DEMO fuel cycle was published by the author in [89] and is summarized in this chapter.

### 6.1.1 Permeator Boundary Conditions and Setup

#### Boundary Conditions

During reactor operation the torus exhaust gas represents the main contributor of the permeator input ( $F_{\text{ret}}$  ⑧). This may be complemented by other inputs of similar requirements. For the reference case this is  $F_{\text{NBI-Vac}}$  ⑪. However, streams containing a large fraction of protium are to be avoided as they pollute the INTL and imply an increased effort of the technically complex protium removal. During the dwell phase, the permeators process the bypass stream from the GDCM instead ( $F_{\text{dwell}}$  ⑨), to uphold steady state for this and all subsequent processes. The palladium permeator produces two outputs: (i) the isolated hydrogen permeate ( $F_{\text{INTL}}$  ⑫) and (ii) the retentate ( $F_{\text{exh}}$  ⑬ +  $F_{\text{PEG}}$  ⑭), which consists of non-hydrogen species and residual hydrogen.

#### Permeator Setup

Common design of permeators is a tube-in-tube design, consisting of a cylindrically shaped membrane, mounted coaxially within a tubular casing [88]. The self-supporting membrane separates a pressurized inner tube from an evacuated outer ring tube to prevent pressure induced deformation of the membrane. The gas feed is injected by a compressor into the inner tube at high pressure. Additionally, a mass flow controller upstream and a throttle valve downstream control the throughput of the permeator and produce quasi-stationary conditions on the feed side. A vacuum pump evacuates the outer tube to uphold the pressure gradient over the membrane. The permeator setup as well as the schematic of the tube-in-tube design is shown in Figure 6.2. The permeator in the model mirrors the parameters chosen in the experiments, which ran under fusion-relevant conditions. They are summarized in Table 6.2. The hydrogen removal in the EPS is implemented as a two-staged process, each with multiple permeators of these dimensions operating in parallel.

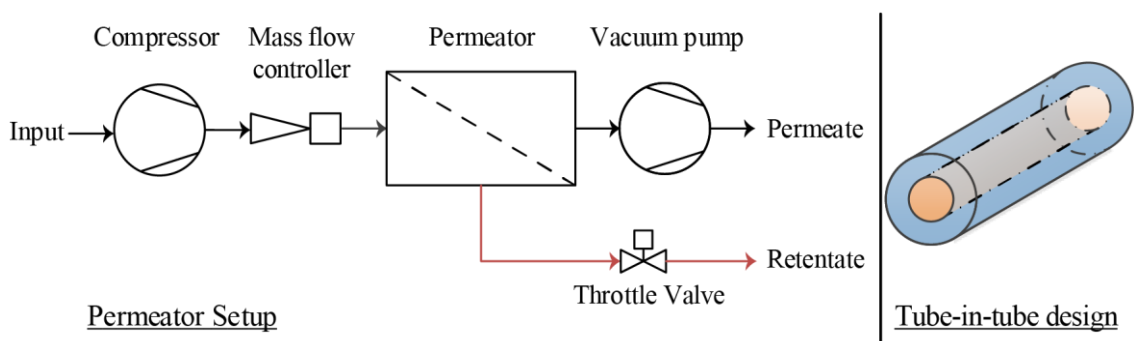


Figure 6.2: Sketch of a single permeator setup as well as a schematic of the tube-in-tube design implemented into the model.

---

## Membrane Parameters

A Pd-Ag alloy is chosen as the membrane material. Palladium provides high hydrogen permeability, while silver increases the durability at high temperatures and long-term stability of the membrane. The membrane thickness is minimized to reduce the diffusion component of the permeation, while still guaranteeing mechanical stability. For self-supporting membranes, it ranges between  $s_{\text{mem}} = 100 \dots 150 \mu\text{m}$  [86][88][90]. This can be further reduced if the membrane is installed onto a support structure. The length of the membrane is chosen as large as possible but capped at  $l_{\text{perm}} = 500 \text{ mm}$ . Longer setups are inhibited by the hydrogen-induced elongation of the membrane material, which occurs under operation [88].

## Temperature

Permeator efficiency is coupled to achievable permeability, which correlates with temperature. For palladium an increase in temperature results in increased permeability. However, the membrane becomes increasingly prone to deformation as the melting point of the components and the welding material is approached. At temperatures above  $450^\circ\text{C}$  the evaporation of silver from the alloy begins to affect the long-term stability of the membrane in a substantial way. Consequently, a constant temperature of  $450^\circ\text{C}$  within the whole reactor is assumed. A homogeneous heating of the permeator membrane is achieved by direct ohmic resistance heating of the membrane.

## Pressure

For pressure-driven permeation the throughput scales linearly with the applied pressure gradient across the membrane. Therefore, increasing the pressure applied by the upstream pump of the permeator is desirable. The maximum pressure in the inner tube is limited by the stability of the membrane and the tritium permeation restrictions to the environment. An absolute pressure of 2 bar in the inner tube is set as the limit. Given the pressure level and short length of permeators in use, the pressure of the inner tube is assumed to be constant, even though hydrogen does permeate over the length of the membrane.

Simultaneously, the achievable pressure in the outer tube is limited only by the capability of its vacuum pump. The experiments of [88] used a vacuum pump achieving a pressure of 1000 Pa over the whole length of the outer tube. Although for DEMO a more powerful vacuum pump could be implemented as well.

Table 6.2: Permeator parameters of a single finger type unit.

Description	Variable	Value	Unit
Permeator length	$l_{\text{perm}}$	500	mm
Membrane thickness	$s_{\text{mem}}$	125	$\mu\text{m}$
Inner tube diameter	$d_{\text{feed}}$	10	mm
Inner tube pressure	$p_{\text{feed}}$	$2 \cdot 10^5$	Pa
Outer tube diameter	$d_{\text{perm}}$	25	mm
Outer tube pressure	$p_{\text{perm}}$	1000	Pa
Temperature	$T_{\text{perm}}$	450	$^\circ\text{C}$

### 6.1.2 Impurity Treatment and Plasma Enhancement Gas Removal

The placement of the different separation processes within the Exhaust Processing System in relation to the palladium permeators depends on their impact on the fuel cycle. If the substance in question is known to hamper the efficiency of palladium permeators - such as carbon monoxide [91] or sulphur compounds [88] - the according process step must be placed upstream. On the contrary, if additional protium or water is used to flush the exhaust stream in a process, it must be installed downstream of the EPS to avoid distorting the balance of the fuel mixture. In any other case, the process is preferably to be implemented as an intermediate step between the two palladium permeator stages. This way on the one hand, the bulk of unbound hydrogen has already been removed from the exhaust gas, which is beneficial to the efficiency of the cracking step. On the other hand, the yield of the second permeator stage will be higher given the increased concentration of unbound hydrogen in its input.

Whereas the noble gases present in the fuel cycle remain inert throughout all processing steps, other elements show high reactivity with hydrogen. Given the high temperatures in the tokamak vessel, the formation of these compound molecules containing hydrogen on a considerable scale must be addressed downstream in the fuel cycle. Chemically bound hydrogen is extracted from these molecules in a series of chemical processes to prevent tritium from escaping the closed fuel cycle as part of the exhaust gas further down the loop. The concentration of these compound molecules increases with the amount of particular non-hydrogen species. A qualitative analysis of the expected impurities and associated separation processes is described below as the degree of contamination is not quantifiable at this stage of the design. Chemically bound hydrogen is treated as impurity unable to permeate the membrane, which effectively reduces the obtainable yield. To quantify the fraction of hydrogen bound in a compound molecule upstream a palladium permeator stage, the model introduces the parameter  $C_{\text{bound}}$ . The following species are considered:

#### Carbon

Carbon has a tendency to bind tritium in particular with the cause of long-term material degradation. For this reason, DEMO in general is designed to minimize its contact with the fuel gas. However, the use of steel as infrastructure material inevitably entails the presence of carbon and consequently the formation of gaseous hydrocarbons (cf. Equation (6.1)) in the process gas.



The reaction can be reverted in a heated nickel catalyst bed, which provides a metallic surface for the hydrogen to temporarily bind on. This process is part of the fuel cycle of JET [92] and is foreseen as a process step in ITER [93]. In DEMO, this represents an intermediate step between the two permeator stages.

---

## Nitrogen

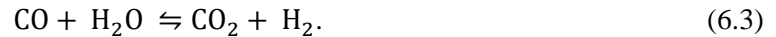
If nitrogen is used as a PEG in the tokamak reactor - as indicated in Table 3.9 - the presence of ammonia and tritiated ammonia isotopologues must be considered as a result of the chemical reaction in Equation (6.2). This has been raised as a serious concern for the design of ITER [94].



Ammonia can be split into its individual parts using a similar nickel catalyst bed used for decarbonisation [93] or a catalytic electrolysis as described by Glugla et al. [95].

## Oxygen

Hydrogen bound in water is processed in the Water Detritiation System as part of the Outer Tritium Loop and is currently not estimated to be processed in the EPS. If the quantity of water is to be reduced prior however, a water gas shift reaction shown in Equation (6.3) using a copper chromite catalyst ( $\text{Cu}_2\text{Cr}_2\text{O}_5$ ) can be implemented similar to the ITER approach [93]. The same process can be used to reduce the carbon monoxide concentration. In that case, the addition of supplemental water ( $\text{H}_2\text{O}$ ) into the Inner Tritium Loop must be considered.



## Recovery of Non-hydrogen species

The recovery of non-hydrogen species is a question of economical nature and thus secondary to the pre-conceptual design phase of DEMO. Of potential interest are the noble gases  $^3\text{He}$ , Xe and Ar. The former represents a rare and valuable by-product of tritium decay. The latter two can be recovered with cryo-traps to form a closed loop of PEG gases. The different boiling temperatures  $T_{\text{boil}}$  are given in Table 3.2. In that case, decay tanks are required prior to reinjection as these PEGs become activated in the torus environment [28].

## Modelling

Modelling of the PEG and Impurity Removal subsystems is not considered in detail within the fuel cycle simulator given the yet poorly defined quantity of impurities. It is assumed that (i) all ammonia is split in the Impurity Removal system block prior to the first permeator stage and that (ii) a fraction ( $C_{\text{bound,I}} = 1.0\%$ ) of all hydrogen upstream of the first permeator stage is chemically bound, and thus does not permeate or contribute to the partial pressure of hydrogen. Then, in the Catalytic Cracking system block - in between the two permeator stages - (iii) all compound hydrogen is restored to its unbound molecular state ( $\eta_{\text{crack}} = 1.00$ ). For comparison, for the ITER impurity processing facility a value of  $C_{\text{bound,Iter}}(C_n\text{Q}_m + \text{NQ}_3) = 1.2\text{ mol}\%$  and a tritium recovery rate of  $10^9:1$  are assumed [96]. The Plasma Enhancement Gases argon and xenon are removed in final step of the EPS with an assumed efficiency of  $\eta_{\text{PEG}} = 0.99$ . The concentration of  $^3\text{He}$  throughout the fuel cycle is very small ( $<1 \cdot 10^{-6}\text{ mol}\%$ ). Its recuperation would signify an additional setup of significant scale and is neglected.

### 6.1.3 Permeator Modelling

Pressure driven permeation through the palladium membrane is implemented using the approach described in Chapter 3.2. The permeator model in the fuel cycle simulator uses Equation (6.4) - a variation of Equation (3.21) - which takes into account the presence of impurities and different hydrogen isotopes [97].

$$J(Q) = \#_{\text{perm}} \cdot y(Q) \cdot \frac{A_{\text{perm}}}{s_{\text{mem}}} \cdot Pe(Q) \cdot \sqrt{\Delta p}, \quad (6.4)$$

where  $J(Q)$  is the permeation flow of a specific hydrogen isotope  $Q$  in mol/s and  $\#_{\text{perm}}$  denotes the number of permeators operated in parallel.  $A_{\text{perm}}$  and  $s_{\text{mem}}$  are given by the permeator dimensions in Table 6.2. The permeability  $Pe$  of the different hydrogen isotopes  $Q$  is calculated at  $T_{\text{perm}}$  using Equation (3.20) and the values in Table 6.3. The model assumes an ideal permeator, which indicates infinite hydrogen selectivity and negligible material degradation over time. For non-hydrogen species as well as hydrogen compound molecules these assumptions yield  $Pe = 0$ .

A 1-dimensional discretization into  $N$  finite volumes is implemented along the length of the permeator. This captures the effect of the monotonous decrease of hydrogen partial pressure in the inner tube towards the permeator back end. To evaluate a sensible degree of discretization, multiple simulations are performed for  $N = 10, 25, 50, 100$  and  $200$ . For  $N < 50$  the results differ considerably. Conversely, results for  $N \geq 50$  deviate marginally from another but entail increasing computational effort as  $N$  increases. Consequently,  $N = 50$  is chosen. To account for the dynamic input boundary, a transient mass balance is formulated in Equation (6.5) for every species around each node.

$$\frac{dI_{\text{node}}(Q,n)}{dt} = F_{\text{node}}(Q,n-1) - J(Q,n) - F_{\text{node}}(Q,n), \quad (6.5)$$

where  $I_{\text{node}}(Q,n)$  denotes the time-dependent inventory of isotope  $Q$  in node  $n$  in the unit of mol.  $F_{\text{node}}(Q,n)$  represents the retentate downstream the same isotope and node.  $J(Q,n)$  is calculated using Equation (6.4). Non-hydrogen species are calculated using the same approach. They simply propagate through the inner tube and leave the reactor as part of the retentate.

The input stream is injected into the permeator as  $F_{\text{feed}}(Q) = F_{\text{node}}(Q,0)$  at a total pressure  $p_{\text{feed}}$ . The retentate  $F_{\text{node}}(Q,N)$  is extracted at the end of the column. The sum of all permeation flows represents the permeate output  $F_{\text{perm}}(Q) = \sum_n J(Q,n)$ . As hydrogen diffuses through the membrane as single atoms, the permeate leaves the device as isotopologues in thermodynamic equilibrium at  $T_{\text{perm}}$ .

Table 6.3: Pre-exponential and exponential factors to calculate the permeability for the three hydrogen isotopes through Pd/Ag. Tritium permeation data are available for 673 K only [87].

Isotope	$Pe_0$ (mol/(ms · √Pa))	$E_A$ (J/mol)	Source
Protium	$7.63 \cdot 10^{-8}$	6600	[86]
Deuterium	$3.37 \cdot 10^{-8}$	3980	[86]
Tritium	$Pe = 6.6 \cdot 10^{-9}$ (at 673 K)		[87]

Due to the permeation occurring, the mass balance of the inner tube forces either a reduction of pressure over the length of the tube  $I_{\text{node}}(n-1) > I_{\text{node}}(n)$  or a decrease in flow velocity  $F_{\text{node}}(n-1) > F_{\text{node}}(n)$ . Given the high compression and short length of the permeator, the pressure is assumed to remain constant. Rearrangement of ideal gas law yields the flow velocity  $v_{\text{node}}(n)$  as a nodal variable.

$$v_{\text{node}}(n) = \frac{RT_{\text{perm}} \cdot F_{\text{node}}(n)}{p_{\text{feed}} \cdot \pi d_{\text{feed}}}. \quad (6.6)$$

A performance criterion - the efficiency  $\eta_{\text{perm}}$  of a permeator - is defined as the ratio of hydrogen permeated  $F_{\text{perm}}$  over hydrogen fed  $F_{\text{feed}}$ .

$$\eta_{\text{perm}} = \frac{F_{\text{perm}}}{F_{\text{feed}}(Q_2)}. \quad (6.7)$$

The theoretical limit of achievable hydrogen permeation  $\eta_{\text{theo}}$  can also be derived from Equation (6.4). Permeation ceases to occur, once the partial pressure of the permeating species - in this case hydrogen - is equal on both sides of the membrane. For any given feed composition, the efficiency of the permeator is maximized by increasing the pressure ratio. Also, the hydrogen content left in the retentate is correlated to the capacity of the vacuum pump downstream the permeate. This consideration is quantified in Equation (6.8).

$$\eta_{\text{perm}} = \eta_{\text{theo}} \cdot K_{\text{perm}} = 1 - \frac{p_{\text{perm}} \cdot y_{\text{perm}}(Q_2)}{p_{\text{feed}} \cdot y_{\text{feed}}(Q_2) \cdot (1 - C_{\text{bound}})}, \quad (6.8)$$

where  $y_{\text{feed}}(Q_2)$  and  $y_{\text{perm}}(Q_2)$  denote the molar fraction of all hydrogen species combined in the feed and permeate gas. The latter is given as  $y_{\text{perm}}(Q_2) = 1$  due to the ideal permeator assumption. A fraction of the hydrogen input  $C_{\text{bound}}$  is bound as compound hydrogen and cannot permeate.

For example, in the reference case, the input composition of the Exhaust Processing System is  $y_{\text{feed}}(Q_2) \approx 0.86$ . With  $C_{\text{bound,I}} = 1\%$  this yields  $\eta_{\text{theo,I}} \approx 99.4\%$  for the first stage. However, to achieve this ideal efficiency a permeator setup of infinite dimensions would be required. Therefore, a dampening factor  $K_{\text{perm}} < 1$  is implemented in the assessment to retrieve a realistic target value. For the first permeator stage in the Reference Design Point  $K_{\text{perm,I}} = 0.95$  is assumed, which yields a target efficiency of  $\eta_{\text{perm,I}} = 94.5\%$ .

The same procedure is applied for the second stage except that the retentate of the first permeator stage constitutes the input boundary condition of the second stage. The intermediate catalytic cracking is assumed at high efficiency  $C_{\text{bound,II}} = 1\% \cdot C_{\text{bound,I}}$ . The second stage dampening factor is assumed identical to the one in the first stage at  $K_{\text{perm,II}} = 0.95$ .

Given these parameters, the permeation efficiency of the first and second stage  $\eta_{\text{perm,I}}$  and  $\eta_{\text{perm,II}}$  of any given throughput can now be related in dependency of the amount of permeators used,  $\#_{\text{perm,I}}$  and  $\#_{\text{perm,II}}$ , as well as for a variation of permeator parameters.



### 6.1.4 Permeator Validation

To validate the code, a comparison is drawn between the results of the permeator simulation and fusion-relevant permeator experimental data. For this purpose, minor changes are applied to the process parameters in order to adapt the simulation to the boundary conditions of the selected experimental setup [90].

Here, the membrane thickness deviates with  $s_{\text{mem}} = 113 \mu\text{m}$  from the parameters listed in Table 6.2. Furthermore, a single permeator is used in the experiment with a feed stream  $F_{\text{feed}} = 3.24 \cdot 10^{-4} \text{ mol/s}$  composed of helium and protium in a ratio of 15:1. All other model parameters remain unchanged. This way, the model is validated only for the application of protium. An extrapolation to the other hydrogen isotopes is given by consideration of the different material properties, specifically the influence of the permeability defined by the values listed in Table 6.3.

Figure 6.3 shows the hydrogen removal efficiency  $\eta_{\text{perm}}$  of the permeator for different membrane temperatures  $573 \text{ K} \leq T_{\text{perm}} \leq 723 \text{ K}$  and feed pressures  $1 \text{ bar} \leq p_{\text{feed}} \leq 7 \text{ bar}$  for both the experimental and the modelling results. In general, an increase of the hydrogen removal efficiency is observed for higher membrane temperatures and upstream pressures.  $\eta_{\text{perm}}$  correlates with the total amount of hydrogen permeated  $F_{\text{perm}}$  as per Equation (6.7), given that the throughput upstream is fixed in the setup. Provided that in addition, the thickness of the membrane  $s_{\text{mem}}$  and the outer ring tube pressure  $p_{\text{perm}}$  remain constant in the setup, the change in permeation flux  $j$  - and thereby the amount permeated  $F_{\text{perm}}$  - must correlate to the remaining parameters: the upstream pressure  $p_{\text{feed}}$  and the permeability  $Pe$  (cf. Equation (3.21)). Increasing  $p_{\text{feed}}$  results in a higher driving force applied over the membrane and yields larger amounts of hydrogen permeated  $\eta_{\text{perm}} = f(\sqrt{p_{\text{feed}}})$ . The permeability of the membrane is tied to the temperature as per the Arrhenius approach (cf. Equation (3.20)).

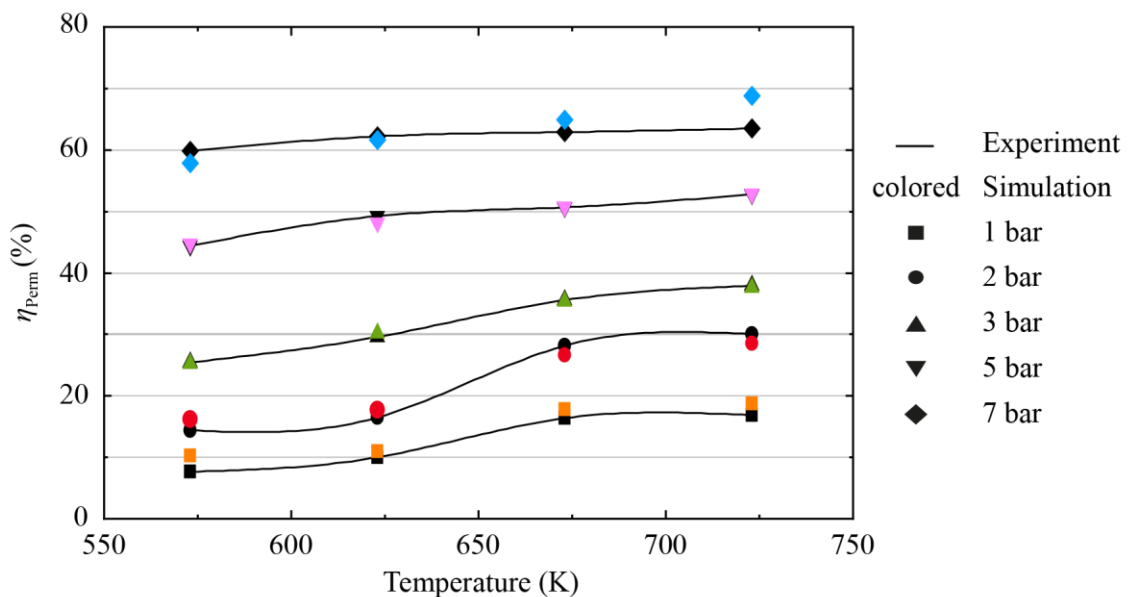


Figure 6.3: Hydrogen removal efficiency over temperature for various upstream pressures between 1 and 7 bar. The graph shows a comparison between experimental data (black lines and dots) [90] and simulation results (coloured dots)[89].

---

For low pressures ( $p_{\text{feed}} = 1 \dots 2$  bar) an inflection type behaviour can be observed for  $\eta_{\text{perm}}$  in both the experiment and the model, where in the temperature range of  $623 \text{ K} < T_{\text{perm}} < 673 \text{ K}$ ,  $\eta_{\text{perm}}$  increases whereas for higher temperatures ( $T_{\text{perm}} > 700 \text{ K}$ ), it stagnates. This phenomenon results from processing large fractions of inert gas while applying a low upstream pressure. In detail, as the temperature increases, so does the amount of hydrogen permeating through the membrane, especially at the beginning of the permeator, where the driving force is the highest. As  $\eta_{\text{perm}}$  correlates to the integral amount of hydrogen permeated, for the overall hydrogen removal efficiency to stagnate at higher temperatures, less hydrogen must then permeate within the latter half of the permeator. For a constant total pressure over the length of the upstream tube, less hydrogen equals more inert gas, which - in the context of the experiment conducted - represents an accumulation of helium (as observed during the experiment [90]). As the velocity in the inner ring tube is tied to the upstream pressure as per Equation (6.6), for low pressures ( $p_{\text{feed}} \leq 2$  bar) hydrogen is not propelled to the rear end of the permeator in sufficient quantity to make use of the increased permeability at high temperatures, whereas for high pressures ( $p_{\text{feed}} > 2$  bar) the phenomenon vanishes.

For a pressure of  $p_{\text{feed}} = 1$  bar, the model overpredicts the achievable hydrogen removal efficiency of the permeator. The maximum deviation between model and experiment, at the boundary condition of  $T_{\text{perm}} = 573 \text{ K}$  amounts to an absolute deviation of  $\Delta\eta_{\text{perm}} = 2.33 \text{ mol}\%$ . At a feed pressure of  $p_{\text{feed}} = 2$  bar, the inflection type behaviour observed in the experiment is reproduced by the model, but less pronounced. For low temperatures higher yields are calculated ( $\Delta\eta_{\text{perm}} \leq 1.73 \text{ mol}\%$ ), whereas for higher temperatures a lower efficiency is predicted ( $\Delta\eta_{\text{perm}} \geq -2.18 \text{ mol}\%$ ).

Within the pressure range of  $3 \text{ bar} \leq p_{\text{feed}} \leq 5 \text{ bar}$ , a good agreement between experimental data and model can be observed. Specifically, the hydrogen removal efficiency is predicted by the model with a maximum relative deviation from the experiment of 2 % for all temperatures.

At particularly high pressures  $p_{\text{feed}} = 7$  bar, Santucci et al. [90] report a singularity where the hydrogen removal efficiency reaches a plateau for temperatures  $T_{\text{perm}} > 623 \text{ K}$ , without providing an explanation for the phenomenon observed. In contrast, the model assumes an ideal system and obtains increasing hydrogen removal efficiencies for higher temperatures. Hence, the model in the presented form cannot be validated for upstream pressures  $p_{\text{feed}} > 5$  bar and the addition of a dampening function must be considered for applications at high pressure.

For the process parameters envisaged in the fusion cycle ( $p = 2$  bar &  $T = 723 \text{ K}$ ), the relative deviation is calculated in Equation (6.9).

$$1 - \frac{\eta_{\text{perm}}(\text{simulation})}{\eta_{\text{perm}}(\text{experiment})} = 1 - \frac{28.57 \text{ mol}\%}{30 \text{ mol}\%} = 4.78 \%. \quad (6.9)$$

This error is sufficiently reflected in the simulation for a dampening factor  $K_{\text{perm}} = 0.95$  as assumed above. As a result, the model approach is regarded as valid for the purpose of providing a good estimation of the permeator performance in the fuel cycle.

### 6.1.5 Permeator Modelling Results

After initialisation or a shift in input quantity and composition, the permeator model converged to a steady state solution within less than 60 iterations steps (at a step size of 1 second) once the deviation has propagated through all nodes. In stand-alone, the simulation computes at a rate of  $(50 \dots 200) \times$  real time, depending on input perturbations. In case of strongly reduced input, e.g. if no bypass stream ⑨ replaces the torus exhaust stream ⑧ during the dwell period, the solver fails as  $\eta_{\text{perm}}$  exceeds  $\eta_{\text{theo}}$  and the permeator feed side is deprived of hydrogen. Therefore, the fuel cycle simulator ensures that the feed stream remains within the same order of magnitude at any time.

Figure 6.4 depicts the hydrogen fraction  $y_{\text{Q}_2}$  of the upstream tube over the length of the permeator for both stages and for variations of several process parameters. In all figures,  $y_{\text{Q}_2}$  decreases in value over the length of the permeator from inlet to outlet ( $0 \text{ cm} \rightarrow l \rightarrow 50 \text{ cm}$ ). The gradual decline of the hydrogen fraction in the inner ring tube results from the increasing permeation of hydrogen to the outer ring tube, whereas non-hydrogen species remain. The total amount permeated correlates a separation efficiency  $\eta_{\text{perm}}$  as per Equation (6.7).

Overall a high permeation rate ( $\eta_{\text{perm}} > 70 \%$ ) is observed. Therefore, the discrepancy of permeabilities for the different isotopes is found to have only a minor impact on the output. The heavier isotopes are simply extracted further downstream in the permeator setup.

The reference case, which incorporates the performance requirements and process parameters set in the modelling section, is marked in green in all instances. Table 6.4 lists the throughput and composition of the input and output streams of all subsystems of the Exhaust Processing System for the Reference Design Point.

The number of permeators required for the reference case are  $\#_{\text{perm,I}} = 37$  in the first stage and  $\#_{\text{perm,II}} = 8$  in the second stage, which yields hydrogen removal efficiencies of  $\eta_{\text{perm,I}} = 94.87 \%$  and  $\eta_{\text{perm,II}} = 94.39 \%$ , respectively. This corresponds to permeation fluxes of  $j_{\text{perm,I}} = 139.99 \text{ Pa m}^3/(\text{s m}^2)$  and  $j_{\text{perm,II}} = 36.53 \text{ Pa m}^3/(\text{s m}^2)$  as well as retrieval of  $\eta_{\text{perm,I+II}} = 99.71 \%$  of the hydrogen input.

Table 6.4: Throughput and composition up- and downstream of both permeator stages for the Reference Design Point.  $y(\text{imp})$  indicates the combined fraction of all impurities part of which  $y(\text{bound})$  is the fraction of compound hydrogen. Isotopologues are omitted for readability.

Stream	$F_{\text{feed,I}}$ ⑧+⑪	$F_{\text{perm,I}}$	$F_{\text{ret,I}}$	$F_{\text{feed,II}}$	$F_{\text{perm,II}}$	$F_{\text{ret,II}}$ ⑬+⑭	Unit
$F$	109.49	80.99	28.49	28.49	4.95	23.54	$(\text{Pa} \cdot \text{m}^3/\text{s})$
$y(\text{H})$	0.96	1.23	0.19	0.22	1.00	0.02	(mol%)
$y(\text{D})$	43.08	55.25	8.49	9.37	55.37	0.69	(mol%)
$y(\text{T})$	33.94	43.53	6.69	7.40	43.63	0.54	(mol%)
$y(\text{imp})$	22.02	-	86.17	83.01	-	98.75	(mol%)
$y(\text{bound})$	0.79	-	3.00	0.0	-	0.0	(mol%)

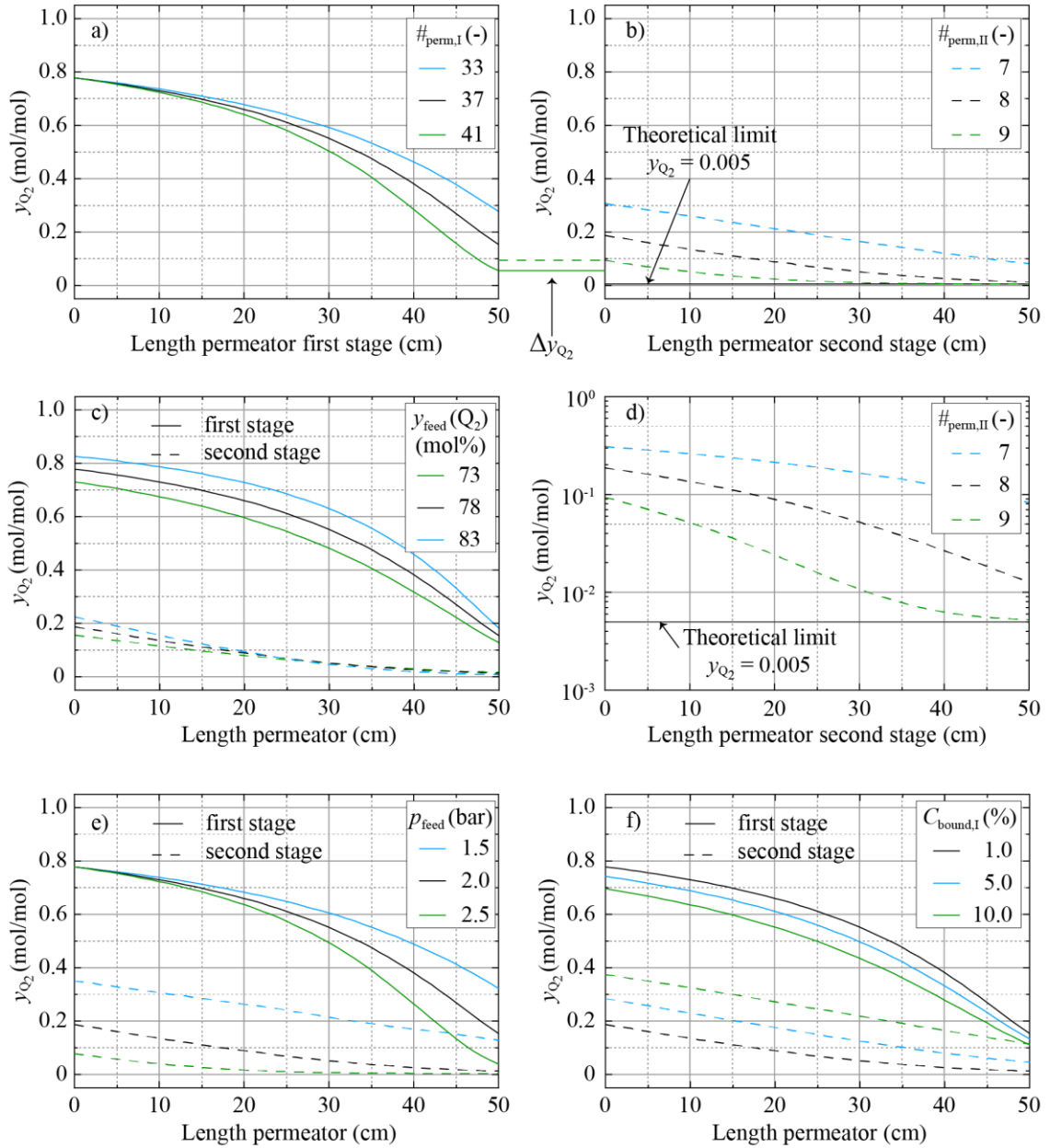


Figure 6.4: Hydrogen fraction profiles of stream in the inner tube - the upstream chamber of the permeator - over the length of both permeator stages for six process parameter variations a) through f). The reference case is always marked in black colour and only a single parameter is modified in each case. The first permeator stage is denoted as a continuous line, whereas the second stage is denoted with a dashed line. Downstream the first permeator stage, chemically bound hydrogen is cracked. This results in an increase of the hydrogen fraction upstream the second permeator stage. This effect is displayed between a) and b) as  $\Delta y_{Q_2}$ .

- a) for a varying number of permeators in the first stage.
- b) for a varying number of permeators in the second stage.
- c) for a varying fraction of hydrogen input to the first stage.
- d) Logarithmic plot of b) which displays the approximation to the theoretical limit.
- e) for a variation of the feed pressure in both stages.
- f) for a varying amount of chemically bound hydrogen input to the first stage  $C_{bound,I}$ .

Four parameter studies are performed, varying the number of permeators as well as the upstream composition and pressure. The efficiencies  $\eta_{perm}$  obtained for the parameter studies, shown in Figure 6.4 a) - f), vary as listed in Table 6.5.

Table 6.5: Hydrogen removal efficiencies of the parameter studies. The plots and colours refer to Figure 6.4. In comparison, the reference case in black is given as  $\eta_{\text{perm,I}} = 94.87\%$  and  $\eta_{\text{perm,II}} = 94.39\%$  for all parameter variations.

Plot	variation of	$\eta_{\text{perm,I}}$		$\eta_{\text{perm,II}}$		Unit
		green	blue	green	blue	
a)+b)+d)	$\#_{\text{perm}}$	98.35	89.03	94.76	79.80	(mol%)
c)	$y_{\text{feed}}$	94.62	95.31	91.19	97.15	(mol%)
e)	$p_{\text{feed}}$	86.39	98.82	72.90	95.27	(mol%)
f)	$C_{\text{bound,I}}$	84.04	94.46	69.37	87.98	(mol%)

Figure 6.4 a) shows the hydrogen fraction over the length of the first permeator stage for the boundary conditions of the Reference Design Point and a varying number of  $\#_{\text{perm,I}}$ . The output of the first stage is fed to the second stage depicted in Figure 6.4 b), where a similar parameter study is conducted for a varying number of  $\#_{\text{perm,II}}$ . Both figures display the dependency of permeate yield on the increase in permeation area. For the same upstream boundary conditions ( $y_{Q_2} = 78\text{ mol\%}$  at  $l = 0\text{ cm}$ ), setups with higher number of permeators and thus larger permeation area, yield increasingly larger permeation fluxes as per Equation (6.4). Therefore, the hydrogen fraction in the upstream progressively diverges over the length of the permeators and the obtainable hydrogen removal efficiency scales with the amount permeators used.

A notable detail is revealed by the logarithmic plot of the second stage, which is shown in Figure 6.4 d). As can be observed for the dashed green line in the latter half of the permeator stage,  $y_{Q_2}$  and thereby the permeation throughput begins to stagnate once the theoretical limit is approached. For setups with very high hydrogen removal efficiencies, the pressure difference approaches zero towards the end of the permeator leading to an asymptotic behaviour and acts as a soft cap to the permeator design.

A mismatch can be seen between the output of the first stage and the input of the second stage indicated as  $\Delta y_{Q_2}$  between the two plots a) and b). This discrepancy represents the decomposition of hydrogen compound molecules in the catalytic cracking step, which increases the fraction of hydrogen gas upstream the second stage. For the RDP a value of  $C_{\text{bound,I}} = 1\text{ mol\%}$  is assumed, which correlates to  $F_{\text{bound,I}} = 0.86\text{ Pa} \cdot \text{m}^3/\text{s}$ . For the assumed perfect retrieval of hydrogen ( $\eta_{\text{crack}} = 1.00$ ) in the intermediate cracking step, this yields an increase of the hydrogen fraction upstream the second permeator stage of  $y_{Q_2}(F_{\text{Feed,II}} - F_{\text{ret,I}}) = 3.15\text{ mol\%}$  (cf. Table 6.4).

Figure 6.4 c) and e) depict the influence of modifying the input composition  $y_{\text{feed}}$  and upstream pressure  $p_{\text{feed}}$ , respectively. In the former, the curves converge towards the permeator end, indicating that the setup is less sensitive to this parameter. As the fraction of hydrogen increases, so does the driving force  $\Delta p$ . This leads to a self-regulation of the hydrogen recuperation efficiency for a fixed permeator setup with varying input compositions. Comparing Figure 6.4 a) and e), a change in feed pressure yields comparable results as modifying the amount of permeators. From Equation (6.4) the influence of both parameters is equivalent for a change  $\Delta A_{\text{perm}} \triangleq \sqrt{\Delta p_{\text{feed}}}$ , given that all other parameters remain constant. Again, for a setup using an upstream pressure, the molar fraction of hydrogen approaches asymptotically the theoretical limit towards the end of the column.

For a variation of the concentration of compound hydrogen  $C_{\text{bound,I}}$  in Figure 6.4 f), a convergence of permeator performance - similar to Figure 6.4 c) - can be observed in the first stage. As the value of  $C_{\text{bound,I}}$  increases, the permeator efficiency of the first stage drops and the permeation duty is shifted to the second stage. For  $C_{\text{bound,I}} = 10\%$  the second stage is only able to withdraw as much hydrogen as is set free in the intermediary catalyst bed. This can be observed by comparing the hydrogen fraction at the back-end of both stages for the orange curve in Figure 6.4 f). To counteract the loss of hydrogen removal efficiency given in Table 6.5, additional permeators are required in the second stage of the permeator setup.

In conclusion, the obtainable hydrogen removal efficiency of a permeator setup is best regulated by adjusting the amount of permeators and the upstream pressure as these parameters display a strong influence on the molar fraction of hydrogen over the length of the permeator. In both cases, optimization of the hydrogen removal efficiency is constrained by the theoretical limit. Such a setup consistently yields similar hydrogen removal efficiencies even if the hydrogen fraction upstream deviates over time. The distribution of permeators between the first and second stage is governed by  $C_{\text{bound,I}}$ .

## 6.2 Isotope Rebalancing and Protium Removal

The Isotope Rebalancing and Protium Removal (IRPR) System comprises two tasks: (i) to re-establish equimolar fractions of deuterium and tritium in the fuel gas and (ii) to limit the protium contamination within the Inner Tritium Loop. Both contribute to maintaining peak performance of the fusion reaction. The Temperature Swing Absorption (TSA) process has been identified as suitable technology approach as it fulfils both requirements in a single process step. The implemented TSA model includes a two-column setup [98]. The modelling procedure is summarized in [99]. This process has evolved from a simpler setup using a single sorption column in conjunction with a buffer tank [100].

### 6.2.1 Temperature Swing Absorption Boundary Conditions and Setup

Sole input of the IRPR system is the pure hydrogen permeate from the EPS ( $F_{\text{INTL}}$  (12)). The expected input - given for the RDP in Table 6.1 - shows a disproportional mixture of DT (D : T = 56 : 44) as derived in Equation (6.10). The imbalance stems from the deuterium NBI source assumed for the reference case in Chapter 3.5.

$$\frac{F_{\text{INTL}} \cdot (y_{\text{INTL}}(\text{D}_2) + 0.5 \cdot y_{\text{INTL}}(\text{HD}) + 0.5 \cdot y_{\text{INTL}}(\text{DT}))}{F_{\text{INTL}} \cdot (y_{\text{INTL}}(\text{T}_2) + 0.5 \cdot y_{\text{INTL}}(\text{HT}) + 0.5 \cdot y_{\text{INTL}}(\text{DT}))} = \frac{47.48}{37.41} \approx \frac{56}{44}. \quad (6.10)$$

The protium fraction in  $F_{\text{INTL}}$  is about 1.2 mol%, which originates from hydrogen ingress, quantified in Table 3.10. Two outputs are produced by the TSA process: (i) enriched deuterium mixed with accumulated protium ( $F_{\text{low-trit}}$  (16)) and (ii) enriched tritium ( $F_{\text{high-trit}}$  (17)). For the case of excess deuterium in the fuel cycle as assumed in the RDP, the former output is sent to the ISS for decomposition, whereas the latter is forwarded to the GDCM to rebalance the fuel.

As the achievable tritium enrichment reaches 90 %, only a fraction of the input must be processed by the TSA. The required hydrogen composition in the output is adjusted by implementing a bypass ( $F_{\text{bypass}}$  (15)) to the GDCM at the input of the system. By modifying the bypass ratio, the plant operators can create any desired fuel composition ( $F_{\text{IRPR}}$  (18)) within the boundaries of the system's capability.

The separation principle of the Temperature Swing Absorption process is based on hydrogen-metal interaction, utilizing two metals with antagonistic absorption behaviour for the different hydrogen isotopes. Among possible sorbent candidates, palladium and vanadium are chosen as they show high separation factors and matching temperature and pressure ranges of operation [99]. The process described in the following refers to a single setup with the column parameters listed in Table 6.6. Scale-up to the DEMO throughput is performed thereafter.

Centrepieces of the TSA are two columns - each filled with one of the two absorbing metals in the form of coated particles overflowed by the mixture of hydrogen isotopes. The carrier material and coating procedure are chosen to maximize the available surface of the sorbent. Porous Kieselgur ( $\text{SiO}_2$ ) or crystalline alumina ( $\gamma\text{-Al}_2\text{O}_3$ ) is utilized for this purpose in practise [100][101]. The ratio of sorption material to gas content determines the pressure range of the system. Both columns are designed cylindrical in shape, narrow and long to limit axial diffusion and enhance heat distribution. They are connected via a tube ( $d_{\text{tube}} = 3 \text{ mm}$  and  $l_{\text{tube}} = 3 \text{ m}$ ) to form a large plug flow reactor over the length of both absorption beds. A valve is installed within the tube to separate the columns as needed. Used in tandem, a sharp concentration gradient of hydrogen isotopes forms over the course of several closed loop cycles of alternate heating, cooling and pressure compensation. After the gradient has formed, the concentrated products can be withdrawn from both ends of the column.

The setup of the Isotope Removal and Protium Rebalancing system is shown in Figure 6.5.

The TSA process is inherently of a discontinuous nature, which necessitates certain infrastructure elements in the context of an otherwise continuous fuel cycle. Buffer tanks are installed at the system boundaries that allow for quasi-continuous behaviour and thus seamless integration into the fuel cycle at the expense of local process gas accumulation. Additionally, each column is equipped with its own cooling and heating systems to allow for independent control of the bed temperature.

Table 6.6: Design parameters of the palladium and vanadium absorption columns used in the Temperature Swing Absorption process.

Name	Variable	Palladium	Vanadium	Unit
Column length	$l_{\text{column}}$	6000	6000	(mm)
Column diameter	$d_{\text{column}}$	60	60	(mm)
Sorbent quantity	$I_{\text{metal}}$	19.13	8.58	(mol)
Gas volume	$V_{\text{gas}}$	15.90	15.48	(l)
Initial hydrogen quantity	$\sum q I_{\text{sum}}$	11.65	12.61	(mol)
Upper pressure target	$p_{\text{high}}$	$> 6 \cdot 10^5$	$> 7 \cdot 10^5$	(Pa)
Lower pressure target	$p_{\text{low}}$	$< 5 \cdot 10^3$	$< 6 \cdot 10^3$	(Pa)

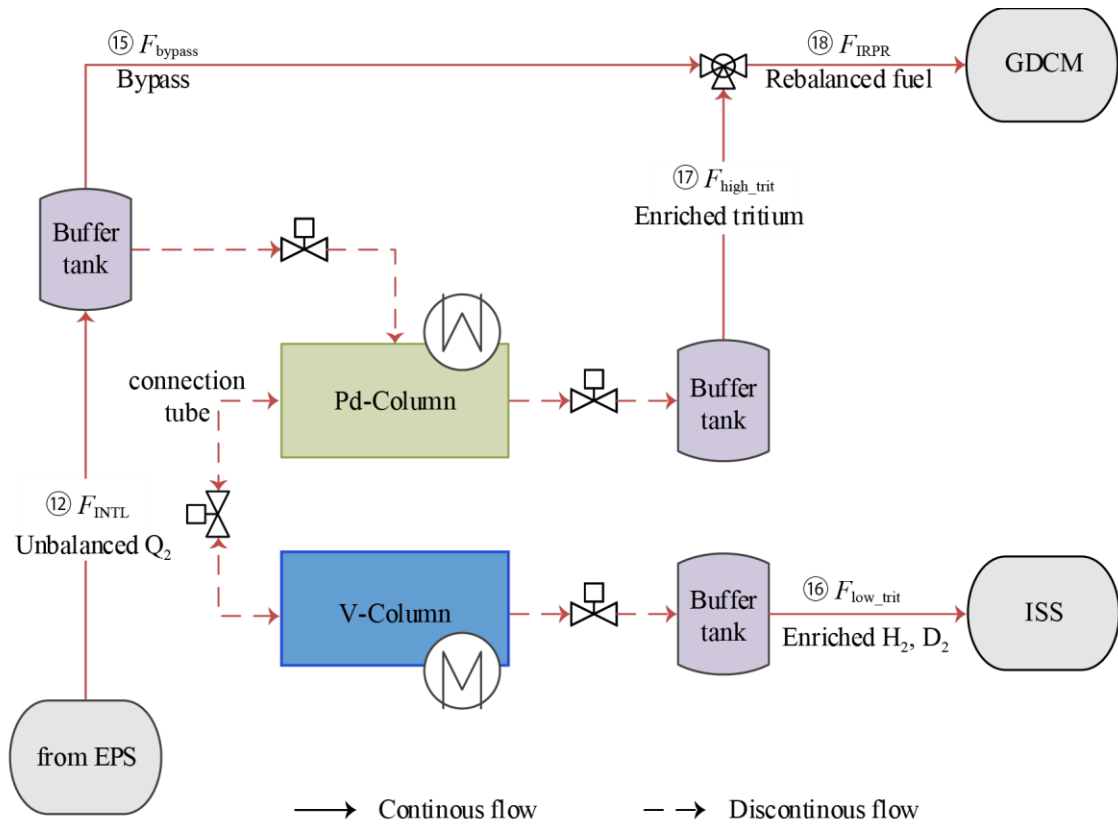


Figure 6.5: The Isotope Rebalancing and Protium Removal system consisting of the two Temperature Swing Absorption beds (Pd- and V-Columns) and surrounding infrastructure.

## Process Cycles

The two absorption columns are heated and cooled alternately which induces absorption and desorption of hydrogen, respectively. This is accompanied by a shift of gas pressure and the equilibrium state in each bed. Between each of these sorption phases (1. & 2. Sorption phase) the valve connecting the two column is opened. The resulting gas flow equalises the pressure between the two systems and once again shifts the equilibrium state in each bed (1. & 2. Flow phase). As the hydrogen isotopes react differently with the two metals, they accumulate at different places throughout the plug flow reactor. The process cycle is depicted in Figure 6.6.

This cycle is repeated multiple times in a closed loop until the isotope purity at the ends of both columns is satisfactory, at which point hydrogen is extracted. This is conducted for each column separately after the corresponding column has been heated (1. & 2. Withdrawal phase). Thereafter, the amount of gas removed is replenished (Feed). In every extended cycle, 5 % of the total hydrogen content is exchanged this way.

It is assumed that each cycle step is sufficiently long to reach reaction equilibrium throughout both columns. For the modelling the cycle times are listed in Table 6.7. Thereby the closed and extended cycle last for  $t_{\text{closed}} = 1100$  s and  $t_{\text{extended}} = 1280$  s, respectively. The temperature ramp is calculated as a linear heating and cooling rate spanning the whole length of the sorption phase.



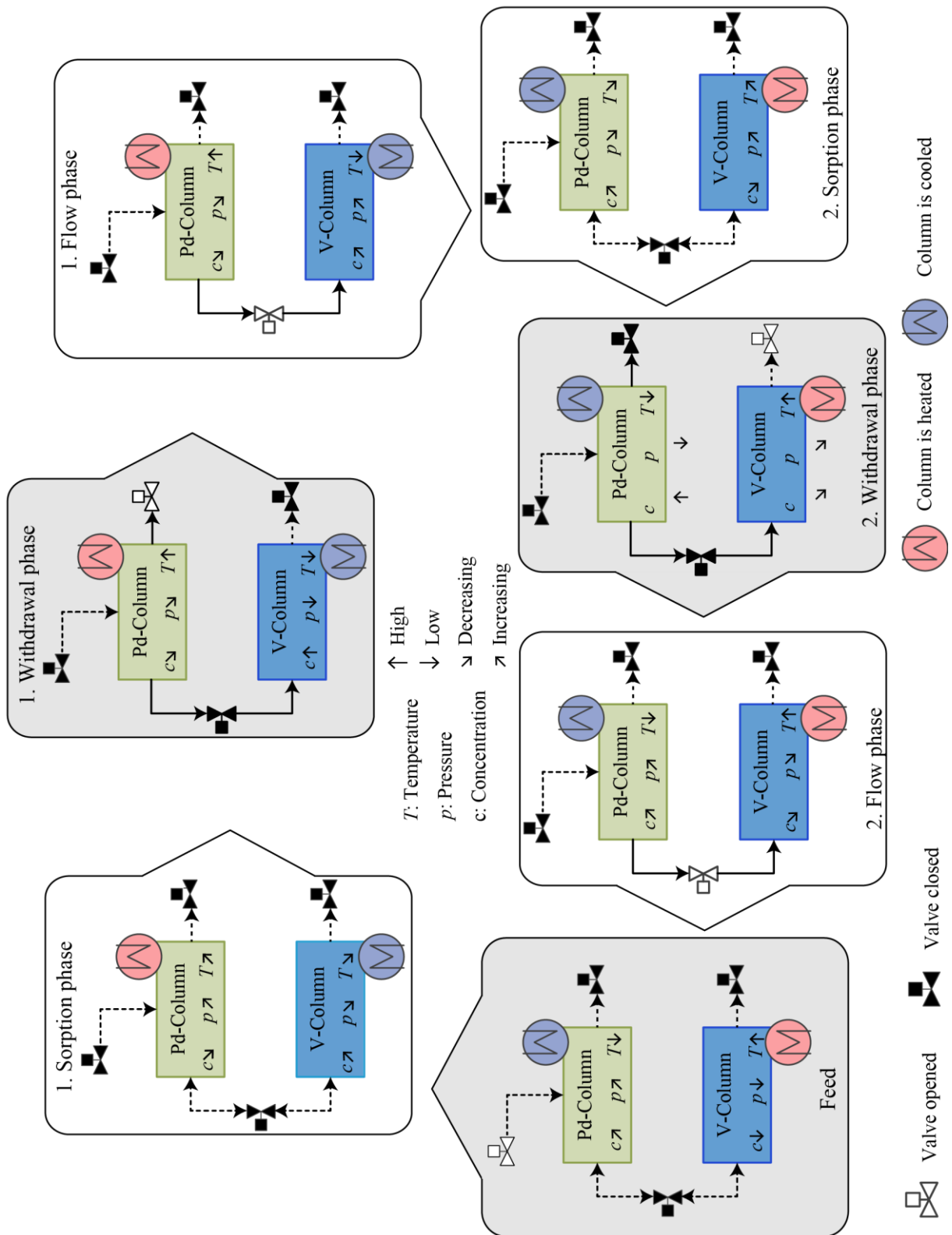


Figure 6.6: The Temperature Swing Absorption phase flow diagram indicating the changes to pressure, temperature and concentration in both columns for each of the seven phases. Grey boxes represent phases of the extended cycle only, where matter is fed or withdrawn.

Table 6.7: Duration and column temperatures of the seven phases of the Temperature Swing Absorption model for the palladium and vanadium columns. Phases marked in grey are part of the extended cycle only.

Cycle phase	Duration	Column temperatures	
	$t$ (s)	$T_{Pd}$ (K)	$T_V$ (K)
Feed phase	60	293	323
1. Sorption phase	250	ramping up	ramping down
1. Withdrawal phase	60	413	273
1. Flow phase	300	413	273
2. Sorption phase	250	ramping down	ramping up
2. Withdrawal phase	60	293	323
2. Flow phase	300	293	323

### 6.2.2 Temperature Swing Absorption Modelling

The separation effect is based on the different material properties of palladium and vanadium (cf. Equation (3.17)). While palladium favourably binds lighter hydrogen atoms ( $K_{HD} > 1$ ), vanadium prefers to absorb heavier isotopes ( $K_{HD} < 1$ ).

The equilibrium pressure of pure hydrogen isotopes can be calculated as a function of the hydrogen isotope saturation  $c_{Q/M}$  and the temperature  $T$  for each metal from material properties values extracted from the literature. Appendix A4 shows the process cycle in the  $pc_{Q/M}$  - diagrams of palladium and vanadium. The calculation formula is given for both in their respective section and varies for different states of absorption. As the concentration of absorbed hydrogen increases, the lattice structure of the metal shifts. These phase transitions are accompanied by an isobaric plateau, which exhibits large reversible absorption capabilities for constant reactor parameters well suited for the TSA process. A study on the hydrogen absorption behaviour and isobaric plateaus is given in [102]. Given the prominent presence of catalytic surface and desorption processes taking place in the absorption beds it is assumed that mixture isotopologues form in the gas phase.

#### Mass balance

By linking the concentration of hydrogen in the solid phase to the pressure in the gas phase, Equation (6.11) can be solved.

$$I_{\text{sum}}(Q) = I_{\text{gas}}(Q) + I_{\text{solid}}(Q), \quad (6.11)$$

where  $I_{\text{gas}}(Q)$  denotes the amount of molecules of a hydrogen isotope  $Q$  in the gas phase, which is tied to the equilibrium pressure  $p_{\text{eq}}$  by the ideal gas law - and  $I_{\text{solid}}(Q)$  denotes the amount of molecules of that hydrogen isotope absorbed in the metal lattice, which is tied to the hydrogen isotope concentration in the solid phase  $c_{Q/M}$  as per Equation (3.14).  $I_{\text{sum}}(Q)$  represents the sum of both. All inventories are given in the unit of mol.

To model the hydrogen concentration profile within both columns, each is discretized into  $N$  nodes in a single dimension along their length. Again, multiple simulation runs are conducted at  $N = 10, 25, 50, 100$  and  $200$  to obtain a reasonable compromise between the resolution of

results obtained and the computation time required. At  $N = 50$  and  $N = 100$  similar results are produced. In comparison, for  $N < 50$ , the results deviated substantially. For a simulation with  $N = 200$  the program crashed repeatedly indicating a computational limit to the single-core simulation capabilities. Consequently,  $N = 50$  is chosen.

In the context of the palladium column,  $n_{Pd} = 0$  correlates to the withdrawal point for tritium enriched species and new matter is fed at  $n_{Pd} = 25$ . For the vanadium column,  $n_V = 51$  represents the output of detritiated hydrogen. The connection tube is given as a single node  $n_{tube}$  and represents the boundary condition between the two columns  $n_{tube} = n_{Pd}(N + 1) = n_V(0)$ . The transient mass balance for a single node  $n$  is written in Equation (6.12).

$$\frac{\delta I_{sum(Q,n)}}{\delta t} = F(Q, n - 1) - F(Q, n) + F_{feed} \cdot y_{feed}(Q), \quad (6.12)$$

where  $F(Q, n - 1)$  and  $F(Q, n)$  denote the nodal input and output flows calculated by Equation (6.18) with the boundary conditions (6.13) to (6.17). Streams  $F$  may assume negative values depending on the direction of flow given the definition of Equation (6.12).

$$\text{Closed valve boundary} \quad F(Q, 0) = 0 \quad \& \quad F(Q, N) = 0 \quad (6.13)$$

$$\text{During 1. Withdrawal phase} \quad F_{Pd}(Q, 0) = F_{extract} \cdot y_{Pd}(Q, 0) \quad (6.14)$$

$$\text{During 2. Withdrawal phase} \quad F_V(Q, N) = F_{extract} \cdot y_V(Q, N) \quad (6.15)$$

$$\text{During Feed phase} \quad F_{feed} = F_{feed,cont} \quad (6.16)$$

$$\text{During 1. \& 2. Flow phase} \quad F_V(Q, 0) = F_{Pd}(Q, N) \quad (6.17)$$

All flows are assumed as laminar tube flow, which can be modelled by the Hagen-Poiseuille equation. Between two points within the absorption beds the molar flow  $F$  is calculated by combining the Hagen-Poiseuille equation [103] with the ideal gas law in Equation (6.18).

$$F = \frac{\pi}{126} \cdot \frac{d^4}{l} \cdot \frac{\Delta p}{\mu_{Hyd}} \cdot \frac{p}{RT}, \quad (6.18)$$

where  $\Delta p$  denotes the pressure difference between the two points,  $p$  and  $T$  denote the volumetric average pressure and temperature between the two points in K and Pa, respectively,  $l$  denotes the distance between the two points and  $d$  denotes the characteristic diameter of the absorption bed in m.  $\mu_{Hyd}$  is the dynamic viscosity of hydrogen in Pa · s, which is calculated as a function of  $T$  and  $p$  in a quadratic interpolation of data points taken from [98] in Equation (6.19).

$$\frac{\mu_{Hyd}}{\text{Pa}\cdot\text{s}} = 8.398 + 0.021 \cdot \frac{T}{\text{°C}} - 8.36626 \cdot 10^{-6} \cdot \frac{T^2}{\text{°C}^2} + 2.16 \cdot 10^{-9} \cdot \frac{p}{\text{Pa}}, \quad (6.19)$$

with the viscosity of hydrogen  $\mu_{Hyd}$  in  $10^{-6}$  Pa · s, the gas pressure  $p$  in Pa in the range of  $10^4 \text{ Pa} \leq p \leq 10^7 \text{ Pa}$  and the gas temperature  $T$  in °C in the range of  $-100 \text{ °C} \leq T \leq 300 \text{ °C}$ .

The column hydrogen inventory is initialized with a uniform molar ratio of H : D : T = 2 : 49 : 49 throughout all nodes of the column.

---

## Palladium

Nishikawa et al. [104] calculates the equilibrium constants  $K_{HD}$  and  $K_{HT}$  of palladium as:

$$K_{HD}(\text{Pd}) = 0.916 \cdot \exp\left(\frac{2100}{RT}\right), \quad K_{HT}(\text{Pd}) = 1.21 \cdot \exp\left(\frac{1980}{RT}\right), \quad (6.20)$$

with the temperature  $T$  in K. As palladium absorbs hydrogen it forms an alloy ( $\text{PdQ}_x$ ) that changes structure with increasing hydrogen concentration as the metal lattice changes from an  $\alpha$ -state at low concentration to a  $\beta$ -state at higher concentrations. To calculate the equilibrium pressure  $p_{eq}$  in the range of operation of the absorption beds, the phase change must be considered. In the literature both the  $\alpha$ - and the  $\beta$ -phase as well as the intermediate  $\alpha\beta$ -phase are described for all three hydrogen isotopes. The threshold concentrations of the phase transition are given in Equation (6.21):

$$c_{Q/M}(\text{Pd}, \alpha \rightarrow \alpha\beta) = 0.03, \quad c_{Q/M}(\text{Pd}, \alpha\beta \rightarrow \beta) = 0.6. \quad (6.21)$$

In the  $\alpha$ -phase, at low concentrations  $c_{Q/M} < 0.03$  of hydrogen in the metal lattice, the equilibrium pressure  $p_{eq}(\alpha)$  in bar is calculated using Sieverts' law (cf. Equation (3.18)), where the Sieverts' constant  $K_s$  is derived in Equation (6.22) from the sorption enthalpy and entropy ( $\Delta H_s$  and  $\Delta S_s$  in J/mol and J/(mol · K), respectively) of the metal hydride:

$$K_s = \exp\left(\frac{-\Delta H_s + \Delta S_s \cdot T}{2RT}\right). \quad (6.22)$$

In the  $\alpha\beta$ -phase the influence of a change in concentration on the equilibrium pressure is negligible. The bulk of absorption takes place in this phase almost isobaric. The Van't Hoff Equation (6.23) links the equilibrium pressure  $p_{eq}(\alpha\beta)$  in bar to the enthalpy  $\Delta H_f$  and entropy  $\Delta S_f$  of formation in J/mol and J/(mol · K).

$$\frac{p_{eq}(\alpha\beta)}{\text{bar}} = \exp\left(\frac{-\Delta H_{f,\alpha\beta} + \Delta S_{f,\alpha\beta} \cdot T}{RT}\right). \quad (6.23)$$

In the  $\beta$ -phase a small variation in concentration causes a large change of the equilibrium pressure. Wicke et al. [105] provide the correlation shown in Equation (6.24) between the two as an extension of the Van't Hoff plot into the  $\beta$ -phase:

$$\frac{p_{eq}(\beta)}{\text{bar}} = \exp\left(\frac{-\Delta H_{f,\beta} + \Delta S_{f,\beta} \cdot T}{RT} + 2 \ln\left(\frac{c_{Q/M}}{1 - c_{Q/M}}\right)\right). \quad (6.24)$$

The enthalpy and entropy of formation assume concentration-dependent values in the  $\beta$ -phase. Sicking [106] provides an empirical formula to calculate the enthalpy of formation for palladium-Hydride in dependence of the concentration as described in Equation (6.25).

$$\Delta H_{f,\beta} = C_1 \cdot c_{Q/M} + C_2. \quad (6.25)$$

In the three phases, the enthalpies and entropies indicated in Equations (6.22), (6.23) and (6.24) differ for the three hydrogen isotopes. For the model, the material properties are implemented using an interpolation based on a collection of experimental data performed by Lässer et al. [107]. The data is listed in Table 6.8 and given the interpolation associated with uncertainties.

Table 6.8: Molar enthalpies and entropies of sorption and formation for the three palladium-hydride isotopes and the three metal phases including the uncertainty are given by the annotated source.

Palladium-Hydride		H <sub>2</sub>	D <sub>2</sub>	T <sub>2</sub>	Unit	Source
α-phase	$\Delta H_s$	19.34	15.78	13.83	(kJ/mol)	[107]
	$\Delta S_s$	107.1	106.2	103.8	(J/(mol · K))	[107]
αβ-phase	$\Delta H_{f,\alpha\beta}$	39.00±0.54	35.35±0.48	33.34±1.00	(kJ/mol)	[107]
	$\Delta S_{f,\alpha\beta}$	92.53±1.32	93.42±1.25	91.69±2.89	(J/(mol · K))	[107]
β-phase	$\Delta H_{f,\beta}$	C <sub>1</sub>	-90016.2	-90016.2	(-)	[106]
		C <sub>2</sub>	100357.60	95542.78	(-)	[106]
	$\Delta S_{f,\beta}$		107.11	106.27	(J/(mol · K))	[107]

## Vanadium

Golubkov et al. [108][109] calculate the separation factors  $K_{HD}$  and  $K_{HT}$  for vanadium as:

$$\log_{10} K_{HD}(V) = 0.36 - 158.5 \cdot T^{-1}, \quad \log_{10} K_{HT}(V) = 0.284 - 154.3 \cdot T^{-1}. \quad (6.26)$$

As hydrogen is absorbed by vanadium several phase changes occur. The system is designed to target a pressure plateau in the given pressure range, which occurs for all three isotopes at high concentrations. In this plateau vanadium(II)-hydride begins to form. The two-phase state can be observed between certain concentration thresholds given in Equation (6.27).

$$c_{Q/M}(V, \alpha \rightarrow \alpha\beta) = 0.88, \quad c_{Q/M}(V, \alpha\beta \rightarrow \beta) = 2.0. \quad (6.27)$$

Although referred to differently in the literature, the phase change is labelled as between a  $\alpha$ -phase and a  $\beta$ -phase to mirror the nomenclature used for palladium. Below the transition point - at hydrogen concentrations  $c < 0.89$  - Mueller et al. [110] propose a semi-empirical formula to calculate the hydrogen pressure for vanadium (Equation (6.28)).

$$\ln \sqrt{\frac{p_{eq}(\alpha)}{p_{Torr}}} = 10.283 + 1.0598 \cdot \ln \left( \frac{c_{Q/M}}{0.89 - c_{Q/M}} \right) - \frac{1}{T} \cdot \vartheta, \quad (6.28)$$

with  $p_{eq}(\alpha)$  as equilibrium pressure in Torr,  $T$  as temperature in K and  $\vartheta$  as substitution parameter given in dependence of  $c_{Q/M}$  in Equation (6.29) and the unit of  $K^{-1}$  [110].

$$\vartheta = 3489.2 + 3269 \cdot c_{Q/M} - 2563 \cdot c_{Q/M}^2 + 762.39 \cdot c_{Q/M}^3 - 4818.3 \cdot c_{Q/M}^4. \quad (6.29)$$

Isobaric absorption governs the transitional  $\alpha\beta$ -phase. The equilibrium pressure can be described in dependence of temperature as shown in Equation (6.30) [111][112].

$$\log_{10} \left( \frac{p_{eq}(\alpha\beta)}{\text{bar}} \right) = -C_3 \cdot T^{-1} + C_4, \quad (6.30)$$

with  $p_{eq}(\alpha\beta)$  in bar. Beyond the second threshold  $c_{Q/M} > 2.0$ , the equilibrium pressure  $p_{eq}(\beta)$  - also in bar - rises exponentially with increasing hydrogen concentration. This is approximated from a graph in [111] with a simple damping function implemented in Equation (6.31). The values of the Constants  $C_3 - C_5$  used in Equations (6.30) and (6.31) are listed in Table 6.9.

$$\log_{10}(p_{eq}(\beta) \cdot \text{bar}^{-1}) = -C_3 \cdot T^{-1} + C_4 + C_5 \cdot (c_{Q/M} - c_{Q/M}(V, \alpha\beta \rightarrow \beta)). \quad (6.31)$$

Table 6.9: Vanadium-Hydride equilibrium pressure parameters for the  $\alpha\beta$  and  $\beta$  phases given as interpolation of experimental data from [111] [112].

Vanadium-Hydride	$H_2$	$D_2$	$T_2$	Unit	Source	
$\alpha\beta$ -phase	$C_3$	2103	2622	2407	(1/K)	H: [111]
	$C_4$	7.34	8.6	7.8	(-)	D+T: [112]
$\beta$ -phase	$C_5$	10	10	10	(-)	this work

### 6.2.3 Temperature Swing Absorption Modelling Results

Given the cyclic nature of the Temperature Swing Absorption with periodic shifts in boundary conditions, a repeating pattern can be observed. To display the output of the model, Figure 6.7 illustrates key process variables observed in both the palladium and vanadium column over the course of two exemplary consecutive cycles. First, Figure 6.7 a) illustrates the temperature ( $T$ ) evolution of both columns, which represent an input parameter and alternate between an upper and a lower temperature as defined for both columns in Table 6.7.

Next, the development over time of the average column pressure  $p$  is given in Figure 6.7 b). Several observations can be made here:

- (i) Induced by the change in temperature in the Sorption phases (cf. Point A in Figure 6.7), the column pressure rises or drops. In this context, a decrease in column temperature entails a drop in pressure, which is tied to hydrogen progressively absorbing into the metal bed. The equilibrium pressure is calculated as a function of temperature as described for the two metals in the previous section.
- (ii) In the Flow phases (cf. Point B in Figure 6.7), the pressure of the two columns converges. By opening the valve in the connection tube between the two columns, matter is transferred to equalize the pressure between the two columns following Equation (6.18). As the pressure compensation overlaps with ab- and desorption, the pressure gradient during this process is not equivalent in the two columns. Additionally, depending on the gaseous content and pressure difference, the pressure of the two columns is not necessarily fully equalized at the end of a Flow phase (cf. Point D).
- (iii) When matter is added to or withdrawn from a column, the pressure changes accordingly. This occurs for the Pd-Column in the 1. Withdrawal phase and the Feed phase and for the V-column in the 2. Withdrawal phase (cf. Point C).

Then, the concentration of bound hydrogen in the metal  $c_{Q/M}$  is given for three different locations throughout the two columns in Figure 6.7 c) as defined by the boundary conditions in Equations (6.13) - (6.17): (i) the columns ends, where matter is withdrawn from ( $n_{Pd} = 1, n_V = 50$ ), (ii) the middle of the column ( $n = 25$ ) and (iii) at the point where the columns are connected ( $n_{Pd} = 50, n_V = 1$ ).  $c_{Q/M}$  changes over time as a function of the column pressure and temperature. For increasing temperatures and decreasing pressure, desorption of hydrogen occurs resulting in a decrease of  $c_{Q/M}$  (cf. Point C and F). Conversely, a decrease in temperature or increase in pressure is followed by absorption and an increase of  $c_{Q/M}$ . The concentration evolution is given by the equilibrium state described in Equations (3.18) and (6.24) for palladium as well as Equations (6.28) and (6.31) for vanadium.

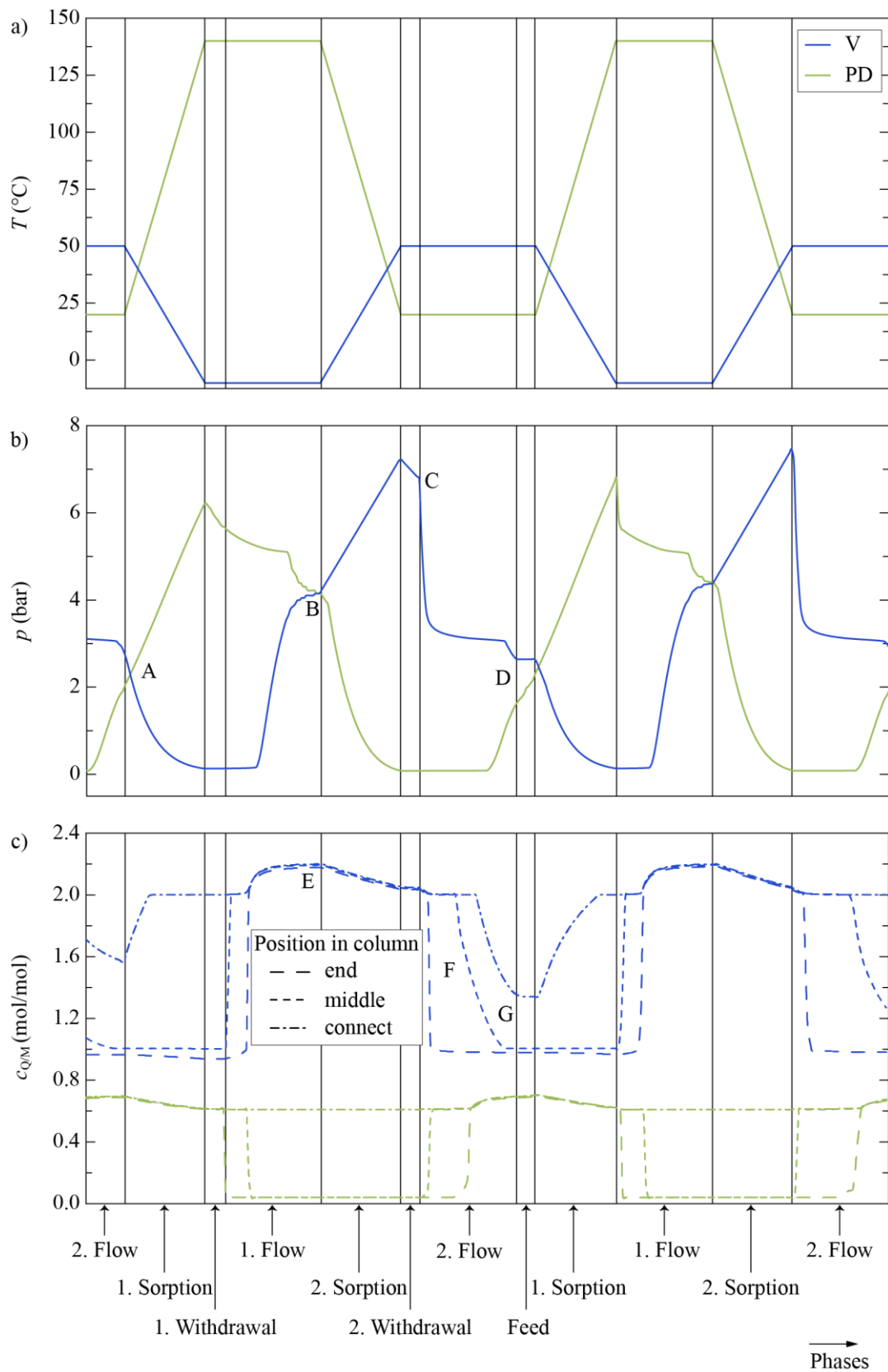


Figure 6.7: Development of the column a) temperature, b) pressure at the column ends and c) solid phase hydrogen concentration at different locations for the palladium (Pd) and vanadium (V) absorption beds over different phases. Letters A through G mark points of interest and are referred to in the text.

This sorption processes are accompanied by transitions between the  $\alpha$ ,  $\alpha\beta$  and  $\beta$ -phases for both metals, which results in formation of concentration plateaus over the course of each TSA-cycle in dependence of the threshold concentrations defined in Equations (6.21) and (6.27). Such a plateau in the  $\beta$ -phase can be seen for the vanadium column in Figure 6.7 c) in Point E, where the column pressure is high and the temperature low. To increase the  $c_{Q/M}$  further above the upper threshold requires the application of a large equilibrium pressure in the vanadium column. In between the two thresholds, steep gradients of  $c_{Q/M}$  mark the transition of the metal through the  $\alpha\beta$ -phase (cf. Point F) during the two flow phases.

Depending on the position within the column, the transition occurs at different points in time. For example, after initiation of a change in boundary conditions, the column ends ( $n_{Pd} = 1, n_V = 50$ ) reach the new steady state almost instantaneously. In contrast, at the connection point of the two columns ( $n_{Pd} = 50, n_V = 1$ ), where matter passes through on its way to the other column, the concentration shift occurs with a delay and is less steep. The different observations are based on the narrow design of the column diameter, which limits the flow. This way, over the course of the entire flow phase matter keeps transitioning from the high pressure column to the low pressure column. Close to the connection point, the formation of the new equilibrium state is therefore delayed. If the two columns are not in pressure equilibrium at the end of a flow phase, no full phase transition from  $\alpha$ - to  $\beta$ -phase can be observed in parts of the column (cf. Point G).

Currently there is no corresponding experiment to adequately validate the results obtained in this work. Therefore, to check for model output consistency, the pressure profile obtained by the simulation is compared to the behaviour of a comparable experimental setup including a palladium-filled column subject to a cyclic heating. Scogin et al. provide the qualitative hydrogen pressure evolution of a Pd-Column over the length of a single cycle [113] as shown in Figure 6.8 in conjunction with the pressure evolution of the equivalent TSA cycle obtained by the simulation. The publication does not provide specific values; therefore, the graph is shown qualitatively. Nonetheless, when scaled to the TSA process, the similarity of the two pressure evolutions is observable, with a linear pressure increase in the 1. Sorption phase followed by two exponential decays over the course of the 1. Flow and 2. Sorption phases approaching a very low pressure in the 2. Flow phase.

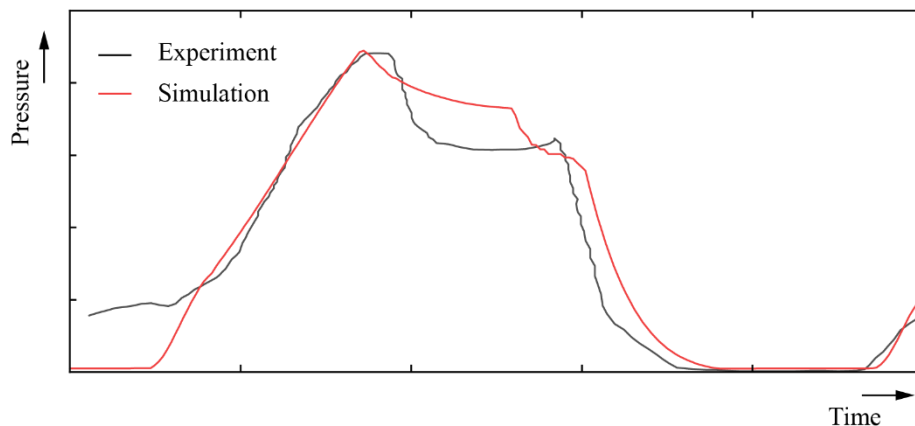


Figure 6.8: Qualitative pressure evolution over the course of a single process cycle including two Sorption and Flow phases for a palladium column implemented in the simulation (red) in comparison to a comparable experimental setup (black) [113].



Sequencing together several of these cycles leads to the formation of a distinct hydrogen isotope concentration profile across the column. Figure 6.9 depicts the change of the hydrogen isotope composition over time in Figure 6.9 a) as well as over the length of the column after a sharp concentration profile is established in Figure 6.9 b) and c).

To enrich tritium in the Pd-column to a high concentration ( $y_{T_2} > 85 \text{ mol}\%$ ), the model requires about 10 cycles (the first 11000 s in Figure 6.9 a)), which are calculated at a rate of  $(0.5 \dots 5) \times$  real time. The initial hydrogen content - consisting of uniform equimolar DT - is enriched with tritium to D : T = 12 : 88 in the palladium column over a period of 10 closed cycles at which point, the semi-continuous process begins with a single extended cycle. For the vanadium column the ratio obtained is H : D : T = 2 : 72 : 26. The two products withdrawn from the column at  $n_V = 50$  and  $n_{Pd} = 0$  represent the isotope composition of  $F_{\text{low-trit}}$  (16) and  $F_{\text{high-trit}}$  (17), respectively.

Importantly, the extended cycles, in which matter is withdrawn and fed, must be spaced out to account for the drop in product quality. Such a drop can be seen for tritium in the palladium column at about  $t = 11000 \text{ s}$  in Figure 6.9 a) and results from the introduction of new matter during the feed phase. In the model procedure - for the boundary conditions of the RDP - an amount of five closed cycles ( $N_{\text{closed}} = 5$ ) followed by the extended cycle is found to be required to repeatedly enrich tritium to  $y_{T_2} > 85 \text{ mol}\%$  and form a recurring cycle.

Once a stable pattern is established, the hydrogen isotope fractions in the gas and solid phase can be displayed over the column length to conclude on the separation efficiency of both columns. Such a profile is shown in Figure 6.9 b) for the Pd-column and Figure 6.9 c) for the V-column. The fraction of tritium drops from  $y_{T_2} > 85 \text{ mol}\%$  at  $n_{Pd} = 0$  to  $y_{T_2} = 40 \text{ mol}\%$  at  $n_{Pd} = 50$  and further to  $y_{T_2} < 30 \text{ mol}\%$  at  $n_V = 50$ . Deuterium represents the dominant counterpart to tritium throughout the whole TSA setup, given that the protium fraction in the feed ( $y_{H_2}(\text{feed}) = 1.2 \text{ mol}\%$ ) and thus overall protium column inventory remains low. Overall, the separation of isotopes is conducted more effectively in the palladium column in comparison to the vanadium column, given the larger separation factors of the metal ( $|K_{HT}(\text{Pd})| > |K_{HT}(\text{V})|$ ).

The inverse properties of both metals resulting in opposing driving forces becomes evident when comparing the gas and solid fractions  $y_{Q_2}$  and  $x_{Q_2}$  for the different isotopes in the two columns. For palladium with a separation factor  $K_{DT} > 1$ , the tritium fraction in the gas phase surpasses the tritium fraction in the solid phase ( $y_{T_2} > x_{T_2}$ ), whereas for vanadium the inverse behaviour is observable.

The logarithmic plots in Figure 6.9 d) and e) display the concentration of protium over the length of both columns. Protium introduced into the TSA process accumulates in the vanadium column. Given the strong separation effect  $K_{HT}$  in palladium the according column is deprived of protium with a maximum of  $y_{H_2} < 0.1 \text{ mol}\%$  at  $n_{Pd} = 50$ . Conversely, at the end of the vanadium column  $n_V > 40$ , protium accumulates up to  $y_{H_2} < 10 \text{ mol}\%$ .

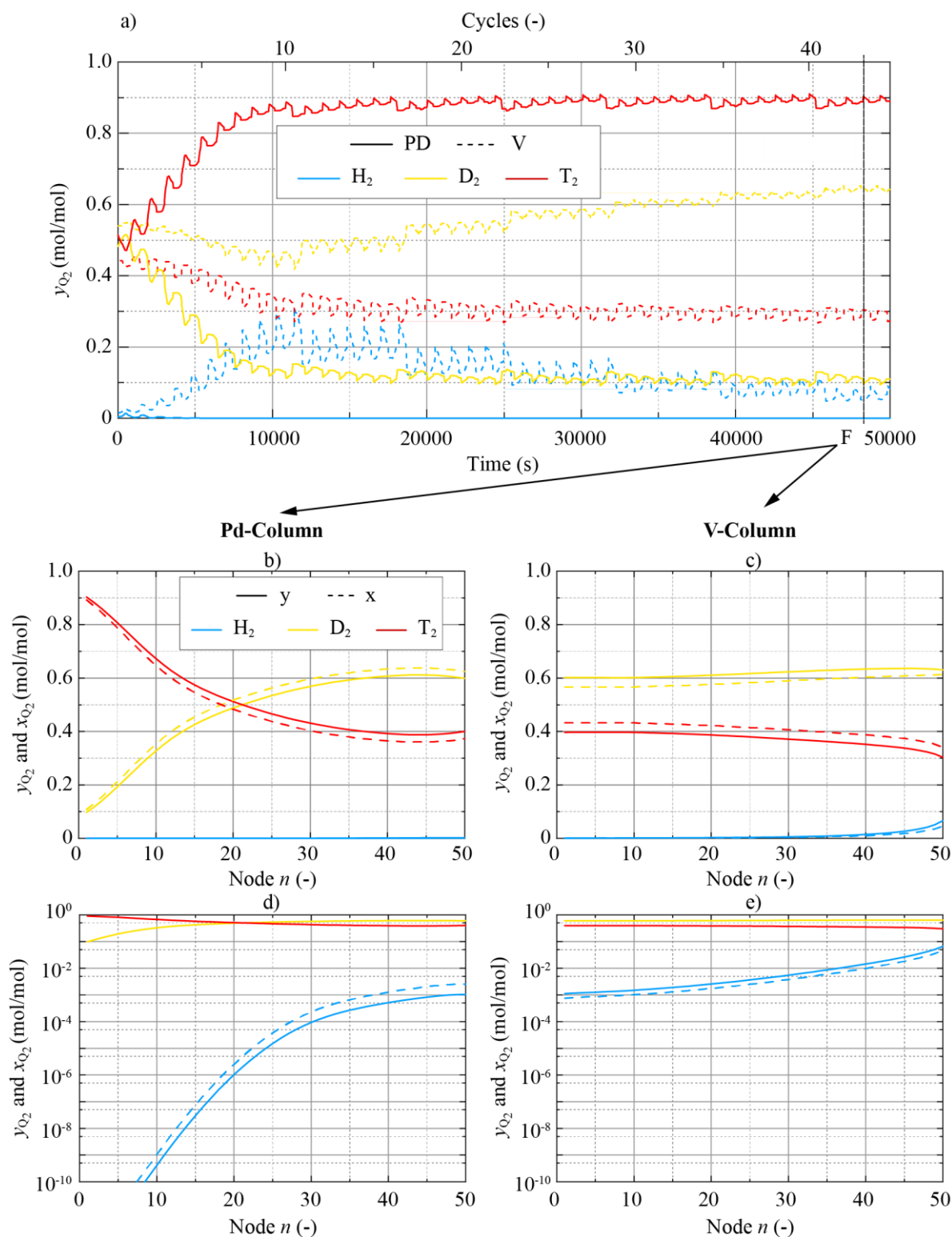


Figure 6.9 a): Evolution of the hydrogen isotope fraction at both ends of the column over time after initialisation at  $t = 0$  s. Figure 6.7 above represents the time window between 38000 to 40500 s and the dashed line marked F denotes the point at which graphs b) through e) are recorded.  
 b) and c) Hydrogen isotope fraction in the gas and solid phase within the two absorption beds, both discretized over their length into  $n = 50$  nodes.  
 d) and e) Logarithmic plots of b) and c) to visualize the distribution of the protium fraction.

## Integration into the fuel cycle

Given the enrichment of isotopes achievable with the Temperature Swing Absorption process, the discontinuous output during the feed and two withdrawal phases must be integrated into the continuous fuel cycle environment using the buffer vessels up- and downstream the column setup. The discontinuous throughput of the TSA setup can be expressed by the input  $F_{\text{feed,disc}}$  during the feed phase as calculated in Equation (6.32).

$$F_{\text{feed,disc}} = 0.05 \cdot \left( \sum_Q I_{\text{sum}} (\text{Pd}) + \sum_Q I_{\text{sum}} (\text{V}) \right) \cdot t_{\text{feed}}^{-1} = 45.91 \text{ Pa} \cdot \text{m}^3/\text{s}. \quad (6.32)$$

The throughput of the two extraction streams (16) and (17) is given by the split fraction  $\kappa$  as  $\kappa \cdot F_{\text{feed,disc}}$  and  $(1 - \kappa) \cdot F_{\text{feed,disc}}$ , in dependence of the output requirements.

An equivalent steady state throughput  $F_{\text{feed,cont}}$  of an IRPR system is calculated from  $F_{\text{feed,disc}}$  with Equation (6.33). Depending on the bypass fraction chosen, multiple systems must be operated in parallel to generate the throughput required for DEMO.

$$F_{\text{feed,cont}} = \frac{t_{\text{feed}}}{N_{\text{closed}} \cdot t_{\text{extended}} + t_{\text{closed}}} \cdot F_{\text{feed,disc}} \approx 0.41 \text{ Pa} \cdot \text{m}^3/\text{s}. \quad (6.33)$$

Given the expectable output quantities, the bypass ratio  $\eta_{\text{bypass}}$  can be calculated by solving for an equimolar fraction of DT as input to the GDCM in Equation (6.34).

$$0 = F_{\text{7}} \cdot \left( y_{\text{7}}(\text{D}) - y_{\text{7}}(\text{T}) \right) + \eta_{\text{bypass}} \cdot F_{\text{12}} \cdot \left( y_{\text{12}}(\text{D}) - y_{\text{12}}(\text{T}) \right) + \kappa \cdot (1 - \eta_{\text{bypass}}) \cdot F_{\text{12}} \cdot \left( y_{\text{16}}(\text{D}) - y_{\text{16}}(\text{T}) \right), \quad (6.34)$$

where  $y(\text{D})$  and  $y(\text{T})$  denote the fraction of the deuterium and tritium isotope of the according stream taken from Table 5.1 and Table 6.1. The split fraction is given as  $\kappa = 62 \%$  from solving a mass balance equation for the IRPR system for any given isotope as per Equation (4.1).

For an equimolar DT composition, the bypass fraction is  $\eta_{\text{bypass}} = 69.72 \%$ . With a similar calculation the amount of protium removed by the IRPR system can be calculated. The concentration of protium drops from  $y_{\text{12}}(\text{H}) = 1.22 \%$  to  $y_{\text{18}}(\text{H}) = 1.05 \%$ , which is equivalent to  $0.32 \text{ Pa} \cdot \text{m}^3/\text{s}$  of protium removed. For an assumed protium ingress of  $0.1 \text{ Pa} \cdot \text{m}^3/\text{s}$  in the DIRM, the IRPR system can thus handle a maximum protium ingress in the INTL of  $0.22 \text{ Pa} \cdot \text{m}^3/\text{s}$ . These are equivalent to the values listed in Table 3.10.

To generate the steady state throughput a number of parallel TSA processes ( $\#_{\text{TSA}}$ ) is required. This is calculated using Equation (6.35).

$$\#_{\text{TSA}} = \frac{F_{\text{12}} \cdot (1 - \eta_{\text{bypass}})}{F_{\text{Feed,cont}}} = \frac{26.02}{0.41} \approx 64, \quad (6.35)$$

where  $F_{\text{Feed,cont}}$  is calculated in Equation (6.33) in dependence of many variables including cycle times and the extraction quantity. Thereby this number can shift drastically if one of the parameters is changed.

---

When considering the hydrogen inventory implied by this setup, a need for optimisation is apparent. Each TSA unit contains on average 24.28 mol of hydrogen in a ratio of H : D : T = 0.4 : 52.2 : 46.4. This corresponds to 69.44 g of tritium per unit. The total IRPR system with 64 TSA units thus contains  $I_{T_2}(\text{IRPR}) = 4.44$  kg of tritium.

## 6.3 Inner Tritium Loop Summary

The Inner Tritium Loop comprises two system blocks. The numbers below refer to the Reference Design Point.

### Exhaust Processing System

The Exhaust Processing System block consists of a two-staged permeator setup with an intermediary cracking step and subsequent removal of Plasma Enhancement Gases. 37 permeators in the first and 8 permeators in the second stage recuperate more than 99.7 % of the hydrogen throughput upstream the EPS ( $F_{\text{INTL}} = 85.94 \text{ Pa} \cdot \text{m}^3/\text{s}$  (12)). Additionally, in a parameter study, the influence of four process parameters on the hydrogen removal efficiency is examined: (i) the upstream pressure, (ii) the upstream hydrogen fraction, (iii) the fraction of chemically bound hydrogen and (iv) the amount of permeators operated in parallel per stage. The hydrogen removal efficiency of the permeator setup exhibits a high sensitivity to the applied pressure and the amount of permeators used, whereas the fraction of chemically bound hydrogen governs the distribution of permeators among the two stages.

The Catalytic Cracking process splits compound hydrogen. PEG removal recuperates argon and xenon from the exhaust stream. For the purpose of this work, this process step is greatly simplified and implemented into the model with an assumed efficiency of  $\eta_{\text{crack}} = 100 \text{ mol}\%$  and  $\eta_{\text{PEG}} = 99 \text{ mol}\%$ , respectively.

### Isotope Rebalancing and Protium Removal

The two tasks of the IRPR system to (i) rebalance the DT fuel mixture and (ii) remove protium are both conducted by a Temperature Swing Absorption process. To handle the throughput required by the fuel cycle, 64 TSA units process about 30 % of the input stream. The rest is bypassed to form a rebalanced fuel stream upstream the torus. The semi-continuous nature of the TSA process imposes the inclusion of buffer tanks and a considerable tritium inventory  $I_{T_2}(\text{IRPR}) = 4.44$  kg.

The two outputs of the IRPR are enriched tritium at a mixture of D : T = 88 : 12 as well as enriched deuterium H : D : T = 2 : 72 : 26. The former stream is deprived of protium and mixed with the bypass to counteract the disequilibrium of the deuterium tritium fuel mixture. The enriched deuterium stream represents 18.77 mol% of the system block input and is sent to the Outer Tritium Loop. Simultaneously, 0.322 Pa · m<sup>3</sup>/s of protium are removed within the INTL from the input stream. This is equivalent to 30 % of the protium upstream the system block.

## 7 The Outer Tritium Loop

The Outer Tritium Loop (OUTL) represents the final clean-up stage of the torus exhaust gas prior to discharge to environment and must primarily guarantee that tritium release to the ambient matches the ALARA requirements. To obtain high separation factors and cope with the different input streams, three interlinked large-scale processes are foreseen.

Process gas contaminated with residual tritium is handled in the first system block - the Exhaust Detritiation System (EDS). Here, hydrogen remnants are converted to water vapour in a combiner and liquefied in a condenser. Any residual tritium in the exhaust gas is flushed with water in a Wet Scrubber Column. All non-hydrogen species traverse the EDS unaffected to be emitted via the stack.

The tritiated water is collected and fed to the second system block - the Water Detritiation System (WDS). Here a counter-flow column is used in tandem with an electrolyser in the Combined Electrolysis and Catalytic Exchange (CECE) process to concentrate tritium in water and produce a stream of detritiated gas at the top of the column.

Separation of pure hydrogen isotopes to a high degree of purity is achieved in a multi-staged Cryogenic Distillation column setup. In tandem with equilibrators, that reduce the proportion of mixture isotopologues in the system block, they form the Isotope Separation System (ISS) - the third system block of the Outer Tritium Loop. The output of this system, in the form of concentrated hydrogen isotopes is sent to the stack or the GDCM.

The OUTL with all system blocks and subsystems is depicted in Figure 7.1. The throughputs between system blocks ⑰–⑳ for the Reference Design Point are listed in Table 7.1.

Table 7.1: Throughput and composition of all streams connecting system blocks in the Outer Tritium Loop for the Reference Design Point of DEMO.

Stream	$F_{Q_2O}$ ⑰	$F_{EDS}$ ⑱	$F_{elec}$ ㉑	$F_{WDS}$ ㉒	$F_{D_2}$ ㉓	$F_{T_2}$ ㉔	$F_{ISS}$ ㉕	$F_{stack}$ ㉖	Unit
$F$	4.22	55.78	2.95	53.10	12.16	4.27	360.80	469.68	(Pa·m <sup>3</sup> /s)
$y(H_2)$	—	<10 <sup>-3</sup>	77.89	73.00	<10 <sup>-9</sup>	<10 <sup>-20</sup>	99.40	84.61	(mol%)
$y(HD)$	—	<10 <sup>-7</sup>	9.43	<10 <sup>-3</sup>	<10 <sup>-3</sup>	<10 <sup>-12</sup>	0.60	0.46	(mol%)
$y(D_2)$	—	<10 <sup>-13</sup>	0.35	<10 <sup>-9</sup>	>99.99	0.26	<10 <sup>-4</sup>	5.47·10 <sup>-5</sup>	(mol%)
$y(HT)$	—	<10 <sup>-8</sup>	10.87	<10 <sup>-5</sup>	<10 <sup>-6</sup>	<10 <sup>-11</sup>	<10 <sup>-5</sup>	5.00·10 <sup>-6</sup>	(mol%)
$y(DT)$	—	<10 <sup>-13</sup>	0.88	<10 <sup>-10</sup>	<10 <sup>-3</sup>	4.87	<10 <sup>-8</sup>	4.34·10 <sup>-9</sup>	(mol%)
$y(T_2)$	—	<10 <sup>-13</sup>	0.59	<10 <sup>-12</sup>	<10 <sup>-10</sup>	94.87	<10 <sup>-12</sup>	1.20·10 <sup>-13</sup>	(mol%)
$y(H_2O)$	86.27	0.62	—	27.00	—	—	—	3.13	(mol%)
$y(HDO)$	7.01	<10 <sup>-4</sup>	—	<10 <sup>-3</sup>	—	—	—	1.04·10 <sup>-4</sup>	(mol%)
$y(D_2O)$	0.18	<10 <sup>-9</sup>	—	<10 <sup>-8</sup>	—	—	—	8.58·10 <sup>-9</sup>	(mol%)
$y(HTO)$	6.05	<10 <sup>-4</sup>	—	<10 <sup>-5</sup>	—	—	—	3.24·10 <sup>-6</sup>	(mol%)
$y(DTO)$	0.33	<10 <sup>-9</sup>	—	<10 <sup>-10</sup>	—	—	—	8.03·10 <sup>-10</sup>	(mol%)
$y(T_2O)$	0.16	<10 <sup>-9</sup>	—	<10 <sup>-12</sup>	—	—	—	1.89·10 <sup>-11</sup>	(mol%)
$y(Imp)$	—	99.38	—	—	—	—	—	11.80	(mol%)

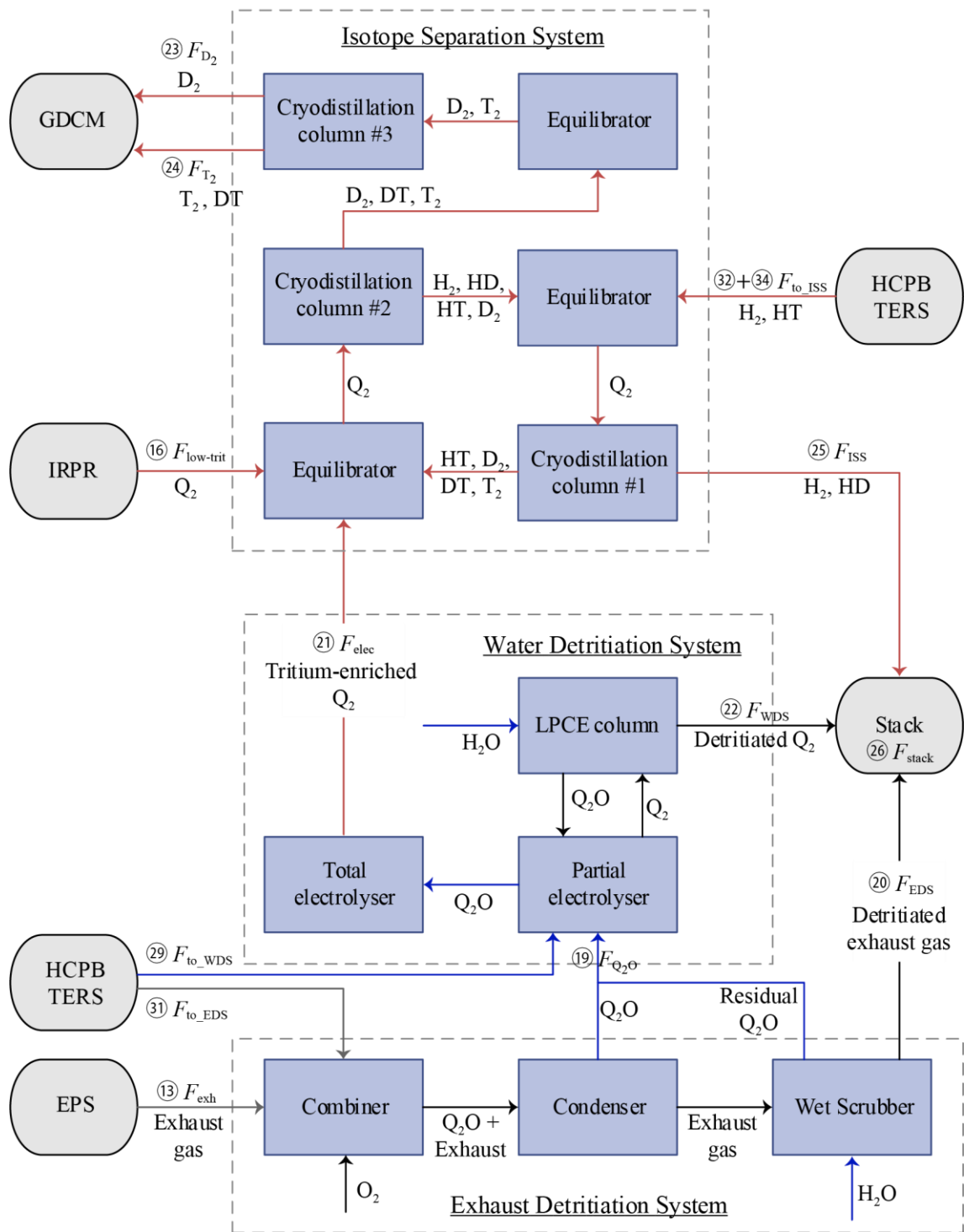


Figure 7.1: Schematic diagram of the Outer Tritium Loop with the three system blocks Exhaust Detritiation, Water Detritiation and Isotope Separation including the main subsystems.

## 7.1 Exhaust Detritiation

The detritiation process of exhaust gas foreseen for the DEMO is adopted from the current JET detritiation setup [114] and includes the Wet Scrubber technology to be implemented at ITER [115]. The setup is designed to treat the exhaust gas in a three-step procedure each representing a subsystem of the EDS. In the first step, the remaining hydrogen is transformed into water by forcing a chemical reaction with oxygen in a combiner. In the second step the mixture of water vapour and exhaust gas passes through a low temperature condenser. The condensed water is collected while the remaining gas stream is routed to a Wet Scrubber column. In this last step, the concentration of residual tritium is minimized by forcing an isotopic exchange reaction with distilled water.

### 7.1.1 Exhaust Detritiation System Boundary Conditions

The EDS is implemented in the fuel cycle to process gas mixtures of non-hydrogen species contaminated with low fractions of tritium. Therefore, the exhaust gas downstream the Exhaust Processing System (EPS) from the previous loop constitutes the primary input (13). At this point - in the fuel cycle the species to be recovered have already been extracted from the exhaust which leaves helium, nitrogen and hydrogen remnants including tritium.

However, there are other tritium contaminated gas streams from various sources throughout DEMO that necessitate a similar treatment. These external system blocks produce exhaust streams of different throughputs, tritium contamination levels and detritiation requirements. Consequently, merging these inputs into a single EPS is not necessarily feasible. Following gas flows are identified to require detritiation of some form:

- (i) The Tritium Extraction and Removal System of the Outer Fuel Cycle produces an output stream containing cooling agent contaminated with tritium (31). For one of the Breeding Blanket concepts - the HCPB, which assumes the worst-case input of large quantities of purge protium (cf. Appendix A1) this is assumed as input to the Exhaust Detritiation System .
- (ii) Inclusion of the secondary confinement of the DEMO fuel cycle is omitted as quantification is not feasible at the current design stage.
- (iii) The detritiation of air and ventilation systems of the power plant is relayed to an outside system due to the huge disparity in boundary conditions.

The technical implementation to process streams (ii) and (iii) can be assumed structurally similar way to the EDS presented in the following. Further inputs to the EDS are given by the supply of oxygen and water for operation of the Combiner and Wet Scrubber column, respectively.

At the top of the scrubber column, the detritiated gas stream leaves the fuel cycle via the stack (20). The water accumulated in the condenser as well as downstream the scrubber column is sent to the WDS system (19).

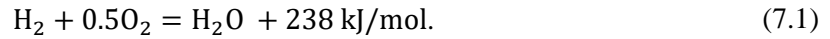
---

### 7.1.2 Exhaust Detritiation System Setup and Modelling

To reproduce the Exhaust Processing System in the model, the main computational effort revolves around the modelling of the Wet Scrubber column. The Condenser and Combiner are represented as straight-forward conversion components and are assumed in steady state operation. The modelling approach is briefly summarized here whereas the input and output quantities are listed and discussed in the section hereafter.

#### Combiner

The combiner subsystem is implemented into the model as a single-stage catalytic recombiner. The exhaust stream containing hydrogen is brought into contact with oxygen in a palladium catalyst environment producing water steam and release of energy. For protium the exothermic radical reaction is exemplified in Equation (7.1).



A comparable setup is used as safety equipment in nuclear fission reactors to limit the release of molecular protium in case of an accident. These recombiners operate at pressures between 1 – 2 bar and temperatures between 0 – 100 °C. Given enough surface area of the catalyst, the recombination reaction does not require external input in form of an activation energy. Instead, autocatalytic conversion begins once the hydrogen concentration reaches a threshold of 1 – 2 vol%. The recombination efficiency - defined as the molar ratio of hydrogen reacting to water over hydrogen fed - is reported as close to unity  $\eta_{\text{comb}} > 99.9 \%$  for these setups [116].

Similar process parameters are implemented into the model. The reaction is modelled in steady state, assuming an isothermal combiner temperature of  $T_{\text{comb}} = 350 \text{ K}$  and an isobaric pressure of  $p_{\text{comb}} = 1 \text{ bar}$ . No distinction is made between the hydrogen isotopes and reactions of non-hydrogen species with any of the reactants are neglected.

Assuming the reaction enthalpy stated above and a conversion rate of  $\eta_{\text{comb}} > 99.99 \%$ , the heat released in the combiner to convert the hydrogen of the input streams ( $F_{\text{O}_2}(\textcircled{13}) + \textcircled{31}) = 3.90 \text{ Pa m}^3/\text{s}$ ) amounts to  $P \approx 400 \text{ W}$ . To fulfil isothermal combiner conditions, this heat load must be dissipated. This way the combiner requires a steady-state input of oxygen equal to  $F_{\text{O}_2} = 1.95 \text{ Pa m}^3/\text{s}$  to maintain the reaction. Given the catalytic surface and the amount of energy released in the combiner, the formation of water molecules is assumed in isotopologic equilibrium at the given temperature. The output stream is calculated following the procedure of computing equilibrium as described in Section 3.3.1. Unconverted hydrogen is propagated to and must be accounted for in the connecting streams and the subsequent process steps.



## Condenser

The condenser subsystem is modelled as a single-stage heat exchanger, where the incoming fluid is cooled to a temperature of  $T_{\text{cond}} = 275$  K. The steam generated in the combiner is condensed here at a constant ambient pressure  $p_{\text{cond}} = 1$  bar. Isothermal conditions are assumed in the model, which are maintained by a condenser cooling infrastructure e.g. by running water through the cooling channels. Assuming a constant heat capacity of water  $c_p(\text{H}_2\text{O}) = 75.4$  J/(mol K), nitrogen  $c_p(\text{N}_2) = 29.1$  J/(mol K) and helium  $c_p(\text{He}) = 20.8$  J/(mol K) for the given temperature range  $T_{\text{cond}} \leq T \leq T_{\text{comb}}$  the required cooling capacity  $H_{\text{cond}}$  is estimated in Equation (7.2).

$$H_{\text{cond}} = \sum_i y_i \cdot F(\textcircled{13} + \textcircled{31}) \cdot c_p(i) \cdot (T_{\text{cond}} - T_{\text{comb}}) = -57.5 \text{ W}. \quad (7.2)$$

Given the small throughput combined with the large fraction of helium and nitrogen in the fluid, the required cooling is negligible. The condensed liquid is collected and directed to the Water Detritiation System, whereas a mixture of the non-hydrogen species, unburned hydrogen gas, and a small fraction of water vapor remains in the gas phase. The water vapour concentration in the gas phase is calculated by implementing the temperature-dependent saturation pressure described in Equation (3.12) at the condenser temperature. The water vapour is assumed in perfect mixture with liquid water, which results in an equal composition of isotopologues in both phases. Exchange reactions of hydrogen isotopologues are neglected as they lack the catalytic surface and high temperatures in the condenser.

## Wet Scrubber

In the Wet Scrubber column liquid water ( $\text{H}_2\text{O}$ ) is brought into contact with the exhaust gas. The gaseous output of the condenser is fed at the bottom of the column and streams upwards through a catalyst bed. The purge water is fed at the top of the column flowing downwards, resulting in a counter-flow arrangement, which promotes isotopic exchange between the liquid and gas phase. The exchange reactions favour binding tritium in the liquid phase, which constitutes the underlying separation principle. The inert exhaust gases are assumed to trespass the column without any interaction. They are discharged as detritiated exhaust stream along with protium gas at the top of the column.

The setup of the Wet Scrubber column is principally alike to the Liquid Phase Catalytic Exchange column of the Water Detritiation System. Both systems are coded in a similar way in the model, with a modified design for the Wet Scrubber column to cope with the large fractions of inert gas running through the column instead of pure hydrogen. The detailed model procedure and results of both detritiation columns are given in Section 7.2 and the column parameters are summarized in Table 7.3.

### 7.1.3 Exhaust Detritiation System Modelling Results

Table 7.2 lists the results of the EDS modelling including the Wet Scrubber output. The consideration of water vapour in the gas stream leads to several remarkable observations. The Condenser can rectify only 91 mol% of its Q<sub>2</sub>O input, whereas the remainder escapes in vapour form. Hence, a final clean-up step in the form of a dryer or scrubber column is a justified requirement for any EDS setup.

The water stream produced by the EDS is small in comparison to the gas stream processed given that the hydrogen in the input stream accounts for less than 7 mol% of the throughput with an isotope ratio of H : D : T = 92.8 : 3.9 : 3.3. The purge gas water stream inserted at the column top is  $F_{\text{H}_2\text{O}} = 0.67 \text{ Pa} \cdot \text{m}^3/\text{s}$ . The high protium content stems from this source as well as the purge gas used in the HCPB.

Given the values for the RDP listed in Table 7.2, the detritiation factor of the EDS system ( $DF_{\text{EDS}}$ ) is calculated in Equation (7.3).

$$DF_{\text{EDS}} = \frac{0.142}{5.13 \cdot 10^{-6}} \approx 27580. \quad (7.3)$$

The Wet Scrubber column alone accounts for a detritiation of  $DF_{\text{WS}} \approx 2390$ . This corresponds to an annual tritium release of 0.430 g/a, 99.97 mol% in the form of HTO vapour.

The impurities in the exhaust gas consist of nitrogen and helium ( $\text{N}_2 : {}^4_2\text{He} = 36 : 64$ ) and small fractions of unrecovered xenon and argon. If the scrubber column is operated in steady state for an entire year, it expels 775.1 kmol/a of matter containing 54.2 mol/a of Ar and 25.4 mol/a of Xe.

Table 7.2: Throughput and composition upstream and downstream the three subsystems of the EDS system block.

Stream	Combiner		Condenser Output		Wet Scrubber Output		Unit
	Input ⑬+⑭	Output	Gas	Q <sub>2</sub> O	Gas ⑳	Q <sub>2</sub> O	
$F$	59.32	59.32	55.76	3.56	55.78	0.67	(Pa · m <sup>3</sup> /s)
$y(\text{H}_2)$	6.03	<10 <sup>-3</sup>	<10 <sup>-3</sup>	—	6.98 · 10 <sup>-4</sup>	—	(mol%)
$y(\text{HD})$	0	<10 <sup>-4</sup>	<10 <sup>-4</sup>	—	1.61 · 10 <sup>-7</sup>	—	(mol%)
$y(\text{D}_2)$	0.27	<10 <sup>-5</sup>	<10 <sup>-5</sup>	—	1.14 · 10 <sup>-11</sup>	—	(mol%)
$y(\text{HT})$	0.05	<10 <sup>-4</sup>	<10 <sup>-4</sup>	—	4.70 · 10 <sup>-9</sup>	—	(mol%)
$y(\text{DT})$	0	<10 <sup>-5</sup>	<10 <sup>-5</sup>	—	7.26 · 10 <sup>-13</sup>	—	(mol%)
$y(\text{T}_2)$	0.22	<10 <sup>-5</sup>	<10 <sup>-5</sup>	—	1.25 · 10 <sup>-14</sup>	—	(mol%)
$y(\text{H}_2\text{O})$	—	5.597	0.51	85.14	0.62	92.29	(mol%)
$y(\text{HDO})$	—	0.50	0.05	7.57	4.01 · 10 <sup>-4</sup>	4.03	(mol%)
$y(\text{D}_2\text{O})$	—	0.01	<10 <sup>-2</sup>	0.20	7.00 · 10 <sup>-8</sup>	0.05	(mol%)
$y(\text{HTO})$	—	0.43	0.04	6.53	1.84 · 10 <sup>-5</sup>	3.50	(mol%)
$y(\text{DTO})$	—	0.03	<10 <sup>-2</sup>	0.37	6.67 · 10 <sup>-9</sup>	0.09	(mol%)
$y(\text{T}_2\text{O})$	—	0.01	<10 <sup>-2</sup>	0.18	1.59 · 10 <sup>-10</sup>	0.04	(mol%)
$y(\text{Imp})$	93.43	93.43	99.40	—	99.38	—	(mol%)

## 7.2 Water Detritiation

The Combined Electrolysis and Catalytic Exchange (CECE) process adopted in the Water Detritiation System of DEMO is a combination of two separation principles each realized in a subsystem. First, the Liquid Phase Catalytic Exchange (LPCE) process relies on the preference of heavier hydrogen isotopes accumulating in water over their lighter counterparts, which remain in the gas phase as hydrogen molecules). Within the column, tritiated hydrogen gas is flushed with water in a counter-flow column packed with steel spacers and a platinum catalyst to improve reactivity [117].

The second principle is based on isotope-dependent reactivity of water during electrolysis. In a partial electrolyser, water from the LPCE column is continuously converted to hydrogen gas. Over time the concentration of heavy isotopes increases within the liquid, while the hydrogen gas is fed back into the column.

### 7.2.1 Water Detritiation System Boundary Conditions and Setup

Input to the WDS is the tritiated water generated in the Combiner and Wet Scrubber of the EDS. Other potential sources where hydrogen is brought into contact with oxygen or water must be considered as well. For example, tritium could permeate into the coolant water, which then requires purification. Regardless of origin, the tritiated water enters the CECE process as input to the electrolyser. Oxygen generated by the electrolysis is constantly removed from the process.

The purified hydrogen gas is withdrawn from LPCE column alongside some water vapour. It is detritiated to the point that it can be discharged to the stack. The accumulated tritium is continuously removed from the partial electrolyser, converted to hydrogen in a second total electrolyser and delivered to the ISS system for separation of isotopes. The setup of the CECE process is shown in Figure 7.2.

### 7.2.2 Water Exchange Column Modelling

The essential part of the LPCE modelling is given by a three-phase mass transfer. Within the column, gaseous hydrogen molecules of each isotopologue  $F_{\text{gas}}(Q_2)$  strive towards the top whereas the liquid water  $F_{\text{liq}}(Q_2O)$  trickles downwards. Additionally water vapour  $F_{\text{vap}}(Q_2O)$  forms at saturation pressure throughout the column and mixes with the hydrogen gas. The vapour content throughout the column is calculated in dependence of a constant temperature  $T = 338 \text{ K}$  throughout the column applying Equation (3.7).

To model the column, a discretization into  $N$  nodes is chosen along its height, starting at  $N = 1$  at the top of the column. In each node, the amount of each isotopologue in the gas, liquid and vapour phases is correlated as indicated in Figure 7.2 assuming instantaneous equilibrium. Given the packing material spread along the column all three phases are assumed in contact with each other and the platinum catalyst. With these assumptions, the separation effect of the LPCE column provided in this work is higher than in a real system. For this reason, a translation of into a height of the column cannot reasonably be estimated by this model.

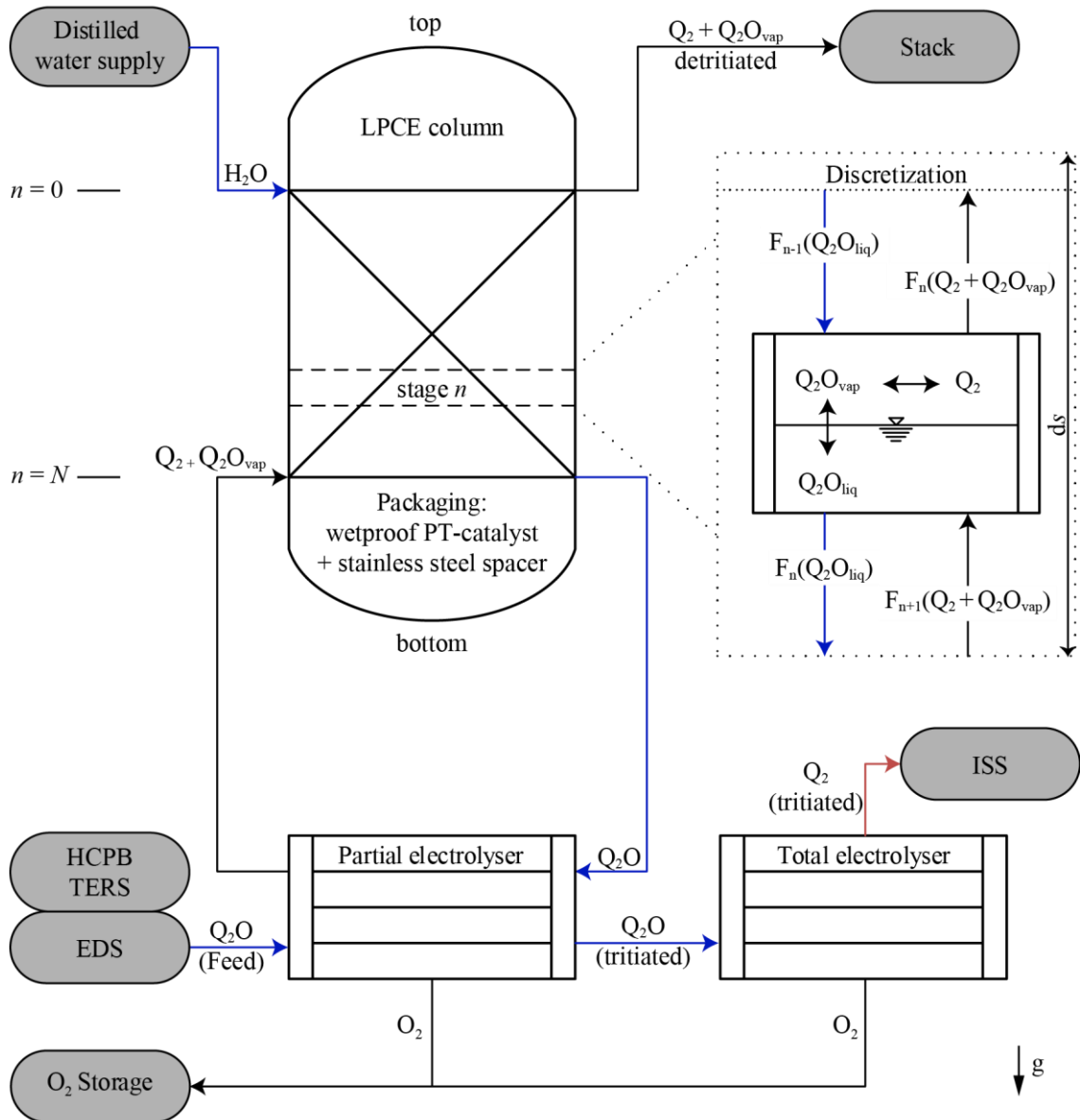


Figure 7.2: Combined Electrolysis and Catalytic Exchange process flowchart comprising a counter flow column and a partial electrolyser as well as the auxiliary boundaries. The discretisation of the Liquid Phase Catalytic Exchange (LPCE) column is indicated at the right highlighting chemical interactions that occur in each node.

The relation of the six isotopologues in three phases considered are:

- Gas↔Gas:** Exchange reaction among gaseous hydrogen molecules occur at equilibrium as described in Section 3.3.1 given the presence of the catalytic surface.
- Gas↔Vapour:** The equilibrium of this reaction is calculated by applying the hydrogen-water interaction elucidated in Section 3.3.3.
- Gas↔Liquid:** Is neglected
- Vapour↔Liquid:** Perfect mixture is assumed among liquid and water vapor.
- Vapour↔Vapour** and (f) **Liquid↔Liquid:** These interactions are already defined as the superposition of interactions (a), (b) and (d). A separate definition of (e) and (f) results in an overdetermined system of equations.

In Busigin [41] the fraction of the exchange reaction (e) is discussed in comparison to (b). The publication concludes that the overall mass transfer can be reasonably simplified to a two-phase mass transfer by neglecting the gas↔liquid interaction, which is applied in this model. Finally, a set of mass balances completes the system of equations by connecting the individual nodes, as given in Equation (7.4).

$$\frac{dI_{\text{total}}(n)}{dt} = F_{\text{gas}}(Q_2, n+1) - F_{\text{gas}}(Q_2, n) + F_{\text{vap}}(Q_2O, n+1) - F_{\text{vap}}(Q_2O, n) + F_{\text{liq}}(Q_2O, n-1) - F_{\text{liq}}(Q_2O, n), \quad (7.4)$$

where  $I_{\text{total}}(n)$  denotes the total inventory of an isotopologue  $Q_2$  in mol regardless of its state in any given node  $1 \leq n \leq N$  of the column. The detritiated gas is also removed at the column top as  $F_{\text{gas}}(Q_2, 1) + F_{\text{vap}}(Q_2O, 1)$ . The in- and output streams from and to the electrolyser set the boundary conditions at the bottom of the column:  $F_{\text{gas}}(Q_2, N+1) + F_{\text{vap}}(Q_2O, N+1)$  and  $F_{\text{liq}}(Q_2O, N)$ , respectively. All streams  $F$  are denoted in the unit mol/s. In steady state, the amount of matter remains constant as described in Equation (7.5).

$$I_{\text{total}}(n) = \sum_{Q_2} I(Q_2 + Q_2O, n) = \text{constant}. \quad (7.5)$$

The distilled feed water is inserted at the column top as  $F_{\text{liq}}(Q_2O, 0)$ . It is assumed that the water is supplied from an external source and consists of distilled water (pure  $H_2O$ ). The amount of water used to continuously flush the column is given in relation to total hydrogen gas inserted at the bottom of the column as the molar feed ratio  $\Lambda$ , defined in Equation (7.6).

$$\Lambda = \frac{F_{\text{feed}}(H_2O)}{\sum_{Q_2} F_{\text{feed}}(Q_2)} = \frac{\sum_{Q_2} F_{\text{liq}}(Q_2O, 0)}{\sum_{Q_2} F_{\text{gas}}(Q_2, N+1) + F_{\text{vap}}(Q_2O, N+1)}. \quad (7.6)$$

To maintain steady state conditions the total of the gas and vapour as well as the liquid stream connecting the nodes are kept constant over time at a flow rate equal to the feed rates inserted at the top and bottom of the column (cf. Equation (7.7)).

$$\Lambda \cdot \sum_{Q_2} F_{\text{gas}}(Q_2, n) + F_{\text{vap}}(Q_2O, n) = \sum_{Q_2} F_{\text{liq}}(Q_2O, n) = F_{\text{feed}}(H_2O). \quad (7.7)$$

The initial condition of liquid water inventory per node is given as a fraction of this value ( $z_{\text{liq}}$ ), which fixes the starting boundary conditions of the column. With Equation (7.6), all streams flowing throughout the column are described in relation to each other and dependence of the input quantity  $\sum_{Q_2} F_{\text{feed}}(Q_2)$ . This way, the column can adapt to a shift in the boundary condition.

The process is operated at a constant temperature  $T_{\text{col}}$  throughout the whole column and a linear pressure profile determined by the total feed gas pressure  $p_{\text{bot}}$  at the bottom node of the column and a set pressure drop per node  $\Delta p_n$  towards the top, which assumes a laminar flow of all phases through the column. The column parameters of the LPCE column and the Wet Scrubber column implemented in the EDS are summarized in Table 7.3.

Table 7.3: Assumed column parameters of the Liquid Phase Catalytic Exchange column in the Water Detritiation System as well as the Wet Scrubber column of the Exhaust Detritiation System.

Description	Variable	LPCE column	Wet Scrubber	Unit
Column temperature	$T_{col}$	338	338	(K)
Bottom node pressure	$p_{bot}$	100000	100000	(Pa)
Pressure loss per node	$\Delta p_n$	100	100	(Pa)
Total node inventory	$I_{total,n}$	6.6	1.0	(mol)
Electrolyser reflux ratio	$C_{reflux}$	0.93	-	(-)
Liquid content	$z_{liq}$	0.5	0.5	(mol%)
Feed ratio	$A$	1	1	(mol/mol)
Number of nodes	$N$	20	15	(-)

### 7.2.3 Electrolyser Modelling

In the electrolyser, water is split into hydrogen and oxygen. For all isotopes, the reaction occurs in parallel but at different reaction rates, which is based on the fact that the required dissociation enthalpy is comparably lower for lighter water molecules [118]. This isotopic effect can be quantified in equilibrium by the separation factor  $K_{elec}$  which weighs the fractions of two individual isotopes A and B in the liquid and the gas phases. Equation (7.8) describes an interpolation of literature data to calculate  $K_{elec}$  in a temperature range of  $274 \text{ K} < T < 333 \text{ K}$ .

$$K_{elec}(AB) = \frac{y_A}{y_B} \cdot \frac{z_B}{z_A} = C_1 \cdot \ln\left(\frac{1000}{T_{elec}}\right) - C_2, \quad (7.8)$$

where  $z$  and  $y$  represent the molar fractions of any two isotopes A and B in water and hydrogen gas in mol/mol, respectively. The constants  $C_1$  and  $C_2$  are listed for all isotope pairings in Table 7.4 for a steel cathode and nickel anode. If the reaction is carried out over a longer period with a constant supply of new feed water, an enrichment of the heavier isotopologues in the liquid phase can be observed.

In the model, the electrolyser is simulated as a single stage that operates in equilibrium and steady state conditions ( $T_{elec} = 300 \text{ K}$ ,  $p_{elec} = 1 \text{ bar}$ ,  $I_{ges} = 5 \text{ mol}$ ) producing three outputs. Firstly, the generated oxygen can be expelled from or reused in a different part of the fuel cycle, for example in the combiner of the Exhaust Detritiation System. Secondly, the detritiated hydrogen gas is recirculated as input to the LPCE column. Finally, the tritiated water accumulating in the liquid phase is transformed to hydrogen in a total electrolyser and transferred to the ISS for further processing. In the fuel cycle simulator this is assumed as a steady state stream withdrawn at the bottom of the electrolyser for the sake of continuity. The quantities of the three outputs are tied to the throughput of the LPCE with a reflux ratio  $C_{reflux}$  defined as the ratio of hydrogen gas output over total input. All oxygen that is produced is removed from the system. The rest represents the steady state output as tritiated liquid water.

Table 7.4: Constants to calculate the separation factors of hydrogen isotopes of the electrolysis process [118].

Separation factor	$C_1$	$C_2$	Unit
$K_{elec}(HD)$	25.678	21.651	(-)
$K_{elec}(HT)$	86.257	80.163	(-)
$K_{elec}(DT)$	2.1042	0.0617	(-)

## 7.2.4 Wet Scrubber Column Modelling Results

Figure 7.3 plots the molar fractions of hydrogen gas  $y_{\text{gas}}(\text{Q}_2)$  and water vapour  $y_{\text{vap}}(\text{Q}_2\text{O})$  of the separate gas and vapour streams  $F_{\text{gas}}$  and  $F_{\text{vap}}$  over the height of the Wet Scrubber column discretized into nodes, respectively. In both, the gas and the vapour phase a similar phenomenon can be observed: protium dominates the column content and non- $\text{H}_2$  isotopologues are increasingly stripped towards the column top ( $n \rightarrow 1$ ). This can be attributed to the separation effect quantified in Equation (3.11) favouring lighter isotopes in the gas phase. The correlation leads to two observable effects: (i) in combination with the abundance of protium in the column, the mixture isotopologues HD and HT are found in larger quantity than their non-protium counterparts and (ii) the fraction of heavier isotopes is up to a magnitude higher in the vapour phase compared to the gas phase. Because of both these effects, residual tritium in the exhaust stream is found almost exclusively in the form of HTO vapour gas.

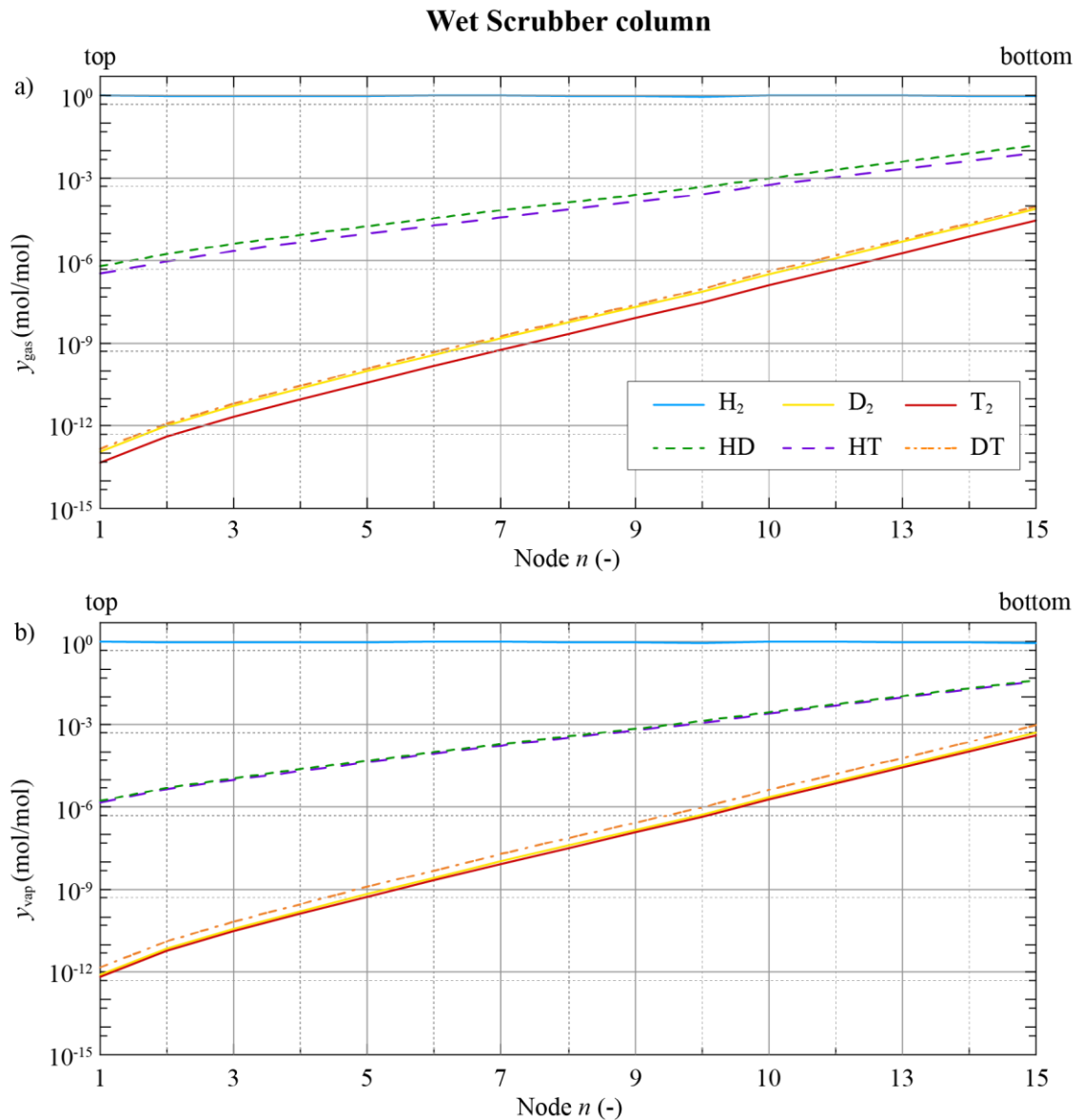


Figure 7.3: Concentration profile of hydrogen isotopologues in a) the gas and b) the vapour phase within the Wet Scrubber column discretized into  $N = 15$  nodes along the height of the column from top ( $n = 1$ ) to bottom ( $n = 15$ ).

## 7.2.5 Water Detritiation System Modelling Results

The molar fractions of hydrogen gas  $y_{\text{gas}}(\text{Q}_2)$  and water vapour  $y_{\text{vap}}(\text{Q}_2\text{O})$  within the LPCE column are plotted in Figure 7.4 for the separate gas and vapour streams  $F_{\text{gas}}$  and  $F_{\text{vap}}$ . Similar to the Wet Scrubber column, non-protium isotopes are progressively removed from bottom to top ( $20 \rightarrow n \rightarrow 1$ ). Again, the column content consists almost exclusively of pure protium and most of the heavy isotopes accumulate in the liquid and vapour phases.

Deuterated species (DQ) are featured more prominently in the LPCE column in comparison to the Wet Scrubber column given that the fraction of deuterium in the input is larger  $y_{\text{in,LPCE}}(\text{D}) = 9.6 \cdot y_{\text{in,WS}}(\text{D})$ .

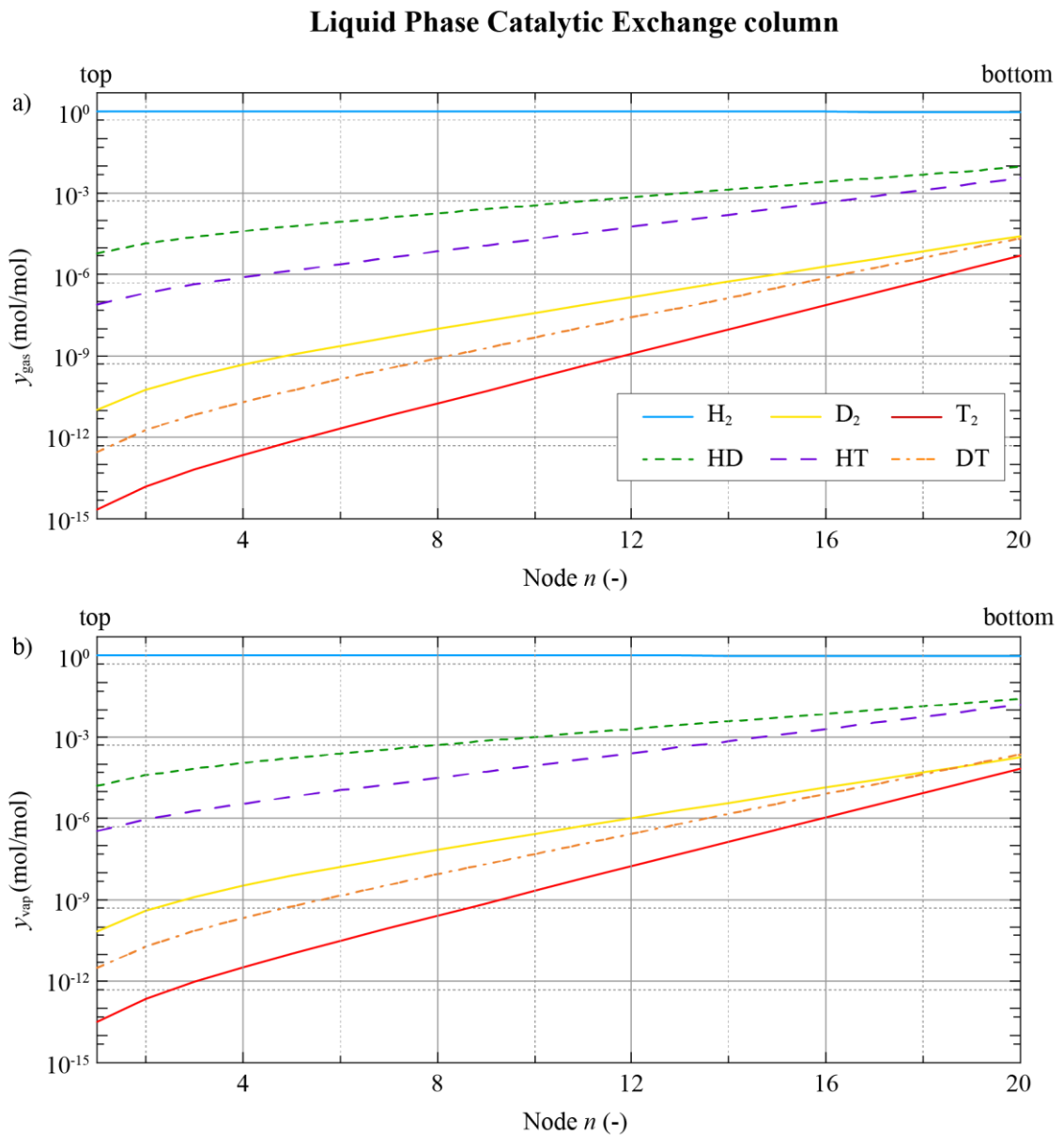


Figure 7.4: Concentration profile of hydrogen isotopologues in the a) gas and b) vapour phase within the of Liquid Phase Catalytic Exchange column discretized into  $N = 20$  nodes along the height of the column from top ( $n = 1$ ) to bottom ( $n = 20$ ).



Tritiated species are reduced to remarkable low concentrations at the top of the column  $n = 1$  near the exhaust to  $y_{\text{vap}}(\text{T}_2\text{O}, 1) < 1 \cdot 10^{-12} \text{ mol/mol}$ .

The input and output streams of the CECE setup are listed in Table 7.5. The large throughputs of the electrolyser and LPCE column stem from the reflux ratio  $C_{\text{reflux}}$ , whereby the gas output of the electrolyser equals 93 mol% of its input.

The heavy isotopes accumulate in the electrolyser with a liquid composition of H : D : T = 88 : 5.5 : 6.5. Given, the high fraction of protium most heavy isotopes are bound in the form HQ isotopologues. The remaining fraction of the input  $1 - C_{\text{reflux}} \cong 7 \text{ mol\%}$  is then transformed from water to molecular hydrogen in the total electrolyser to form one of the input streams to the ISS ( $F_{\text{elec}}$  ⑳).

The detritiation factor of the CECE system block ( $DF_{\text{WDS}}$ ) is calculated as the ratio of the tritiated input ⑲+㉑ over the LPCE gas output ㉒.

$$DF_{\text{WDS}} = \frac{0.191}{4.00 \cdot 10^{-6}} \approx 47550. \quad (7.9)$$

This corresponds to an annual tritium release of 0.208 g/a in the form of tritiated gas and 0.128 g/a as tritiated water vapour. The HT/HTO mixture isotopologue constitutes the majority of the tritium output.

Table 7.5: Calculated throughputs and compositions upstream and downstream the three subsystems of the Exhaust Detritiation system block for the Reference Design Point.

Stream	WDS Input		Electrolyser Output		LPCE Output		Unit
	⑲+㉑	Feed water	Gas	Water	Gas ㉒	Water	
$F$	17.29	38.76	40.12	2.95	53.10	25.78	(Pa · m <sup>3</sup> /s)
$y(\text{H}_2)$	—	—	94.74	—	73.00	—	(mol%)
$y(\text{HD})$	—	—	1.28	—	$4.81 \cdot 10^{-4}$	—	(mol%)
$y(\text{D}_2)$	—	—	$5.24 \cdot 10^{-3}$	—	$9.41 \cdot 10^{-10}$	—	(mol%)
$y(\text{HT})$	—	—	0.59	—	$5.74 \cdot 10^{-6}$	—	(mol%)
$y(\text{DT})$	—	—	$5.28 \cdot 10^{-3}$	—	$2.43 \cdot 10^{-11}$	—	(mol%)
$y(\text{T}_2)$	—	—	$1.39 \cdot 10^{-3}$	—	$1.63 \cdot 10^{-13}$	—	(mol%)
$y(\text{H}_2\text{O})$	96.07	100	2.64	77.89	27.00	95.86	(mol%)
$y(\text{HDO})$	1.71	0	0.32	9.43	$4.99 \cdot 10^{-4}$	2.53	(mol%)
$y(\text{D}_2\text{O})$	$4.30 \cdot 10^{-2}$	0	$1.18 \cdot 10^{-2}$	0.35	$2.44 \cdot 10^{-9}$	$1.77 \cdot 10^{-2}$	(mol%)
$y(\text{HTO})$	2.05	0	0.76	10.87	$9.35 \cdot 10^{-6}$	1.57	(mol%)
$y(\text{DTO})$	$8.03 \cdot 10^{-2}$	0	$2.99 \cdot 10^{-2}$	0.88	$9.4 \cdot 10^{-11}$	$2.26 \cdot 10^{-2}$	(mol%)
$y(\text{T}_2\text{O})$	$3.88 \cdot 10^{-2}$	0	$1.98 \cdot 10^{-2}$	0.58	$8.76 \cdot 10^{-13}$	$6.94 \cdot 10^{-3}$	(mol%)

## 7.3 Isotope Separation

Task of the Isotope Separation System (ISS) is to modify the hydrogen composition and concentrate individual isotopes to a degree of high purity for the purpose of subsequent exhaust or reuse. To accomplish this task, Cryogenic Distillation (CD) columns are used in conjunction with equilibrators in practical applications nowadays. This approach is employed in the ISS of DEMO. The separation itself is obtained within one or multiple CD columns while equilibrators are used to modify the composition of isotopologues in order to minimize fraction of mixture isotopologues. Over time lighter isotopes accumulate in the gaseous phase and strive towards the column top, whereas its heavier counterparts are predominantly found in liquid form towards the bottom of the column. A sharp concentration profile forms over the nodes and the isotopologues can be extracted from both ends at high purity.

### 7.3.1 Cryogenic Distillation Boundary Conditions and Setup

A complete separation of all six hydrogen isotopologues would require a complex 5-column setup, representing a facility of great scale and tritium inventory. In practice, the systems size is reduced by lumping outputs that match the same requirements [119][120]. For the DEMO ISS a three-column setup is proposed, which produces three outputs:

H <sub>2</sub>	-	discharge	Protium and HD can both be emitted via the stack, provided they are sufficiently detritiated and the fraction of HD remains small.
HD	-		
D <sub>2</sub>	-	pure deuterium	This stream allows for fine-tuning of the fuel composition.
HT	-	concentrated tritium	Tritiated isotopologues accumulate in the liquid phase. High fractions of DT are not detrimental to the fuel composition. The fraction of HT, however, must be minimized via equilibrators.
DT	-		
T <sub>2</sub>	-		

Input to the ISS columns are pure hydrogen mixtures stemming from different parts of the fuel cycle, each with a distinct isotope composition listed for the RDP in Table 7.6. Consequently, they are introduced into the process at different components.

As a notable detail in the design of Cryogenic Distillation, any substantial change of expected boundary conditions - concerning input throughput or quantity - entails a complete reconfiguration of the column setup, as they are intrinsically optimized for a single point of operation. Therefore, the three-column layout presented in Figure 7.5 is used to cope with the steady state inputs given by the Reference Design Point.

Table 7.6: Origin, throughput and composition of the Isotope Separation System inputs for the Reference Design Point.

#	Source	Description	Quantity	H:D:T ratio
①⑥	IRPR	Low tritium waste stream	16.13 Pa·m <sup>3</sup> /s	2:82:16
②①	WDS	Accumulated tritium from CECE	2.95 Pa·m <sup>3</sup> /s	88:6:6
③②	TERS (HCPB)	Protium purge gas with breed HT	356.58 Pa·m <sup>3</sup> /s	99:0:1
③④	CPS (HCPB)	Protium coolant with permeated HT	1.55 Pa·m <sup>3</sup> /s	99:0:1
	Σ	Sum of inputs	377.21 Pa·m <sup>3</sup> /s	95:4:1

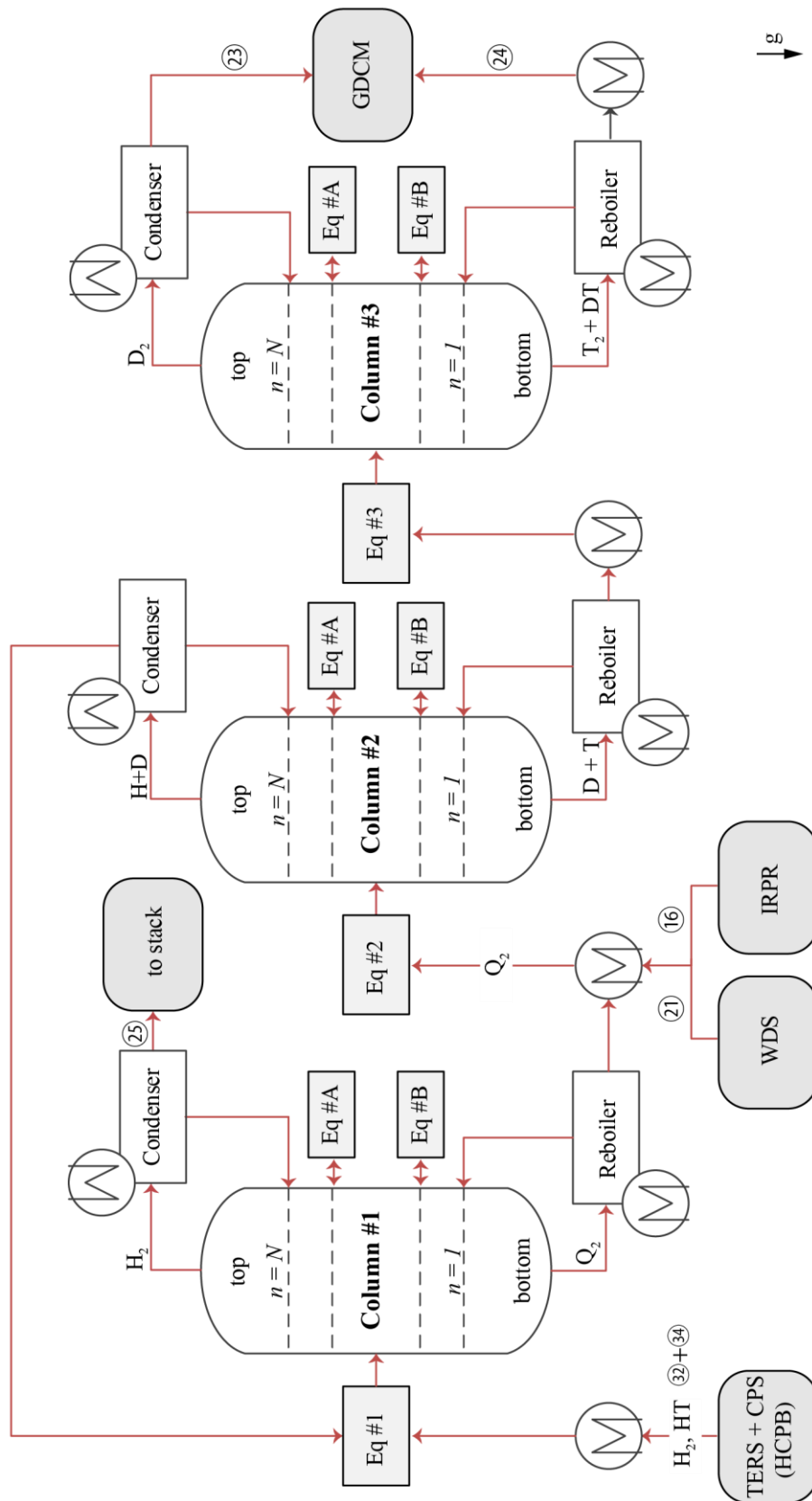


Figure 7.5: Flowchart of the Cryogenic Distillation column setup including three intermediate equilibrators (Eq #1, Eq #2 and Eq #3), the three columns, each equipped with two built-in equilibrators (Eq #A and Eq #B) as well as the input and output streams as implemented into the fuel cycle model.

---

Each of the three CD columns consists of a central column with a partial condenser at the top and reboiler at the bottom. Both the condenser and reboiler produce an output stream of the column. Lighter isotopologues concentrate in the condenser and exit the respective column from there as the top product in gaseous form. Conversely, heavy isotopologues accumulate as liquid in the reboiler and constitute the bottom product of the column. In addition to the three equilibrators (Eq #1, Eq #2 and Eq #3) placed upstream, each column is equipped with two built-in equilibrators (Eq #A and Eq #B), which extract and refeed at two distinct points to reduce the column inventory of mixture isotopologues. Heat exchangers are placed up- and downstream of each column to adjust the temperature of the streams. The setup parameters implemented in the fuel cycle simulator for the RDP are summarized in Table 7.7. The column inventories as well as number of nodes, and position of feed and equilibrator nodes is the result of an iterative process with five minimization criteria (i)-(v) of descending importance:

- (i) tritium output to environment (in  $F_{ISS}$  ②⑤),
- (ii) the ISS tritium inventory,
- (iii) accumulation of mixture isotopologues - especially HT - throughout the column,
- (iv) the amount of impurities in output streams (non-D<sub>2</sub> in  $F_{D_2}$  ②③, non-T<sub>2</sub> in  $F_{T_2}$  ②④ and non-H<sub>2</sub> in  $F_{ISS}$  ②⑤) as well as
- (v) the reflux between columns.

The first column (Column #1) is dedicated to the separation of protium from other isotopes to release-grade purity in the top product. The feed stream - consisting of heavily protonated input from the second column as well as the purge gas from the Outer Fuel Cycle ( $F_{to\_ISS}$  ③② and  $F_{CPS}$  ③④) - passes through the first external equilibrator (Eq #1) and is fed into the middle of the column. This ensures that H<sub>2</sub> (and HD) in the exhaust stream may leave at the condenser sufficiently detritiated and satisfy criterion (i).

The product of the first column reboiler is fed to the second column (Column #2) in conjunction with the input from the IRPR and WDS system blocks ( $F_{low-trit}$  ①⑥ and  $F_{WDS}$  ②②). Again, the mixture passes an equilibrator (Eq #2) prior to injection. The main separation between reusable and expandable hydrogen isotopes takes place in the second column. Lightweight isotopologues are returned to the first column as product extracted at the top, whereas heavier isotopologues are extracted at the bottom and forwarded to the third column. To reduce reflux between the first and second column as per criterion (v), the fraction of tritiated species in the top product must remain very low to avoid reflux ratios. Similarly, all protium in the reboiler product will eventually end up in the top product of the third column and degrade the purity of the deuterium there.

The third column (Column #3) is tasked with the separation of D and T. A large column setup, with many separation nodes is required for this, as the separation efficiency of these isotopes is considerably smaller. However, a large column entails a considerable tritium inventory, which accumulates in the liquid phase. For this reason, the throughputs of the second and third column are considerably smaller than of the first column. Pure deuterium is withdrawn from the condenser of the third column. A mixture of tritium and DT represent the third output stream of the ISS setup. Both outputs are sent to the storage beds.

Table 7.7: Pre-defined column parameters of the three cryo-distillation columns of the Isotope Separation System.

Parameter	Indices	Column #1	Column #2	Column #3	Unit
Number of nodes	$N$	50	55	90	(-)
Feed node	$n_{\text{feed}}$	21	35	55	(-)
Eq #A node	$n_{\text{Eq \#A}}$	19	6	39	(-)
Eq #B node	$n_{\text{Eq \#B}}$	41	49	70	(-)
Equilibrator temperature	$T_{\text{eq}}$	27	27	27	(K)
Extraction ratio	$C_{\text{ext}}$	0.988	0.30	0.60	(-)
Condenser temperature	$T_{\text{top}}$	24	26	25	(K)
Reboiler temperature	$T_{\text{bot}}$	20	22	21	(K)
Column pressure	$p$	101325	101325	101325	(Pa)
Condenser cooling	$H_{\text{ext}}$	2500	1000	1500	(W)
Liquid inventory per node	$I_{\text{liq}}(n)$	5.0	5.0	2.5	(mol)

### 7.3.2 Cryogenic Distillation Modelling

Each column is discretized into  $N$  nodes - numerated in ascending order from top to bottom - and each assumed in equilibrium at all conditions. Three equations are solved for every node to model the column: the mass and energy balance (Equations (4.4) and (3.8), respectively) as well as the vapour liquid equilibrium. The modelling procedure of the latter follows the approach elucidated in Section 3.3. The mass balance for a given isotopologue  $Q_2$  and node  $1 \leq n \leq N$  is calculated with Equation (7.10) for the liquid inventory  $I_{\text{liq}}$ , where the bulk hydrogen resides - given its higher density.

$$\frac{\delta I_{\text{liq}}(Q_2, n)}{\delta t} = \frac{F_{\text{liq}}(Q_2, n-1) - F_{\text{liq}}(Q_2, n) + F_{\text{ext}}(Q_2, n) + F_{\text{vap}}(Q_2, n+1) - F_{\text{vap}}(Q_2, n)}{\delta t} \quad (7.10)$$

where  $F_{\text{liq}}(n)$  and  $F_{\text{vap}}(n)$  denote the liquid and vapour output streams of node  $n$ , both in mol/s.  $F_{\text{ext}}$  represents an external stream added to this particular node also in mol/s. This occurs at the feed-node  $n_{\text{feed}}$  and the two equilibrator nodes  $n_{\text{Eq \#A}}$  and  $n_{\text{Eq \#B}}$ . The heat balance is defined similarly for every isotopologue  $Q_2$  and node  $0 \leq n \leq N$  as derived in Equation (3.8). A temperature profile forms over the height of the column between the values of  $T_{\text{top}}$  in the condenser and  $T_{\text{bot}}$  in the reboiler. Following the steady state assumption, the total liquid inventory remains constant over time.

The partial condenser and reboiler constitute the ultimate nodes 0 and  $N$  of the column model, respectively. The extraction ratio  $C_{\text{ext}}$  indicates the ratio of the total condenser output to feed stream. A simple mass balance around the column - given in Equation (7.11) - fixes the output of the condenser by the steady state assumption for the entire column.

$$\sum_n F_{\text{ext}}(Q_2, n) = F_{\text{liq}}(Q_2, N) + F_{\text{vap}}(Q_2, 0) = F_{\text{vap}}(Q_2, 0) \cdot C_{\text{ext}} \quad (7.11)$$

The reflux ratio in each column is given by the condenser duty  $H_{\text{ext}}$  of the partial condenser at the top of the column, which fixes the liquid output  $F_{\text{liq}}(Q_2, 0)$  as described in Equation (7.12).

$$F_{\text{liq}}(Q_2, 0) \cdot h_{\text{vap}} = H_{\text{ext}}, \quad (7.12)$$

where the heat of vaporization  $h_{\text{vap}} = 4493.6 \text{ J/mol}$  is taken for pure protium from [17]. With these equations, the numerical solver calculates the concentration profile of all hydrogen isotopes in the liquid and the vapour phase.

### Equilibrator modelling

The equilibrators are modelled as a single node process with the equilibrium constants derived in Equations (3.3), (3.4) and (3.5). This is complimented by three mass balances for each isotope. Equation (7.13) exemplifies the mass balance of tritium with the input and output fractions  $y_{\text{in}}(Q_2)$  and  $y_{\text{out}}(Q_2)$  in mol/mol. A numerical solution is produced by the model in dependence of the input composition and the temperature  $T_{\text{eq}}$ .

$$y_{\text{in}}(T_2) + 0.5 \cdot (y_{\text{in}}(\text{HT}) + y_{\text{in}}(\text{DT})) = y_{\text{out}}(T_2) + 0.5 \cdot (y_{\text{out}}(\text{HT}) + y_{\text{out}}(\text{DT})). \quad (7.13)$$

Assuming a low equilibrator temperature, the presence of equilibrators can limit the fraction of mixture isotopologues in output streams and column inventories of the ISS setup.

### 7.3.3 Cryogenic Distillation Modelling Results

To establish steady state conditions after a shift of ISS parameters or input boundary conditions the model requires up to 10000 iteration steps - depending on the induced perturbation. Each iteration step represents a second in the model which is calculated in  $(10 \dots 50) \times$  real time. The columns are initialized with a quantity and composition close to the steady state to reduce computing time.

The following graphs show the liquid concentration profiles of the six hydrogen isotopologues within the three Cryogenic Distillation columns (in order of Column #1, Column #2 and then Column #3) for the steady state throughput given in Table 7.1. The profile for each column is shown over its height discretized into nodes  $0 \leq n \leq N$ , with the partial condenser at the top ( $n = 0$ ) and partial reboiler at the bottom ( $n = N$ ) of the column. Both the linear and logarithmic scale are displayed. The former illustrates the overall composition of the hydrogen content throughout each column and the latter accentuates the separation effect and the influence of the feed node position and built-in equilibrators Eq #A and Eq #B. Thereafter Table 7.8 and Table 7.9 summarize the input and output streams of all ISS subsystems.

Generally, isotopologues of lower molar mass are found in higher concentrations towards the top of each column and dominate the column output at the condenser. Inversely, heavy isotopologues accumulate in the reboiler. The phenomenon is based on the different boiling temperatures and quantified in the model by Equation (3.7). For this reason, as the middle isotope, deuterium naturally accumulates and dominates the liquid inventory in all columns.

The liquid concentration profile of the first Cryogenic Distillation column - dedicated to the enrichment of protium - is shown in Figure 7.6. The column can be split into two sections given a feed stream at  $n = 21$ , containing deuterium and large quantities of protium: A protium-

dominated section above the feed node ( $0 \leq n < 21$ ) and a deuterium-dominated section below ( $21 < n \leq 50$ ). In between, given the presence of both isotopes in high concentrations a local peak of the mixture isotopologue HD ( $z_{HD} \approx 31 \text{ mol\%}$  at  $n = 16$ ) can be observed. Isotopologues heavier than  $D_2$  only occur in considerable quantities below Eq #B with a maximum concentration of  $z_{DT} = 32.67 \text{ mol\%}$  and  $z_{DT} = 14.3 \text{ mol\%}$  at  $n = 50$ .

The logarithmic plot in Figure 7.6 b) displays to which degree the tritiated species are stripped in the protium-dominated section of the column, with the concentrations  $z_{T_2} < z_{DT} < z_{HT} = 5.66 \cdot 10^{-6} \text{ mol\%}$  at  $n = 0$ . In the lower half of Column #1 - within the deuterium-dominated section, protonated species are found in progressively lower concentrations towards the bottom of the column ( $n \rightarrow 50$ ). In steady state, Column #1 contains 250 mol of hydrogen with a composition of  $H : D : T = 34 : 62 : 4$ . The 57.08 g of tritium, present in the form of all three isotopologues (QT), in Column #1 produce a decay heat of 18.50 W.

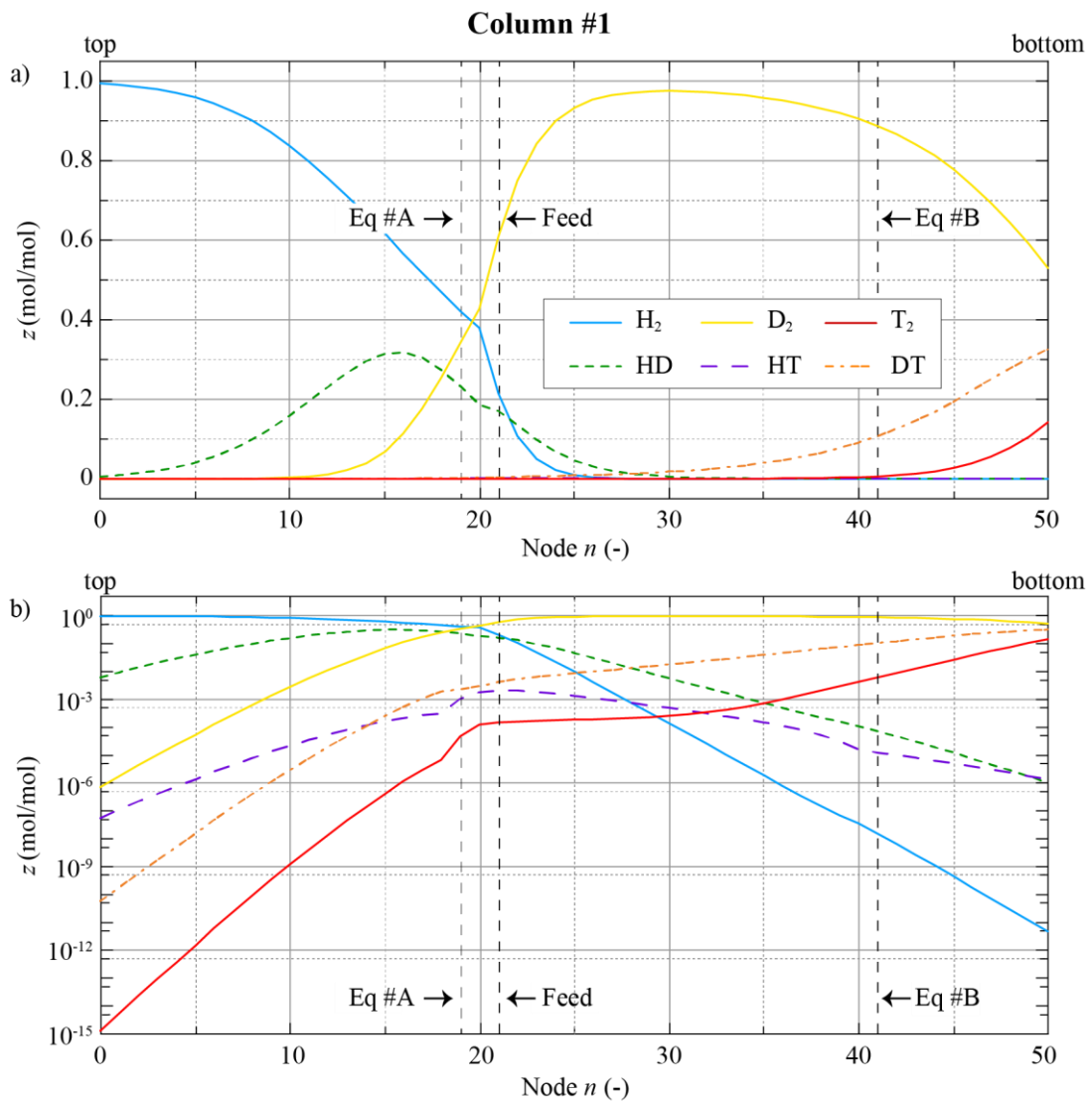


Figure 7.6: Liquid concentration profile of the six hydrogen isotopologues throughout Column #1 discretized over the height into  $n = 50$  nodes from top  $n = 0$  to bottom  $n = 50$ . **Top:** as a linear plot. **Bottom:** as a logarithmic plot. The feed node (Feed) and both built-in equilibrator nodes (Eq #A and Eq #B) are indicated by a dashed line.

The two built-in equilibrators in each column limit the concentration of the mixture isotopologues and are deliberately placed to target the HD and DT peaks within each column. The concentration of HT in particular is inhibited to a strong degree by the presence of equilibrators, which is based on the small equilibrium constant  $K_{HT} \ll 1$  as per Equation (3.4). The phenomenon can be observed in all three columns and the highest fraction of HT obtained throughout the ISS setup occurs close to the feed in the first column at  $z_{HT} = 0.21$  mol% at  $n = 22$ .

Table 7.8 lists the input and output streams of Column #1 as well as of equilibrators Eq #1 and Eq #2. A large fraction of the total ISS throughput is emitted via the condenser product of this column to dispatch of the large quantities of protium purge gas from the HCPB Breeding Blanket. The exhaust gas contains a small fraction of HD ( $z_{HD} \approx 0.6$  mol%) and close to no tritium.

To quantify the efficiency of detritiation in the ISS setup, the detritiation factor ( $DF_{ISS}$ ) is calculated. In this case it is given by the ratio of the tritium content in the input streams (⑩, ⑪, ⑫ and ⑬) over the tritium content in the output stream ⑭ in Equation (7.14).

$$DF_{ISS} = \frac{4.16}{1.02 \cdot 10^{-5}} \approx 406560. \quad (7.14)$$

The bulk detritiation occurs in the first column. With a similar calculation, one obtains from the tritium ratio of the input of Column #1 over the exhaust stream  $DF_{Column\ #1} \approx 131930$ . The tritium input stream of Column #1 is equivalent to the tritium output stream of Eq #1 given in Table 7.8 as  $F(T) = 1.34$  Pa · m<sup>3</sup>/s.

Although, these factors may appear very high, this corresponds to an annual tritium loss of 0.857 g/a, predominantly in the form of HT. Thereby, the tritium loss rate of the Isotope Separation System alone represents a contribution to the annual release, which lies between the annual ITER thresholds for regular (0.6 g/a) and heavy maintenance (2.5 g/a) operation.

Table 7.8: Throughput and composition of the of the Isotope Separation System input as well as the calculated output of equilibrator #1, the first Cryogenic Distillation column and equilibrator #2. Streams ⑫ and ⑬ are given in the Appendix A1. The values marked in grey are used in Equation (7.14) to calculate the detritiation factors.

Stream	Input Feed ⑩+⑪+⑫+⑬	Calculated results				Unit
		Eq #1 out	Column #1		Eq #2 out	
			top ⑭	bottom		
$F(H)$	359.70	359.72	359.71	$5.28 \cdot 10^{-6}$	2.92	(Pa · m <sup>3</sup> /s)
$F(D)$	13.35	4.12	1.09	3.04	16.39	(Pa · m <sup>3</sup> /s)
$F(T)$	4.16	1.34	$1.02 \cdot 10^{-5}$	1.34	4.16	(Pa · m <sup>3</sup> /s)
$\Sigma F(Q_2)$	377.21	365.18	360.80	4.38	23.47	(Pa · m <sup>3</sup> /s)
$y(H_2)$	94.92	97.34	99.40	$4.58 \cdot 10^{-10}$	6.45	(mol%)
$y(HD)$	$7.37 \cdot 10^{-2}$	1.91	0.60	$1.05 \cdot 10^{-4}$	11.15	(mol%)
$y(D_2)$	3.50	0.10	$7.13 \cdot 10^{-5}$	53.00	52.36	(mol%)
$y(HT)$	0.80	0.41	$5.66 \cdot 10^{-6}$	$1.36 \cdot 10^{-4}$	0.79	(mol%)
$y(DT)$	$6.90 \cdot 10^{-3}$	0.14	$5.65 \cdot 10^{-9}$	32.67	23.84	(mol%)
$y(T_2)$	0.70	$9.45 \cdot 10^{-2}$	$1.30 \cdot 10^{-13}$	14.33	5.41	(mol%)



The concentration of hydrogen isotopologues in Column #2 is plotted in Figure 7.7. The content of the column is dominated by deuterium, with significant fractions of protium or tritium towards both ends of the column. Both isotopes are extracted there in conjunction with large fractions of deuterium and deuterated isotopologues and fed to the other two columns. The 275 mol of hydrogen in the column are represented in a ratio of H : D : T = 2 : 94 : 4. The tritium inventory of 58.85 g produces a total decay heat of 19.07 W.

A comparison to the logarithmic plot reveals the pronounced protium stripping effect of the column section below the feed node ( $n > 35$ ). Downstream the reboiler, the fraction of protium accounts for only  $z_{\text{H}} = 3 \cdot 10^{-4}$  mol% at  $n = 55$  of the column output to Eq #3. On the opposite end, the detritiation efficiency of the second column remains at a modest level in comparison to the first column, given the high condenser temperature of  $T_{\text{top}} = 26$  K.

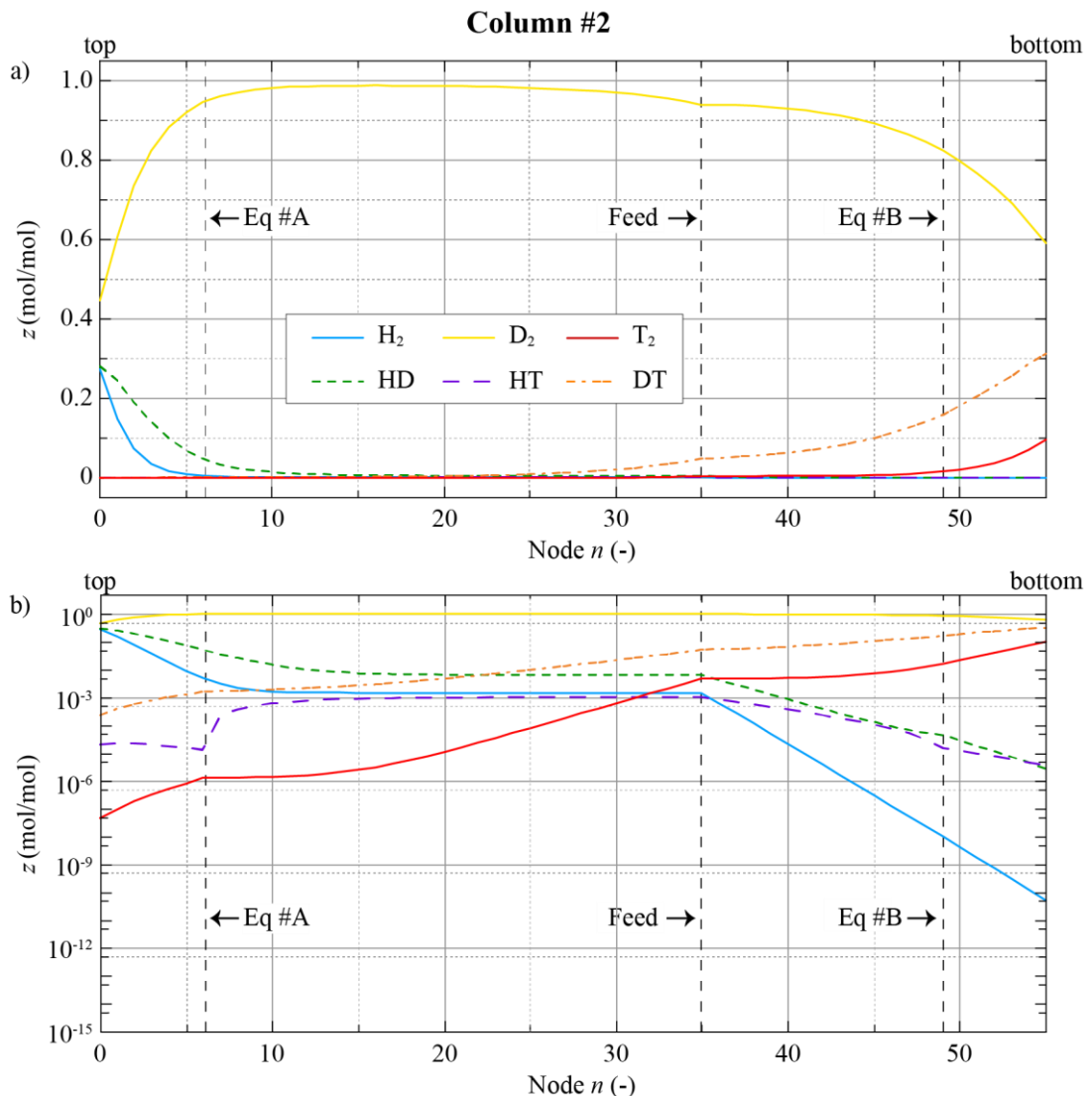


Figure 7.7: Liquid concentration profile of the six hydrogen isotopologues throughout Column #2 discretized over the height into  $n = 55$  nodes from top  $n = 0$  to bottom  $n = 55$ . **Top:** as a linear plot. **Bottom:** as a logarithmic plot. The feed node (Feed) and both built-in equilibrators (Eq #A and Eq #B) are indicated by a dashed line.

The third column, tasked with the separation of the two heavy hydrogen isotopes, accumulates the largest amount of tritiated species in liquid form at its bottom as can be seen in Figure 7.8. To limit the overall column hydrogen content, the hydrogen inventory per node is constrained to  $I_{\text{liq}}(n) = 2.5 \text{ mol}$ , half of the value assumed in the other columns. Still, the column contains considerable amounts of tritium (459.02 g) producing a decay heat of 148.8 W.

In total Column #3 holds 225 mol of hydrogen, distributed among the isotopes as H : D : T =  $10^{-6} : 85 : 15$ . This results from the light isotope being stripped in the previous column. The logarithmic plot in Figure 7.8 b) displays how the fraction of protonated species remains low over the whole column with a peak of  $z_{\text{HD}} = 8.11 \cdot 10^{-4} \text{ mol}\%$  at the top of the column ( $n = 0$ ). Additionally, T2 and DT are progressively stripped towards the top of the column ( $n \rightarrow 0$ ).

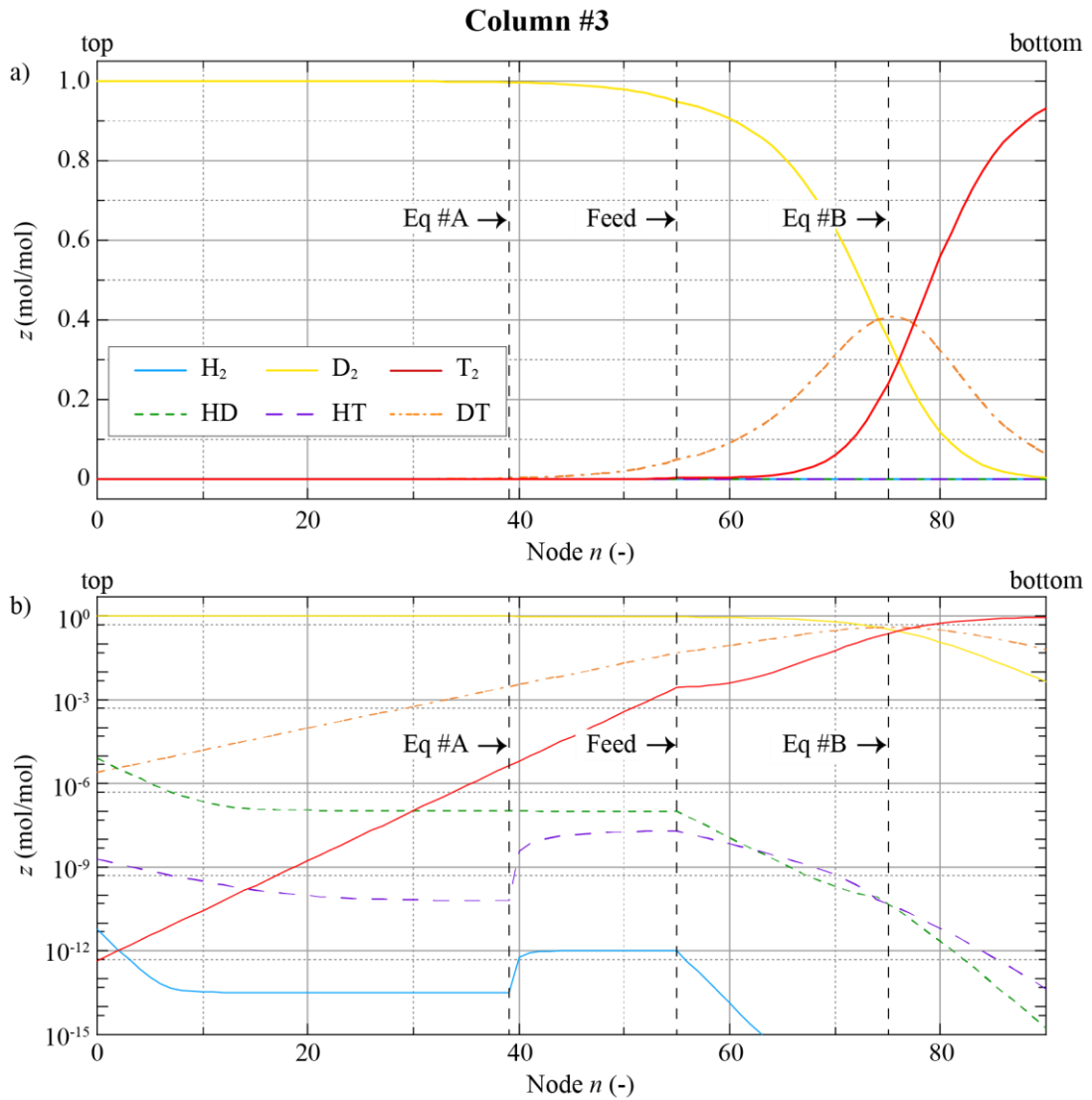


Figure 7.8: Liquid concentration profile of the six hydrogen isotopologues throughout Column #3 discretized over the height into  $n = 90$  nodes from top  $n = 0$  to bottom  $n = 90$ . **Top:** as a linear plot. **Bottom:** as a logarithmic plot. The feed node (Feed) and both built-in equilibrator nodes (Eq #A and Eq #B) are indicated by a dashed line.

Particularly, the design of this column must consider the two design criteria of a low tritium inventory - favouring a small tritium stripping section - and the obtained tritium purity in the reboiler - favouring a large tritium stripping section. Given the priority assignment with regards to the minimization criteria of a low tritium inventory (ii) and output purity (iv), the feed node is positioned in the lower half of the column ( $n_{\text{Feed}} = 55$ ).

Given the large fraction of deuterium in the input stream ( $z_D:z_T = 75:25$ ), Column #3 is split into a large deuterium enriched section above ( $n < 75$ ) and a smaller tritium section below ( $n > 75$ ). In-between the two sections, a distinct peak of the DT isotopologue forms close to the bottom of the column at ( $z_{DT} \approx 41$  mol% at  $n = 75$ ). In this context, Eq #A limits the formation of mixture isotopologues in the upper section  $n < 40$  of the column, whereas Eq #B minimizes the formation of DT in the bottom section of the column by placing it exactly in the node with the DT peak ( $n = 75$ ). Still, given the proximity to the bottom, the mixture isotopologue is represented in the bottom product with a considerable fraction of 4.87 mol%. If the column is designed differently to move the DT peak further to the bottom ( $n \rightarrow 90$ ), the fraction of deuterium in the tritium enriched output increases. Conversely, if the DT peak is aimed higher within the column ( $n \rightarrow 0$ ), the tritium inventory rises. To design the column and solve this optimization problem, the tritium inventory is constrained to  $I_{\text{Column \#3}} < 500$  g and the deuterium fraction in the bottom product is limited to  $z_D < 5$  mol%.

The outputs of the condenser and evaporator nodes of Column #2 and Column #3 as well as of the third equilibrator Eq #3 in between are shown in Table 7.9. Deuterium is isolated by this setup at very high purities ( $z_{D_2} = 99.999$  mol%) from the condenser of the third column. The bottom product is less pure ( $z_D = 3.6$  mol%), which stems from DT peak close to the bottom of the third column.

Table 7.9: Throughput and composition of the second and third Cryogenic Distillation column and auxiliary systems.

Stream	Column #2		Eq #3	Column #3		Unit
	top	bottom	out	top ②③	bottom ②④	
$F(\text{H})$	2.91	$4.93 \cdot 10^{-5}$	$4.93 \cdot 10^{-5}$	$4.93 \cdot 10^{-5}$	$6.55 \cdot 10^{-14}$	(Pa · m <sup>3</sup> /s)
$F(\text{D})$	4.13	12.27	12.27	12.15	0.12	(Pa · m <sup>3</sup> /s)
$F(\text{T})$	$8.56 \cdot 10^{-4}$	4.16	4.16	$1.96 \cdot 10^{-5}$	4.16	(Pa · m <sup>3</sup> /s)
$\Sigma F(Q_2)$	7.04	16.43	16.43	12.16	4.27	(Pa · m <sup>3</sup> /s)
$y(\text{H}_2)$	27.36	$4.55 \cdot 10^{-9}$	$1.42 \cdot 10^{-8}$	$6.18 \cdot 10^{-10}$	$< 1 \cdot 10^{-20}$	(mol%)
$y(\text{HD})$	28.07	$2.34 \cdot 10^{-4}$	$5.55 \cdot 10^{-4}$	$8.11 \cdot 10^{-4}$	$1.01 \cdot 10^{-13}$	(mol%)
$y(\text{D}_2)$	44.55	43.42	58.41	99.9989	0.26	(mol%)
$y(\text{HT})$	$1.93 \cdot 10^{-3}$	$3.89 \cdot 10^{-4}$	$4.82 \cdot 10^{-5}$	$2.33 \cdot 10^{-7}$	$2.97 \cdot 10^{-12}$	(mol%)
$y(\text{DT})$	$2.24 \cdot 10^{-2}$	37.51	32.55	$3.22 \cdot 10^{-4}$	4.87	(mol%)
$y(\text{T}_2)$	$4.28 \cdot 10^{-6}$	19.07	9.04	$6.92 \cdot 10^{-11}$	94.87	(mol%)

---

## 7.4 Storage Solutions

Intermediary buffer tanks are employed in different parts of the fuel cycle and are vital part of IRPR or GDCM systems. These gas storage tanks for short-to midterm dwell times are assumed as stainless steel vessels. Treatment against protium outgassing from walls is required.

### 7.4.1 Getter Bed Boundary Conditions and Setup

For the purpose of long-term storage of the hydrogen - in particular of tritium - this work adapts the established approach to utilise depleted uranium storage beds [121]. In the form of  $UQ_3$ , hydrides exhibit considerably reduced loss rates in comparison to its volatile pure gaseous counterpart.

Although hydrogen is stored safely in this manner, the response times of such getter beds is not suited to cope with the transient behavior implied by the pulsed operation. Consequently, the solid absorption beds are not integrated into the immediate hydrogen path through the three-loop architecture of the fuel cycle. Instead, they serve as macroscopic sink or source term of hydrogen species.

Three storage bed subsystems can be distinguished: (i) the storage of pure deuterium or a heavily deuterated hydrogen compositions ( $F_{D_2}$  ②③), (ii) the storage of pure tritium or heavily tritiated hydrogen compositions ( $F_{T_2}$  ②④) and (iii) the storage of all hydrogen circulated in the fuel cycle independent of composition in a case of emergency or an extended shutdown period.

These long-term storage beds are connected to the fuel cycle via the GDCM system via stream  $F_{top-up}$  ⑩.

### 7.4.2 Getter Bed Modelling and Results

The equilibrium pressure of hydrogen can be correlated to the bed temperature. For uranium getter beds a certain hysteresis is observed between the ab- and desorption. Therefore, two empiric correlations are implemented from Kolasinski et al. [122], describing the two processes separately in Equations (7.15) and (7.16).

$$\text{Absorption: } \log_{10}(p_{eq}) = 11.08 - 4216 \cdot T_{bed}^{-1}, \quad (7.15)$$

$$\text{Desorption: } \log_{10}(p_{eq}) = 11.81 - 4701 \cdot T_{bed}^{-1}, \quad (7.16)$$

where  $p_{eq}$  denotes the equilibrium pressure in Pa and  $T_{bed}$  is the temperature considered for the bed in K. The process dynamic can then be controlled by modifying  $T_{bed}$ . For example, by increasing the temperature  $T_{bed}$ : 400 → 700 K, the equilibrium pressure in the bed increases  $p_{eq}$ : 1.1 → 125000 Pa. The maximum heating and cooling rate are set to 0.5 K/s. In the fuel cycle simulator, a simple control scheme - summarized in Figure 7.9 is used to link the change of  $T_{bed}$  to the bed inventory and task.

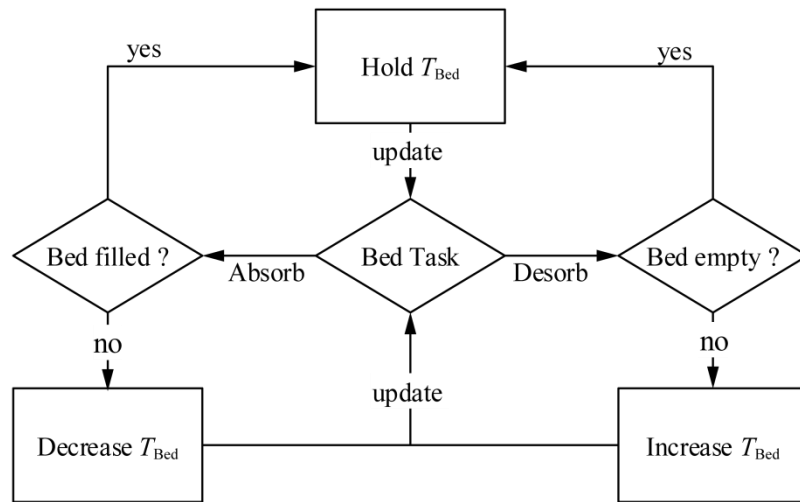


Figure 7.9: Control scheme implemented into the storage beds of the fuel cycle simulator to respond to a shift in quantity and quality.

Then, Equations (3.15) and (3.16) can be coupled with a simple transient mass balance Equation (7.17) to form a determined system of equations.

$$\frac{dI_{\text{ges}}}{dt} = \frac{d(I_{\text{gas}} + I_{\text{solid}})}{dt} = F_{\text{top-up}}, \quad (7.17)$$

where  $F_{\text{top-up}}$  represents the connecting stream to and from the GDCM in mol/s. Figure 7.10 shows the evolution of the absorption bed hydrogen inventory over time for an exemplary case. For low temperatures  $T < 500$  K, the hydrogen absorbs into the solid phase. Conversely, as temperature increases, hydrogen is released as gas and can be withdrawn from the process.  $I_{\text{ges}}$  changes as  $F_{\text{top-up}}$  is modified by the GDCM to uphold the fuel cycle mass balance.

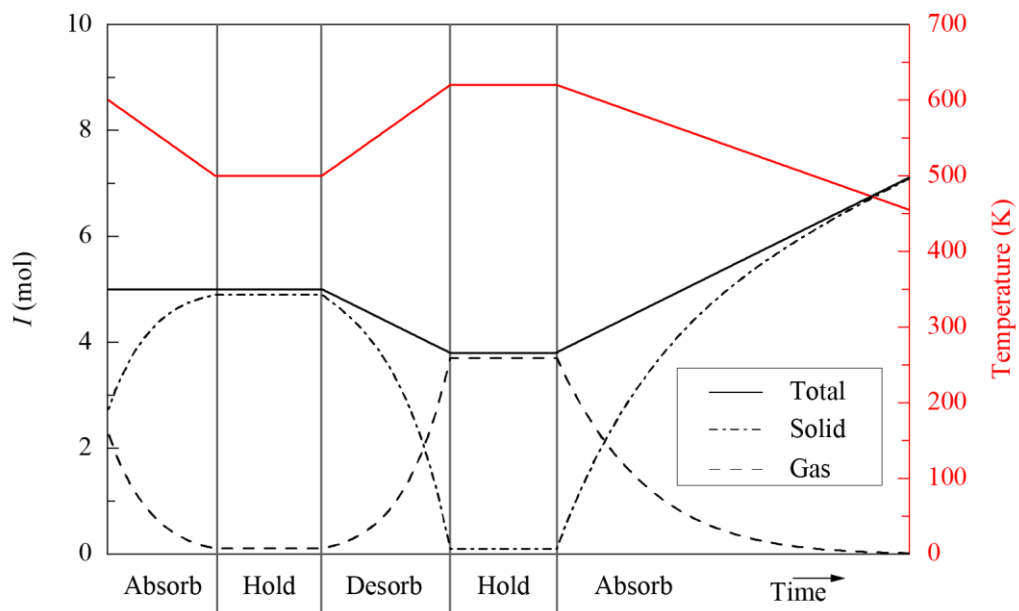


Figure 7.10: Qualitative trend of the uranium getter bed inventories as a function of a shift of temperature and total inventory over time.

---

## 7.5 Outer Tritium Loop Summary

The Outer Tritium Loop comprises three detritiation facilities and a long-term storage system. The figures below refer to the Reference Design Point.

### Exhaust Detritiation System

The EDS comprises a Combiner, Condenser and a Wet Scrubber Column to remove deuterium and tritium from the exhaust stream. It also disposes of non-hydrogen species introduced to the fuel cycle. All of the helium ash generated in and all nitrogen injected into the fusion reactor can be removed this way. The same applies to the Plasma Enhancement Gases argon and xenon, which are not recuperated prior.

99.93 mol% of the deuterium as well as 99.996 mol% of tritium upstream the EDS are recuperated and transformed to water. The fraction of protium in hydrogen exhaust gas downstream the Wet Scrubber column is  $y_{WS}(H_2 + H_2O) = 99.995$  mol%.

### Water Detritiation System

The WDS comprises a Liquid Phase Catalytic Exchange Column and a partial Electrolyser to detritiate water. 99.84 mol% of the deuterium as well as 99.998 mol% of tritium upstream the WDS are recuperated and concentrated in the electrolyser.

The accumulated heavy isotope mixture is withdrawn and send to the ISS with a composition of  $H : D : T = 88 : 5.5 : 6.5$ . The tritium concentration is stripped from the exhaust stream to a high degree in the LPCE column. The hydrogen gas is emitted with a protium purity of  $y_{LPCE}(H_2 + H_2O) = 99.996$  mol%.

### Isotope Separation System

A three-staged Cryogenic Distillation column setup isolate the three isotopologues at high purity. A total of 9 equilibrators are implemented to minimize mixture isotopologues.

Large quantities of protium exit the fuel cycle with high purity  $y_{ISS}(H_2) = 99.3$  mol%. The remaining 0.7 mol% are mostly HD. The purities obtained for the three isotopes are  $y_{ISS}(H) = 99.97$  mol%,  $y_{ISS}(D) = 99.999$  mol% and  $y_{ISS}(T) = 97.3$  mol%.

### Long-term Storage

Uranium getter beds are implemented into the fuel cycle to store excess amounts of hydrogen over longer periods of time. The detritiation factors obtained for the RDP are:

$$DF_{EDS} = 27583, \quad DF_{WDS} = 47553, \quad DF_{ISS} = 406556.$$

This amounts to annual loss of 0.985 g/a of tritium in molecular form and 0.638 g/a of tritium as water for the entire fuel cycle. Bulk of the deuterium and tritium losses occurs as the mixture isotopologue HQ and HQO.

# 8 Fuel Cycle Holistic Simulation

Now that all major processes are presented in isolation and steady state as well as quantified for the Reference Design Point, they can be integrated into and analysed as part of the whole fuel cycle. This chapter covers the aspects in fuel cycle modelling that result from the interplay of its components and derives concepts to modify and optimize the fuel cycle further.

In the first section, an estimate of the fuel cycle tritium inventory is derived. Wherever possible, the process inventory of a subsystem is embedded, provided that the corresponding process is modelled in sufficient depth. Otherwise, a tritium inventory is estimated using a residence time approach. From there, the tritium sink term of decay is deduced and incorporated into the examination of the system-wide mass balances of all modelled species. In particular, the different source and sink terms of the three hydrogen isotopes are investigated.

All these considerations refer to the DEMO Reference Design Point postulated in Section 3.4. In the likely event that the Fuel Cycle in the future faces conditions and throughputs that differ from RDP, adjustments must be made. Therefore - in Section 8.2 - key fuel cycle boundary conditions such as the fusion reactor throughput are varied in a parameter study. The extent to which the variation results in different requirements and how the fuel cycle can be adapted accordingly is discussed. This way, the fuel cycle can be scaled or modified to suit a wide range of boundary conditions.

The parameter studies still assume steady state operation. Therefore, in the third section, the behaviour of each component in a transient environment is examined. A distinction is made between a discussion of the transient start-up of each component and how to efficiently bridge the interim dwell period.

In the final section, the fuel cycle performance is compared to its design criteria. The critical fuel cycle elements are pointed out and their optimization potential is discussed.

## 8.1 Tritium Inventory and Mass Balances

### 8.1.1 Preliminary Tritium Inventory

Given the rarity and decay of tritium, its total inventory represents a key design aspect of a fusion power plant. The implementation of physics-based models in this work can be used to generate a first estimate of the tritium inventory of every fuel cycle subsystem.

As important as the parameter may be, it is coincidentally difficult to produce a sound estimation of the tritium inventory using a modelling approach in the mutable state of the pre-conceptual design phase. The estimation of the tritium inventories are considered bearing following caveats in mind:

First, the results of the work focus on the fuel cycle performance in the steady state and under assumption of the boundary conditions described in the Reference Design Point. Long-term

---

effects, such as plant availability or outages, are disregarded. This aspect is investigated for DEMO in [123].

Secondly, the model fidelity, especially of the subsystems in DIRT, is not sufficient to derive a tritium inventory. To quantify the tritium inventory of these systems, Equation (8.1) is used, which uses the residence time approach described in Equation (4.1) and imposes steady state conditions.

$$F_{in,Q} = \frac{I_Q}{\tau} \text{ for } \frac{dI_Q}{dt} = 0. \quad (8.1)$$

Since the input streams  $F_{in,Q}$  for each system are listed in detail in Table 5.1, Table 6.1 and Table 7.1, a direct correlation between the tritium inventory  $I_T$  and an average residence time  $\tau$  can be established. For subsystems with unknown tritium inventory, an estimate can thus be made by assuming the residence time. Conversely, in systems with a known inventory, an expected residence time can be calculated.

Thirdly, only the operating inventory - which signifies the tritium inventory that is actively processed - is described. The passive tritium inventory represents a large contributor, which is not assessable. The assessment of the passive tritium inventory scopes:

- Permeation into and retention of tritium in steel and other solid infrastructure.
- Permeation into and retention of tritium in the irradiated first wall of the torus
- Additional tritium inventory due to redundant implementation of subsystems.
- Tritium irrecoverable from storage beds
- The tritium inventory of infrastructure components such as pumps, pipes and heat exchanges

Although large uncertainties remain, the assessment of a preliminary tritium inventory provides an order of magnitude estimate. Most critically, it is made apparent, which system blocks process large quantities of tritium and therefore must be optimized. Additionally, the contribution of tritium decay to the overall loss term can be evaluated.

Table 8.1 lists the estimated tritium input streams, residence times and inventories of all fuel cycle subsystems covered in this work. If a residence time is assumed for a subsystem, the according entry is marked with an ■<sup>a</sup> in Table 8.1. Subsystems in which the reaction behaviour is determined by resolving a mass balance, the tritium inventories can be extracted. The according entry is then denoted as ■<sup>b</sup> and an equivalent residence time is provided.

In both cases, a brief discussion follows the table, elucidating how the number is conceived.



Table 8.1: Tritium throughput, residence times and inventory of the different fuel cycle elements. Residence time assumptions are marked as ■<sup>a</sup>. Tritium inventories derived from this work are marked as ■<sup>b</sup>.

Loop	System block	Subsystem	$F_{in,T}$ (Pa m <sup>3</sup> /s)	$\tau$ (s)	$I_T$ (g)
Torus		Tokamak	209.867	10 <sup>a</sup>	5.574
DIR Loop	MIS	PLS	229.592	1800 <sup>a</sup> [123]	1097.689
		GPS	24.733	60 <sup>a</sup>	3.942
		MIV	44.458	60 <sup>a</sup>	7.085
	Vacuum	MFP+LDP+LRP	208.528	60 <sup>a</sup>	33.233
	GDCM	Buffer vessel	250.233	60 <sup>a</sup>	39.879
INT Loop	EPS	Permeators	37.535	1.15	0.115 <sup>b</sup>
		Impurity removal	2.282	300 <sup>a</sup>	1.818
	IRPR	Buffer vessel	11.327	2·10 <sup>5</sup> <sup>a</sup>	6.318
		TSA	11.327	144254	4443.918 <sup>b</sup>
OUT Loop	EDS	Combiner	0.142	300 <sup>a</sup>	0.113
		Condenser	0.142	300 <sup>a</sup>	0.113
		Wet Scrubber	0.012	5159	0.17 <sup>b</sup>
	WDS	LPCE column	0.207	1068	0.587 <sup>b</sup>
		Electrolyser	0.397	968	1.021 <sup>b</sup>
	ISS	Column #1	1.344	15991	57.079 <sup>b</sup>
		Column #2	4.159	5327	58.853 <sup>b</sup>
Column #3		4.158	41558	459.024 <sup>b</sup>	
Outer Fuel Cycle		BB+TERS+CPS	0.945	36000 <sup>a</sup> [123]	90.322
$\Sigma$					<b>6301.3</b>

Given the low density and particle confinement times in plasma, the tokamak residence time is assumed at  $\tau_{Tokamak} = 10$  s.

Fundamental principle of the DIRT subsystems is to rapidly process its throughput, hence low residence times are assumed here. In vacuum, gases are processed at a high flow speed, which substantiates the assumption made for the associated pumps MIV, MFP, LDP and LRP. The GPS is a system of low complexity. The accumulation of tritium in it is based solely on the bypass ratio implemented in the RUN-VENT cycle. Even though the residence may be chosen small at  $\tau = 60$  s, the tritium inventory of these subsystems is a substantial contributor by nature of the large quantities of tritium processed in them.

The most critical system in the DIRT is the Pellet Launching System, which requires freezing of hydrogen from ambient temperature to  $< 15$  K, which is expected to contribute significantly to the residence time. Coleman et al. assume a value of  $\tau_{PLS} = 1800$  s [123], which results in a tritium inventory well above 1 kg. To assess and optimize this component and in particular the throughput of the liquefier and the extruder setup is subject of further research.

The GDCM buffer vessel is designed in this work with a capacity of holding supply for the fusion reactor for 60 seconds (cf. Section 5.4). For a different buffer requirement, one easily obtains the resulting inventory by applying Equation (8.1).

---

The permeator inventory is an output generated by the model via solving the upstream mass balance according to Equation (6.5). The bulk tritium resides in the permeators of the first stage, which holds 91 % of the subsystem's tritium content. The low tritium inventory and residence time stem from the small scale of the setup, with a gas volume of the first stage of  $V = 1.45$  l for all 37 permeators combined.

The IRPR is a semi-continuous process and tritium will accumulate in the buffer vessels installed up- and downstream the TSA setup. This amount can be minimized by staggering the process cycles of the 64 TSA beds and spreading the feed phases. This way Equation (8.2) can be used to calculate the residence time as a ratio of the duration of one process cycle over the amount of TSA beds operated in parallel.

$$\tau_{\text{IRPR,buffer}} = \frac{N_{\text{closed}} \cdot t_{\text{extended}} + t_{\text{closed}}}{\#_{\text{TSA}}} = \frac{6780 \text{ s}}{64} \approx 105 \text{ s}, \quad (8.2)$$

with the values taken from Table 6.7 and Equation (6.35). This residence time must be considered twice to account for the upstream and downstream buffer vessels.

The largest contribution by far resides in the TSA beds of the IRPR system, with a tritium inventory per TSA unit of about 70 g as derived in Section 6.2. For 64 units implemented in the RDP, this amounts to more than 4.4 kg of tritium. Applying Equation (8.1) a residence time of over 40 h ( $\tau = 144254$  s) is obtained. The large inventory originates from the semi-continuous nature of the process and the inherent long cycle times it entails. An improvement of the amount of hydrogen output per extended cycle (5 % in this work) or the overall cycle time (about 2 hours per extended cycle), can alleviate this issue substantially. Such a reworked setup must guarantee that the output does maintain the grade of achieved purity, however.

The amount of tritium processed in the Impurity Removal, Condenser and Combiner is comparably small. Consequently, for high residence times of 5 minutes, the accumulation of tritium in these systems is only a minor contributor.

Similarly, the tritium concentration in the Wet Scrubber and LPCE column as well as the Electrolyser is minuscule. The tritium inventories of the ISS setup are discussed in Section 7.3. The residence time of the Outer Fuel Cycle is also taken from [123] and represents a lumped residence time for the three system blocks BB+TERS+CPS. This totals to a fuel cycle tritium inventory of about  $I_{T_2} = 6.3$  kg with the largest fraction held by the IRPR system.

### 8.1.2 Mass Balances

To maintain a steady state of operation, the fuel cycle mass balance must be monitored carefully for every species. Observation of the Gas Distribution Control and Metering System as nodal point of the fuel cycle yields the throughput of every species and the amount recuperated in each fuel cycle loop as listed in Table 8.2. For deuterium, a distinction is made between the pure deuterium and deuterium in the fuel mixture to account for the different requirements of the NBI and fuel gas composition. The difference between input and output then corresponds to the amount of each species that must be supplemented to the fuel cycle from outside via  $F_{\text{top-up}}$  (10).

Table 8.2: Throughput of the fuel cycle for the RDP and recuperation rates of the individual loops for all species injected into the reactor. The according streams are denoted by the encircled number.

Species	MIS input (Pa · m <sup>3</sup> /s)	MIV (Pa · m <sup>3</sup> /s)	DIRL (Pa · m <sup>3</sup> /s)	INTL (Pa · m <sup>3</sup> /s)	OUTL (Pa · m <sup>3</sup> /s)	top-up (Pa · m <sup>3</sup> /s)
H	5.50 ①,③	0.96 ④	3.80 ⑦	0.73 ⑱	<10 <sup>-4</sup> ㉓	-
Pure D <sub>2</sub>	10.6 ②	0	0	0	12.16 ㉓	-1.55 ⑩
D in DT	254.33 ①,③	44.46 ④	171.49 ⑦	34.29 ⑱	0.11 ㉔	3.98 ⑩
T in DT	254.33 ①,③	44.46 ④	170.99 ⑦	34.78 ⑱	4.16 ㉔	-0.067 ⑩
N <sub>2</sub>	20.0 ①	0	0	0	0	20.0 ⑩
Argon	0.390 ①	0	0	0.386 ⑭	0	0.04 ⑩
Xenon	0.226 ③	0.044 ④	0	0.180 ⑭	0	0.02 ⑩

Figure 8.1 compares the contributions of different system blocks to the retrieval of the three hydrogen isotopes. In general, a comparable recovery rate can be observed for the MIV, MFP and IRPR bypass as these are not implemented into the model as isotope-sensitive. The differences result from isotope specific considerations and are discussed separately below.

A large fraction of argon and xenon is recuperated in the Exhaust Processing System due to high separation factor assumed in the PEG removal  $\eta_{\text{PEG}} = 99\%$ . The nitrogen gas is not recovered and must be fully replenished. With the listed steady-state nitrogen throughput of 20 Pa · m<sup>3</sup>/s, a two-hour pulse of DEMO requires 63.4 mol/pulse of nitrogen. Helium is not listed as it is always fully discharged from the fuel cycle. A single pulse produces 4.24 mol/pulse of He.

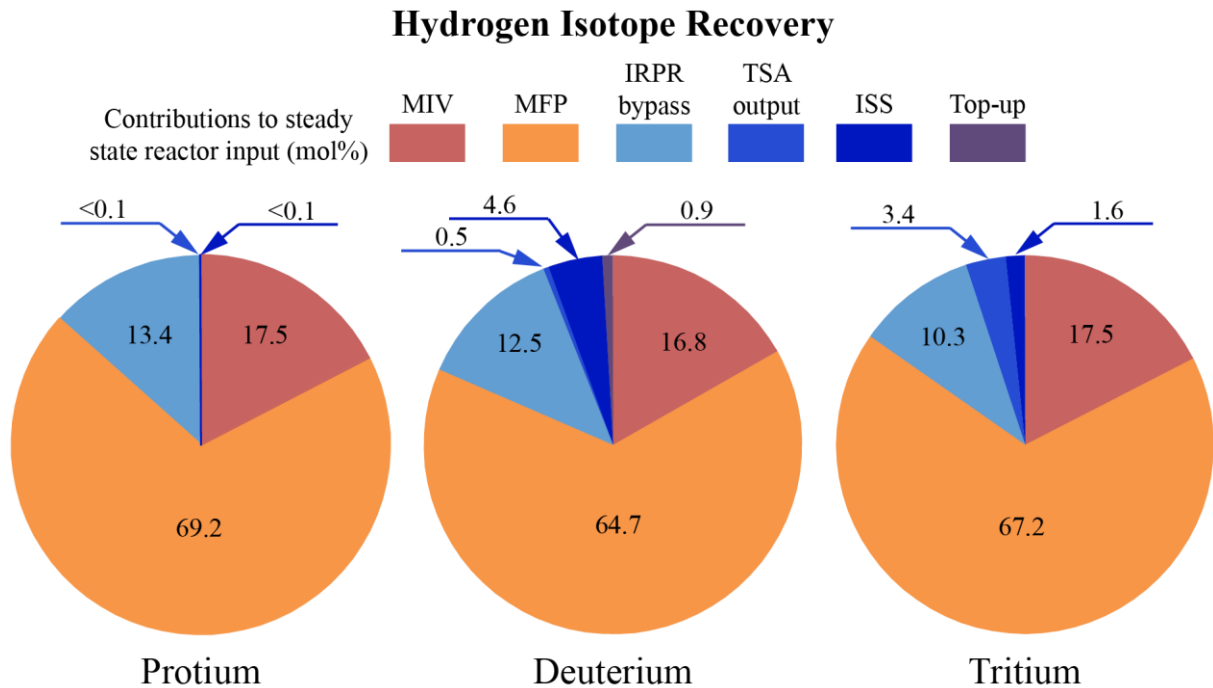


Figure 8.1: Contribution to the recuperation of the three hydrogen isotopes protium, deuterium and tritium of the different separation processes throughout the fuel cycle (numbers given in mol%).

## Tritium

By design, a surplus of tritium is produced in the Outer Fuel Cycle, which feeds it into the Inner Fuel Cycle via the Isotope Separation System. The excess generated correlates to the Tritium Breeding Ratio  $TBR$  as quantified in (8.3).

$$F_{\text{excess}} = F_{\text{burn}} \cdot (TBR - 1) = 0.068 \text{ Pa} \frac{\text{m}^3}{\text{s}} = 1.278 \frac{\text{g}}{\text{pulse}}, \quad (8.3)$$

with  $TBR = 1.05$  and  $F_{\text{Burn}}$  as calculated in Equation (2.2). In comparison, over the period of a two-hour pulse, the reactor burns  $F_{\text{burn}} = 25.56 \text{ g/pulse}$  for a thermal power of  $P_{\text{thermal}} = 2000 \text{ MW}$ . Simultaneously the Breeding Blankets of DEMO generate  $F_{\text{Breed}} = 26.88 \text{ g/pulse}$ .

Using Equation (2.3), the steady state tritium decay rate is calculated from the tritium inventory to  $F_{\text{decay}} = 4.23 \cdot 10^{-3} \text{ Pa} \cdot \text{m}^3/\text{s}$ . If kept constant over the period of a year, this corresponds to an annual decay rate of  $F_{\text{decay}} = 354.52 \text{ g/a}$ . The fraction of tritium decay amounts to about  $y_{\text{decay}} \approx 6.3 \text{ mol}\%$  of the surplus generated. The losses to the environment represent only a negligible sink term in comparison  $y_{\text{loss}} \approx 1.29 \cdot 10^{-3} \text{ mol}\%$ .

Figure 8.2 puts into relation, which amount of  $F_{\text{excess}}$  is stored, decayed and lost over the period of a two-hour pulse. The bar on the right specifies the contributions of Outer Tritium Loop system blocks to the tritium loss term.

As tritium is generated only during operation, but losses and decay persist over the whole plant lifetime, DEMO must at least perform 279 pulses per year to remain breakeven on tritium self-sufficiency. This corresponds to an annual plant availability of  $Av = 6.35 \%$ . Above this threshold, tritium accumulates over time. In the fuel cycle simulator, the tritium surplus is withdrawn as the bottom product of Column #3 at a purity of 97.3 % and stored in the uranium getter beds.

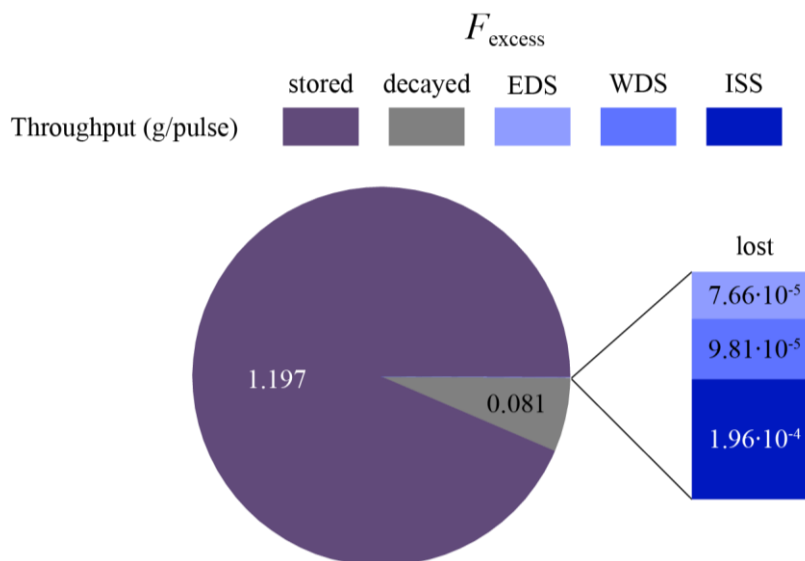


Figure 8.2: Destination of the tritium surplus generated ( $F_{\text{excess}}$ ) over a two-hour pulse of DEMO (values given in g per two-hour pulse).

## Deuterium

Deuterium is not generated by Breeding Blankets. Hence the combined amount of deuterium fused in the tokamak and discharged to environment must be replenished via external supply. During pulsed operation, the two sink terms contribute the fraction marked in Figure 8.3 a). Notably, only about 55 % of the steady state deuterium top-up is eventually burned in the reactor.

In general, the loss rate of the deuterium isotope is much higher than of tritium. This is based on the lower separation efficiencies from protium  $K_{HD} < K_{HT}$  for all separation processes implemented in the OUTL. The contribution to deuterium losses in the form of the mixture isotopologue HD at the head of Column #1 of the ISS stands out in particular. Here, more than 99.96 mol% of the deuterium losses occur for the entire fuel cycle.

## Protium

For the RDP, the fraction of protium among hydrogen isotopes upstream the torus amounts to 1.07 mol%. In steady state, the combined protium ingress of  $0.322 \text{ Pa} \cdot \text{m}^3/\text{s}$  assumed for the DIRT and INTL in Table 3.10 is removed by the IRPR system.

For the OUTL, the ingress of protium is negligible to the amount added as flushing agent. Figure 8.3 b) compares the different source terms of protium. Figure 8.3 c) follows up on this observation and displays the contribution of the three separation processes to the protium sink terms. Every atom of protium added to the fuel cycle results in a larger ISS setup, where the largest fraction of the total protium input is removed from the process.

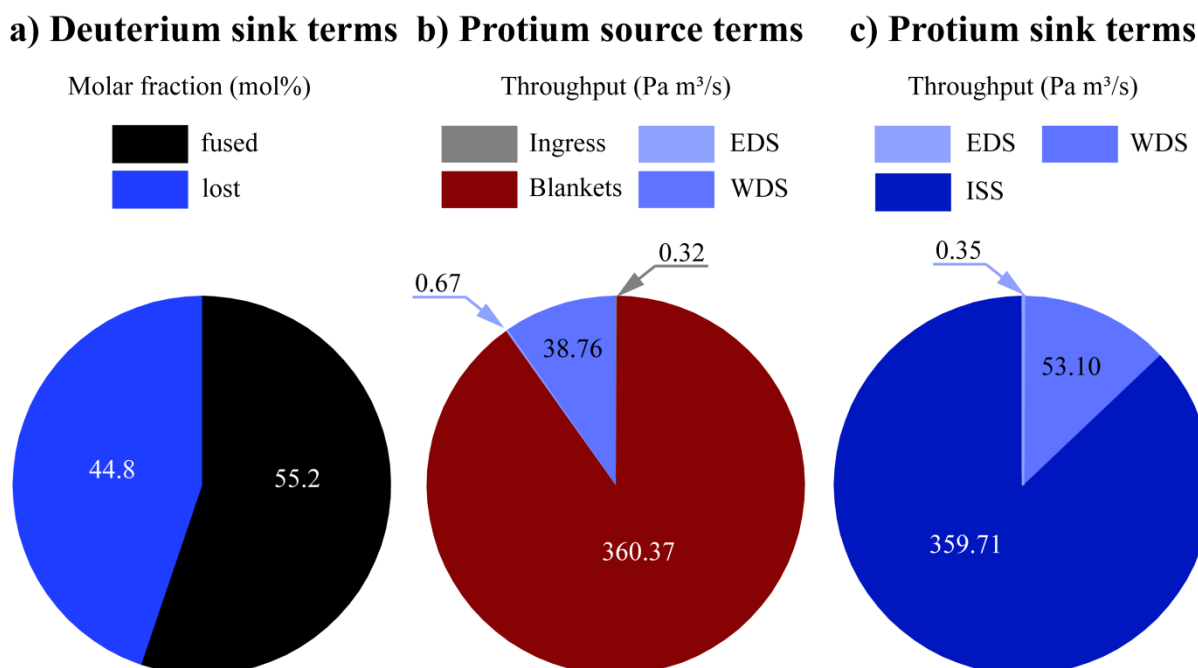


Figure 8.3: a) The deuterium sink terms in relation to the total amount supplied in steady state in mol%  
 b) Contribution of the different protium source terms to the total protium input throughout the fuel cycle in  $\text{Pa} \cdot \text{m}^3/\text{s}$ .  
 c) Protium sink terms represented as a fraction of the total protium input in  $\text{Pa} \cdot \text{m}^3/\text{s}$ .

---

## 8.2 Parameter Study of Input Boundaries

According to the current state of knowledge, the Reference Design Point described in the previous chapters covers a representative state of operation. A different set of boundary conditions than assumed in this work is equally conceivable, in particular as the plasma scenario to be taken for DEMO is still under discussion. The design of the fuel cycle - in individual parts or as a whole - must then be adapted accordingly. In this section, following key boundary conditions are modified and a suitable adaption of the fuel cycle is discussed:

- A variation of the reactor throughput, by changing the burn-up fraction  $\beta = 0.1 \dots 5 \%$ .
- A variation of the hydrogen removal efficiency of the DIRT  $\eta_{DIR} = 0 \dots 99 \%$ .
- Fuel cycle architecture considerations for a different hydrogen isotope mass balance.
- The influence of the different Breeding Blanket concepts.

### 8.2.1 Change of the burn-up fraction

A reactor tritium throughput of  $F_{MIS}(T) = 210.19 \text{ Pa} \cdot \text{m}^3/\text{s}$  (5) and a tritium fusion reaction rate  $F_{Burn} = 1.34 \text{ Pa} \cdot \text{m}^3/\text{s}$  are assumed in the RDP. These values yield a burn-up fraction of  $\beta = 0.64 \%$  as defined in Equation (2.4). The actual burn-up fraction can drastically deviate from this figure as a result of e.g. an alteration of the matter injection efficiency  $\eta_{MIS}$  as showed in Table 5.2. A substantial variation of the tokamak design parameters can yield a similar effect. In any case, consideration of a broad spectrum of possible burn-up fractions  $\beta = 0.1 \dots 5 \%$  is a sensible examination to make. Assuming  $F_{Burn}$  remains constant and thereby the generated thermal fusion power, the resulting tritium throughput entering the tokamak ranges between  $F_{MIS}(T) = 1336.53 \dots 26.73 \text{ Pa} \cdot \text{m}^3/\text{s}$ .

To account for a potential change in throughput, the fuel cycle system blocks are examined on their scalability within these boundaries. Each fuel cycle loop bears different limitations to linear scale-up, hence they are discussed separately.

#### Direct Internal Recycling Loop

All system blocks of the DIRT already encompass a scale-up from current experimental setups. Therefore, the number of required units can be calculated. The results are shown for critical subsystems in Table 8.3. As can be seen for a fusion reactor of low efficiency ( $\beta = 0.1 \%$ ), this approach results in high number of parallel subsystems. As the available space in the torus vicinity imposes a tight restriction on the unit count of most DIRT subsystems, this approach is bound to fail for  $\beta = 0.1 \%$ . Simultaneously, the tritium inventory of the DIRT would increase by a factor of 6. The issue can be alleviated by improving the throughput of a single unit, which must obey to certain inherent process limitations.

Within the MIS, scaling of the extruder throughput is constricted thermally and mechanically (e.g. by cooling rate or torque [66]), hence no significant scale-up is to be expected. The centrifuge parameter  $rn$  can be tweaked to adjust its throughput up to a point where the pellet speed affects the pellet delivery efficiency  $\eta_{PLS}$ . Scaling of the GPS and MIV systems can be regarded as non-issue in this context.

Table 8.3: Scaling of selected Direct Internal Recycling Loop subsystems for different burn-up fractions  $\beta$ .

Block	Parameter	$\beta = 0.1 \%$	$\beta = 0.64 \%$	$\beta = 5 \%$	Throughput per unit
$F_{\text{MIS}} \textcircled{5}$	(Pa m <sup>3</sup> /s)	2772.12	445.41	74.58	
PLS	#extruder	62	10	2	$F = 47 \text{ Pa} \cdot \text{m}^3/\text{s}$
	#centrifuge	31	5	1	$F = 96 \text{ Pa} \cdot \text{m}^3/\text{s}$
MFP	$A_{\text{foil}}$	519.1 m <sup>2</sup>	81.2 m <sup>2</sup>	10.1 m <sup>2</sup>	$j_{\text{MFP}} = 4.265 \text{ Pa m/s}$
	#MFP	166	26	4	$A_{\text{foil}} = 3.14 \text{ m}^2$
Vacuum	#LDP	91	12	3	$Q = 30 \text{ Pa} \cdot \text{m}^3/\text{s}$
	#LRP	1090	176	31	$Q = 2.5 \text{ Pa} \cdot \text{m}^3/\text{s}$

Assessment of vacuum pump requirement alteration proves difficult, provided that pressure regime and sub-divertor layout shifts with reactor throughput. For decreasing throughputs conductance may progressively inhibit the performance, whereas high throughputs pose the necessity for improved pumping speeds across the vacuum system block.

A possible solution to the high number of Liquid Ring Pumps is the implementation of a booster stage in between the high vacuum and backing pumps. An additional compression would relieve the specifications for the LRP performance. The Metal Foil Pump efficiency can be improved by increasing the pumping probability  $\chi_{\text{Pump}}$  and permeation flux  $j_{\text{MFP}}$ . This however requires energizing to a large extent particles. To evaluate the extent of optimization potential of these pumps is subject of further research.

### Inner Tritium Loop

In principle, the throughput of the EPS and IRPR can be scaled by adjusting the number of unit blocks  $\#_{\text{perm}}$  and  $\#_{\text{TSA}}$  as shown in Table 8.4. The implications of modifying the permeator setup are discussed in Chapter 6.1. Notably, as  $\beta$  increases, so does the fraction of impurities in the exhaust stream, which reduces the hydrogen removal efficiency of the permeators. For high throughputs, the permeator dimensions need to be expanded to create more surface area  $A_{\text{perm}}$  per unit. This is, however, limited by the hydrogen-induced swelling of the palladium membrane, which demands a dedicated setup and certain boundaries to inhibit mechanical stress [124]. Similar reasoning also prevents increasing the upstream pressure.

The size of the IRPR system is tied to the amount of DT imbalance imposed on the fuel cycle, which is not directly dependent on the value of  $\beta$ . A variation of the throughput may cause a shift in the DT imbalance in an indirect way, however.

If the protium ingress and DT imbalance remain constant as  $\beta$  changes, the fuel cycle can simply be adapted by adjusting the bypass fraction of the IRPR system and the size of the system block remains the same. For a low throughput  $F_{\text{INTL}} \textcircled{12}$ , this results in omitting the bypass stream entirely and feeding the IRPR with a fraction of  $F_{\text{DIR}} \textcircled{7}$  to uphold the mass balance requirements.

Table 8.4: Scaling of the Inner Tritium Loop subsystems for different burn-up fractions  $\beta$ .

Block	Parameter	$\beta = 0.1 \%$	$\beta = 0.64 \%$	$\beta = 5 \%$	Throughput per unit
	$F_{Ret} \textcircled{8}$ (Pa m <sup>3</sup> /s)	509.21	99.23	32.65	
EPS	# <sub>perm,I</sub>	214	37	9	$\eta_{perm,I} = 140.0$ Pa m/s
	# <sub>perm,II</sub>	48	8	3	$\eta_{perm,II} = 36.5$ Pa m/s
	$F_{INTL} \textcircled{12}$ (Pa m <sup>3</sup> /s)	494.29	85.77	19.36	
	$\eta_{Bypass}$	94.65 %	69.13 %	0 %	
IRPR	# <sub>TSA</sub>	~65	65	~65	$F_{feed,cont} = 0.41$ Pa · m <sup>3</sup> /s

### Outer Tritium Loop

All system blocks of the OUTL contain single unit processes optimized for one point of operation only. Linear scaling of the throughputs by increasing column diameters does not yield comparable results. Additionally, as the total amount of tritium lost  $F_{loss}$  is capped indifferent of the fuel cycle size, the detritiation requirements tighten as  $\beta$  decreases. For each of the three separation processes, the overall size and number of stages increase substantially.

#### 8.2.2 Change of Direct Internal Recycling fraction

The greatest novelty implemented for the DEMO fuel cycle is the DIR concept. Depending on the performance of the Metal Foil Pumps the fraction  $\eta_{DIR}$  of hydrogen throughput bypasses the Inner Tritium Loop entirely. Considering a change to the value of  $\eta_{DIR} = 0 \%$  ... 99 % has two primary implications on the fuel cycle design.

First, the throughputs of the two vacuum pump trains downstream the MFP, processing separately the DIR  $F_{DIR} \textcircled{7}$  and exhaust stream  $F_{Ret} \textcircled{8}$  shift in quantity and the distribution of pumps must be adjusted accordingly. In addition to the shift, if  $\eta_{DIR}$  is lowered, so is the amount of matter compressed by the Metal Foil Pumps. To compensate this reduction of pumping speed, the capacity of the remaining vacuum system must be scaled up.

Secondly, the system downstream the DIRL is to be adapted to accommodate a different throughput. For a reduced efficiency of the MFP subsystem, the simplest solution is to increase the amount of permeators implemented into the Exhaust Processing System. Thus, in a parameter study, the permeator setup is analyzed for a variation of its input quantity. Specifically, the Reference Design Point assuming  $\eta_{DIR} = 82 \%$  is compared to  $\eta_{DIR} = 50 \%$  as well as  $\eta_{DIR} = 0 \%$ . Similar to Figure 6.4, the resulting hydrogen isotope fraction in the upstream tube is mapped across the length of the permeator in Figure 8.4. The number of permeators in each case is adapted such to attain the same gas composition at the interface downstream the second stage.

If  $\eta_{DIR}$  is reduced, the hydrogen fraction increases in the exhaust stream, which in turn results in an increased efficiency per permeator and a non-linear scaling of the permeator numbers. To achieve the same hydrogen removal efficiency  $\eta_{perm} = 99.71 \%$  as for the RDP the amount of permeator units required increases from 45 to 92 for  $\eta_{DIR} = 50 \%$  and 164 for  $\eta_{DIR} = 0 \%$ , respectively. Figure 8.4 b) also shows the amount of permeators used in each stage.



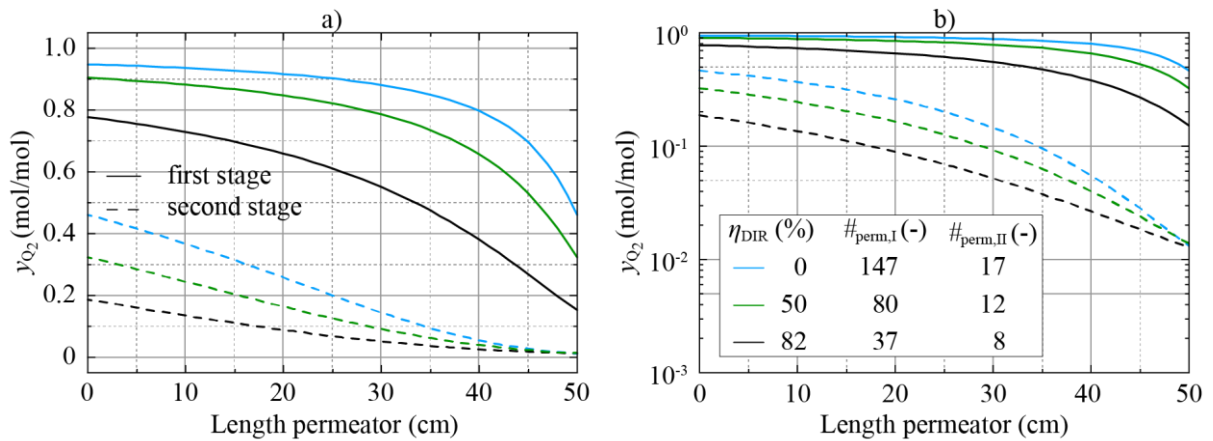


Figure 8.4: Parameter study for different fractions of  $\eta_{DIR}$  as a) linear and b) logarithmic plot. The number of permeators are adapted such to attain the same gas composition at the interface to the next system downstream the second stage.

In the opposite case - as  $\eta_{DIR}$  approaches unity - the EPS can be reduced in scale. However, this does not translate to a reduction of throughput of the IRPR system block, because of the mass imbalance of protium ingress and the DT imbalance. As the fraction of the exhaust stream decreases, so does the potency of the IRPR block, as a lower fraction of the overall throughput remains to modify the isotope composition. The threshold is reached if no bypass stream  $F_{bypass}$  (15) is used in the IRPR system as per Equation (6.34). For the assumptions made for the RDP (cf. Table 3.10), this occurs at  $\eta_{DIR} \approx 94\%$ . Beyond this point, a fraction of  $F_{DIR}$  (7) must be withdrawn and fed to the IRPR to uphold mass balance requirements and ensure reactor fueling in a proper composition. Although technically feasible, this approach defeats the purpose of the fast-recycling approach for that portion.

In principle, the task can be achieved as well by upscaling the system blocks of the OUTL but considering the large ramifications of upscaling three system blocks designed for a single point of operation this option is far less attractive.

It can be concluded, that much reduced fractions of  $\eta_{DIR}$  can justifiably be buffered by upscaling the EPS system block. This conclusion is tied, however, to the assumption that the scale up of the vacuum pumping system is feasible.

### 8.2.3 Change of Hydrogen Composition

In the RDP, the fuel composition is assumed as an equimolar fraction of D and T upstream the torus to maximize the cross section of the fusion reaction. A deliberate shift of composition is a conceivable strategy to counteract certain behavior within the plasma or to reduce the plant tritium inventory.

Independent of which point of operation is considered optimal, maintaining it within a certain margin over the course of several pulses will remain as a requirement. The mass balance between deuterium and tritium must therefore be considered as well as the strategy of inhibiting the concentration of protium. To uphold steady state composition requires optimization of several system blocks and precise understanding of the interplay of the processes therein. The RDP

assumes the values postulated in Table 3.10. Various scenarios arise for a deviation from these values and a fuel cycle layout must be adapted correspondingly.

To define the performance requirements of the three primary actuators: (i) the IRPR, (ii) the ISS and (iii) external top-up, let  $Q_L$  be the difference between the source and sink terms of a given loop  $L$  and isotope  $Q$ . Source terms in this context are all external inputs, such as permeation into the loop or supply, such as the deuterium NBI. The sink terms are defined for tritium in Section 2.2. For the other isotopes, the same definition applies, except decay must not be considered. Equation (8.4) exemplifies this for protium in the DURL.

$$F_{\text{source}}(\text{DIRL}, \text{H}) - F_{\text{sink}}(\text{DIRL}, \text{H}) = H_{\text{DIRL}}. \quad (8.4)$$

## DT fuel

Now, for the DT equilibrium different scenarios can be distinguished. First the overall mass balance fixes the boundary condition of the top-up stream:

- (a) Overall deuterium surplus:  $D_{\text{DIRL}} + D_{\text{INTL}} + D_{\text{OUTL}} > 0 \rightarrow$  Remove deuterium,
- (b) Overall deuterium shortage:  $D_{\text{DIRL}} + D_{\text{INTL}} + D_{\text{OUTL}} < 0 \rightarrow$  Add deuterium,
- (c) Overall tritium surplus:  $T_{\text{DIRL}} + T_{\text{INTL}} + T_{\text{OUTL}} > 0 \rightarrow$  Remove tritium,
- (d) Overall tritium shortage:  $T_{\text{DIRL}} + T_{\text{INTL}} + T_{\text{OUTL}} < 0 \rightarrow$  Add tritium.

In scenarios (a) and (c), the total surplus quantity must represent a high purity output stream of the ISS to allow for effective removal of that isotope. In case (b), deuterium is to be added from outside and in scenario (d) the fuel cycle fails to achieve tritium self-sufficiency. The duty of the Isotope Rebalancing system is given by consideration of the INTL and DURL mass balances:

- (e) INTL deuterium surplus:  $D_{\text{DIRL}} + D_{\text{INTL}} > 0 \rightarrow$  IR removes deuterium,
- (f) INTL deuterium shortage:  $D_{\text{DIRL}} + D_{\text{INTL}} < 0,$
- (g) INTL tritium surplus:  $T_{\text{DIRL}} + T_{\text{INTL}} > 0 \rightarrow$  IR removes tritium,
- (h) INTL tritium shortage:  $T_{\text{DIRL}} + T_{\text{INTL}} < 0.$

The RDP assumes scenario I and Equation (6.34) can be used to determine the bypass ratio  $\eta_{\text{bypass}}$  of the IRPR system. In the case of a tritium surplus (g), the interconnection displayed in Figure 6.5 is inverted and the tritium-enriched stream  $F_{\text{high-trit}} \textcircled{17}$  feeds into the ISS instead of the deuterated stream  $F_{\text{low-trit}} \textcircled{16}$ . In that case,  $\eta_{\text{bypass}}$  is derived by Equation (8.5).

$$0 = F_{\textcircled{7}} \cdot (y_{\textcircled{7}}(\text{D}) - y_{\textcircled{7}}(\text{T})) + \eta_{\text{bypass}} \cdot F_{\textcircled{12}} \cdot (y_{\textcircled{12}}(\text{D}) - y_{\textcircled{12}}(\text{T})) \\ + (1 - \kappa) \cdot (1 - \eta_{\text{Bypass}}) \cdot F_{\textcircled{12}} \cdot (y_{\textcircled{17}}(\text{D}) - y_{\textcircled{17}}(\text{T})). \quad (8.5)$$

For a combination of scenarios (f) and (h), the Isotope Rebalancing system can be omitted as rebalancing is automatically provided by the top-up.

## Protium

Concerning protium, the duty of the Protium Removal and ISS system is given by scenarios (i) and (j), respectively. The inverse scenario - in which the total amount of protium is declining over time - can be disregarded as trivial in this context.

- (i) INTL protium ingress:  $H_{DIRL} + H_{INTL} > 0 \rightarrow$  PR removes protium,  
 (j) Overall protium ingress:  $H_{DIRL} + H_{INTL} + H_{OUTL} > 0 \rightarrow$  ISS removes protium.

In the RDP, Protium Removal and Isotope Rebalancing are combined into the same TSA process. The maximum amount of protium removed this way is then tied to the design parameters of the IRPR system. Steady state is achieved when Equation (8.6) is satisfied.

$$H_{DIRL} + H_{INTL} = F_{INTL} \cdot y_{INTL,H} \cdot (1 - \eta_{bypass}) \cdot \kappa, \quad (8.6)$$

where  $F_{INTL}$  and  $y_{INTL,H}$  are the throughput and molar fraction of protium upstream of the IRPR system in mol/s and mol/mol, respectively.  $\eta_{bypass}$  and  $\kappa$  are defined in Section 6.2. If Equation (8.6) is not satisfied, the molar fraction of protium in the fuel gas will increase (>) or decrease (<) until a new steady state protium concentration is matched.

Equation (8.7) then relates  $y_{INTL,H}$  to  $y_{MIS,H}$ .

$$\left( (F_{MIS} \cdot y_{MIS,H} + H_{DIRL}) \cdot (1 - \eta_{DIR}) + H_{INTL} \right) \cdot \eta_{perm} = F_{INTL} \cdot y_{INTL,H}, \quad (8.7)$$

where  $F_{MIS}$  and  $y_{MIS,H}$  are the throughput and molar fraction of protium upstream the torus in mol/s and mol/mol, respectively.  $\eta_{DIR}$  and  $\eta_{perm}$  are the hydrogen removal efficiency of the Metal Foil Pumps (cf. Section 5.2) and the Exhaust Processing System (cf. Section 6.1).

Importantly, the influence of protium ingress in the two loops is not equivalent, given that a large portion of  $H_{DIRL}$  is recycled internally and bypasses the Protium Removal. From Equation (8.7) one obtains the weighting factor  $H_{DIRL} \hat{=} H_{INTL} \cdot (1 - \eta_{DIR})$ . Thereby, ingress of protium in the INTL is easier to remove than ingress in the DIRL. Combining Equations (8.6) and (8.7) yields Equation (8.8), which correlates the protium concentration in the fuel gas to the process parameters of the DEMO fuel cycle and the expected ingress of protium.

$$F_{MIS} \cdot y_{MIS,H} = \frac{H_{DIRL} + H_{INTL}}{(1 - \eta_{bypass}) \cdot \kappa \cdot \eta_{perm} \cdot (1 - \eta_{DIR})} - \frac{H_{INTL}}{(1 - \eta_{DIR})} - H_{DIRL}. \quad (8.8)$$

As protium is accumulated with deuterium in the TSA setup, this equation can only be used in scenarios I, (f) and (h). In the case of scenario (g) Protium Removal must be realized separately from the Isotope Removal System.

---

## 8.2.4 Impact of the Outer Fuel Cycle Performance

The choice of the Breeding Blanket concept governs to a large extent the requirements of the OUTL. In consequence, all concept candidates currently iterated need to be incorporated as potential boundary conditions. The HCPB and WCLL concepts described in Appendixes A1 and A2 incorporate all system blocks under discussion and provide a quantification of expectable outputs.

In the fuel cycle simulator, the Outer Fuel Cycle is implemented as a modifiable boundary condition. Each of the three major components (BB, TERS & CPS) is modelled for both concepts as a black box system block with a number of adjustable parameters. The performance and output quantities are taken from the literature or estimated for each concept.

Leakage from the first wall and the BB into the coolant must be considered. For the reactor leakage Katayama et al. performed estimations [125]. For the Breeding Blanket the considerations strongly depend on the implemented concept. Here, leakage from the Breeding Blanket is quantified only. The effect can be moderated by taking anti-permeation measures (e.g. anti-permeation coatings). This is indicated in the following as the Permeation Reduction Factor ( $PRF \geq 1$ ).

The integral Tritium Breeding Ratio defined in Equation (2.8) is assumed conservatively as  $TBR = 1.05$ . To achieve this number, more than three quarters of the reactor first wall must be covered in blankets, with the rest attributed to the divertor, heating, MIS and diagnostic ports. The  $TBR$  of each blanket section must consequently be designed to exceed  $TBR_{BB} > 1.20$ . This is achieved by maximising the torus wall coverage factor within the blankets and a simultaneous lithium breeder enrichment of the isotope  ${}^6\text{Li}$ . The latter exhibits a larger neutron cross section of the reaction described in Equation (2.6) over the reaction of  ${}^7\text{Li}$  in Equation (2.7). These considerations are covered in [10].

Of the two concepts, the HCPB is chosen as boundary condition for the Reference Design Point. The decision is concluded after observation of several implications resulting from the two concepts. The main decision drivers are:

- (i) The TERS output of the HCPB concept represents the worst-case assumption - given the large quantities of protium purge used - and implies a heavy additional duty on the OUTL Loop.
- (ii) In the WCLL concept, the ramifications of the TERS technology choice are not yet foreseeable. The implemented model is heavily based on assumptions and represents a trivial boundary condition (pure tritium), easily retrofitted into any fuel cycle.
- (iii) Separation of hydrogen from helium coolant represents a manageable task.
- (iv) The CPS system of the WCLL remains a largely unsolved issue. Permeation of considerable amounts of tritium are expected into the coolant water and represent a critical technical requirement to be overcome. The topic is currently under investigation [126].

For the WCLL concept, a substantial increase of the WDS system is to be expected, whereas requirements of the EDS and ISS are reduced.

## 8.3 Transient Behaviour

### 8.3.1 Fuel Cycle Initialization

Steady state is assumed as standard point of operation throughout all processes in the fuel cycle. To reach this standard point of operation however, each process must carry out a start-up. In this section, the different processes modelled in the fuel cycle simulator are examined regarding their start-up period  $t_{\text{start}}$ , which is defined as the time span between a generic initialization and the convergence to a steady state. As the fuel cycle simulator described in this work supports transient modelling,  $t_{\text{start}}$  can be determined by observing the simulation time after initialisation. From this, the inertia of each subsystem to a change in operating parameters can be assessed. Notably, as reaction kinetics is generally not incorporated into the model code,  $t_{\text{start}}$  provides only a rough estimation of the start-up process.

In the case of continuous processes, such as the separation columns of the Outer Tritium Loop, an optimal operating point is predetermined by their boundary conditions. After initialisation from any point or a parameter change, the system converges towards a steady state. Using Cryogenic Distillation as an example, Figure 8.5 depicts the molar fraction of the deuterium isotopologue in the liquid phase  $z_{\text{D}_2}$  throughout the column for different points in time after initialisation. The steady state refers to Figures 7.6, 7.7 and 7.8 for Columns #1, #2 and #3, respectively. Deuterium is chosen in this context because it is present prominently in all three columns. To display the behaviour, a simple initial value is assumed for each column.

$$0 < z_{\text{D}_2}(\text{CD \#1}) < 0.8, \quad z_{\text{D}_2}(\text{CD \#2}) = 0.6, \quad z_{\text{D}_2}(\text{CD \#3}) = 0.8. \quad (8.9)$$

Figure 8.5 b) in particular shows how the deuterium profile becomes more pronounced over time. The two outputs at the top ( $n = 0$ ) and bottom of the column ( $n = 55$ ) then influence the equilibrium of the other two columns (cf. Figure 8.5 a) and c)). Since Columns #1 and #2 pass on part of their output to each other, a feedback loop is created. This adds inertia to the system. For example, as the amount of deuterium at the top of Column #2 increases, the deuterium inventory in the first column also increases over time until, at steady state, the composition at the head of the second column equals the composition at the  $n_{\text{feed}}$  in the first column. Similarly, the deuterium content in Column #3 increases from  $t = 1000$  s over  $t = 10000$  s to steady state. For the CECE process a similar feedback loops results from the interplay of the electrolyser and the LPCE column. The Wet Scrubber column lacks such a feature and converges significantly faster. The permeator adapts to change within  $N$  iterations steps, where  $N$  is the number of nodes chosen in the discretization.

In discontinuous processes that are divided into several phases, i.e. in this work the TSA process implemented in the Inner Tritium Loop, there is no single operating point that represents the optimum state. Instead, the end point is shifted with every phase change. The transient behaviour of the TSA process and convergence to a consistent output is shown in Figure 6.9 a). All other processes in the fuel cycle which are not discretized, such as the system blocks in the DIRL, do not display transient behaviour. The output quantity and composition are modelled as function of the input and not of time. The start-up times of the different processes are summarised in Table 8.5 in the next section.

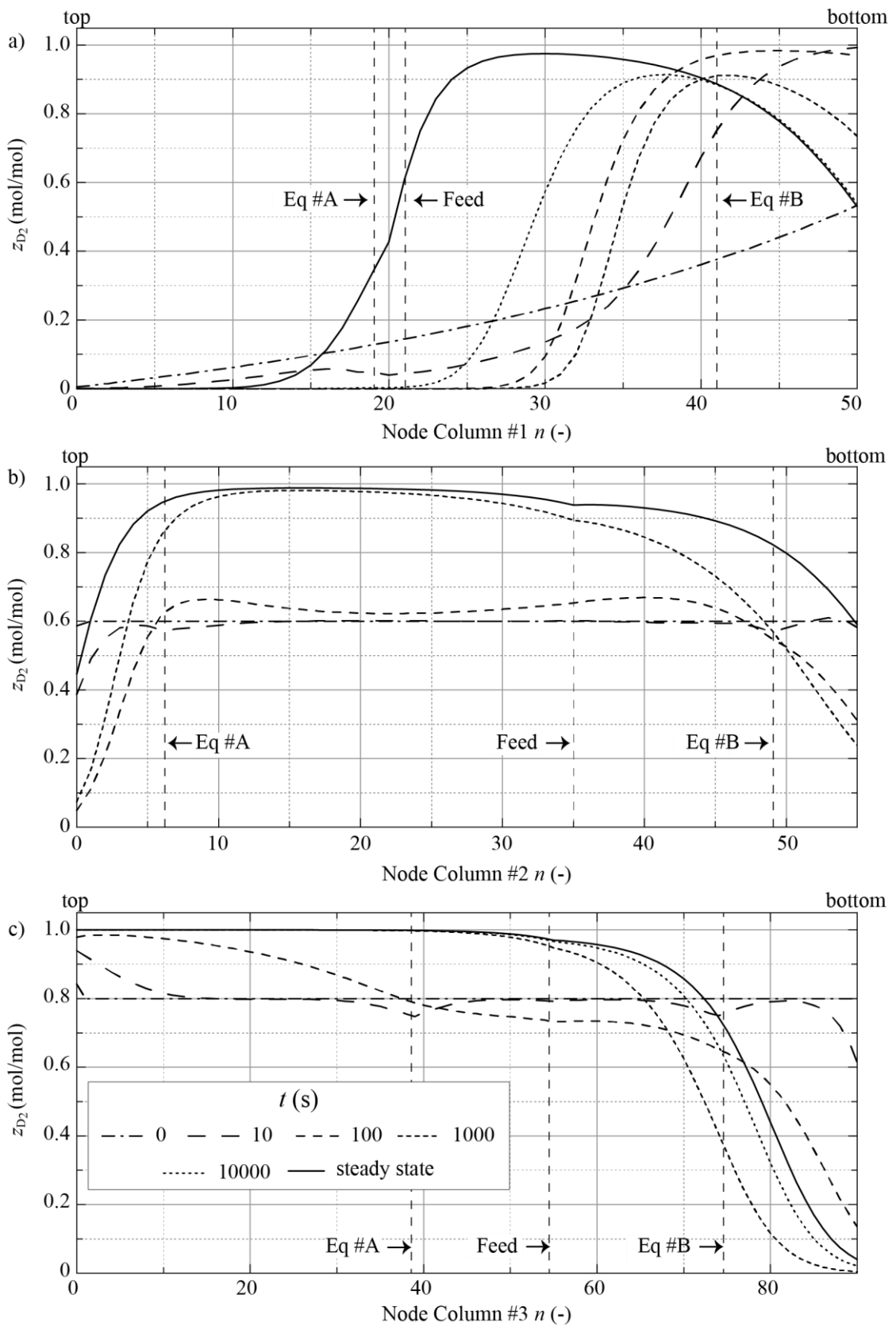


Figure 8.5: Liquid deuterium isotopologue ( $D_2$ ) fraction over the height of (a) Column #1, (b) Column #2 and (c) Column #3 from top to bottom and for different points in time after initialisation of the simulation.

### 8.3.2 Dwell Phase

The current setup of DEMO foresees two hours of fusion operation interrupted by a dwell phase of about twenty minutes. As a chemical plant, the majority of the fuel cycle processes involved must be maintained in a steady state over this short period of time to keep peak performance. The dwell bypass introduced in Section 5.4 guarantees a uniform boundary condition for the Exhaust Processing System and all system blocks downstream.

Concerning the DURL, the screw extruders of the Pellet Launching System are also assumed to require steady state to maintain operation temperature. In the fuel cycle simulator, they dump all frozen hydrogen output into the Matter Injection Vacuum, which feeds back into the GDCM. The three-way valve of the RUN-VENT cycle in the GPS is closed to the fuel cycle and NBI is assumed shut down as well. The torus is evacuated assuming Equation (8.10).

$$\frac{dt_{\text{torus}}}{dt} = F_{\text{outgas}} - S \cdot p_{\text{torus}}, \quad (8.10)$$

where  $F_{\text{outgas}} = 0.1 \text{ Pa} \cdot \text{m}^3/\text{s}$  is assumed as the only remaining input source of the torus and concurrently the protium ingress assumed in Table 3.10 for the RDP. The pumping speed of the high vacuum pumps  $S = 100 \text{ m}^3/\text{s}$  is given in Table 5.3. Whereas the vacuum pumps will maintain operation to pump away the outgassed species, the separation function of the Direct Internal Recycling is not required during the dwell phase. Hence during this period, the MFP is not operated by simply turning off the plasma source. The output of the torus then governs the throughput of the vacuum pumps downstream the retentate path  $F_{\text{ret}}$  (8). Table 8.5 summarizes the behaviour of every subsystem during the dwell phase.

Table 8.5: Dwell behaviour and process start-up period for all fuel cycle subsystems.

Loop	System block	Subsystem	Dwell behaviour	$t_{\text{start}}$ (s)
Torus		Tokamak	is evacuated	-
DIR Loop	MIS	PLS	maintains steady state	-
		GPS	full recirculation	-
		MIV	full recirculation	-
	Vacuum	MFP	stops	-
		LDP+LRP	evacuates torus	-
	GDCM	Buffer vessel	creates dwell bypass	-
INT Loop	EPS	Permeators	maintains steady state	10
		Impurity removal	maintains steady state	-
	IRPR	Buffer vessel	maintains steady state	-
		TSA	maintains steady state	11000
OUT Loop	EDS	Combiner	maintains steady state	-
		Condenser	maintains steady state	-
		Wet Scrubber	maintains steady state	1000
	WDS	LPCE column	maintains steady state	6000
		Electrolyser	maintains steady state	-
	ISS	CD columns	maintains steady state	20000
		Equilibrator	maintains steady state	-
Outer Fuel Cycle		BB	no tritium generation	-
		TERS+CPS	maintains steady state	-

The transient modelling in the Aspen Custom Modeler requires continuous boundary conditions to operate properly. Therefore, the dwell phase of 1200 s includes a ramp-up and ramp-down of 50 seconds each. The throughputs up and downstream the torus as well as the dwell bypass is shown for the transition periods as well as the dwell phase in Figure 8.6. Whereas the input streams (in red) show a sharp profile during the transmission, the torus output streams and retentate stream display a transient behaviour beyond the ramping periods.

In summary, to account for the pulsed operation of a tokamak fusion reactor, the fuel cycle must include a regulatory mechanism to remove the influence of a periodic change in input boundary conditions to the delicate isotope separation processes in the Inner and Outer Tritium Loop. Equally crucial is to perpetuate the overall throughput as well as to maintain a constant isotopic composition upstream of the IRPR and the Outer Tritium Loop system blocks.

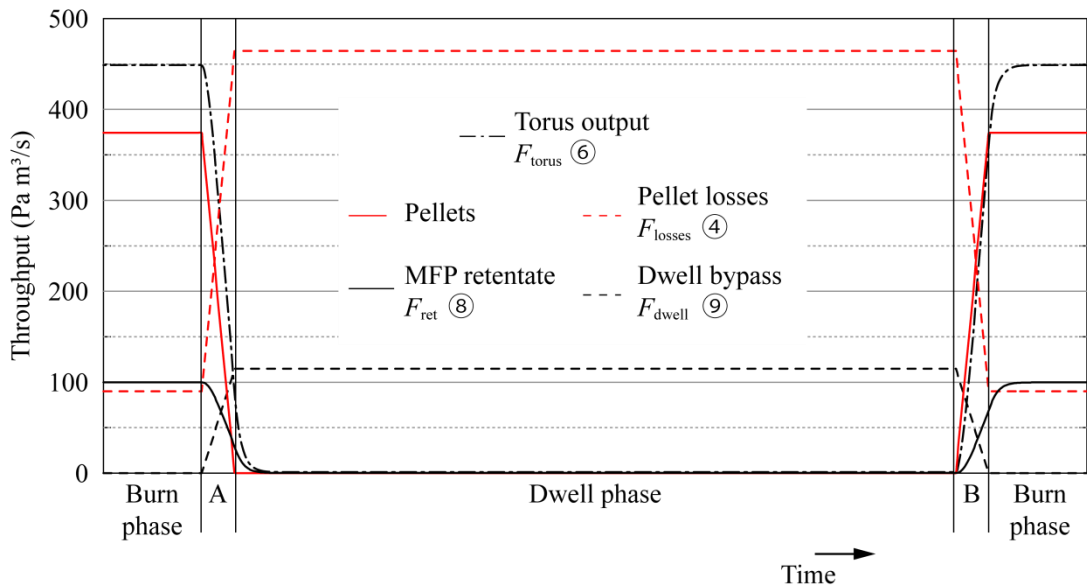


Figure 8.6: Throughput of various streams over time that shift in quantity over the dwell phase. Intermediate periods A and B mark the ramp-down and ramp-up of plasma operation and each represent 50 s of the 1200 s total dwell period expected for DEMO.



## 8.4 Performance Evaluation and Optimization Potential

### 8.4.1 Meeting Design Criteria

Design criteria of the fuel cycle include the tritium self-sufficiency, limitation of the loss term and maintenance of fuel gas mass balances. Given these criteria, the performance of the fuel cycle as modelled in the fuel cycle simulator can be evaluated.

The tritium self-sufficiency is given for the RDP of DEMO with an annual plant availability exceeding 7 % at a TBR = 1.05. This provides a considerable buffer for the built-up of a tritium surplus and guarantees the start-up inventory of future fusion power plants.

The system-wide loss of tritium amounts to about 1.6 g/a. In the absence of available administrative thresholds for the DEMO reactor, this cannot be evaluated conclusively. However, the obtained value is between the ITER limits of 0.6 g/a for a normal operation year (cf. Equation (3.26) and of 2.5 g/a for heavy maintenance years. If stricter guidelines are imposed onto DEMO, further detritiation measures will have to be taken, with the consequence of higher required detritiation efficiencies and/or a higher tritium inventory.

A balanced mixture of the deuterium and tritium fuel can be maintained in steady state by implementing the system blocks IRPR and ISS in the way presented. Protium concentration stabilizes at a concentration of about 1 % for an assumed protium ingress of  $0.32 \text{ Pa} \cdot \text{m}^3/\text{s}$ .

### 8.4.2 Optimization Potential

Within the scope of the three-loop fuel cycle architecture and the technology selection given in Section 2.4, the Reference Design Point covers to a high degree the available potential for optimization.

A reconsideration of the fuel cycle design or at least the underlying assumptions postulated in the RDP, can be derived from this work. The inclusion of a semi-continuous process in the IRPR system with inherently low equivalent steady state throughputs certainly leads to high residence times and thereby considerable tritium inventories. It must be considered whether the function foreseen for the IRPR system can just as well be integrated into the ISS system block. As a result, the design of the fuel cycle can be simplified. The permeate output of the EPS  $F_{\text{INTL}}$  (12) is then split into a large bypass stream  $F_{\text{bypass}}$  (15) and a split stream is fed directly to the ISS.

Based on the assumption that protium and deuterium can be recovered from the ISS column with the same purity as calculated for the RDP, the new bypass fraction can be reduced to  $\eta_{\text{bypass}} = 22.34 \text{ mol}\%$ . This assumption inherently entails a larger fraction of tritium entering the ISS column and thus also the atmosphere. At the same time, the size and energy requirements of the cryogenic application increase.

In general fuel cycle elements that concentrate tritium in solid or liquid phase are to be implemented carefully by aiming for reduced process time and reduced inventory at higher throughput.



# 9 Summary and Outlook

## Summary

Within the scope of this work, the entire Inner Fuel Cycle of a full-scale fusion power plant is built from scratch and integrated into a holistic simulation programme. The behaviour of the key components is depicted and interconnected by means of simplified physics based models to allow for integral feasibility of the fuel cycle and judge on the performance of individual components at reactor conditions. The relevant boundary conditions of the Inner Fuel Cycle are introduced, and its function and three-loop architecture are derived from them.

All models are integrated in the Aspen Custom modeller to depict the entire fuel cycle allowing for some systems also to apply transient boundary conditions. The toolset developed allows both to optimize individual components independently of each other and to analyse interactions with other subsystems.

In addition to the six hydrogen isotopologues in the form of molecular gas and water, the fusion product helium and the Plasma Enhancement Gases argon, xenon and nitrogen are embedded in the model code. Each subsystem has been either described by an established verified model or in case of unavailability a verification procedure has been executed.

A reference case is setup for the first-of-a-kind DEMO fusion power plant, from which important operating parameters can be deduced for this and all subsequent power plants. The underlying physics of all relevant technologies for processing hydrogen is derived from the literature, broken down and implemented into the fuel cycle simulator. With the understanding gained, each subsystem is dimensioned for the reference case.

In the Direct Internal Recycling Loop, the throughputs of the subsystems are derived from the set boundary conditions and by scaling up current experimental setups. A torus throughput of  $450 \text{ Pa} \cdot \text{m}^3/\text{s}$  is processed by 26 Metal Foil Pumps, which extract and directly recycle more than 80 % of the hydrogen. A total of 15 Linear Diffusion Pumps and 178 Liquid Ring Pumps are used evacuate the torus to below 10 Pa and compress its steady state throughput to ambient pressure. The recycled fraction is mixed with other fuel cycle output streams in a gas valve box and reintroduced into the torus via three different injection methods. Among them are ten twin-extruders combined with five centrifuge accelerators that deliver frozen hydrogen pellets to the plasma core.

In the Inner Tritium Loop, a two-staged permeator setup with 45 units recuperates more than 99.5 % of the remaining hydrogen from the exhaust gas. The chemistry of compound hydrogen molecules is elucidated and considered in a simplified approach in the model.

In a subsequent semi-continuous Temperature Swing Absorption process, the fuel mixture of deuterium and tritium is rebalanced to equimolar composition within 64 units. Simultaneously, the protium ingress into the fuel cycle is counteracted.

---

In the Outer Tritium Loop, three processes have been implemented to detritiate the exhaust streams and optimised for a tight constraint. With the help of purge water in counter flow columns and a three-staged Cryogenic Distillation process less than 1.6 g of tritium leak from DEMO's fuel cycle over the course of a year. The three isotopes of hydrogen can be isolated in high purities.

An operational tritium plant inventory of about 6.3 kg is derived. The main contributors are the Temperature Swing Absorption, the Pellet Injection and the Cryogenic Distillation system blocks. The mass balance of all processed species is established and the individual source and sink terms are quantified. In a parameter study, the torus throughput, Metal Foil Pump efficiency and fuel gas composition are varied. Scalability is examined and considerations on an adaptive fuel cycle layout are presented to cope with a large range of boundary conditions. The transient behaviour during start-up and the tokamak dwell phase are discussed.

In summary, for a reference case, the functionality of the entire fuel cycle of a fusion power plant is verified and cohesively reproduced in its entirety. From it, the number of individual components required as well as the tritium inventories associated with each step can be estimated.

## **Outlook**

In this work, modelling of a fusion fuel cycle is based on mass balances and simplified kinetics. In particular the assumption of instant thermal equilibrium as governing driving force limits the validity of the results to an indicative nature. Hence, the model fidelity - in particular of isotope separation processes - must be expanded to include kinetics and thermal inertia. This enables the model to predict performance and tritium inventories of its components more accurately.

In this context, the Temperature Swing Absorption is to be examined in detail. The setup of the Isotope Rebalancing and Protium Removal system chosen in this work represents a novel approach and a modification of a conventional separation process. Currently there is no corresponding experiment to adequately validate the results obtained in this work. Especially, the large tritium inventory resulting from the discontinuous operation must be investigated to draw a conclusion on the applicability of this process in a fusion power plant.

In a subsequent study, a qualification of uncertainties in each subsystem is required. The parameter study conducted in this work is restricted to the variation of specific fuel cycle parameters across system block boundaries and neglects the error introduced in individual models based on material properties. The inclusion of an uncertainty analysis on a subsystem level allows for a detailed assessment of error propagation across systems and helps identify crucial limitations.

As a consequence of added complexity combined with the limited computing power of a single processor core, such an improved fuel cycle simulator is presumably unable to include all system blocks in its current Aspen Custom Modeler framework. To circumvent this problem, either the fuel cycle simulator must be ported to a different software capable of parallelization or the simulation task must be partitioned into multiple smaller units with fixed boundary conditions. For example, each fuel cycle loop could be considered individually. However, this approach prohibits the analysis of uncertainty propagation across the system boundaries.

This work is limited to DEMO's inner fuel cycle, with the Outer Fuel Cycle treated as a highly simplified boundary condition. A noteworthy point of discussion is the high protium input originating from HCPB breeder blanket as derived in Appendix A1. This represents about 95 % of the total input of the ISS column and increases the size and energy demand of this component immensely. An iteration of this interface based on this work is a worthwhile consideration. For a holistic view, the fuel cycle is ideally expanded to include the Outer Fuel Cycle. Furthermore, other interfaces such as the balance of plant or plant footprint must be taken into account.

To estimate the energy consumption of the fuel cycle, an energy balance must be setup for all subsystems. Importantly a closer look should be taken at processes that are bound to require large amounts of energy, such as cryogenic applications and electrolysis. If this is integrated comprehensively into the simulation, the influence of the individual processes can be quantified, and the overall fuel cycle can be optimised for this design criterion.

The control feature of the fuel cycle simulator is currently limited to regular operation including a bypass solution for the dwell phase. If exceptional situations, such as partial system failures, emergency shutdowns or highly transient boundary conditions are to be taken into account, an extension of the control setup is indispensable.

---

# References

- 
- [1] M. Kikuchi, K. Lackner, M.Q. Tran (Editors): *“Fusion Physics”*, INTERNATIONAL ATOMIC ENERGY AGENCY (IAEA), Vienna, Austria (2012)  
**no doi / ISBN: 978-92-0-130410-0**
- 
- [2] Y. Xu: *“A general comparison between tokamak and stellarator plasmas”*, Matter and Radiation at Extremes Vol.1, Iss.4 (2016) pp.192-200  
**doi: 10.1016/j.mre.2016.07.001**
- 
- [3] E. Joffrin, P. de Vries, R. Felton, X. Litaudon, T. Loarer, P. Lomas, D. Mazon, V. Pericoli-Ridolfini, P. Thomas et al.: *“Steady state and stationary long pulse operation in JET”*, 32<sup>nd</sup> EPS Conference on Plasma Physics, Tarragona, Spain (27.06-01.07 2005) ECA Vol.29, Iss.C (2005) pp.5-9  
**no doi / TRN: FR0503566115668**
- 
- [4] F. Sartori, G. de Tommasi, F. Piccolo: *“The Joint European Torus”*, IEEE Control Systems Magazine Vol.26, Iss.2 (2006) pp.64-78  
**doi: 10.1109/MCS.2006.1615273**
- 
- [5] A.W. Morris, C.D. Challis, I.T. Chapman, M. Cox, G.M. Fishpool, A. Kirk, K.G. McClements, H.F. Meyer, J. Milnes et al.: *“MAST accomplishments/plans in support of fusion next-steps”*, IEEE 25<sup>th</sup> Symposium on Fusion Engineering, San Francisco, CA, United States of America (2013)  
**doi: 10.1109/SOFE.2013.6635408**
- 
- [6] A. Herrmann, O. Gruber: *“Chapter 1: ASDEX Upgrade - Introduction and Overview”*, Fusion Science and Technology Vol. 44 (2003) pp.569-577  
**doi: 10.13182/FST03-A399**
- 
- [7] S. Coda, J. Ahn, R. Albanese, S. Alberti, E. Alessi, S. Allan, H. Anand, G. Anastassiou, Y. Andr e et al.: *“Overview of the TCV tokamak program: scientific progress and facility upgrades”*, Nuclear Fusion Vol.57, Iss.10 (2017) 102011  
**doi: 10.1088/1741-4326/aa6412**
- 
- [8] G.M. Contessa, L. Affinito, M. Angelone, M. Guardati, S. Sandri, R. Villari: *“Divertor Tokamak Test facility - Interim Design Report”*, ENEA Frascati Research Center (2019), Frascati, Italy  
**no doi / ISBN: 978-88-8286-378-4**
- 
- [9] ITER Organization: *“ITER Research Plan within the Staged Approach (Level III - Provisional Version)”*, ITER Technical Report No. ITR-18-003 (2018)  
**no doi / weblink:** (accessed 15.01.2022)  
<https://www.iter.org/technical-reports?id=9>
- 
- [10] G. Federici, C. Bachmann, L. Barucca, C. Baylard, W. Biel, L.V. Boccaccini, C. Bustreo, S. Ciattaglia, F. Cismondi et al.: *“Overview of the DEMO staged design approach in Europe”*, Nuclear Fusion Vol.59, Iss.6 (2019) 066013  
**doi: 10.1088/1741-4326/ab1178**
- 
- [11] W. Biel, M. de Baar, A. Dinklage, F. Felici, R. K nig, H. Meister, W. Treutterer, R. Wenninger: *“DEMO diagnostics and burn control”*, Fusion Engineering and Design Vol.96-97 (2015) pp.8-15  
**doi: 10.1016/j.fusengdes.2015.01.046**
- 
- [12] EUROFUSION, K.H. Nordlund: *“European Research Roadmap to the Realisation of Fusion Energy”*, EUROfusion, Programme Management Unit (PMU), Garching, Germany (2018)  
**no doi / ISBN: 978-3-00-061152-0**
-

- 
- [13] J.-L. Boutard, A. Alamo, R. Lindau, M. Rieth: “*Fissile core and Tritium-Breeding Blanket: structural materials and their requirements*”, *Comptes Rendus Physique* Vol.9, Iss.3-4 (2008) pp.287-302  
**doi: 10.1016/j.crhy.2007.11.004**
- 
- [14] M. Rubel: “*Fusion Neutrons: Tritium Breeding and Impact on Wall Materials and Components of Diagnostic Systems*”, *Journal of Fusion Energy* Vol.38 (2019) pp.315-329  
**doi: 10.1007/s10894-018-0182-1**
- 
- [15] G.A. Spagnuolo, R. Arredondo, L.V. Boccaccini, M. Coleman, I. Cristescu, G. Federici, F. Franza, G. Belit, C. Moreno et al.: “*Integration issues on tritium management of the European DEMO Breeding Blanket and ancillary systems*”, *Fusion Engineering and Design* Vol.171 (2021) 112573  
**doi: 10.1016/j.fusengdes.2021.112573**
- 
- [16] S.J. Zinkle, A. Möslang, T. Muroga, H. Tanigawa: “*Multimodal options for materials research to advance the basis for fusion energy in the ITER era*”, *Nuclear Fusion* Vol.53, Iss.10 (2013) 104024  
**doi: 10.1088/0029-5515/53/10/104024**
- 
- [17] P.C. Souers, “*Hydrogen Properties for Fusion Energy*”, University of California Press, Ltd., Berkeley, CA, United States of America (1986)  
**no doi / ISBN-13: 9780520055001**
- 
- [18] D. Rapisarda, I. Fernandez, I. Palermo, M. Gonzalez, C. Moreno, A. Ibarra, E. Mas de les Valls: “*Conceptual Design of the EU-DEMO Dual Coolant Lithium Lead Equatorial Module*”, *IEEE Transactions on Plasma Science* Vol. 44, Iss.9 (2016) pp.1603-1612  
**doi: 10.1109/TPS.2016.2561204**
- 
- [19] L.M. Giancarli, M. Abdou, D.J. Campbell, V.A. Chuyanov, M.Y. Ahn, M. Enoeda, C. Pan, Y. Poitevin, E. Rajendra Kumar et al.: “*Overview of the ITER TBM Program*”, *Fusion Engineering and Design* Vol.87, Iss.5-6 (2012) pp.395-402  
**doi: 10.1016/j.fusengdes.2011.11.005**
- 
- [20] C. Day, B. Butler, T. Giegerich, B. Ploeckl, S. Varoutis: “*A smart three-loop fuel cycle architecture for DEMO*”, *Fusion Engineering and Design* Vol.146, Iss.B (2019) pp.2462-2468  
**doi: 10.1016/j.fusengdes.2019.04.019**
- 
- [21] C. Day, T. Giegerich: “*The Direct Internal Recycling concept to simplify the fuel cycle of a fusion power plant*”, *Fusion Engineering and Design* Vol.88, Iss.6-8 (2013) pp.616-620  
**doi: 10.1016/j.fusengdes.2013.05.026**
- 
- [22] C. Day, B. Butler, T. Giegerich, P.T. Lang, R. Lawless, B. Meszaros: “*Consequences of the technology survey and gap analysis on the EU DEMO R&D programme in tritium, matter injection and vacuum*”, *Fusion Engineering and Design* Vol.109-111, Iss.A (2016) pp.299-308.  
**doi: 10.1016/j.fusengdes.2016.03.008**
- 
- [23] R. Lawless, B. Butler, A. Hollingsworth, P. Camp, R. Shaw: “*Tritium Plant Technology Development for a DEMO Power Plant*”, *Fusion Science and Technology* Vol.71, Iss.4 (2017) pp.679-686  
**doi: 10.1080/15361055.2017.1290948**
- 
- [24] T. Giegerich, C. Day: “*The KALPUREX-process - A new vacuum pumping process for exhaust gases in fusion power plants*”, *Fusion Engineering and Design* Vol.89, Iss.7-8 (2014) pp.1476-1481  
**doi: 10.1016/j.fusengdes.2014.03.082**
-



- 
- [25] Y. Hörstensmeyer, B. Butler, C. Day, F. Franza: “*Analysis of the EU-DEMO fuel cycle elements: Intrinsic impact of technology choices*”, Fusion Engineering and Design Vol.136, Iss.A (2018) pp.314-318  
**doi: 10.1016/j.fusengdes.2018.02.015**
- 
- [26] Britannica Global Edition, *Encyclopædia Britannica*, Oxford University Press (2016), Oxford, United Kingdom  
**no doi / ISBN: 978-1625134189**
- 
- [27] M.B. Kalinoswki: “*International Control of Tritium for Nuclear Nonproliferation and Disarmament*”, Science and Global Security Monograph Series, CRC Press 2004, London, United Kingdom  
**doi: 10.1201/9780203569337**
- 
- [28] R.J. Walker, M.R. Gilbert. “*Neutron activation of impurity seeding gases within a DEMO environment*”, Fusion Engineering and Design Vol.124 (2017) pp.892-895  
**doi: 10.1016/j.fusengdes.2017.01.057**
- 
- [29] VDI-Gesellschaft Verfahrenstechnik und Chemieingenieurwesen (Publisher): “*VDI-Wärmeatlas*“, 11<sup>th</sup> Edition, Springer-Verlag, Berlin Heidelberg 2013, Part D.3 Thermophysikalische Stoffeigenschaften, D 3.1. Table 1. Kritische und andere skalare Daten  
**doi: 10.1007/978-3-642-19981-3**
- 
- [30] Y.H. Huang, G.B. Chen: “*A practical vapor pressure equation for helium-3 from 0.01 K to the critical point*”, Cryogenics Vol.46, Iss.12 (2006) pp.833-839  
**doi: 10.1016/j.cryogenics.2006.07.006**
- 
- [31] Y. Zhang, J.R. Evans, S. Yang: “*Corrected Values for Boiling Points and Enthalpies of Vaporization of Elements in Handbooks*”, Journal of Chemical & Engineering Data Vol.56, Iss.2 (2011) pp.328-337  
**doi: 10.1021/je1011086**
- 
- [32] S. Angus, B. Armstrong (editors): “*International Thermodynamic Tables of the Fluid State, Argon*”, Butterworths-Heinemann, London, England 1972  
**doi: 10.1016/C2013-0-04195-3**
- 
- [33] F. Theeuwes and R.J. Bearman: “*The p,V,T behavior of dense fluids V. The vapor pressure and saturated liquid density of xenon*”, Journal of Chemical Thermodynamics Vol.2, Iss.4 (1970) pp.507-512  
**doi: 10.1016/0021-9614(70)90100-X**
- 
- [34] B.J. Peters: “*Development of a Hydrogen-Selective Vacuum Pump on the Basis of Superpermeation*”, KIT Open (2020) Karlsruhe Institute of Technology, Karlsruhe Germany. Doctoral Thesis at the Faculty of Mechanical Engineering  
**doi: 10.5445/IR/1000122305**
- 
- [35] C. San Marchi, B.P. Somerday, R.S. Larson, S.F. Rice: “*Solubility of hydrogen and its isotopes in metal from mixed gases*”, Journal of Nuclear Material Vol.372, Iss.2-3 (2008) pp.421-425  
**doi: 10.1016/j.jnucmat.2007.02.016**
- 
- [36] W.M. Jones: “*Thermodynamic Functions for Tritium Deuteride. The Dissociation of Tritium Deuteride. Equilibria among the Isotopic Hydrogen Molecules*”, Journal of Chemical Physics Vol.17 (1949) pp.1062-1064  
**doi: 10.1063/1.1747113**
- 
- [37] J.W. Pyper, P.C. Souers: “*The Chemical Equilibria Relating the Isotopic Hydrogens at Low Temperatures*”, Technical Report UCRL-52104 (1976)  
**doi: 10.2172/7224681**
-

- 
- [38] P.C. Souers: “*Cryogenic Hydrogen Data Pertinent to Magnetic Fusion Energy*”, Lawrence Livermore National Laboratory Report, Livermore, CA, United States of America (1979) UCRL-52628  
**doi: 10.2172/6205719**
- 
- [39] A.E. Sherwood: “*Vapor pressure of HD, HT, and DT*”, Fluid Phase Equilibria Vol.51 (1989) pp.327-338  
**doi: 10.1016/0378-3812(89)80374-7**
- 
- [40] E.R. Grilly: “*The Vapor Pressures of Hydrogen, Deuterium and Tritium up to Three Atmospheres*”, Journal of the American Chemical Society Vol.73, Iss.2 (1951) pp.843-846  
**doi: 10.1021/ja01146a103**
- 
- [41] A. Busigin: “*Rigorous Two-Fluid and Three-Fluid Liquid Phase Catalytic Exchange Models and their Application*”, Fusion Science and Technology Vol.71, Iss.3 (2017) pp.438-443  
**doi: 10.1080/15361055.2017.1293411**
- 
- [42] H.C. Urey: “*The Thermodynamic Properties of Isotopic Substances*”, Journal of Chemical Society (Resumed) (1947) pp.562-581  
**doi: 10.1039/JR9470000562**
- 
- [43] N. Matsunaga, A. Nagashima: “*Saturation Vapor Pressure and Critical Constants of H<sub>2</sub>O, D<sub>2</sub>O, T<sub>2</sub>O, and their Isotopic Mixtures*”, International Journal of Thermodynamics Vol.8, Iss.6 (1987) pp.681-694  
**doi: 10.1007/BF00500788**
- 
- [44] Y. Igitkhanov, R. Fetzer: “*Effect of steady state and ELMy heat loads on the PFC of DEMO*”, Fusion Engineering and Design Vol.124 (2017) pp.478-482  
**doi: 10.1016/j.fusengdes.2016.12.032**
- 
- [45] D. Perrault: “*Safety issues to be taken into account in designing future nuclear fusion facilities*”, Fusion Engineering and Design Vol.109-111, Iss.B (2016) pp.1733-1738  
**doi: 10.1016/j.fusengdes.2015.10.012**
- 
- [46] P. Cortes, M. Iseli, N. Taylor: “*Sensitivity Studies on the Accidental Impact of 1 G of Tritium for ITER Site Specific Characteristics*”, Fusion Science and Technology Vol.60, Iss.3 (2011) pp.865-868  
**doi: 10.13182/FST11-A12555**
- 
- [47] T. Giegerich, C. Day, C. Gliss, X. Luo, H. Strobel, A. Wilde, S. Jimenez: “*Preliminary configuration of the torus vacuum pumping system installed in the DEMO lower port*”, Fusion Engineering and Design Vol.146, Iss.B (2019) pp.2180-2183  
**doi: 10.1016/j.fusengdes.2019.03.147**
- 
- [48] M.A. Abdou, E.L. Vold, C.Y. Gung, M.Z. Youssef, K. Shin: “*Deuterium-Tritium Fuel Self-Sufficiency in Fusion Reactors*”, Fusion Technology Vol.9, Iss.2 (1986) pp.250-285  
**doi: 10.13182/FST86-A24715**
- 
- [49] W. Kuan, M.A. Abdou: “*A New Approach for Assessing the Required Tritium Breeding Ratio and Startup Inventory in Future Fusion Reactors*”, Fusion Technology Vol.35, Iss.3 (1999) pp.309-353  
**doi: 10.13182/FST99-A84**
- 
- [50] R. Kasada, S. Kwon, S. Konishi, Y. Sakamoto.: “*A system dynamics model for stock and flow of tritium in fusion power plant*”, Fusion Engineering and Design Vol.98-99 (2015) pp.1804-1807  
**doi: 10.1016/j.fusengdes.2015.03.047**
-

- 
- [51] Z. Zhu, B. Nie, D. Chen: “A system dynamics model for tritium cycle of pulsed fusion reactor”, Fusion Engineering and Design Vol.118 (2017) pp.5-10  
**doi: 10.1016/j.fusengdes.2017.02.049**
- 
- [52] S.S Ananyev, A.V. Sptysin, B.V. Kuteev: “Concept of DT fuel cycle for a fusion neutron source DEMO-FNS”, Fusion Engineering and Design Vol.109-111, Iss.A (2016) pp.57-60  
**doi: 10.1016/j.fusengdes.2016.03.053**
- 
- [53] F. W. Perkins, D.E. Post, N.A. Uckan, M. Azumi, D.J. Campbell, N. Ivanov, N.R. Sauthoff, M. Wakatani., W.M. Nevins et al.: “ITER Physics Basics, Chapter 1: Overview and summary”, Nuclear Fusion Vol.39, Iss.12 (1999) 2137  
**doi: 10.1088/0029-5515/39/12/301**
- 
- [54] W. Kuan, M.A. Abdou, R.S. Willms: “Dynamic Simulation of a Proposed ITER Tritium Processing System”, Fusion Technology Vol.28, Iss.3P1 (1995) pp.664-671  
**doi: 10.13182/FST95-A30480**
- 
- [55] A. Busigin, P. Gierszewski: “CFTSIM-ITER dynamic fuel cycle model”, Fusion Engineering and Design Vol.39-40 (1998) pp.909-914  
**doi: 10.1016/S0920-3796(98)00222-1**
- 
- [56] I.-R. Cristescu, L. Dörr, A. Busigin, D. Murdoch: “ITER Dynamic Tritium Inventory Modeling Code”, Fusion Science and Technology Vol.48, Iss.1 (2005) pp.343-348  
**doi: 10.13182/FST05-A939**
- 
- [57] E. Carella, C. Moreno, F.R. Ugorri, D. Rapisarda, A. Ibarra: “Tritium modelling in HCPB breeder blanket at a system level”, Fusion Engineering and Design Vol.124 (2017) pp.687-691  
**doi: 10.1016/j.fusengdes.2017.01.051**
- 
- [58] A. Ovcharov: “More Precise Values of Separation Factors in Water-Hydrogen Isotopic Exchange for Modeling of Combined Electrolysis and Catalytic Exchange Process”, Fusion Science and Technology Vol.71, Iss.3 (2017) pp.333-338  
**doi: 10.1080/15361055.2016.1273693**
- 
- [59] P. Moin: “Fundamentals of Engineering Numerical Analysis”, 2<sup>nd</sup> Edition, Cambridge University Press, Cambridge, United Kingdom (2010)  
**doi: 10.1017/CBO9780511781438**
- 
- [60] P.T. Lang, P. Cierpka, O. Gehre, M. Reichm C. Wittmann, A. Lorenz, D. Frigione, S. Kalvin, G. Kocsis, S. Maruyama: “A system for cryogenic hydrogen pellet high speed inboard launch into fusion device via guiding tube transfer”, Review of Scientific Instruments Vol.74, Iss.9 (2003) pp.3974-3983  
**doi: 10.1063/1.1602940**
- 
- [61] M.J. Watson, M. Gadeberg, T.T.C. Jones, R.M.A. Lucock, V. Riccardo, J. Tait, P. Twynam, A.D. Walden, S. Wijetunge, B. Willies: “Improvement, Commissioning and Operation of the JET pellet centrifuge”, Fusion Engineering Vol.18 (1999) pp.326-329  
**doi: 10.1109/FUSION.1999.849849**
- 
- [62] S.K. Combs, L.R. Baylor, S.J. Meitner, J.B.O. Caughman, D.A. Rasmussen, S. Maruyama: “Overview of recent developments in pellet injection for ITER”, Fusion Engineering and Design Vol.87, Iss.5-6 (2021) pp.634-640  
**doi: 10.1016/j.fusengdes.2012.01.039**
- 
- [63] P.T. Lang, C. Day, E. Fable, Y. Igithkanov, F. Köchl, R. Mooney, B. Pégourié, B. Ploekl, R. Wenninger, H. Zohm.: “Considerations on the DEMO pellet fuelling system”, Fusion Engineering and Design Vol.96-97 (2015) pp.123-128  
**doi: 10.1016/j.fusengdes.2015.04.014**
-

- 
- [64] B. Ploeckl, C. Day, A. Frattolillo, Y. Igithkanov, P.T. Lang, B. Pégourié, H. Zohm: “*Matter injection technology for DEMO, state of the art*”, Fusion Engineering and Design Vol.123 (2017) pp.186-191  
**doi: 10.1016/j.fusengdes.2017.02.020**
- 
- [65] S.J. Meitner, L.R. Baylor, S.K. Combs, D.T. Fehling, J.M. McGill, D.A. Rasmussen, J.W. Leachman: “*Twin-screw extruder development for the ITER pellet injection system*”, 23<sup>rd</sup> IEEE/NPSS Symposium on Fusion Engineering, San Diego, CA, United States of America (2009) pp.1-4  
**doi: 10.1109/FUSION.2009.5226408**
- 
- [66] J.T. Fisher: “*Diagnostic Twin Screw Extruder For Characterizing Fusion Fuel Production*”, Ph.D. Dissertation at the Washington State University, WA, United States of America (2015)  
**no doi / weblink** (accessed 15.01.2022):  
<https://s3.wp.wsu.edu/uploads/sites/44/2014/08/Fisher-Final-Dissertation.pdf>
- 
- [67] P.T. Lang, F. Cismondi, C. Day, E. Fable, A. Frattolillo, C. Gliss, F. Janky, B. Pégourié, B. Ploeckl: “*Optimizing the EU-DEMO pellet fueling scheme*”, Fusion Engineering and Design Vol.156 (2020) 111591  
**doi: 10.1016/j.fusengdes.2020.111591**
- 
- [68] B. Ploeckl, P.T. Lang, J. Jehl, M. Prechtel, S. Sotier: “*Comparison of different pellet injection systems for ELM pacing*”, Fusion Engineering and Design Vol.86, Iss.6-8 (2011) pp.1022-1025  
**doi: 10.1016/j.fusengdes.2011.02.007**
- 
- [69] P. Sonato, P. Agostinetti, T. Bolzonella, F. Cismondi, U. Fantz, A. Fassina, T. Franke, I. Furno, C. Hopf, I. Jenkins: “*Conceptual design of the DEMO neutral beam injectors: main developments and R&D achievements*”, Nuclear Fusion Vol.57, Iss.5 (2017) 056026  
**doi: 10.1088/1741-4326/aa6186**
- 
- [70] P. Sonato, P. Agostinetti, U. Fantz, T. Franke, I. Furno, A. Simonin, M.Q. Tran: “*Conceptual design of the beam source for the DEMO Neutral Beam Injectors*”, New Journal of Physics Vol.18 (2016) 125002  
**doi: 10.1088/1367-2630/18/12/125002**
- 
- [71] S. Hanke, C. Day, T. Giegerich, Y. Igithkanov, Y. Kathage, X. Luo, S. Varoutis, A. Vazquez Cortes, T. Härtl et al.: “*Progress of the R&D programme to develop a metal foil pump for DEMO*”, Fusion Engineering and Design Vol.161 (2020) 111890  
**doi: 10.1016/j.fusengdes.2020.111890**
- 
- [72] Y. Nakamura, N. Obyabu, H. Suzuki, Y. Nakahara, A.I. Livshits, M.E. Notkin, V. Alimov, A. Busnyuk: “*Development of divertor pumping system with superpermeable membrane*”, Fusion Engineering and Design Vol.49-50 (2000) pp.899-904  
**doi: 10.1016/S0920-3796(00)00332-X**
- 
- [73] A.I. Livshits, M.E. Notkin, A.A. Samartsev: “*Physico-chemical origin of superpermeability — Largescale effects of surface chemistry on “hot” hydrogen permeation and absorption in metals*”, Journal of Nuclear Materials Vol.170, Iss.1 (1990) pp.79-94  
**doi: 10.1016/0022-3115(90)90329-L**
- 
- [74] B.J. Peters, S. Hanke, C. Day: “*Metal Foil Pump performance aspects in view of the implementation of Direct Internal Recycling for future fusion fuel cycles*”, Fusion Engineering and Design Vol.136, Iss.B (2018) pp.1467-1471  
**doi: 10.1016/j.fusengdes.2018.05.036**
-

- 
- [75] X. Luo, C. Day: “*Investigation of a New Monte Carlo Method for the Transitional Gas Flow*”, AIP Conference Proceedings Vol.1333 Iss.1 (2011), pp.272-276  
**doi: 10.1063/1.3562660**
- 
- [76] C. Day, K. Battes, B. Butler, S. Davies, L. Farina, A. Frattolillo, R. George, T. Giegerich, S. Hanke et al.: “*The pre-concept design of the DEMO tritium, matter injection and vacuum systems*”, Fusion Engineering and Design Vol.179 (2022) 113139  
**doi: 10.1016/j.fusengdes.2022.113139**
- 
- [77] K. Battes, C. Day, V. Rohde: “*Basic considerations on the pump-down time in the dwell phase of a pulsed fusion DEMO*”, Fusion Engineering and Design Vol.100 (2015) pp.431-435  
**doi: 10.1016/j.fusengdes.2015.07.011**
- 
- [78] C. Gliss, R. Ambrosino, C. Bachmann, S. Ciattaglia, D. Flammini, T. Giegerich, S. Jiménez, A. Wilde: “*Initial integration concept of the DEMO lower horizontal port*”, Fusion Engineering and Design Vol.146, Iss.B (2019) pp.2667-2670  
**doi: 10.1016/j.fusengdes.2019.04.078**
- 
- [79] S. Varoutis, F. Bonelli, C. Day, Y. Igithkanov: “*Optimization of pumping efficiency and divertor operation in DEMO*”, Nuclear Materials and Energy Vol.12 (2017) pp.668-673  
**doi: 10.1016/j.nme.2017.04.001**
- 
- [80] N. Dongari, A. Sharma, F. Durst: “*Pressure-driven diffusive gas flows in micro-channels: From the Knudsen to the continuum regimes*”, Microfluidics and Nanofluidics Vol.6, Iss.5 (2009) pp.679-692  
**doi: 10.1007/s10404-008-0344-y**
- 
- [81] S. Varoutis, Y. Igithkanov, C. Day: “*Assessment of the 3D geometrical effects on the DEMO divertor pumping efficiency*”, Nuclear Materials and Energy Vol.19 (2019) pp.120-123  
**doi: 10.1016/j.nme.2019.02.021**
- 
- [82] E. Lind, F. Steinhaus: “*Development of a large, linear jet, mercury diffusion pump having high pumping speeds in the 10–6mm. mercury absolute pressure range*”, Vacuum Vol.3, Iss.2 (1953) pp.190  
**doi: 10.1016/0042-207X(53)90313-3**
- 
- [83] T. Giegerich: “*Novel vacuum pumping concepts for fusion power plants*”, KIT Open (2016) Karlsruhe Institute of Technology, Karlsruhe Germany  
**doi: 10.5445/IR/1000056126**
- 
- [84] T. Giegerich, C. Day, M. Jäger: “*Mercury ring pump proof-of-principle testing in the THESEUS facility*”, Fusion Engineering and Design Vol.124 (2017) pp.809-813  
**doi: 10.1016/j.fusengdes.2017.03.119**
- 
- [85] C. Gliss, S. Ciattaglia, W. Korn, I. Moscato: “*Initial layout of DEMO buildings and configuration of the main plant systems*”, Fusion Engineering and Design Vol.36, Iss.A (2018) pp.534-539  
**doi: 10.1016/j.fusengdes.2018.02.101**
- 
- [86] F.J. Ackerman, G.J. Koskinas: “*Permeation of hydrogen and deuterium through palladium-silver alloys*”, Journal of Chemical and Engineering Data Vol.17, Iss.1 (1972) pp.51-55  
**doi: 10.1021/jc60052a011**
- 
- [87] M. Glugla, I.-R. Cristescu, I. Cristescu, D. Demange: “*Hydrogen isotope separation by permeation through palladium membranes*”, Journal of Nuclear Materials Vol.355, Iss.1-3 (2006) pp.47-53  
**doi: 10.1016/j.jnucmat.2006.04.003**
-

- 
- [88] S. Tosti, A. Adrover, A. Basile, V. Camilli, G. Chiappetta, V. Violante: “*Characterization of thin wall Pd-Ag rolled membranes*”, International Journal of Hydrogen Energy Vol.28, Iss.1 (2003) pp.105-122  
**doi: 10.1016/S0360-3199(02)00034-4**
- 
- [89] Y. Hörstensmeyer, S. Tosti, A. Santucci, G. Bruni: “*Permeator Simulations for the EU-DEMO Fuel Cycle*”, Fusion Science and Technology Vol.76, Iss.1 (2020) pp.232-237  
**doi: 10.1080/15361055.2019.1705690**
- 
- [90] A. Santucci, M. Incelli, M. Sansovini, S. Tosti.: “*Catalytic membrane reactor for tritium extraction system from He purge*”, Fusion Engineering and Design Vol.109-111, Iss.A (2016) pp.642-646  
**doi: 10.1016/j.fusengdes.2016.02.028**
- 
- [91] C.P. O’Brien, I.C. Lee: “*CO Poisoning and CO Hydrogenation on the Surface of Pd Hydrogen Separation Membranes*”, Journal of Physical Chemistry C Vol.121, Iss.31 (2017) pp.16864-16871  
**doi: 10.1021/acs.jpcc.7b05046**
- 
- [92] A.N. Perevezentsev, A. Bell, P. D. Brennan, C. Gibbons, J. Hemmerich, S. Knipe, R. Stagg, J. Yorkshades: “*Design and Commissioning of Upgraded Impurity Processing System at the JET Facilities*”, Fusion Science and Technology Vol.41, Iss.3P2 (2002) pp.1014-1017  
**doi: 10.13182/FST02-A22737**
- 
- [93] D. Leger, P. Dinner, H. Yoshida, R. Fleming, J. Anderson, A. Andreev, M. Asahara, J.C. Boissin, P. Finn et al.: “*ITER fuel cycle*“, International Atomic Energy Agency (IAEA), ITER Documentation Series No. 31 (1991), Vienna, Austria  
**no doi / weblink** (accessed 15.01.2022):  
[https://inis.iaea.org/collection/NCLCollectionStore/\\_Public/23/015/23015809.pdf](https://inis.iaea.org/collection/NCLCollectionStore/_Public/23/015/23015809.pdf)
- 
- [94] L. Laguardia, R. Caniello, A. Cremona, G. Gatto, G. Gervasini, F. Ghezzi, G. Granucci, V. Mellera, D. Minelli et al.: “*Influence of He and Ar injection on ammonia production in N<sub>2</sub>/D<sub>2</sub> plasma in the medium flux GyM device*”, Nuclear Materials and Energy Vol.12 (2017) pp.261-266  
**doi: 10.1016/j.nme.2017.05.009**
- 
- [95] M. Glugla, R.D. Penzhorn, J.K. Anderson, J.R. Bartlit: “*On the Synthesis, Selfradiolysis, and Catalytic Decomposition of Tritiated Ammonia and Methane*”, Fusion Technology Vol.14, Iss.2 (1988) pp.683-688  
**doi: 10.13182/FST88-A25213**
- 
- [96] A. Busigin, S.K. Sood, K.M. Kalyanam: “*New High Temperature Isotopic Exchange Fuel Processing Loop Design for ITER*”, Fusion Technology Vol. 20, Iss.2 (1991) pp.179-185  
**doi: 10.13182/FST91-A29688**
- 
- [97] G. Bruni, S. Cordiner, S. Tosti: “*A novel procedure for the preliminary design of dense metal membrane modules for hydrogen separation*”, International Journal of Hydrogen Energy Vol.41, Iss.44 (2016) pp.20198-20209  
**doi: 10.1016/j.ijhydene.2016.09.092**
- 
- [98] S. Blust: “*Material characterization and transient 1D-Modelling of absorption-based separation process*”, Master thesis supervised by Prof. Dr.-Ing. J. Sauer and the author (2018), Karlsruhe Institute of Technology (KIT), Department of Chemical and Process Engineering, Institute of Catalysis Research and Technology (IKFT)  
**Master Thesis - not published**
-

- 
- [99] C. Neugebauer, Y. Hörstensmeyer, C. Day: “*Technology Development for Isotope Rebalancing and Protium Removal in the EU-DEMO Fuel Cycle*”, Fusion Science and Technology Vol.76, Iss.3 (2020) pp.215-220  
**doi: 10.1080/15361055.2019.1704139**
- 
- [100] L.K. Heung, H.T. Sessions, A.S. Poore, W.D. Jacobs, C.S. Williams: “*Next-Generation TCAP Hydrogen Isotope Separation Process*”, Fusion Science and Technology Vol.54, Iss.2 (2008) pp.399-402  
**doi: 10.13182/FST08-33**
- 
- [101] C. Laquerbe, D. Ducret, A. Ballanger, T. Pelletier, O. Baudouin, P. Sere Peyrigain: “*Optimization of a Thermal Cycling Absorption Process Design by Dynamic Simulation*”, Fusion Science and Technology Vol.41, Iss.3 (2002) pp.1121-1125  
**doi: 10.13182/FST02-A22758**
- 
- [102] Y.W. Wong, F.B. Hill: “*Equilibrium and kinetics studies of hydrogen isotope exchange on vanadium hydride*”, Journal of American Institute of Chemical Engineers Vol.25, Iss.4 (1979) pp.592-599  
**doi: 10.1002/aic.690250404**
- 
- [103] J. Pfitzner: “*Poiseuille and his law*”, Anaesthesia Vol.31, Iss.2 (1976) pp.273-275  
**doi: 10.1111/j.1365-2044.1976.tb11804.x**
- 
- [104] M. Nishikawa, T. Shiraishi, K. Murakami: “*Solubility and Separation Factor of Protium-Deuterium Binary Component System in Palladium*”, Journal of Nuclear Science and Technology Vol.33, Iss.6 (1996) pp.504-510,  
**doi: 10.1080/18811248.1996.9731943**
- 
- [105] E. Wicke, H. Brodowsky, H. Züchner: “*Hydrogen in Metals II, Chapter 3: Hydrogen in Palladium and Palladium Alloys*”, Topics in Applied Physics Vol.29 (1978) pp.73-155  
**doi: 10.1007/3-540-08883-0**
- 
- [106] G. Sicking: “*Über das Absorptions- und Verteilungsgleichgewicht von Tritium an Palladium*”, Zeitschrift für Physikalische Chemie Vol.93 (1974) pp.53-64  
**doi: 10.1524/zpch.1974.93.1-6.053**
- 
- [107] R. Lässer, K.-H. Klatt, P. Mecking, H. Wenzl: “*Tritium in Metalle: Präparationstechnik (Tritiumlabor); Eigenschaften von Tritium in Vanadium, Niob, Tantal und Palladium*”, Berichte der Kernforschungsanlage Jülich 1800, V, 146 p. Jülich, Germany (1982)  
**Jülich Report FZJ-2016-04796 - no doi / weblink** (accessed 15.01.2022):  
<https://juser.fz-juelich.de/record/818324>
- 
- [108] A.N. Golubkov, A.A. Yukhimchuk: “*Equilibrium Pressure of Protium and Deuterium over Vanadium Dihydride Phase*”, Hydrogen Materials Science and Chemistry of Metal Hydrides. NATO Science Series (Series II: Mathematics, Physics and Chemistry) Vol.71 (2002) pp.255-264  
**doi: 10.1007/978-94-010-0558-6\_24**
- 
- [109] A.N. Golubkov, A.A. Kononenko, A.A. Yukhimchuk: “*Thermodesorption of vanadium-hydride-based hydrogen isotope sources*”, Fusion Science and Technology Vol.48, Iss.1 (2005) pp.527-533  
**doi: 10.13182/FST05-A981**
- 
- [110] W.M. Mueller, J.P. Blackledge, G.G. Libowitz: “*Metal Hydrides, 1<sup>st</sup> Edition*”, Academic Press, Cambridge, Massachusetts, United States of America (1968)  
**doi: 10.1016/C2013-0-12462-2**
- 
- [111] J.J. Reilly, R.H. Wiswall: “*Higher hydrides of vanadium and niobium*”, Inorganic Chemistry Vol.9, Iss.7 (1970) pp.1678-1682  
**doi: 10.1021/ic50089a013**
-

- 
- [112] R.C. Bowman, R.S. Carlson, A. Attalla, C.J. Wiedenheft, R.J. DeSando: “*Metal Tritide Technology*”, Proceedings of the symposium on tritium technology related to fusion reactor systems, Miamisburg, OH, United States of America Vol.89 (1974) pp.89-104  
**no doi, weblink** (accessed 15.01.2022):  
[https://inis.iaea.org/collection/NCLCollectionStore/\\_Public/07/229/7229752.pdf?r=1](https://inis.iaea.org/collection/NCLCollectionStore/_Public/07/229/7229752.pdf?r=1)
- 
- [113] J.H. Scogin, A.S. Poore: “*Startup and Operation of a Metal Hydride Based Isotope Separation Process*”, Fusion Technology Vol.28, Iss.3P1 (1995) pp.736-741  
**doi: 10.13182/FST95-A30492**
- 
- [114] F. Sabathier, D. Brennan, N. Skinner, B. Patel: “*Assessment of the performance of the JET exhaust detritiation system*”, Fusion Engineering and Design Vol.54, Iss.3-4 (1998) pp.547-553  
**doi: 10.1016/S0920-3796(00)00583-4**
- 
- [115] A.N. Perevezentsev, B.M. Andreev, M.B. Rozenkevich, Y.S. Pak, A.V. Ovcharov, S.A. Marunich: “*Wet scrubber technology for tritium confinement at ITER*”, Fusion Engineering and Design Vol.85, Iss.7-9 (2010) pp.1206-1210  
**doi: 10.1016/j.fusengdes.2010.03.005**
- 
- [116] F. Fineschi, M. Bazzichi, M. Carcassi: “*A Study on the Hydrogen Recombination Rates of Catalytic Recombiners and Deliberate Ignition*,” Nuclear Engineering and Design Vol. 166, Iss.3 (1996) pp.481-494  
**doi: 10.1016/S0029-5493(96)01264-2**
- 
- [117] D.A. Spagnolo, A.I. Miller: “*The CECE Alternative for Upgrading/Detritiation in Heavy Water Nuclear Reactors and for Tritium Recovery in Fusion Reactors*”, Fusion Technology Vol.28, Iss.3P1 (1995) pp.748-754  
**doi: 10.13182/FST95-A30494**
- 
- [118] L.P. Roy: “*Influence of Temperature on the Electrolytic separation factor of hydrogen isotopes*”, Canadian Journal of Chemistry Vol.40, Iss.7 (1962) pp.1452-1460  
**doi: 10.1139/v62-219**
- 
- [119] M. Kinoshita, Y. Matsuda, Y. Naruse, K. Tanaka: “*Computer Analysis on Steady State Separation Characteristics of Hydrogen Isotope Separation System by Cryogenic Distillation*”, Journal of Nuclear Science and Technology Vol.18, Iss.8 (1981) pp.525-539  
**doi: 10.1080/18811248.1981.9733286**
- 
- [120] A. Ovcharov, R. Szczepanski, J. Kosek, N. Pedrosa, X. Lu, L. Basili, R. Lo Frano, D. Aquaro: “*Rigorous Dynamic Simulation of Cryogenic Distillation of Hydrogen Isotopologues in the Fuel Cycle of a Thermonuclear Reactor Based on UV Flash*”, Fusion Science and Technology Vol.76, Iss.3 (2020) pp.179-190  
**doi: 10.1080/15361055.2019.1689891**
- 
- [121] H. Kang, D. Chung, S. Yun: “*Development of depleted uranium bed for tritium fuel cycle and basic absorption/desorption experiments*”, Fusion Engineering and Design Vol.132 (2018) pp.86-89  
**doi: 10.1016/j.fusengdes.2018.04.123**
- 
- [122] R.D. Kolasinski, A.D. Shugard, C.R. Tewell, D.F. Cowgill.: “*Uranium for hydrogen storage applications: A materials science perspective*”, Technical Report No. SAND2010-5195 (2010), Sandia National Laboratories, NM and CA, United States of America  
**doi: 10.2172/993617**
- 
- [123] M. Coleman, Y. Hörstensmeyer, F. Cismondi: “*DEMO tritium fuel cycle: performance, parameter explorations, and design space constraints*”, Fusion Engineering and Design Vol.141 (2019) pp.79-90  
**doi: 10.1016/j.fusengdes.2019.01.150**
-



- 
- [124] S. Tosti, A. Basile, L. Bettinali, F. Borgognoni, F. Gallucci, C. Rizzello: “*Design and process study of Pd membrane reactors*”, International Journal of Hydrogen Energy Vol.33, Iss.19 (2008) pp.5098-5105  
**doi: 10.1016/j.ijhydene.2008.05.031**
- 
- [125] K. Katayama, Y. Someya, K. Tobita, H. Nakamura, H. Tanigawa, M. Nakamura, N. Asakura, K. Hoshino, T. Chikada et al.: “*Estimation of Tritium Permeation Rate to Cooling Water in Fusion DEMO Condition*”, Fusion Science and Technology Vol.71, Iss.3 (2017) pp.261-267  
**doi: 10.1080/15361055.2017.1288423**
- 
- [126] L. Noschese, A. Santucci, S. Tosti, F. Romanelli: “*Tritium permeation modelling in DEMO WCLL cooling system*”, Fusion Engineering and Design Vol.161 (2020) 112046  
**doi: 10.1016/j.fusengdes.2020.112046**
- 
- [127] A. Ciampichetti, F.S. Nitti, A. Aiello, I. Ricapito, K. Liger, D. Demange, L. Sedano, C. Moreno, M. Succi: “*Conceptual design of Tritium Extraction System for the European HCPB Test Blanket Module*”, Fusion Engineering and Design Vol.87, Iss.5-6 (2012) pp.620-624  
**doi: 10.1016/j.fusengdes.2012.01.047**
- 
- [128] F.A. Hernández, P. Pereslavtsev, G. Zhou, Q. Kang, S. D’Amico, J. Neuberger, L.V. Boccaccini, B. Kiss, G. Nádasí et al.: “*Consolidated design of the HCPB Breeding Blanket for the pre-Conceptual Design Phase of the EU DEMO and harmonization with the ITER HCPB TBM program*”, Fusion Engineering and Design Vol.157 (2020) 111614  
**doi: 10.1016/j.fusengdes.2020.111614**
- 
- [129] F.A. Hernández, F. Arbeiter, L.V. Boccaccini, E. Bubelis, V.P. Chakin, I. Cristescu, B.E. Ghidersa, M. González, W. Hering et al.: “*Overview of the HCPB Research Activities in EUROfusion*”, IEEE Transactions on Plasma Science Vol.46, Iss.6 (2018) pp.2247-2261  
**doi: 10.1109/TPS.2018.2830813**
- 
- [130] A. Santucci, M. Incelli, L. Noschese, C. Moreno, F. Di Fonzo, M. Utili, S. Tosti, C. Day: “*The issue of Tritium in DEMO coolant and mitigation strategies*”, Fusion Engineering and Design Vol.158 (2020) 111759  
**doi: 10.1016/j.fusengdes.2020.111759**
- 
- [131] F. Franza, L.V. Boccaccini, P. Ciampichetti, M. Zucchetti: “*Tritium transport analysis in HCPB DEMO blanket with the FUS-TPC code*”, Fusion Engineering and Design Vol.88, Iss.9-10 (2013) pp.2444-2447  
**doi: 10.1016/j.fusengdes.2013.05.045**
- 
- [132] A. Del Nevo, E. Martelli, P. Agostini, G. Bongiovì, G. Caruso, G. Di Gironimo, P.A. Di Maio, M. Eboli, R. Gianmusso et al.: “*WCLL breeding blanket design and integration for DEMO 2015: status and perspectives*”, Fusion Engineering and Design Vol.124 (2017) pp.682-686  
**doi: 10.1016/j.fusengdes.2017.03.020**
- 
- [133] M. Utili, A. Tincani, L. Candido, L. Savoldi, R. Zanino, M. Zucchetti, D. Martelli, A. Venturini: “*Tritium Extraction From HCLL/WCLL/DCLL PbLi BBs of DEMO and HCLL TBS of ITER*”, IEEE Transactions of Plasma Science Vol.47, Iss.2 (2019) pp.1464-1471  
**doi: 10.1109/TPS.2018.2886409**
- 
- [134] F.R. Ugorri, C. Moreno, E. Carella, J. Castellanos, A. Del Novo, A. Ibarra: “*Preliminary System Modeling for the EUROfusion Water Cooled Lithium Lead Blanket*”, Fusion Science and Technology Vol.71, Iss.3 (2017) pp.444-449  
**doi: 10.1080/15361055.2016.1273712**
-

- 
- [135] Y. Hatano, K. Watanabe, A. Livshits, A. Busnyuk, V. Alimov: “*Effects of bulk impurity concentration on the reactivity of metal surface: Sticking of hydrogen molecules and atoms to polycrystalline Nb containing oxygen*”, Journal of Chemical Physics Vol.127, Iss.20 (2007) 204707  
**doi: 10.1063/1.2804874**
-

# Appendix

## A1 The Helium Cooled Pebble Bed Breeding Blanket

In the Breeding Blankets of the HCPB concept, solid layers of lithium and a neutron multiplier are stacked alternately in form of radially arranged pebble beds in poloidal direction. The lithium is embedded in an ortho-silicate matrix ( $\text{Li}_4\text{SiO}_4$ ) in the form of a pebble bed. As neutrons hit the Breeding Blankets, tritium forms within the pebbles. To remove the generated tritium, the bed is overflowed with huge quantities of helium purge gas (10000  $\text{Nm}^3/\text{h}$ ). To improve the tritium capture efficiency, the purge gas is doped with protium to force a hydrogen exchange reaction at the pebble surface. Currently the foreseen protium dosage amounts to 0.1 % of the helium throughput  $F_{\text{in}}(\text{H}_2) = 281.3 \text{ Pa} \cdot \text{m}^3/\text{s}$ .

The substitution of protium with deuterium as flush gas is under discussion, which would lower protium ingress at the cost of worse exchange reactivity at the pebble surface. Additionally, given the large throughput of the purge gas, this approach results in a substantial source of fuel gas disequilibrium. Therefore, deuterium should be disregarded for this application.

Furthermore, the presence of oxygen in the silicate structure will force a fraction of the gas mixture downstream the BB to be partially oxidized [127]. In summary, large quantities of protium with a fraction of tritium in the form of HT or HTO as well as helium is the expected output of the system block. The whole concept is described in [128] as an evolution of the ITER test blanket modules.

The tritiated purge gas is directed to the TERS, where the hydrogen mixture is isolated from the helium carrier in series of Molecular Sieve Beds (MSB) [129]. Prior to that, tritiated water is condensed out, separated and directed to the Water Detritiation System. The MSB collect the hydrogen gas and send them to the ISS system. In addition to hydrogen gas, the sieve beds are bound to capture a fraction of the helium carrier. A permeator subsystem - like the one employed in the EPS - is therefore installed downstream the sieve beds. The permeate ( $Q_2$ ) and retentate ( $Q_2 + \text{He}$ ) are directed to the ISS and EDS. The non-captured helium is returned to the Breeding Blankets after being topped-off and doped with new protium.

In addition to the application as purge gas, helium doubles as the coolant in the HCPB concept. In a separated cycle even larger quantities of helium are circulated to maintain a constant temperature during operation (2400 kg/s). A part of the hydrogen content permeates from the BB into the coolant loops. The hydrogen concentration in the coolant is kept in check by bypassing a fraction of the throughput into absorption beds [130].

The setup of the HCPB blanket as implemented into the fuel cycle is shown in Figure 9.1. The output of the HCPB as published in [129] is shown in Table 9.1. However, these values are not scaled for a fusion power plant of  $P_{\text{Thermal}} = 2000 \text{ MW}$ . Calculated from Table 9.1, the steady-state output of tritium is  $F_{\text{breed}} = 0.944 \text{ Pa} \cdot \text{m}^3/\text{s}$  as opposed to a tritium consumption of  $F_{\text{burn}} = 1.34 \text{ Pa} \cdot \text{m}^3/\text{s}$ . The Breeding Blanket hydrogen throughput from Table 9.1 is thus scaled for  $F_{\text{breed}} = F_{\text{burn}} \cdot \text{TBR}$  to satisfy the requirement of tritium self-sufficiency of DEMO.

To calculate the Reference Design Point following assumptions are made:

- The Tritium Breeding Ratio is 1.05 as assumed in the RDP.  $TBR = 1.05$
- 90 % the Breeding Blanket output is processed in the TERS.  $\alpha_{HCPB} = 0.9$
- The TERS condenser and MSB remove all their water and hydrogen input, respectively.  $\eta_{to\_WDS} = 1.0$   
 $\eta_{MSB} = 1.0$
- The Molecular Sieve Bed output is contaminated with 10 % He.  $\gamma_{MSB}(He) = 1/11$
- The TERS permeator subsystem has a removal efficiency of 99 %  $\eta_{to\_ISS} = 0.99$
- The leak rate from the BB to the helium coolant loops is assumed as 0.37 % [131] for the throughput of both H<sub>2</sub> and HT.  $\eta_{leak} = 0.0037$
- Permeation of water in this context is neglected.  $\eta_{Q_2O} = 0.0$
- No anti-permeation coatings are applied.  $PRF = 1$
- The CPS hydrogen output matches the leak rate.  $F_{leak} = F_{CPS}$

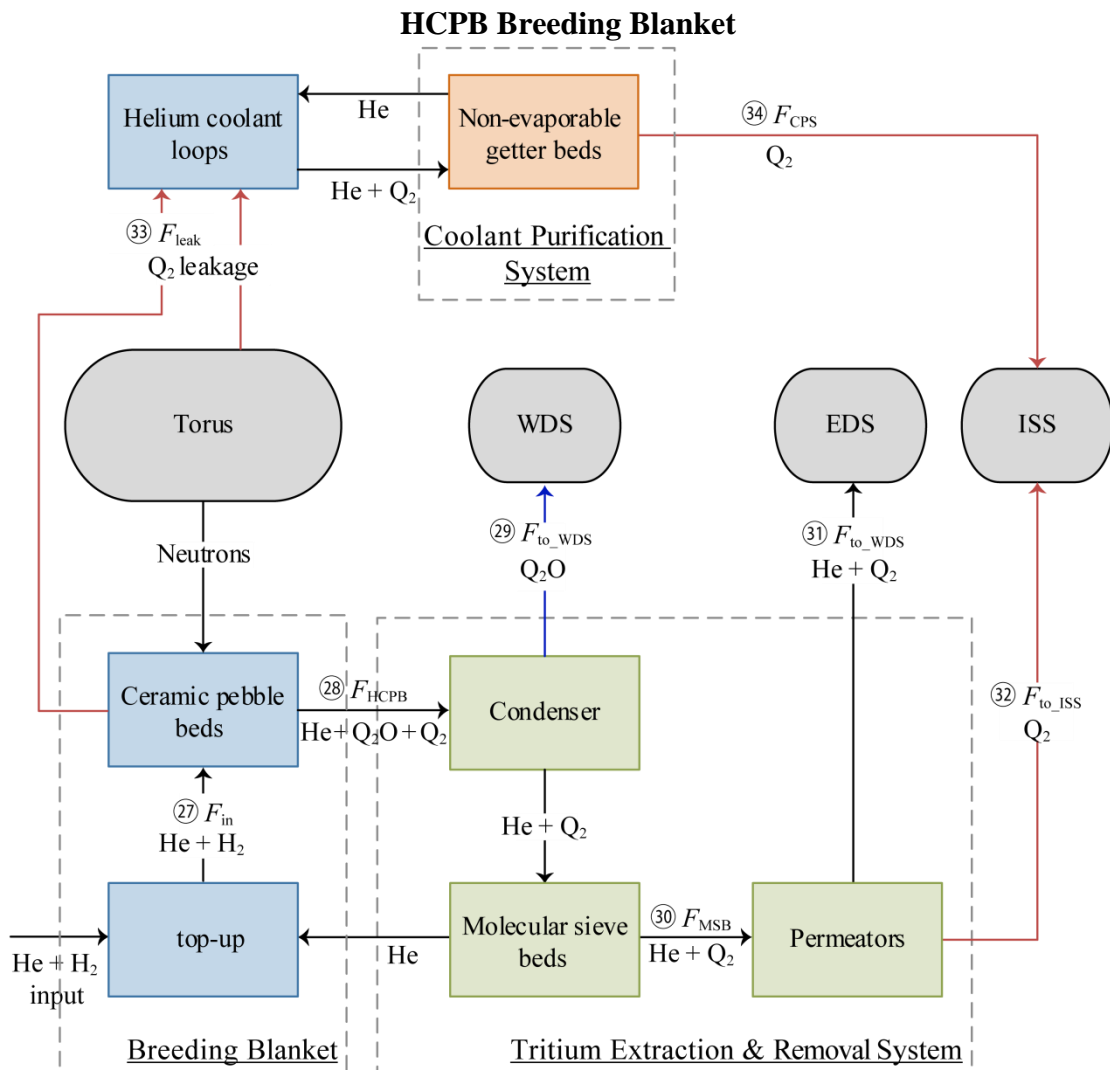


Figure 9.1: Flowchart of the Helium Cooled Pebble Bed concept with the three system blocks “Breeding Blanket”, “Tritium Extraction and Removal” as well as “Coolant Purification System” as implemented into the fuel cycle simulator.

Table 9.1: Expected throughputs and composition of the Outer Fuel Cycle system blocks, with the HCPB Breeding Blanket outputs taken from [129]. Helium  $F(\text{He})$  and hydrogen  $F(\text{Hyd}) = F(\text{Q}_2) + F(\text{Q}_2\text{O})$  are split for readability.

Stream	$F_{\text{in}}$	$F_{\text{HCPB}}$	$F_{\text{to\_WDS}}$	$F_{\text{MSB}}$	$F_{\text{to\_EDS}}$	$F_{\text{to\_ISS}}$	$F_{\text{leak}}$	$F_{\text{CPS}}$	Unit
$F(\text{He})$	$2.81 \cdot 10^6$	$2.81 \cdot 10^6$	-	26.90	26.90	-	-	-	(Pa $\cdot \text{m}^3/\text{s}$ )
$F(\text{Hyd})$	281.39	281.39	8.78	242.07	2.42	239.65	1.04	1.04	(Pa $\cdot \text{m}^3/\text{s}$ )
$y(\text{H}_2)$	99.54	95.77	-	99.25	99.25	99.25	99.25	99.25	(mol%)
$y(\text{HT})$	0.08	0.73	-	0.75	0.75	0.75	0.75	0.75	(mol%)
$y(\text{H}_2\text{O})$	0.37	3.48	99.25	-	-	-	-	-	(mol%)
$y(\text{HTO})$	$2.84 \cdot 10^{-3}$	0.03	0.75	-	-	-	-	-	(mol%)

This is scaled by a factor of  $\sim 1.5$  and used as boundary condition for the RDP in Table 9.2:

Table 9.2: Expected throughputs and composition of the HCPB Outer Fuel Cycle system blocks after application of the scaling factor to the values of Table 9.1. Helium  $F(\text{He})$  and hydrogen  $F(\text{Hyd}) = F(\text{Q}_2) + F(\text{Q}_2\text{O})$  are split for readability.

Stream	$F_{\text{in}}$ (27)	$F_{\text{HCPB}}$ (28)	$F_{\text{to\_WDS}}$ (29)	$F_{\text{MSB}}$ (30)	$F_{\text{to\_EDS}}$ (31)	$F_{\text{to\_ISS}}$ (32)	$F_{\text{leak}}$ (33)	$F_{\text{CPS}}$ (34)	Unit
$F(\text{He})$	$2.81 \cdot 10^6$	$2.81 \cdot 10^6$	-	32.74	32.74	-	-	-	(Pa $\cdot \text{m}^3/\text{s}$ )
$F(\text{Hyd})$	418.07	418.07	13.06	360.18	3.6	356.58	1.55	1.55	(Pa $\cdot \text{m}^3/\text{s}$ )
$y(\text{H}_2)$	99.54	95.77	-	99.25	99.25	99.25	99.25	99.25	(mol%)
$y(\text{HT})$	0.08	0.73	-	0.75	0.75	0.75	0.75	0.75	(mol%)
$y(\text{H}_2\text{O})$	0.37	3.48	99.25	-	-	-	-	-	(mol%)
$y(\text{HTO})$	$2.84 \cdot 10^{-3}$	0.03	0.75	-	-	-	-	-	(mol%)

## A2 The Water Cooled Lithium Lead Breeding Blanket

In the Water Cooled Lithium Lead (WCLL) concept, an alloy is liquefied and continuously circulated through the Breeding Blanket. The liquid metal combines enriched  $^6\text{Li}$  as breeder with the neutron multiplier lead. The pre-conceptual design for DEMO is summarized in [132].

Downstream the blanket, the generated tritium is extracted from the liquid metal by a separation process yielding pure tritium. Several technologies are investigated in the context of ITER and DEMO to be implemented in the TERS. ITER will include a Gas-Liquid Contactor for this purpose, with an estimated hydrogen removal efficiency of  $\eta_{\text{GLC}} < 40\%$ . Potential substitute candidates for DEMO are the Permeation Against Vacuum and Vacuum Sieve Tray technologies, each with a theoretical efficiency of  $\eta_{\text{PAV}} > 80\%$  and  $\eta_{\text{VST}} > 80\%$ . However, they remain to be tested to reach comparable technical maturity. A comparative analysis can be found in [133].

Cooling of the WCLL is achieved by circulating a tremendous amount of water ( $720 \text{ m}^3 \text{ H}_2\text{O}$ ). Given the elevated temperatures, a considerable fraction of the tritium generated in the Breeding Blankets is expected to leak into the water coolant ( $F_{\text{leak}} = 37.4 \text{ g/d}$ ) [134]. This yields  $\eta_{\text{leak}} \approx 11.6\%$  of the tritium generated in a full-power day and impede the tritium self-sufficiency requirement. Therefore, anti-permeation coatings and a Water Detritiation System must be installed. The latter can be realised as an in-line or off-line facility of similar design to the CECE column implemented in the WDS system, which remains to be decided. This issue and suitable approaches are discussed in [126]. The setup of the WCLL blanket - as implemented into the fuel cycle - is shown in Figure 9.2. The expected outputs to the fuel cycle of the WCLL concept are summarized in Table 9.3.

To quantify the expected output of the WCLL concept, following assumptions are used to generate the values in Table 9.3. The resulting throughputs do not represent a considerable burden on the Inner Fuel Cycle ( $\textcircled{37}$  is pure tritium and  $\textcircled{39}$  is only a small input to the OUTL). Therefore, the values are not included as a boundary condition to the fuel cycle in this work.

- All of the Breeding Blanket output is processed in the TERS.  $\alpha_{\text{WCLL}} = 1.0$
- Permeation Against Vacuum is assumed as TERS technology.  $\eta_{\text{PAV}} = 0.8$
- A Permeation Reduction Factor of 100 is achieved. The resulting leak rate from the BB to the water coolant loops is 0.374 g/d.  $\text{PRF} = 100$   
 $\eta_{\text{leak}} = 0.0012$
- No permeation occurs from the coolant loops back into the BB.  $\eta_{\text{leak\_back}} = 0.0$
- The CPS system is operated online in a separate WDS system. The tritium throughput of the CPS matches the leak rate. Tritium is extracted at a purity of 10 % in the form of HT.  $y_{\text{HT}} = 0.2$   
 $F_{\text{CPS}} = 5 \cdot F_{\text{leak}}$

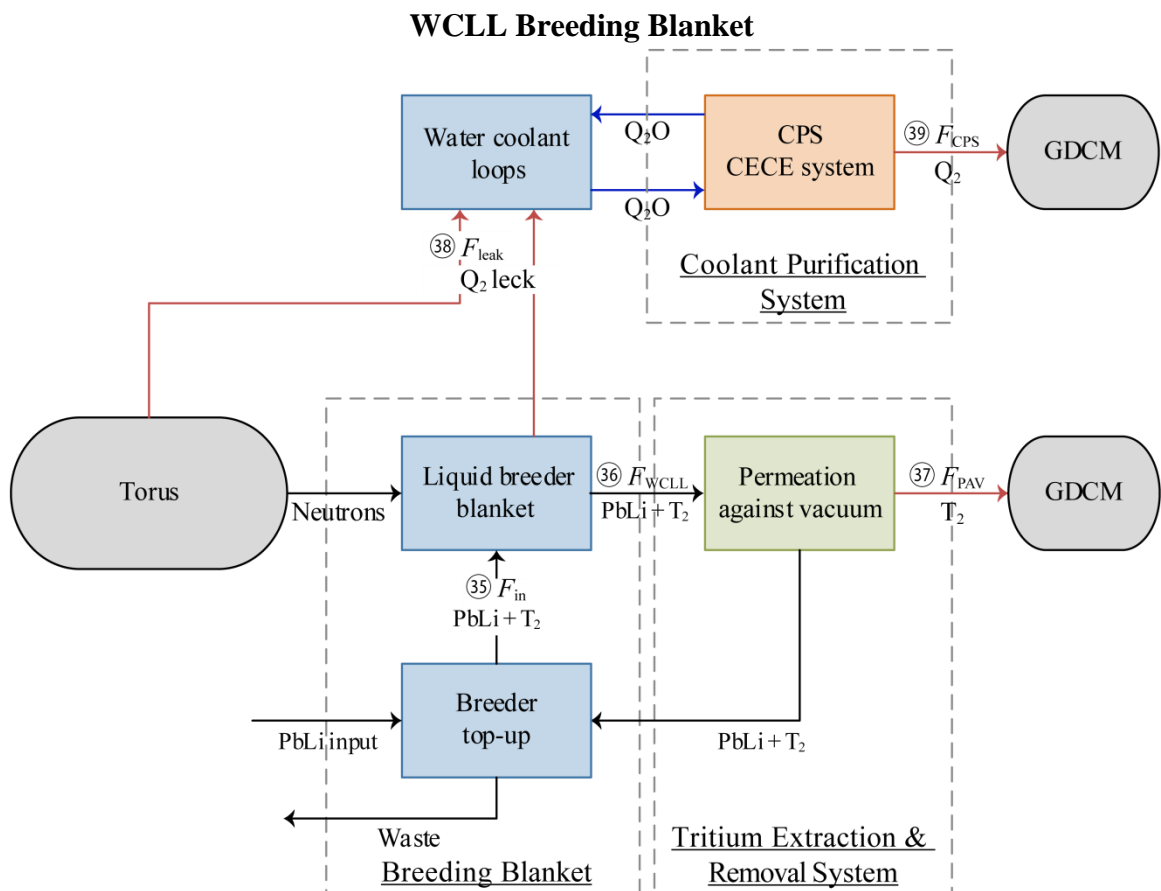


Figure 9.2: Flowchart of the Water Cooled Lithium Lead Outer Fuel Cycle concept with the three system blocks “Breeding Blanket”, “Tritium Extraction and Removal” as well as “Coolant Purification System” as implemented into the fuel cycle model.

Table 9.3: Expected throughputs and composition of the Water Cooled Lithium Lead system blocks. The carrier streams of PbLi and water are omitted for readability. Tritium generation is assumed at a Tritium Breeding Ratio of  $TBR = 1.05$  and a thermal output of  $P_{\text{thermal}} = 2 \text{ GW}$ . The leak rate is taken from [134] reduced by a Permeation Reduction Factor of 100.

Stream	$F_{\text{in}}$ $\textcircled{35}$	$F_{\text{WCLL}}$ $\textcircled{36}$	$F_{\text{PAV}}$ $\textcircled{37}$	$F_{\text{leak}}$ $\textcircled{38}$	$F_{\text{CPS}}$ $\textcircled{39}$	Unit
$F(Q_2)$	0.47	1.87	1.50	$1.87 \cdot 10^{-2}$	$8.15 \cdot 10^{-2}$	$(\text{Pa} \cdot \text{m}^3/\text{s})$
$y(\text{H}_2)$	0	0	0	0	0.8	(mol%)
$y(\text{HT})$	0	0	0	0	0.2	(mol%)
$y(\text{T}_2)$	100.0	100.0	100.0	100.0	0	(mol%)

### A3 Diffusion Process through a Metal Foil

The diffusion through the foil can be calculated by the local concentration gradient between the two surfaces of the foil. To quantify this plasma or atomic driven permeation in the fuel cycle simulator, a calculation approach similar to Equation (3.21) is implemented from [34] in Equation (9.1).

$$j_{\max} = \left(\frac{Pe}{s}\right)^2 \cdot \Delta c_{\text{diss}}, \quad (9.1)$$

where  $j_{\max}$  is the upper threshold of molar hydrogen flux in  $\text{mol}/(\text{m} \cdot \text{s} \cdot \sqrt{\text{Pa}})$  and  $\Delta c_{\text{diss}}$  is the equivalent concentration gradient in  $\text{Pa} \cdot \text{s}/\text{mol}$  based on a several process specific parameters given in Equation (9.2).

$$\Delta c_{\text{diss}} = \frac{\chi_{\text{perm}}}{2\sigma_u \alpha_{m,u}} \cdot \sqrt{\frac{\pi \tilde{M}}{2}} \cdot (RT)^{1.5}, \quad (9.2)$$

where  $\sigma_u$  and  $\alpha_{m,u}$  denote the surface roughness factor and sticking coefficient for molecular hydrogen in the upstream chamber.

The sticking coefficient  $\alpha_m$  and permeability  $Pe$  of Niobium are given by the Arrhenius equations in Equations (9.3) and (9.4).

$$\alpha_m(\text{Nb}) = \alpha_{m,0} \cdot \exp\left(\frac{E_{\alpha_m}}{RT}\right), \quad (9.3) \quad Pe(\text{Nb}) = Pe_0 \cdot \exp\left(\frac{E_A}{RT}\right), \quad (9.4)$$

With  $\alpha_{m,0}$  and  $Pe_0$  as the pre-exponential factors in (-) and  $\text{mol}/(\text{m} \cdot \text{s} \cdot \sqrt{\text{Pa}})$ , respectively. The exponential factors  $E_{\alpha_m}$  and  $E_A$  are denoted in eV with the values listed in Table 9.4.

Assuming a smooth surface ( $\sigma_u = 1$ ), a thin metal foil ( $s = 0.1 \text{ mm}$ ), a transmission probability of  $\chi = 0.3$  and a foil temperature of  $T = 600 \text{ }^\circ\text{C}$ , one obtains  $\Delta c_{\text{diss}} \approx 4.44 \cdot 10^6 \text{ Pa} \cdot \text{s}/\text{mol}$ . Equation (9.1) then yields a maximum permeation flux for tritium in such a setup of  $j_{\max} = 0.71 \text{ Pa m}^3/(\text{s m}^2)$ . This represents a higher throughput than measured in the experimental results of [34] but lower than the value obtained in the DSMC calculation. In consequence, both the experimental setup and the DSMC calculation must be improved. The former must demonstrate higher permeation fluxes by adjusting the setup parameters and the latter must be checked concerning its assumed boundary conditions.

Table 9.4: Hydrogen sticking coefficients and permeabilities in dependence of isotope of niobium.

$\alpha_{m,0}(-)$	$E_{\alpha_m}$ (eV)	Source	Isotope	$Pe_0$ $\left(\frac{\text{mol}}{\text{m} \cdot \text{s} \cdot \sqrt{\text{Pa}}}\right)$	$E_A$ (eV)	Source
0.01	0.14	[135]	H	$0.13 \cdot 10^{-7}$	-0.260	[34]
			D	$0.14 \cdot 10^{-7}$	-0.276	
			T	$0.15 \cdot 10^{-7}$	-0.217	

## A4 Hydrogen Absorption in Vanadium and Palladium

Figure 9.3 and Figure 9.4 show the desorption pressure  $p$  over hydrogen concentration in metal  $c_{Q/M}$  for vanadium [111] and palladium [107], respectively. The figures include the process cycle of the Temperature Swing Absorption process throughout the four phases: (i) 1. Sorption Phase, (ii) 1. Flow Phase, (iii) 2. Sorption Phase and (iv) 2. Flow Phase.

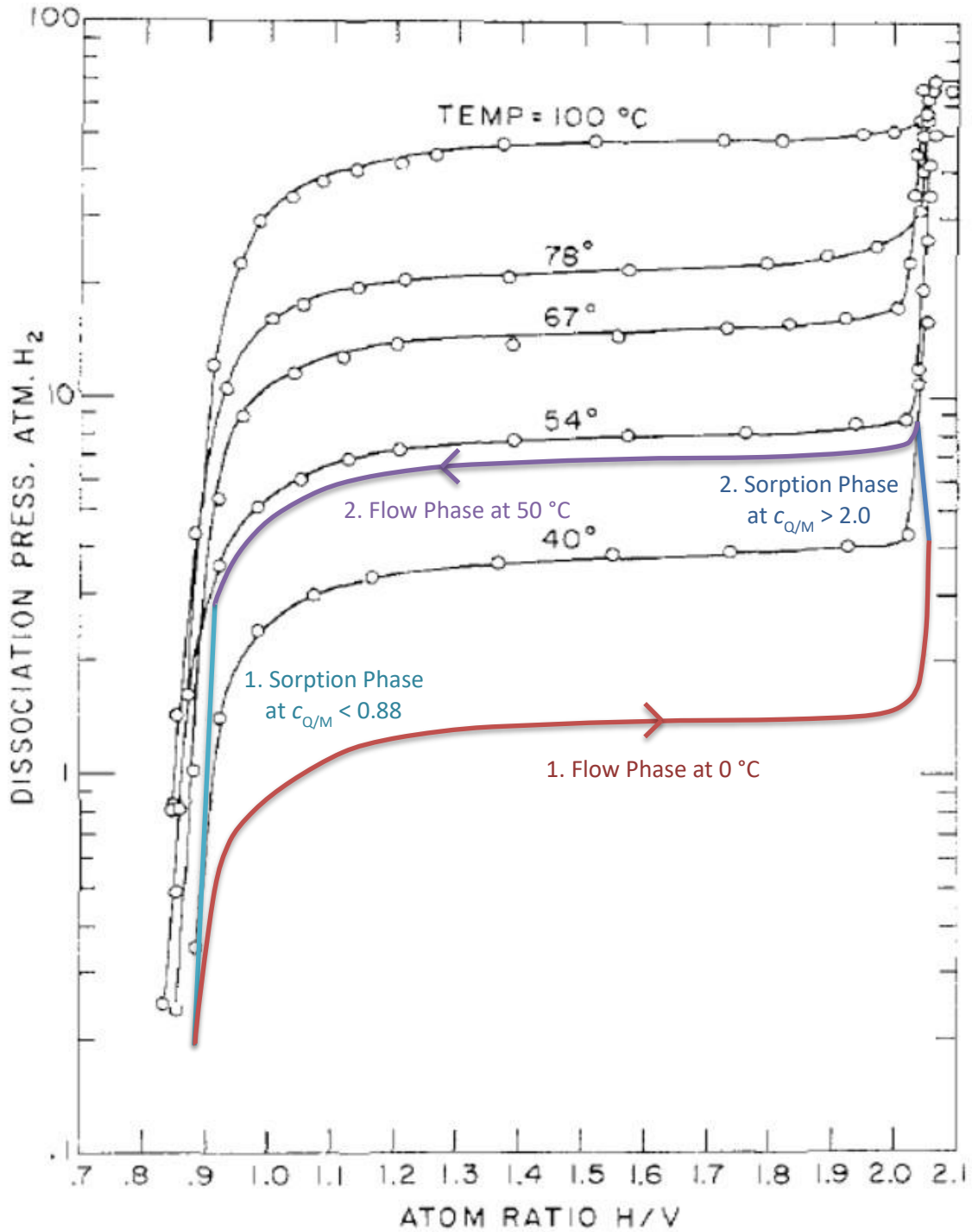


Figure 9.3: The vanadium desorption pressure isotherms for protium as a function of  $c_{Q/M}$  (shown here as “H/V”). A distinct isobaric behaviour can be seen in the  $\alpha\beta$  transition phase between  $0.88 < c_{Q/M} < 2.0$ . The graph is taken from [111] with the TSA process cycles displayed in colour.



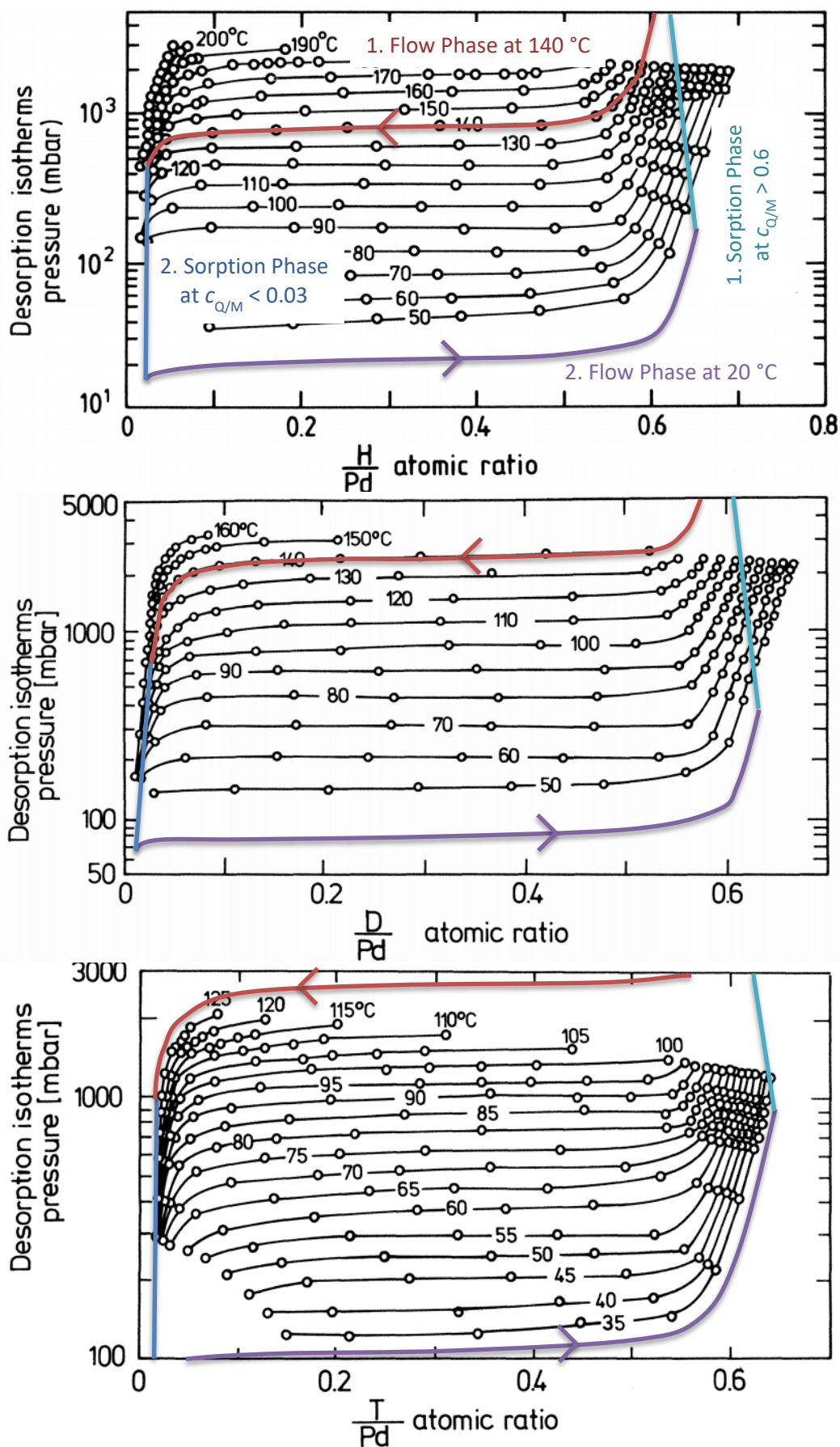


Figure 9.4: The palladium desorption pressure isotherms for all three hydrogen isotopes as a function of  $c_{Q/M}$  (shown here as “Q/Pd”). A distinct isobaric behaviour can be seen in the  $\alpha\beta$  transition phase between  $0.03 < c_{Q/M} < 0.6$ . Graphs are taken from [107] with the TSA process cycles displayed in colour.